The University Of Sheffield.

Catalytic Micromotors

By:

David Alexander Gregory

A dissertation submitted to the University of Sheffield in accordance with the requirements of the degree of Doctor of Philosophy

The University of Sheffield

The Department of Biological and Chemical Engineering.

Submission Date

April 2016

Word Count: 53042

Abstract

This thesis concerns self-motile “micromotors” using catalytic decomposition reactions to produce autonomous motion in fluids via a variety of phenomena including self-phoresis, and bubble propulsion. Catalytic micromotors may open new approaches to microfluidic transport, but require further development to realise their potential. I investigated the motion generating mechanisms for micron-sized spherical Janus particles (at low volume fractions), powered by platinum catalysed decomposition of hydrogen peroxide, and examined relationships between catalyst thickness, catalytic reaction rate and propulsion velocity, as well as the influence of salts on propulsion velocity. The data points to a new electrokinetic propulsion mechanism, and highlights potential difficulties in deploying phoretic devices in high salt fluids, including biological fluids. It was then shown that convective motion of spherical catalytically active particles can be induced purely by increasing volume fraction, even for particles that in isolation do not exhibit enhanced motion.

Studies were also made of larger, bubble-propelled spherical platinum catalytic devices. For the first time propulsive trajectories of such devices were quantified in terms of persistence length, fractal dimension and mean squared gyration. It was found that confining the catalyst to discrete regions increased directionality, but the character of motion was found to remain highly stochastic compared to phoretic swimmers. These bubble-propelled devices required no addition of surfactant for motion in water, so their motion in biological fluids was also investigated. It was found that biocompatibility was low and motion here required a surfactant mainly to inhibit biofouling of the platinum catalyst.

Finally, a 3D inkjet drop-on-demand printing method was used to make biocompatible, catalytic bubble-propelled, micro-rockets using catalase instead of platinum. These printed silk micro-rockets are the first of their kind and show high biocompatibility and longevity, as well as having a composition and shape that can be digitally defined.

Dedication

This thesis is dedicated to my parents and family,

For their endless love, support and encouragement.

I also dedicate this thesis in loving memory of

Eva Paterna

for the support she gave to me during my childhood

as well as to Inge and Laszlo Devay,

for all their encouragement.

Acknowledgements

I would like to thank my supervisor Dr Stephen Ebbens for supporting me throughout my entire PhD with lots of help and suggestions and Dr Andrew Campbell for helping me with some of the LabVIEW calculation algorithms for persistence length and fractal dimension.

Furthermore I would like to thank Yu Zhang and her Supervisor Xiubo Zhao for their supportive work in the silk swimmer collaboration, in particular Yu's help making the silk solutions and printing the particles I needed for analysis.

I also thank Dr C. Hurley from the Kroto Research institute for gathering XPS data for me and Dr E. Haq for taking some AFM images.

Finally I would like to thank the entire CBE department for their support and allowing me to use their facilities as well as the physics department for allowing me to use the Cleanroom and AFMs.

I acknowledge the support of S. Ebbens EPSRC CAF Fellowship (EP/J002492/1) to fund my PhD.

Declaration

I declare that the work in this dissertation was carried out in accordance with the Regulations of the University of Sheffield. The work is original except where indicated by special reference in the text and no part of the dissertation has been submitted for any other degree. Any views expressed in the dissertation are those of the author and in no way represent those of the University of Sheffield. The dissertation has not been presented to any other University for examination either in the United Kingdom or overseas.

SIGNED: ..... DATE:.....

Publications

[1] S. Ebbens, D. A. Gregory, G. Dunderdale, J. R. Howse, Y. Ibrahim, T. B. Liverpool, R. Golestanian, "Electrokinetic effects in catalytic platinum-insulator Janus swimmers," EPL (Europhysics Letters), vol. 106, p. 58003, 2014.

[2] D. A. Gregory, A. I. Campbell, and S. J. Ebbens, "Effect of Catalyst Distribution on Spherical Bubble Swimmer Trajectories," The Journal of Physical Chemistry C, 2015/06/10 2015.

[3] D. A. Gregory, Y. Zhang, P.J. Smith, X Zhao and S. J. Ebbens, "Reactive inkjet printing of biocompatible enzyme powered silk micro-rockets," Small, Vol.12, p.4048, 2016.

Conference Papers

[1] D. A. Gregory, Y. Zhang, P. J. Smith, S. J. Ebbens, X. Zhao, “Altering the Bubble Release of Reactive Inkjet Printed Silk Micro-rockets”, in Printing For Fabrication (NIP), Society for Imaging Science and Technology, Manchester 2016, p.452.

[2] Y. Zhang, D. A. Gregory, P. J. Smith, X. Zhao, “Regenerated silk fibroin as an inkjet printable biomaterial”, in Printing For Fabrication (NIP), Society for Imaging Science and Technology, Manchester 2016, p.406.

Posters

[1] “Electrokinetic effects in catalytic Pt-insulator Janus swimming devices” at 4th International Colloid Conference in March 2014 in Madrid (Spain).

[2] “Reactive Inkjet Printing of Biocompatible Silk Micro-rockets” at E-MRS (Symposium F: Advanced Materials for Printing) in May 2016 in Lille (France).

[3] “Controlling trajectory behaviour of bubble propelled self-motile micromotors via catalyst distribution” at International Symposium Micro- and Nanomachines in June 2016 in Hannover (Germany)

Oral Presentations

[1] “Electrokinetic Effects in Catalytic Pt-insulator Janus Swimming Devices” at 88th Colloid and Surface Science Symposium in June 2014 in Pennsylvania USA.

[2] “Altering the Bubble Release of Reactive Inkjet Printed Silk Micro-Rockets”, Focal talk at Printing for Fabrication September 2016, Manchester, UK.

Table of Contents

List of Tables

List of Figures

1. Introduction

1.1. Motion at small length scales

When viewing small particles (micro or nanometre range) suspended in a solution (e.g. in water) under a microscope they are seen to move around randomly. This is Brownian motion, due to the thermal energy of the surrounding fluid [1]. In view of this ubiquitous motion, it is clear that useful propulsion generating mechanisms, the focus of this work, must result in velocity magnitudes that exceed Brownian motion velocity.

Based on our macroscopic experiences the most obvious mechanisms for propulsion generation use reciprocal deformations, e.g. when humans swim they do so by moving their arms and legs back and forwards. However, deformations do not have the same effect on small scale devices due to the dominance of viscous forces over inertia. Viscosity is the gradual deformation of a fluid by sheer stress (τ $[N/m^2]$) or tensile stress. The dynamic (shear) viscosity (μ $[Ns/m^2]$) for a Newtonian fluid (as illustrated in Figure 1-1) can be expressed as $\tau = \mu \frac{dc}{dy}$,which is also known as Newton's Law of Friction, where dc [m/s] is the unit velocity and dy [m] the unit distance between layers.

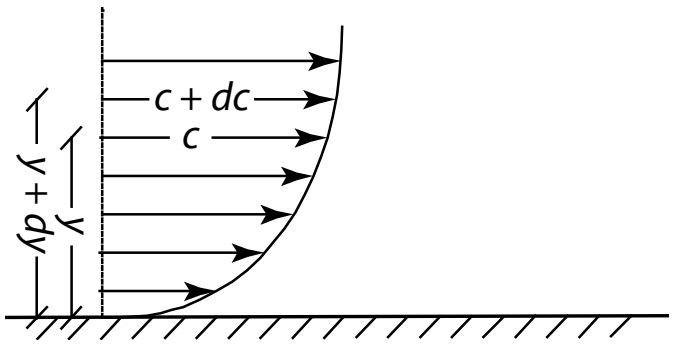

Figure 1-1 Diagram showing the shearing stress for a Newtonian fluid between layers of a non-turbulent fluid moving in straight parallel lines where the dynamic viscosity can be expressed as $\tau = \mu dc / dy$

The kinematic viscosity ν $[m^2/s]$, also known as momentum diffusivity, is described as the ratio of dynamic viscosity to density, here no force is involved, and therefore the kinematic viscosity is given by $\nu = \frac{\mu}{\rho}$, where ρ $[kg/m^3]$ is the density of the fluid.

In order to determine the dominating forces at small length scales the Reynolds number (*Re*) can be calculated. It is given by dividing the inertial forces by the viscous forces as shown in Eq. {1.1}, where '*a*' is the dimension of the object, '*v*' is its velocity, 'ρ' is the density of the liquid and 'μ' the liquid's viscosity.

$$\mathrm{Re} = \frac{av\rho}{\mu} \qquad \{1.1\}$$

Purcell [2] looked into how the size of an object affects the Reynolds number. For an average-sized human swimming in water the Reynolds number may be of the order of 10^4, whereas for a guppy Purcell suggests it could be 10^2. However, for microorganisms such as bacteria and algae, which have a size of about one micron, the Reynolds number is 10^{-4} or 10^{-5}. For such organisms inertia is of no relevance. For example, when looking at one of these organisms in water with a kinematic viscosity of 10^{-2} cm/sec and an average speed of 30 microns/sec, if it is necessary to push the organism in order for it to move, upon removal of the force the organism will travel around 0.1 Å before it stops, which will take it about 0.6 microseconds. This makes it obvious that inertia plays a vanishing role at this scale and only forces that are exerted precisely at the time of movement determine any movement, while conventional propulsion systems using reciprocal motion fail to cause propulsion [3, 4]. The example of a miniature scallop gaining no propulsion but simply moving back and forth by opening and closing its shell further emphasizes

this point [2]. The way the scallop achieves motion at the macroscale is that it opens its shells slowly and then quickly closes its shells, causing a jet of water to be squirted out propelling it forward. At low Reynolds numbers, however, time does not matter, so if the scallop opens its shell slowly and closes it fast it will land at exactly the same position again, because at this scale inertia is negligible.

Despite this, there are various natural microorganisms that have evolved active propulsion systems and are able to move at the micro scale. These systems build on the principle of non-reversible motion. For example, in order to achieve propulsion *Spirillum volutans* (a bacterium) moves its body in a waving fashion and then a spiral wave flows down the tail, similar to a corkscrew twisting into a cork [5]. *Escherichia coli* is another very well-known microbe that uses a flagellum to propel itself forward. The flagellum in simple terms works like a flexible oar [6]. Figure 1-2 emphasises how complex the design of a bacterial flagellum really is, with the different parts of the flagellum controlled by different motor proteins as described in Jarrel et al.[5].

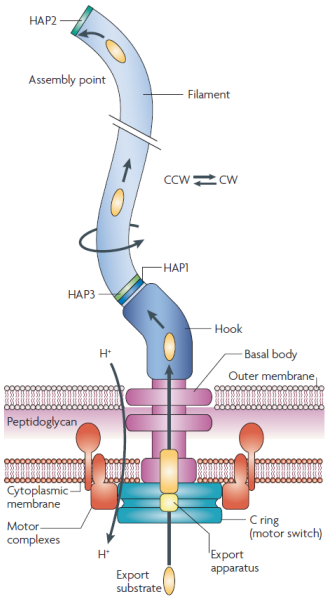

Figure 1-2 Model of the bacterial flagellum – structure and assembly, taken from [5]

Other bacteria have small mycoplasma ‘legs’ that walk along the cell´s body allowing for gliding motion, such as shown in Figure 1-3 of the bacterium Flavobacterium johnsoniae [5]. These are just some examples of the vast possibilities nature has found to overcome the problems of motion at small length scales.

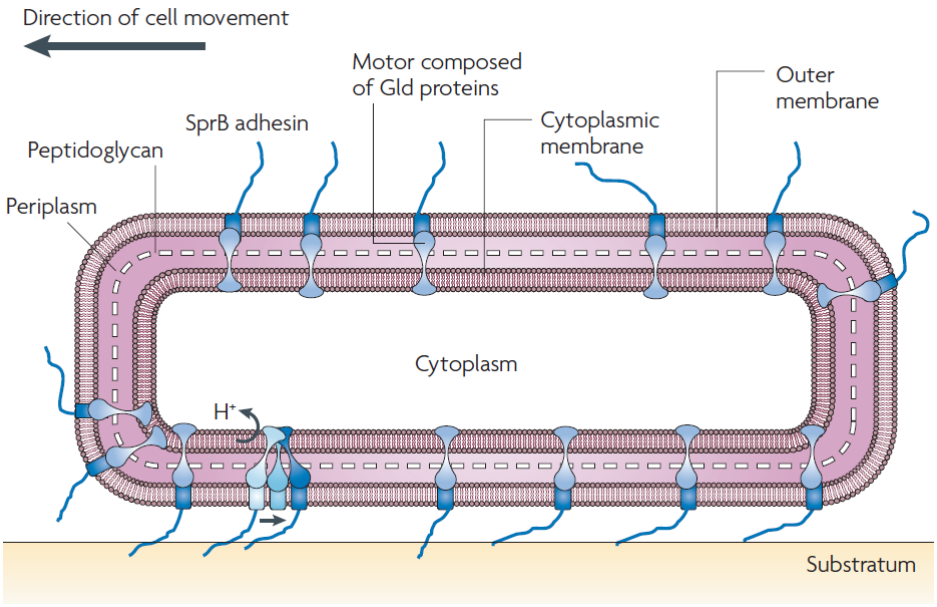

Figure 1-3 Model of the *Flavobacterium johnsoniae* gliding motility, taken from [5]

As the diagrams show, all these processes for propulsion are very complex and have taken millions of years of evolution to be created. The chemical processes that take place in order to move a flagellum are at present too complex to be replicated synthetically and therefore another approach needs to be taken in order to achieve motion at small scales. Synthetic flagella have been attached to cells, but these require external fields in order to generate motion [7]. Similarly, because an actively working flagellum is still too difficult to create synthetically, those from bacteria such as E.coli have been genetically modified and have then been tethered onto surfaces to make use of the flagellum for microfluidic applications [8]. These processes are in general not suitable for large scale production processes.

Therefore in order to synthetically produce particles that can move on their own in a liquid at the micro- and nano-scale, a simpler approach, which has attracted increasing research attention over that last ten years, has emerged. Either an interfacial gradient is generated over a particle via surface chemical reactions [9], or particles are propelled via gas bubbles , which are expelled from the surface of the object, again due to chemical reactions [10]. Self-motile particles such as these are often referred to as 'swimmers', micro-jets or micromotors. In order to be called self-motile particles, they must have no need for any external forces or fields to power propulsion, but simply rely on chemical reactions / effects on their surface to act as the motor [11].

At this stage it may be asked for what applications synthetic, self-motile particles might be used in the future. The most widely discussed putative application for these devices is to aid targeting for drug delivery systems [12] and thus help achieve safer delivery of drugs or other chemicals in the human body, i.e. to decrease the unwanted side-effects of drugs by increasing the drug concentration in the target organs at a lower systemic dosage [13]. Other applications include: nano-scale drilling [14], cargo transport [15-24] of small objects or chemicals, lab-on-a-chip [25, 26] based applications as well as water remediation [27] and biodegradation of biological and chemical warfare agents [28], and oil-spill clean-up [29].

In the first experimental chapter, Chapter 3, special emphasis is put onto spherical Janus-particles, which undergo propulsion that is not obviously caused by the release of bubbles. Janus, in this context, refers to particles being made up of two different hemispheres. For example, where one hemisphere has been coated with a platinum (Pt) cap and the other is uncoated, exposing the particles material

composition, in this case polystyrene (PS). Figure 1-4 is a schematic representation of one of these colloids [30] (Chapter 1 Movie S1.1 shows an animation of this, Supportive CD).

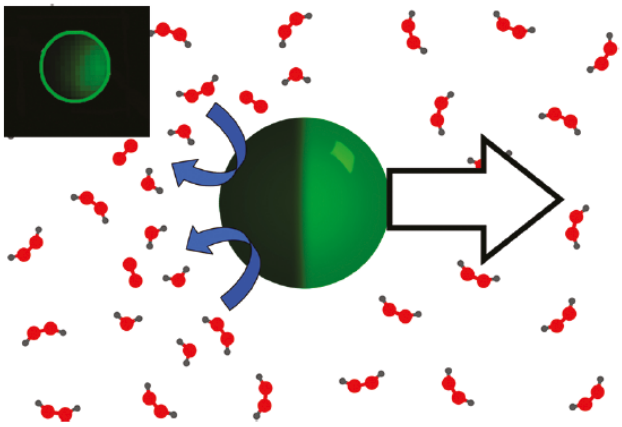

Figure 1-4 Schematic of a Janus-particle, the dark side represents the platinum coating and the bright green the uncoated part, which is also fluorescent. The molecules represent hydrogen peroxide, water and oxygen; hydrogen peroxide is asymmetrically decomposed by the Janus-particle. The concentration gradient of the fuel is thought to cause the propulsion as indicated by the arrow, taken from [30], (Chapter 1 Movie S1.1 shows an animation of this, Supportive CD).

The asymmetry of these particles is the key to their propulsion mechanism. If Janus-particles are put into an aqueous solution containing H_2O_2, they start to display an enhanced motion [30]; which can be described as 'swimming'. This self-induced swimming is due to an asymmetric catalytic reaction taking place on the surface of the Pt layer; this reaction degrades H_2O_2 into oxygen and water. (See reaction (1.1) [31] where the rate limiting constraints are shown as k_1 and k_2).

$$H_2O_2 + Pt \xrightarrow{k_1} Pt\left(H_2O_2\right) \xrightarrow{k_2} H_2O + \frac{1}{2}O_2 + Pt \qquad (1.1)$$

There are many examples of asymmetrical catalyst-coated devices showing propulsion based on this reaction [31-33]. It is thought that there are two main phoretic mechanisms that can propel catalytic motors, which are described in

Section 1.1.1 below. The first, self-diffusiophoresis, pre-dates the first experimental observations with spherical Janus particle catalytic swimmers, whereas the second, self-electrophoresis, was developed to explain specific observations with rod-shaped catalytic swimming devices made from two segments with differing composition and so also described as “Janus” catalysts. In Chapters 5, 6 and 7, larger catalytic micromotors (30 μm and more), which produce motion due to visible nucleation, growth and detachment of gaseous oxygen bubbles, are considered. Note that these devices still share the same catalytic driving reaction (decomposition of H_2O_2) as the smaller devices considered in Chapter 3: the oxygen is generated from reaction (1.1), (in Chapter 7 the enzyme catalase replaces the role of platinum). However, the increased device size reduces the energetic cost associated with nucleating bubbles on highly curved surfaces [34, 35] and this then enables the production and bubble release mechanism, rather than the phoretic situation where the produced oxygen is solvated. Section 1.1.2 reviews this bubble swimming mechanism in more detail, and describes some prominent examples from the literature. This chapter then provides a general introduction to the main themes that have motivated me, link the experimental work presented in this thesis, and present some of the most significant current challenges for the development and use of catalytic swimmers. These challenges include improving device biocompatibility, Section 1.2 (Chapters 3, 6 and 7) controlling and measuring device trajectories, Section 1.3 (Chapters 4, 5 and 7), and enabling efficient flexible device manufacture Section 1.4 (Chapter 7).

1.1.1. Phoretic mechanisms

1.1.1.1. Self-diffusiophoresis

One way in which reaction (1.1) can produce motion is by generating a concentration gradient of H_2O_2 across the PS/Pt colloid, a mechanism referred to as self-diffusiophoresis. For spherical Janus-particles the chemical reaction (1.1) takes place on the Pt particle surface and produces more product molecules than reactants. The resulting asymmetric distribution of the reaction products across the entire colloid propels the particle [32], in the case of PS/Pt Janus colloids usually away from the platinum-coated side. This effect is analogous to diffusiophoresis: the mechanism by which colloids show enhanced motion in response to an external solute concentration gradient [36, 37].

Theoretical analysis of self-diffusiophoresis for the spherical geometry shown in Figure 1-4 has suggested that the 'swimming' velocity depends on the reaction rate as shown in Eq. {1.2}, where V [μm/s] is the velocity, k [$\mu m^{-2}s^{-1}$] is the reaction rate, D_0 the diffusion coefficient for H_2O_2, μ [Å] the diffusiophoretic mobility, α [Å] the hydrodynamic radius and λ represents the range of interaction between the solute and the particle [32].

$$V = \frac{\mu k}{4D_0} = \frac{3\pi}{2} k\alpha\lambda^2 \qquad \{1.2\}$$

The reaction rate represented here will be the rate limiting reaction rate (either k_1 or k_2) as shown in reaction equation (1.1). The parameters shown in Eq. {1.2} are affected by temperature [38], particle size [31], asymmetry [39], surface roughness [40] and viscosity of the bulk solution [38, 41], which have all been shown to modify propulsion velocity.

Howse et al. [32] investigated how the hydrogen peroxide fuel concentration can affect the velocity of colloids with a nominal diameter of 1.62 µm and a platinum thickness of 5.5 nm. They utilised the mean squared displacement (MSD) method of finding the velocity for the Janus colloids (the MSD method is described in detail in Section 2.3.2). As shown in Figure 1-5, trajectory data shows increasing motion as the hydrogen peroxide concentration increases from 0 % to 10 % w/v, consistent with Eq. {1.2}. They postulated that the reaction rate is dependent on two reaction rate constants (1.1): k_1, which is the rate at which H_2O_2 forms a complex with platinum and k_2 the rate of breakup of H_2O_2 into water and oxygen, and has a similar behaviour to Michaelis-Menten kinetics, for which they find the reaction rate to be:

$$k = k_2 \frac{[H_2O_2]_{vol}}{[H_2O_2]_{vol} + k_2 / k_1} \qquad \{1.3\}$$

where, in order to fit Eq. {1.2} and {1.3} to the experiment data in Figure 1-6, they find $\alpha = 1.2$ Å, $\lambda = 5$ Å, $k_1 = 4.4 \times 10^{11}$ µm^{-2}s^{-1}, and $k_2 = 4.8 \times 10^{11}$ µm^{-2}s^{-1}.

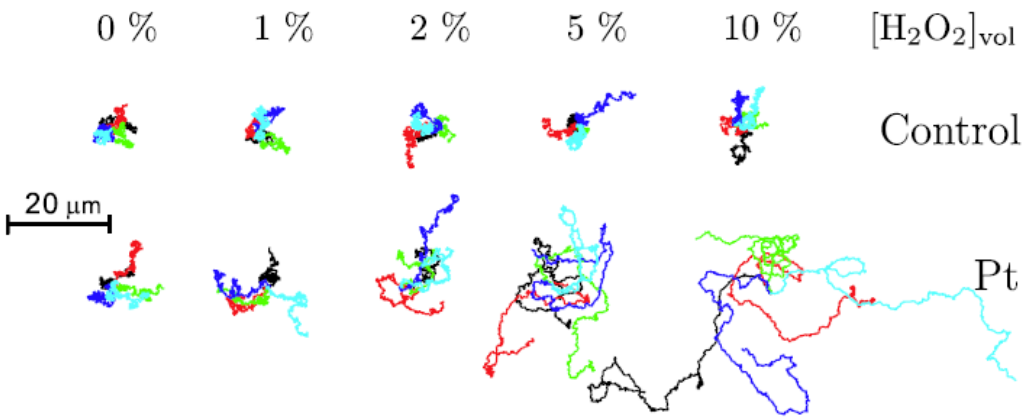

Figure 1-5 Trajectories over 25 sec for 5 particles of the control (blank) and platinum-coated particles in water and varying solutions of hydrogen peroxide, taken from [32].

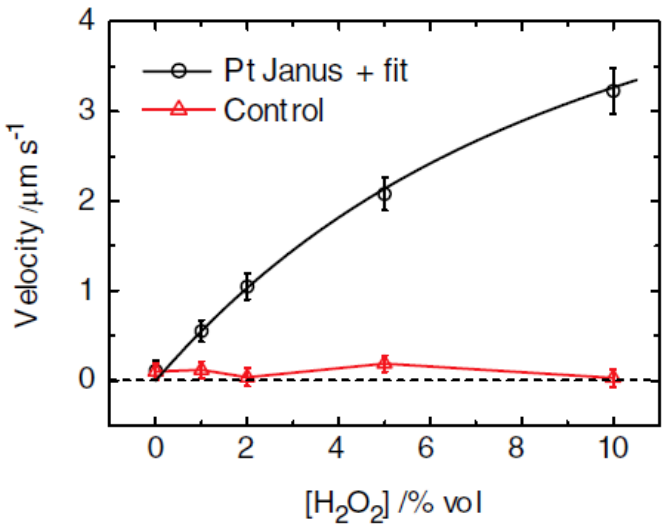

Figure 1-6 Velocity determined from the $\Delta t \ll \tau_R$ behaviour for the control (△) and Pt-coated particles (○). The solid line is the line of best fit using Eqs. ({1.2}) and ({1.3}), with a = 1.2 Å, λ = 5 Å, $k_1 = 4.4 \times 10^{11}$ μm^{-2}s^{-1}, and $k_2 = 4.8 \times 10^{11}$ μm^{-2}s^{-1}. Taken from [32].

1.1.1.2. Self-electrophoresis

A second potential phoretic mechanism that can cause objects to move without the release of bubbles is the self-generation of electric field gradients: self-electrophoresis. This mechanism is related to electrophoresis, the movement of colloids caused by an externally applied field [42]. For example, Wang, et al. [43] created and tested various bimetallic nanorods which produce motion on the addition of hydrogen peroxide fuel and self-electrophoresis appears to be the main mechanism responsible, see Table 1.1. These rods can be viewed as electrochemical cells, with one end serving as the anode, and the other as the cathode, with the conductive contacting halves allowing transfer of electrons. At the anode of the rods, hydrogen peroxide fuel is converted into oxygen and hydrogen ions (oxidation) Eq.(1.2), and at the cathode hydrogen peroxide reacts with hydrogen ions to form water (reduction) Eq.(1.3).

$$anode: H_2O_{2(aq)} \rightarrow O_{2(g)} + 2H^+_{(aq)} + 2e^- \quad (1.2)$$

$$cathode: H_2O_{2(aq)} + 2H^+_{(aq)} + 2e^- \rightarrow 2H_2O_{(l)} \quad (1.3)$$

An example Pt/Au rod in Figure 1-7 illustrates this. It is possible to predict the leading end of motion according to the metal combination of the rod and the electrical potential of each metal, which determine the reduction or oxidation reaction at either end. Speeds of these various rods, which were 2 µm in length and had a metal ratio of 1:1, were reported to be between 5 µm/s and 30 µm/s depending on the combination and averaging at ~20 µm/s [43].

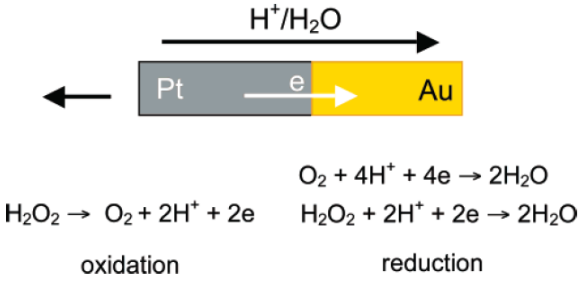

Figure 1-7 Bipolar electrochemical decomposition of H_2O_2 at a Pt-Au nanorod. In the electrokinetic mechanism, H^+ moves from the anode end to the cathode end of the rod, resulting in nanorod motion in the opposite direction. The dominant cathode half reaction is actually oxygen reduction rather than H_2O_2 reduction, taken from [43].

Table 1.1 Velocity and leading end data for bimetallic nanorods in 5 wt % aqueous H_2O_2 solution, taken from [43].

bimetallic nanorod	speed (µm/s)	leading end (observed)
Rh-Au	**23.8±2.9**	**Rh**
Pt-Au	**20.0±3.8**	**Pt**
Pd-Au	**15.3±2.0**	**Pd**
Pt-Ru	**30.2±4.0**	**Pt**
Au-Ru	**24.0±2.0**	**Au**
Rh-Pt	**17.0±3.0**	**Rh**
Rh-Pd	**16.2±1.8**	**Rh**
Pt-Pd	**13.6±2.3**	**Pt**
Ni-Au	**4.75±1.1**	**Ni**
Ag-Au	**6.20±1.2**	**Ag**
Au-Co	**7.10±1.4**	**Au**

1.1.2. Bubble propelled motion

As described above, another motion producing mechanism for larger catalytic swimming devices is bubble propulsion [10]. Active particles undergoing motion via bubble release can be primarily divided into two geometrical groups, tube-like particles and spherical particles.

1.1.2.1. Tube-like microswimmers

There are several publications [26, 27, 44-51] describing rolled up nanotube swimmers based on the decomposition of hydrogen peroxide by platinum localised on the inside of the tube. Rolled up nanotubes, or microtubes are also referred to as micro-jets or micromotors. However, not all microtubes are based on platinum and hydrogen peroxide as their reaction mechanism. Microtubes based on zinc and generating hydrogen bubbles in acidic media are described by Gao et al. [52], however, unlike Pt-based microtubes, these zinc-based ones use up zinc as part of the reaction to produce hydrogen gas $\left(2H^{+}_{(aq)} + Zn_{(s)} \rightarrow H_{2(g)} + Zn^{2+}_{(aq)}\right)$.

The mechanism by which tube-like micromotors propel themselves via bubble propulsion is described in detail by Li et al. [44]. To date it appears that all tube-like micromotors that contain their reaction materials on the inside of the tubes need the addition of surfactants such as Triton X 100 or SDS in order to lower surface tension to allow bubble propulsion to take place [53]. This in turn leads to important challenges in the pursuit of biocompatibility which are discussed later in Section 1.2 (Chapter 6).

1.1.2.2. Spherical Micromotors

As well as nanotubes or microtubes, spherical micromotors can also produce propulsion based on bubble release. One such system is described by Gibbs and Zhao [10], where particular detail was given to how the forces of bubble propulsion work on a spherical particle and how the surface tension of the bulk solution changes the propulsion, see Figure 1-8 (a).

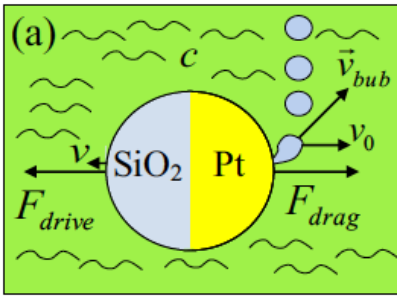

Figure 1-8 (a) Force and velocity schematic of a Pt-coated microsphere in hydrogen peroxide solution resulting in bubble formation and propulsion. [10].

The equation {1.4} was derived to express the velocity v in terms of hydrogen peroxide concentration and surface tension, where R_g is the universal gas constant, T is temperature, R is the bubble radius, α is the Langmuir adsorption constant, c is the bulk hydrogen peroxide concentration, γ the surface tension, and ρ_{O_2} the density of oxygen.

$$v \propto N \frac{R_g T \rho_{O_2} v_0}{\mu a P} \gamma^2 \frac{k\alpha c}{1+\alpha c} \qquad \{1.4\}$$

Surprisingly there are very few examples of confirmed spherical bubble propelled micromotors based on platinum as a catalyst: the vast majority of spherical micromotors are based on chemical reactions that tend to use up the particle body, meaning these particles have a finite lifetime. The following are some examples of bubble swimmers in this category: Gao, et al. [54] demonstrated a novel, multi-fuel

driven swimmer producing bubble-propelled motion in hydrogen peroxide and in strong acidic or basic solutions such as HCl and NaOH [54]. Oxygen bubbles are produced in hydrogen peroxide fuel using the Pd layer as a catalyst (Eq.(1.4)) and hydrogen bubbles in acidic or basic fuel solutions, as shown in Eq.(1.5) and Eq. (1.6), where the hydrogen bubbles are generally smaller than the oxygen bubbles.

$$2H_2O_{2(aq)} \xrightarrow{Pd} 2H_2O_{(l)} + O_{2(g)} \quad (1.4)$$

$$2Al_{(s)} + 6H^{+}_{(aq)} \rightarrow 2Al^{3+}_{(aq)} + 2H_{2(g)} \quad (1.5)$$

$$2Al_{(s)} + 2OH^{-}_{(aq)} + 2H_2O_{(l)} \rightarrow 2AlO^{-}_{2(aq)} + 3H_{2(g)} \quad (1.6)$$

A different water-driven, spherical, bubble-propelled micromotor is also described by Gao, et al. [55]. In this case the particle core consists of an aluminium-gallium (Al-Ga) alloy made via microcontact mixing and coated on one side with titanium via electron-beam evaporation, as illustrated in Figure 1-9.

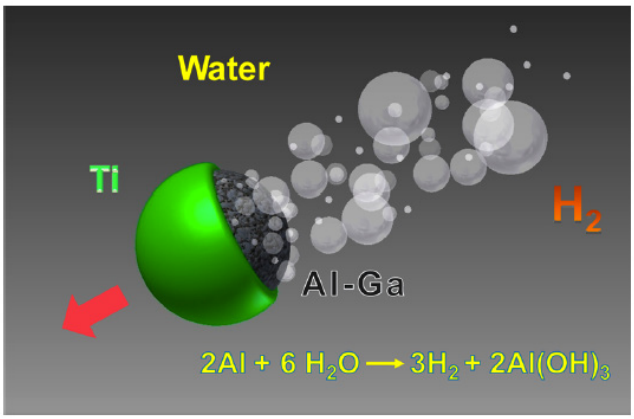

Figure 1-9 Schematic of water-driven hydrogen propelled Al-Ga/Ti micromotor. The dark hemisphere is the Al-Ga alloy and the Green hemisphere the Ti coating, taken from [55].

Particles with a diameter of 20 µm were described as moving in rapid directional motion of 3 mm/s in water treated with 0.1 M Triton X 100, where the bubbles were said to be of an average size of 10 µm in diameter [55].

A slightly different elliptical-shaped Janus particle, 100 µm in diameter and 10 µm in thickness made of gold and a Pt-Pd alloy, is described by Reddy and Clasen [56]. Due to its bimetallic properties, the propulsion mechanism of this Janus particle is dependent on the hydrogen peroxide concentration. At low hydrogen peroxide concentrations the disks are said to undergo self-diffusiophoresis. At high hydrogen peroxide concentrations on the other hand these particles undergo bubble propulsion at the liquid/air interface as shown in the schematic in Figure 1-10, providing generation of oxygen becomes greater than the rate of oxygen diffusion into the solution.

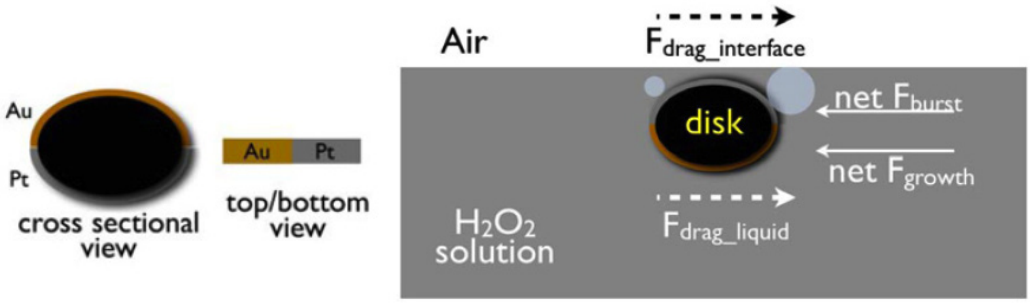

Figure 1-10 (Left) Schematic showing the Janus disk ~100 µm in diameter. (Right) Schematic showing the forces acting on the micro-disk during self-propulsion at the air/liquid interface. The forward propulsion is due to asymmetric distribution of oxygen bubble growth and burst. The drag on the self-propelling micro-disk arises from the bulk liquid and the air/liquid interface, taken from [56].

Due to the high mass of the disks they sink to the bottom in water, but with the addition of hydrogen peroxide fuel bubbles forming on the surface of the particles provide buoyancy to lift them to the air/liquid interface. Reddy and Clasen [56] describe the propulsion of the elliptical-shaped Janus disks to be due to both bubble growth and bubble burst actions, as shown in the velocities and distance travelled in

Figure 1-11. The propulsion due to oxygen bubble growth is smooth and nearly equal to the bubble radius (which follows the inverse square law during growth), while the propulsion due to the bursting of bubbles is then described as ballistic propulsion of much higher velocities approximately three orders of magnitude greater than the bubble growth propulsion.

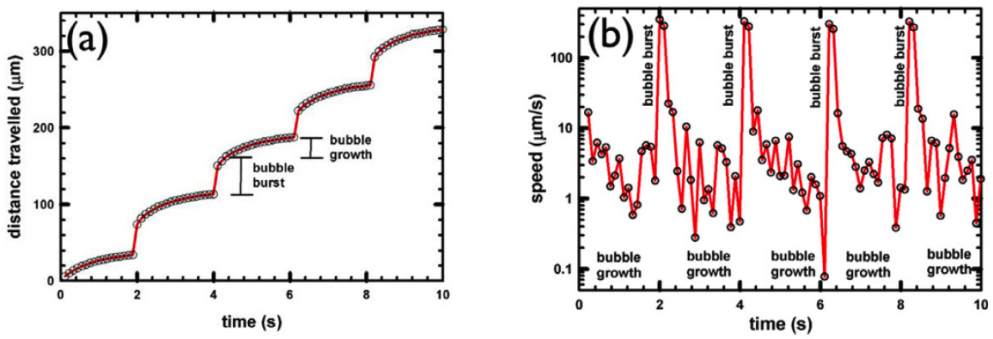

Figure 1-11 (a) distance travelled by the Janus disks due to oxygen bubble growth and burst processes (b) the same data but showing the velocity instead of distance travelled, taken from [56].

Other Water-Driven micromotors described by Gao, et al. [29] are bubble-propelled via magnesium. In this case magnesium reacts in water to form magnesium hydroxide and hydrogen gas. The possible use of these Janus swimmers in oil drop capture and transport, for applications such as cleaning up oil spills at sea is demonstrated in Figure 1-12. The gold layer can be modified with self-assembled monolayers (SAMs) of long chain alkanethiols to create strong surface hydrophobicity in order to collect oil droplets. Reported propulsion velocities are 90 μm/s in 0.3 M NaCl and 300 μm/s in 3 M NaCl. The velocities do not notably change in the case of SAM modified gold surfaces.

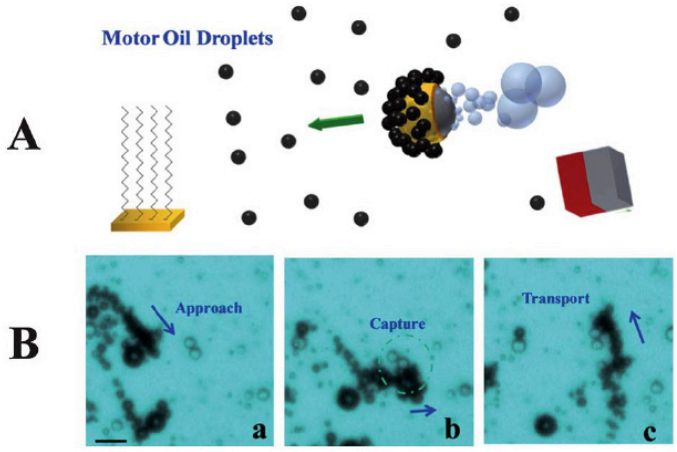

Figure 1-12 (A) Schematic of the seawater-driven Janus micromotors capturing Motor Oil Droplets. (B) Time Lapse images taken from a movie (a) approach of the micromotor to oil droplets (b) capture of droplets on motor (c) transport of captured oil droplets in seawater. Scale bar 50 µm, taken from [29].

Li, et al. [28] have demonstrated the production of photoreactive, water-driven spherical micromotors made of TiO_2/Au/Mg. These micromotors create a highly reactive oxygen species that efficiently destroys the cell membranes of the anthrax simulant Bacillus globigii spores, as shown in Figure 1-13. The preparation of these particles involves multiple steps. Initially 20 µm magnesium (Mg) particles are spun cast onto a glass slide and then coated with gold nanoparticles via a sputter coating process, during which the sample is rotating, after which TiO_2 is applied via atomic layer deposition for 120 cycles at 100˚C. The motors are nearly fully coated with TiO_2/Au, as can be seen from the schematic in Figure 1-13, with only a ~2 µm opening of the Mg core to water. Just like the previously described Au/Ni/Ti/Mg particles it is important for the water to contain a high concentration of salt, such as is contained in seawater, in order to prevent a build-up of $Mg(OH)_2$ from inhibiting the reaction of Mg with water, as shown in Eq. (1.7). If not prevented, the solid reaction product, magnesium hydroxide, would normally form a passivation layer on the Mg surface thus quickly inhibiting the reaction.

$$Mg_{(s)} + 2H_2O_{(aq)} \rightarrow Mg(OH)_{2(s)} + H_{2(g)} \qquad (1.7)$$

In order to stop the deposition of magnesium hydroxide a micro-galvanic and pitting corrosion process is put in place. A micro-galvanic process is induced by the gold (Au), nickel (Ni) and titanium (Ti) layers on the surface of the Janus particle together with the free chloride ions from the salt water. Aggressive anionic species such as chloride are able to penetrate the passivation layer and are transported into the pit in order to balance the charge as the Mg^{+} cation concentration builds up. This causes the hydroxide ions to be depleted and the environment becomes weakly acidic, due to the build-up of Cl^{-} and Mg^{+} ions and stops further passivation due to $Mg(OH)_2$. The Mg^{+} ions near the surface of the pit then react with water to form H_2 gas, Eq. (1.8).

$$2Mg^{+}_{(aq)} + 2H_2O_{(aq)} \xrightarrow{Cl^{-}} 2Mg^{+}_{(aq)} + 2OH^{-}_{(aq)} + 2H_{2(aq)} \qquad (1.8)$$

This autocatalytic process takes place as long as there is a consistent electrolytic migration of Cl^{-} ions into the pit. The galvanic element caused by the Au/Ni/Ti layer further enhances the electrochemical corrosion and dissolution of Mg on exposed regions increasing the reaction rate Increasing salt concentration also enhances reaction rates and therefore propulsion [29].

The motors are said to have a lifetime of 15 minutes (for 20 µm spheres). The particles are reported to move at an average speed of 80 µm/s in an environment containing 0.08 M NaCl. To have a similar lifetime in seawater, which has a higher salt concentration of ~0.54 M, they report that the particles need to be 30 µm in diameter as the reaction speed and therefore erosion of Mg increases with increasing salt concentration. Because these particles have a TiO_2 layer they exhibit UV sensitive properties that allow them to create highly active oxygen species that

can destroy spores of environmentally dangerous agents such as those from the anthrax simulant Bacillus globigii spores. Figure 1-13 B shows how the propulsion of the particles vastly increases spore destruction via the micromotors when radiated with UV light.

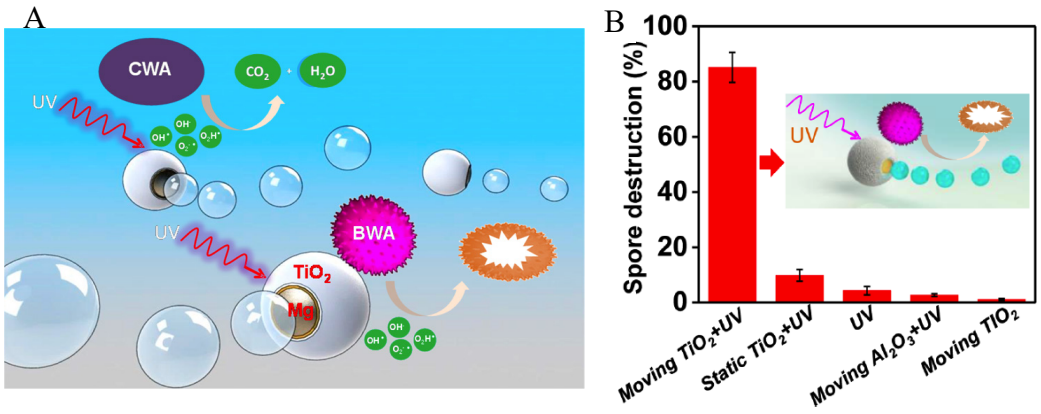

Figure 1-13 (A) Schematic representation of the self-propulsion and photocatalytic degradation of biological warfare agents (BWA) and chemical warfare agents (CWA) by TiO_2 /Au/Mg (B) Statistical Plot showing the efficiency of spore destruction under different conditions, taken from [28].

1.2. Biocompatibility of Micromotors

For the vast majority of proposed application areas such as medical diagnosis and drug delivery, conferring biocompatibility is of vital importance. In order for micromotors to be biocompatible there are a variety of problems that need to be overcome. Depending on the application areas the number of requirements for micromotors can magnify as applications become more demanding. As an illustration, using micromotors as medical diagnostic devices (e.g. Lab-On-A-Chip) there are relatively few challenges, mainly related to solution compatibilities, compared to the challenges with releasing micromotors into a living organism. In the latter case we must question if the micromotors are toxic themselves to the life-forms that they might interact with. An example relevant to bimetallic nanorods is described by Niidome, et al. [57], where they find that gold nanorods are highly

cytotoxic in vitro, but after being Polyethylene glycol (PEG) coated the nanorods show little cytotoxicity and are no longer rapidly cleared from the blood when intravenously administered. A coating of PEG stops particles from having non-specific interactions within the body, this means causing less interactions with blood components that would otherwise induce activation of the complement system, which therefore reduces the clearance of these particles from the blood. This effect is called the *stealth effect* [58]. Non-stealth nanoparticles that are injected into the blood can quickly become removed from the blood by macrophages, which is why it is important to create biocompatible particles that will linger in the blood system for a longer time in order to achieve their desired goals of drug delivery to the target tissue [59]. Permeability of these particles can also be important for drug delivery as some parts of the body or some cells may have distinctive barriers to be overcome [60] such as the diffusion through cell membranes, size is an important governing factor in these cases.

While these issues are general concerns for any colloidal system proposed for use in the body, there are specific additional issues for micromotors due to their requirement for specific fuel molecules and solution properties in order to achieve motion, which are now discussed in turn.

1.2.1. Effects of Salt

Since biological systems contain many different salts [61] it is important to look into any effects these might have on the swimming devices. In Paxton, et al. [62] electrophoretic bimetallic nanorods (Pt/Au) were investigated and it was noted that adding lithium nitrate ($LiNO_3$) or sodium nitrate ($NaNO_3$) to bulk solutions containing H_2O_2, causes the velocity of these rods to decrease by 80% and the

oxygen evolution to decrease by 33%. Consequently it appears that salt fundamentally affects the electrophoretic mechanism in a way that is not solely related to reaction rate reduction. However, the effect of salt on the performance of the apparently self-diffusiophoretic spherical catalytic Janus swimmer has not previously been studied. The first experimental chapter in this thesis (Chapter 3) explores this issue in detail. For bubble swimmers a variety of studies have found that salt has little effect on velocity. This is a clear advantage for devices with this mechanism and so in the later experimental chapters focus shifts to this device type (Chapters 5-7). [55]

1.2.2. Importance of Surfactants for bubble-propelled micromotors

In general it is desirable to design micromotors which require the minimum number of additives to be present in the solution in which motion is required. This is especially true for deployments within biological fluids where each additive may have undesirable interactions with the multitude of molecules present in these complex solutions. In Section 1.1.2.1 the importance of surfactants added to the bulk solutions for tube-like microswimmers to allow the ingress of fuel into the tubes and enable their propulsion mechanism was mentioned. Soler, et al. [26] give an example of the use of microjets for “Lab-on-a-Chip” applications, where they are dispersed into a mixture of serum and red blood cells acting as micro-stirrers. Fuel H_2O_2 and the surfactant Triton X 100 need to be added to the solution to start the catalytic reaction, while the mixture simulating real blood has to be diluted down to one tenth of the concentration of blood to decrease the viscosity of the solution. In Gao, et al. [55] the velocities (of Al/Ga spherical micromotors, Figure 1-9) were reported to be 1.3 mm/s in a 10 mM salt solution and 0.1 mm/s in a 1 M NaCl solution (containing 0.1M Triton X 100), compared to a velocity of 45 μm/s

in 3 M NaCl in the absence of surfactant. As previously mentioned another example is that of Ag and MnO_2 powered particles undergoing propulsion. Wang, et al. [63] reported that in both cases the surfactant SDS (0.5%) is needed to ensure proper propulsion. The water-driven micromotors (Figure 1-12) described by Gao, et al. [29] also need a surfactant (Triton X 100) to ensure proper bubble release by the micromotors. The TiO_2/Au/Mg micromotors (Figure 1-13) also showed the need of added surfactant (0.075% of Triton X 100). Table 1.2 lists some of the current bubble propelled swimmers and their velocities together with the need of surfactant. This table indicates the almost exclusive need for surfactant in the current bubble propelled systems.

Table 1.2 Comparison of different swimming devices in various media and the need of surfactants.

Authors	Type of device	Surfactant	Velocity	Medium / Fuel
Wang et al.[64]	PEDOT/Au-catalase(microjets)	Yes	120 µm/s	2% H_2O_2
Vicario et al.[65]	SiO_2/Synthetic Manganese catalase	No	35 µm/s	5% H_2O_2 in CH_3CN / Glycerol
Wang et al.[66]	PEDOT/PEDOT-COOH/Ni/Pt (microjets)	Yes	88 µm/s	1% H_2O_2 in PBS buffer
Wang et al.[67]	PAPBA/Pt (microjets)	Yes	40 µm/s	5% H_2O_2 in Human Serum
Wang et al.[68]	Ti/Fe/Au/Pt (microjets)	Yes	85 µm/s	7.5% H_2O_2 in Human Serum (1:4 diluted)
Wang et al.[69]	Ti/Ni/Au/Pt (microjets)	Yes	125 µm/s	3% H_2O_2 in Protein solutions
Wang et al.[70]	PANI/Pt (microjets)	Yes	1.4 mm/s	5% H_2O_2
Pumera at al.[71]	Cu/Pt (microjets)	Yes	365 µm/s	3% H_2O_2
Sanchez et al.[72]	Ti/Fe/Pt (microjets)	Yes	130µm/s	4% H_2O_2 in 25% cell medium
Sanchez et al.[73]	Ti/Cr/Pt (microjets)	Yes	500 µm/s	1% H_2O_2
Solovev et al.[16]	Ti/Fe/Pt (microjets)	Yes	220 µm/s	7.5% H_2O_2
Gregory et al.[74]	PS/Pt (spheres) / Chapter 4	No	1.8 mm/s	2% H_2O_2
Wang et al.[55]	Al/Ga (Janus spheres)	Yes	3 mm/s	Water
Wang et al. [28]	TiO_2/Au/Mg (spherical micromotors)	Yes	80 µm/s 120 µm/s	Water Seawater
Wang et al. [29]	Mg/Ti/Ni/Au (Janus spheres)	Yes	90 µm/s	Seawater

Kumar et al.[75]	Carbon/acrylic/Pt (catalytic fish ~1 cm)	Yes	175 mm/s	15% H_2O_2
Zhu et al. [76]	PEGDA/Pt. nanoparticles (optical printed Microfish)	NA	780 μm/s	15% H_2O_2

In view of these findings the crucial role of surfactants in bubble-propelled micro-engines was investigated and compared with presently known working systems by Wang, et al. [77]. They investigated how anionic (i.e. sodium dodecyl sulphate; SDS), cationic (i.e. cetyltrimethyl-ammonium bromide (CTAB)) and non-ionic (i.e. Polyethylene glycol sorbitan monolaurate (Tween 20)) surfactants influenced microjet motion. They reported that for anionic surfactants such as SDS there is a critical micelle concentration (CMC) of ~0.24 wt% above which increasing surfactant concentration has no noticeable effect on the motion of the microjets. Their findings are consistent with the theory of surfactant adsorption at interfaces [78]. At increasing anionic surfactant concentrations below the CMC the surface adsorption of SDS increases while the interfacial tension decreases resulting in better detachment of bubbles from the surface and enhanced motility. It is pointed out that at very high surfactant concentrations the increasing viscosity of the solution might have a slowing effect on the microjets [79]. In conclusion they noted that the propulsion of microjets is strongly affected by the nature of surfactant used. Neither cationic or non-ionic surfactants show any significant benefit whereas anionic surfactants i.e. SDS vastly increase the propulsion of microjets up to the CMC of SDS. Here, in this context, Chapter 6 considers the role of surfactant on a simple spherical bubble propulsive swimmer driven by platinum.

1.2.3. Catalyst and fuel molecule limitations

One of the most obvious limitations for many current catalytic micromotors is the reliance on hydrogen peroxide fuel, which is known to be toxic to living organisms

at high concentrations. A new approach is therefore required to create swimmers that propel in a similarly efficient or an even more efficient manner and do not rely on the degradation of H_2O_2. It has therefore been proposed to use enzymes as the catalyst (motors) for propulsion as they can perform a wide range of room temperature decomposition reactions using more biologically compatible components (e.g. glucose oxidase with glucose and oxygen as a fuel source in conjunction with catalase enzyme). However, despite this goal, for initial comparative studies, catalase (CAT) (see Figure 1-14) has often been studied as it also decomposes hydrogen peroxide, is relatively robust, and has a famously rapid turnover rate [80].

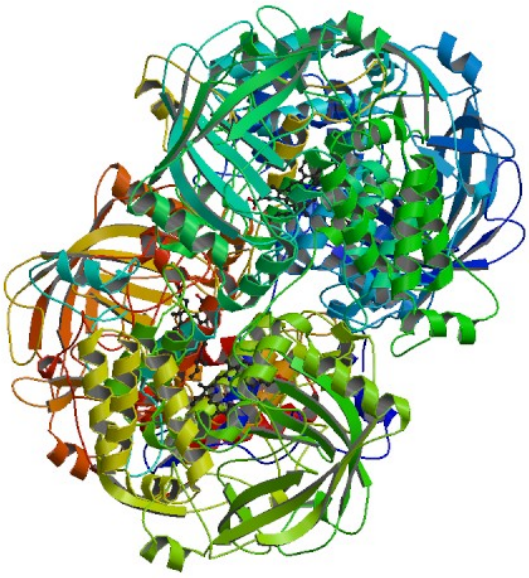

Figure 1-14 Crystal structure of bovine liver catalase (Protein Database Bank (PDB) entry 1TH2 [80])

CAT is a haemoprotein, which is a metalloprotein containing a metal ion core, in this case iron (Fe). Eq. (1.9) shows the presumed reactions taking place. The actual mechanism with which CAT degrades hydrogen peroxide is still unknown but a proposed mechanism is shown in Alfonso-Prieto, et al. [81].

$$\begin{aligned} &\text{Enz (Por} - \text{Fe}^{III}) + H_2O_2 \rightarrow \text{Cpd I (Por}^{\cdot+} - \text{Fe}^{IV} = \text{O}) + H_2O \\ &\text{Cpd I (Por}^{\cdot+} - \text{Fe}^{IV} = \text{O}) + H_2O_2 \rightarrow \text{Enz (Por} - \text{Fe}^{III}) + H_2O + O_2 \end{aligned} \quad (1.9)$$

Cpd I refers to a highly active species for oxidation reactions (it is a high-valent iron intermediate), characterized to be an oxoferryl porphyrin (Por) cation radical [81]. Figure 1-15 shows a representation of the active site where the iron core lies.

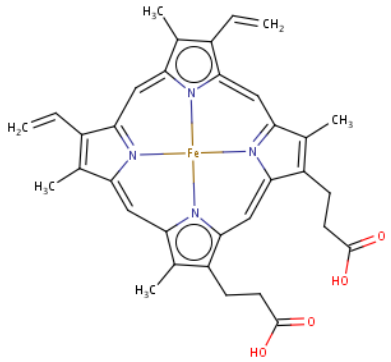

Figure 1-15 The active (heme) site of bovine liver catalase with the Iron core (protoporphyrin ix containing Fe). (source: PDB entry 1TH2 [80])

In order to utilise enzymes for catalytic swimming it is necessary to localise the enzyme at specific locations on the body of the propulsive particle. There are various methods how enzymes can be immobilized onto surfaces. The methods can be categorized into three groups [82]: ***adsorption*** [83], ***covalent binding*** (cross-linking) [84, 85] and ***incorporation*** [86]. Adsorption is when the enzymes (proteins) adsorb onto the surface and hold an affinity to stay immobilised via forces such as van der Waals and hydrophobic forces [83, 87, 88]. Covalent binding is the chemical attachment of a part of the enzyme to the surface or a molecule attached to the surface. Incorporation refers to enzyme entrapment or encapsulation, which is discussed in Chapter 7. Some examples of enzyme powered propulsive devices have been reported in the literature. Orozco, et al. [64] created enzyme-powered microjets using covalent attachment of the highly reactive

enzyme catalase to the inner surface of a tube coated in gold. The covalent attachment method used for these microjets was a chemistry using self-assembled monolayers (SAM) of a mixture of 11-mercaptoundecanoic acid (MUA) / 6-mercaptohexanol (MCH) onto the gold surface to which catalase was attached via carbodiimide chemistry (EDC stabilised with N-hydroxysuccinimide (NHS)).

An example of a multi-enzyme self-propelling ensemble is shown in Pantarotto, et al. [89] where the enzymes glucose oxidase (GOx) and CAT are both immobilised onto a multi-walled carbon nanotube (MWCNT). (See Figure 1-16) Here the two enzyme reactions are linked via hydrogen peroxide. Under the catalysis of GOx oxygen reacts with glucose to form gluconolactone and hydrogen peroxide while CAT catalyses the breakdown of hydrogen peroxide to form water and molecular oxygen. However, the amount of oxygen produced by CAT is not enough to keep the reaction with GOx going and to do this it is necessary to have a constant flow of oxygen over the sample.

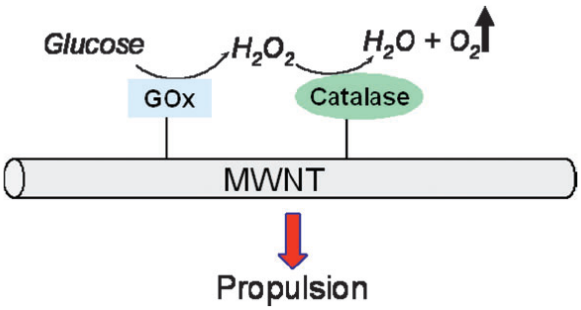

Figure 1-16 Biohybrid propulsion system. GOx and CAT immobilized onto a multi- walled carbon nanotube, taken from [89].

CAT as a catalyst for hydrogen peroxide has also been mimicked by Vicario, et al. [65] where a manganese synthetic catalyst was immobilized covalently onto an object via a tether. The catalyst decomposed hydrogen peroxide in a similar way as CAT, into water and oxygen, causing movement of the object.

1.3. Trajectory control and analysis

In addition to conferring biocompatibility for useful application of the micromotors it is also necessary to produce certain types of propulsive trajectories, for example directed linear translation to enable transport functions. For this reason, there have been extensive publications based on different trajectory influencing production processes that alter the trajectory behaviour of phoretic Janus micromotors. The motivation for these investigations was to produce devices that have a well-defined motion character that can be used for applications. For example, one aim has been to introduce a propulsive angular velocity into the trajectory of these micromotors by using manufacturing techniques such as, glancing angle deposition [90] and self-assembly [91]. This could benefit applications such as fluidic mixing. Other methods have considered the challenge of demonstrating autonomous directional control which is desirable to enable transport applications. Approaches include increasing the mass of the catalytic cap to introduce gravitaxis (where the gravitational force influences the orientation of the Janus cap) [92]. Surface micromotors trapped at the air / liquid interface also generate more linear trajectories due to quenching of the rotational diffusion coefficient (τ_R) [93]. Similarly to this the directing influence of channels and boundaries on the trajectories of Janus particles were reported in Das et al. [94]. All these behaviours were confirmed by means of physical and mathematical models some of which are described later on in Section 2.3.

Methods to control trajectories of bubble propelled micromotors are also important in order to enable many functional applications, however a lack of an established methodology for comparing trajectories for these devices has led to many findings being only qualitatively described. For example, Gao et al. [55], report the

difference in propulsion behaviour with and without the Ti layer masking part of the particle and it was concluded that a masked particle has a much more directional motion than an unmasked particle (mentioned in the previous Section (1.1.2.2), see Figure 1-9). However, no actual analysis of trajectories, was shown to prove the impact of the Ti layer on the directionality of motion. Wang and Wu [9] also investigated the propulsion of PS-Pt dimers. They observed [9] that these undergo bubble propulsion of three different motion types, namely linear, clockwise and counter clockwise circular motion as shown in Figure 1-17. The dimers are reported to have propulsion velocities of ~ 40 μm/s in a 10% hydrogen peroxide solution. The different kinds of motion arise from the fact that bubbles can be formed on different parts of the Pt dimer surface. As shown in Figure 1-17 if the bubble grows at the far end of the Pt coating (a) the motion is linear but on the other hand if it grows off centre then the particles undergo a circular motion ((b) and (c)). The motion here was only described in a purely observational manner and no analytical approach was used.

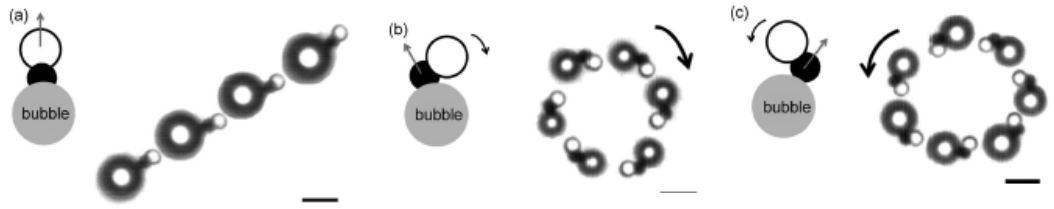

Figure 1-17 Three types of motion of Pt-PS hybrid dimers (a) linear, (b) clockwise, and (c) counter clockwise motion. Scale bar 5 μm, taken from [9].

In another example Wang, et al. [63] looked at two other catalysts to decompose hydrogen peroxide that might be used for bubble propelled micromotors. They showed that silver (Ag) particles and manganese dioxide (MnO_2) particles undergo bubble propulsion, with Ag particles showing much better propulsion than MnO_2 particles. The authors claimed that particles that were half-coated with gold via

sputter coating do not show any enhancement in propulsion i.e. more directional motion. The authors however did not specify how the trajectories of the uncoated and Janus particles were analysed to reach this conclusion. The particles were reported to have three different propulsion behaviours represented by their trajectories: circular, curved and self-rotating and these are claimed to be the cause of the inhomogeneity and asymmetry of the Ag motors used.

These examples illustrate the lack of robust analytical techniques presently employed over this part of the micromotor field, which is why I have investigated various techniques such as fractal dimension (Section 2.3.3), persistence length (Section 2.3.4) and mean squared gyration in order to quantitatively analyse the motion and directionality of differently fabricated PS/Pt-based spherical bubble-propelled micromotors in experimental Chapter 5.

1.4. Fabrication process of Micromotors

Spherical micromotors undergoing phoretic mechanisms have in general been fabricated by means of spin coating colloids onto a surface and then evaporating metals such as platinum onto one hemisphere, thus producing Janus particles (Figure 1-4) [32, 92, 95]. Bimetallic nanorods on the other hand require porous templates and multistage electrochemical processes for their manufacture [96]. The synthesis / fabrication processes are in general not useful for mass production techniques. There have, however, been recent suggestions to produce micromotors via printing techniques in order to allow for cheaper mass production plus in some cases for digital definition of structure. Two examples currently exist, where in the first case Kumar et al. [75] used a layer-by-layer screen printing approach in order to generate large scale self-motile fish that can ‘swim’ by bubble propulsion in hydrogen peroxide fuel. By using multiple stencils together with different inks they

could generate ‘fish’ in the region of 1 cm in length with specific materials in different regions of the fish, i.e. a chitosan/Pt tail to drive the fish via bubble propulsion, an acrylic body and a mid-body made of carbon / nickel which allows for magnetic guidance of the fish via external magnetic fields (see Figure 1-18). This method however still has the need to generate micromotors via a multiple stage process, so is not ideal for large scale manufacturing.

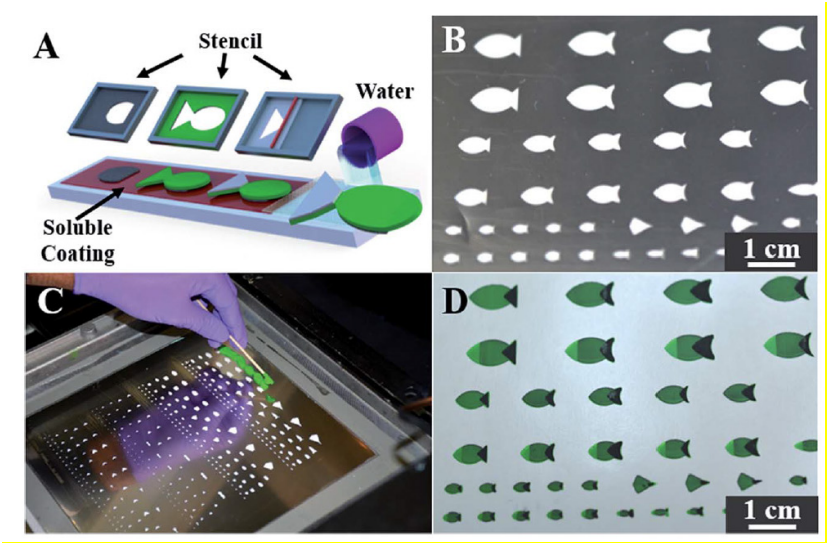

Figure 1-18 (A) Schematic illustration of the layer-by-layer screen-printing microfabrication of the synthetic catalytic fish: sequential printing of specific layers based on different modified inks for localizing different functionalities at specific sections of the printed fish. (B) Image of the stainless steel stencil containing the pre-cut design of the entire fish shape using different dimensions and shapes. (C) Image of mass fabrication procedure; coloured acrylic ink is physically applied onto the stencil above the pattern before a squeegee or doctor blade pushes the ink across the design. (D) Image of an array of mass-printed fish on a water-dissolvable coated substrate using the stencil shown in (B), taken from [75].

The second optical printing method by Zhu et al. [76], achieves the fabrication of much smaller, multi-factionalized fish-shaped devices via microscale continuous optical printing (μCOP) using a UV light source which is focused in the correct locations via a Computer-Aided Design (CAD) software and a digital micromirror device (DMD), see Figure 1-19. For this method it is important to note that all inks need to contain UV curable precursors, which in this case are poly(ethylene glycol)

diacrylate (PEGDA) based hydrogels. This allows for the incorporation of other functional particles such as platinum and magnetic nanoparticles during the curing process and thus by changing ink solutions above the substrate it is possible to generate multi-functional PEGDA based particles. This method is said to have a resolution of ~1 µm. For this method once again there is the need for a multiple stage process and inks are restricted to being UV curable.

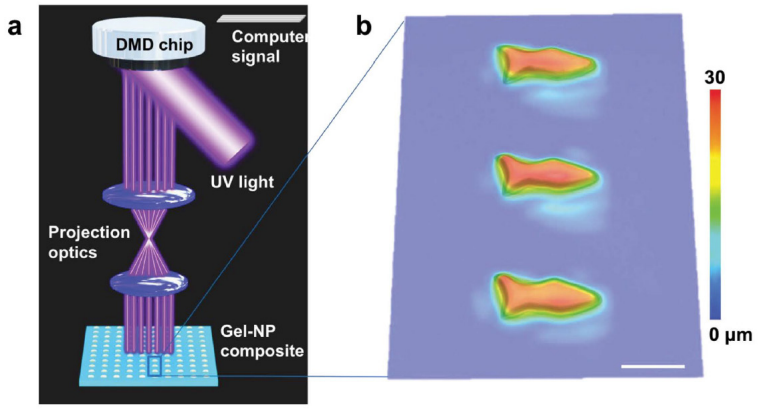

Figure 1-19 a) Schematic illustration of the µCOP method to fabricate microfish. UV light illuminates the DMD mirrors, generating an optical pattern specified by the control computer. The pattern is projected through optics onto the photosensitive monomer solution to fabricate the fish layer-by-layer. b) 3D microscopy image of an array of printed microfish. Scale bar, 100 µm, taken from [76].

Based on these examples I have developed a novel approach utilising inkjet printing of silk material to generate micro-rockets and which is described in my final experimental Chapter 7. This novel method incorporates both the capability of swimming motion together with biocompatible components. Inkjet printing overcomes the need for production in multiple stages and allows for the simple printing of various inks digitally predefined by software.

1.5. Schematic overview of Micromotors produced in this Thesis

The following schematic, Figure 1-20, gives an overview of the micromotors that were produced throughout this Thesis. The following micromotors from Figure 1-20 were used in each Chapter:

- Chapter 3 (a) and (b)
- Chapter 4 (b) and (c) size 1-5 µm
- Chapter 5 (b), (c), (d) size: 30 µm
- Chapter 6 (b)
- Chapter 7 (e) and (f).

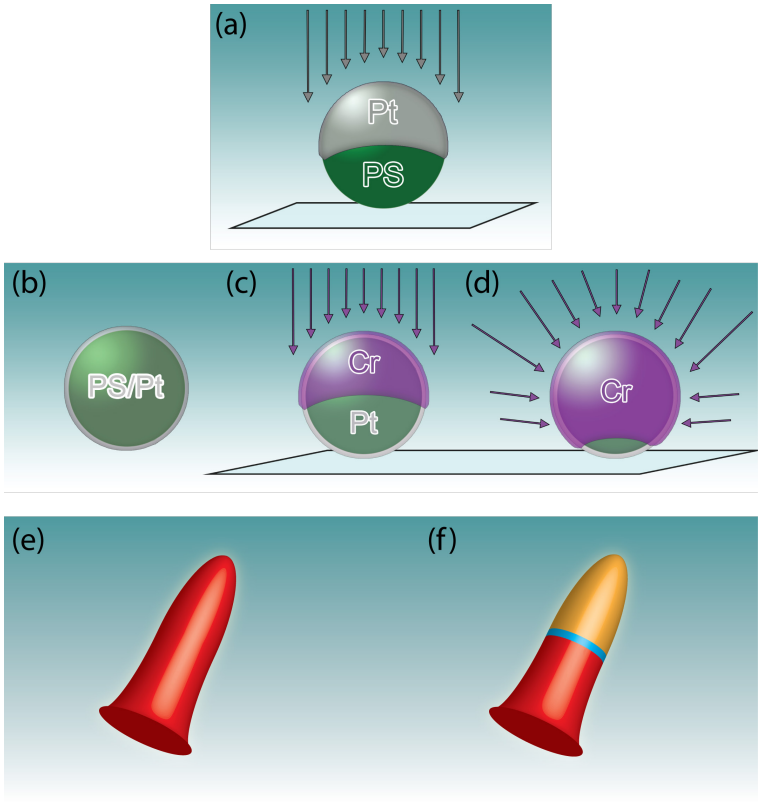

Figure 1-20 Micromotor schematic overview: **Propulsion via Phoretic Phenomena**: (a) Polystyrene (PS) / Platinum (Pt) ***Janus*** colloids, (b) PS colloids coated chemically with Pt. size range 1 – 5 µm in diameter (***symmetrically active particles***); **Bubble propulsion:** (b) PS/Pt via Chemical coating 30 µm diameter (***symmetrically active particles***), (c) micromotor "(b) 30 µm" with extra E-beam coating of Chromium (Cr) (***Janus***), (c) micromotor "(b) 30 µm" with extra sputter coated Cr layer (***Pore***), (e) ***Fully active silk micro-rocket*** (containing catalase enzyme, Silk and PEG_{400}), (f) ***Janus Silk micro-rocket*** (**orange**: silk / PEG_{400}, **blue**: Poly(methyl methacrylate) (PMMA) barrier layer, **red**: silk, catalase enzyme, PEG_{400})

2. Methods

In this chapter I describe the general sample preparation, analytical and mathematical methods I have used in the following experimental chapters. Each individual chapter contains further details of the specific procedures used.

2.1. Preparation techniques

The following techniques were used to make Catalytic Janus Spheres.

2.1.1. Plasma Cleaning

For the experiments described in this thesis it was important to have clean substrate surfaces prior to spin coating procedures, metal evaporation procedures or covalent coupling chemistry. The method chosen to achieve this was plasma cleaning, to avoid the use of aggressive chemicals which could damage the materials being cleaned. Figure 2-1 shows a simple schematic of a plasma coating/etching machine. Samples were loaded into the vacuum chamber, which was then evacuated until base pressure had been achieved [97]. Then the gas (in this case oxygen), required for the desired plasma, was bled into the chamber via a needle valve bringing the chamber to a pressure between 0.01 and 1 mBar. The gas was bled into the chamber for 15 minutes to ensure any other residual gases had been replaced. Once this incubation had been completed the plasma was ignited by applying a potential to the electrodes via a high frequency generator as depicted in the schematic.

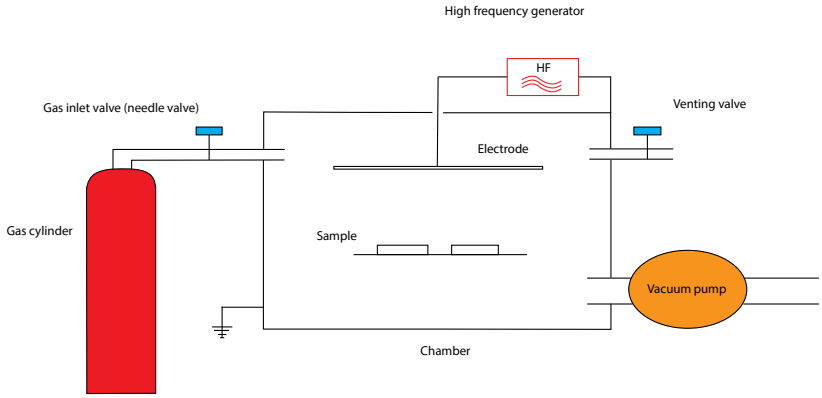

Figure 2-1 schematic of a plasma etching system

The generation of plasma in a plasma coater works in a similar way to that of the plasma generated by a magnetron as described in Section 2.1.3.3, where the high electric field from the electrodes breaks the atoms of the gas into charged ions which then bombard the sample surface and react with the sample or contaminant molecules. Depending on which gas is used to generate the plasma different chemical reactions are possible. In some cases these can alter the hydrophobicity of the sample surface due to changes in surface roughness. In the studies reported in this thesis oxygen plasma was used, which ensured that any hydrocarbons present on the sample`s surface were removed by reacting with the oxygen ions from the plasma to form carbon dioxide. This then leaves a clean surface which can be chemically modified or otherwise treated as shown in Figure 2-2 [97, 98]. For my studies I used a Diener electronic (ZEPTO) Plasma-Surface System.

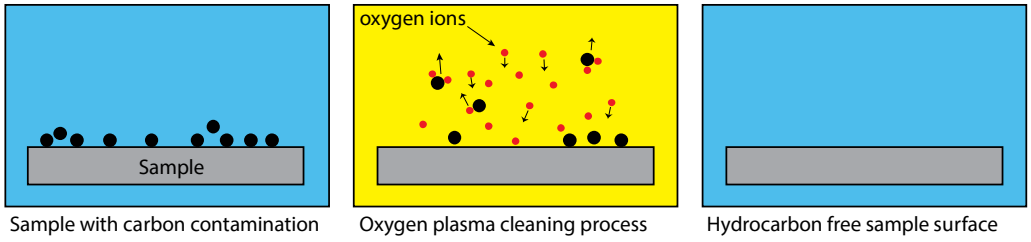

Figure 2-2 Schematics showing different effects plasma can have on samples. A: Oxygen plasma used for cleaning hydrocarbon contamination off samples, schematic adapted from Diener user manual.

2.1.2.Spin Coating

Spin coating is a process where a solution or suspension is dropped onto a fast rotating substrate allowing it to evenly spread out on the surface of the substrate creating an even, thin film or distribution of suspended particles. Throughout the studies reported in this thesis, I have therefore deployed spin coating to deposit colloids onto a substrate (generally glass slides) as a precursor to evaporation in order to create Janus particles. Spin coating allows quick generation of these samples. Figure 2-3 (and Movie S2.1) illustrates the basic procedure of a spin coating process. In general the substrate is held in place during the spinning procedure by means of a vacuum while a pipette is used to drop the sample onto the middle of the surface while this is spinning. As the suspensions used in the present study contained water / ethanol and insoluble colloids (i.e. micron-sized polystyrene particles (PS)) the colloids were left behind after the bulk solution had evaporated.

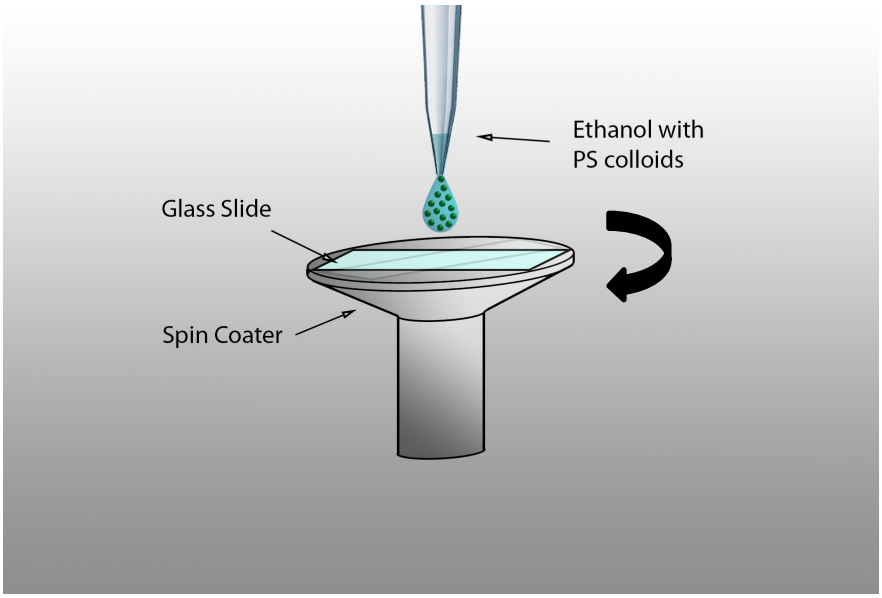

Figure 2-3 Schematic of the spin coating process, the surface on which the glass slide rests rotates at the programmed speeds and has a partial vacuum that holds the glass slide in place (Animation Movie S2.1, Supportive CD).

It was important to determine the right spin coating settings as well as to select the best sample concentrations to ensure a homogenous distribution and avoid the formation of colloidal bilayers. Also, for samples prepared for sputter coating it was important that the colloidal particles did not touch, to avoid shadowing effects during evaporation to ensure that all particles had coatings that were comparable. In this study the ratio of deionised water to pure ethanol used was varied according to which specific colloid was used. Depending on the ratio of ethanol and water used to suspend the colloidal particles and the concentration of the particles, the particles are deposited on the substrate further apart or closer together with respectively a lower or higher percentage of particles touching [99].

2.1.3. Evaporation – Coating of Metals

In the present work evaporation played a key role in creating small micromotors that use e.g. platinum as a catalyst for a chemical reaction which in turn drives the motion of these particles. All three coating techniques discussed here take place under vacuum, which is generally in the region of 10^{-7} mbar for thermal and e-beam and 10^{-3} mbar for sputter coating.

2.1.3.1. Thermal evaporation

Thermal Evaporation of platinum onto PS colloids was used for part of the work in this thesis until electron beam, when it became available, was used to replace this technique. As can be seen in Figure 2-4 the chamber consists of two high current electrodes between which a tungsten filament or boat is placed onto which the material for evaporation is loaded. The sample onto which the materials should be evaporated is then placed at a suitable height, upside-down above the filament. Evaporation will then occur by applying a current which is high enough to melt and

then evaporate the materials. Depending on which materials are used this current can be extremely high, as is the case for evaporation of platinum (around 90 Amps, for the Edwards evaporator used in this work). Because platinum has a very high melting point (1768°C) thermal evaporation using this method is often extremely difficult and can easily exceed the maximum currents allowed for the equipment, as was the case in this study. In order to avoid overheating the evaporation of platinum has to be done in short bursts allowing for the cables to cool down. Furthermore, for samples such as PS colloids, waiting times of around 15 minutes are necessary between evaporation bursts, to ensure the PS colloids do not melt. A shutter can be closed above the filament to stop the deposition abruptly once the required amount has been coated. This is necessary as otherwise evaporation could continue for some time after the electrical current has stopped, due to the residual heat. An Edwards 306 evaporator system was used for all samples produced by thermal evaporation for the studies reported in this thesis.

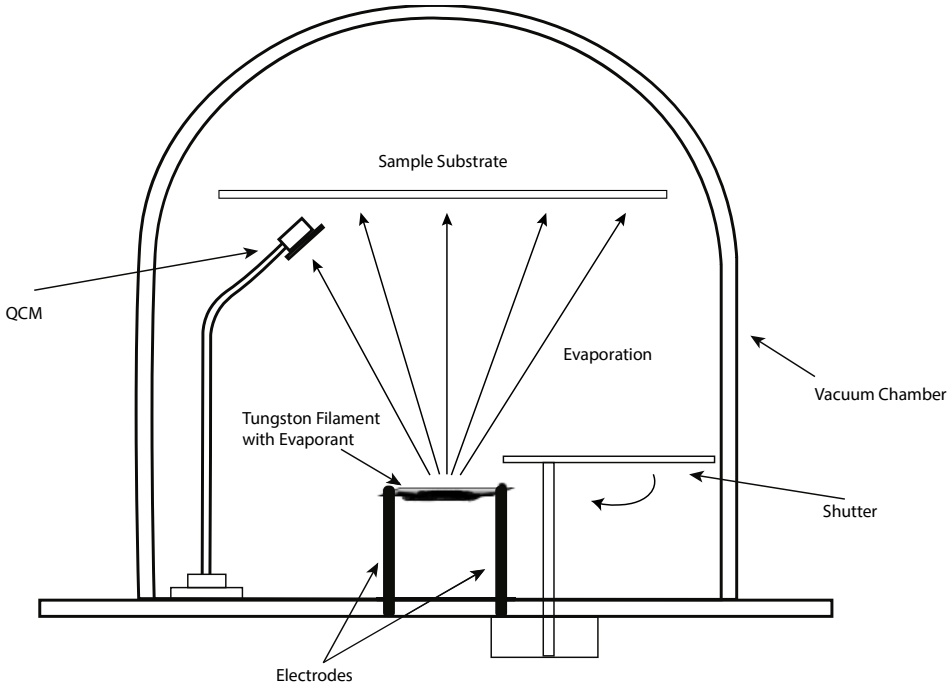

Figure 2-4 Schematic of a Thermal Evaporator

2.1.3.2. Electron beam evaporation

As indicated in the previous section electron beam (E-beam) evaporation is an alternative to thermal evaporation for metals with high melting point such as platinum. E-beam evaporation also has two other key advantages over thermal evaporation. It causes much less contamination as only the material is heated and not the crucible (the container with the evaporant Figure 2-5). Moreover, water cooling of the crucible reduces contamination levels still further. Switching to this method was beneficial for experiments in this thesis and was found to prevent de-lamination of metals during reactivity measurements (see Chapter 3 Section 3.4.4). The system used in this thesis was a combination Moorfield E-beam and magnetron sputter coating system, as pictured in Figure 2-5 (right); evaporation again takes place in a chamber under high vacuum but in this case the tungsten filament is replaced by a crucible made of an appropriate material, such as tungsten or graphite, into which the material for evaporation is placed, as shown in Figure 2-5 (left). For platinum, gold and chromium graphite crucibles were used in the studies here. An accelerated electron beam is focused and directed via electromagnets into the crucible and on impact, depending on its intensity and beam width, the material is superheated and evaporated by transferring the kinetic energy of the electrons into heat. As there are many electrons impacting a very small area this energy is sufficient to heat the material enough to cause evaporation or sublimation. A potential of 10 KeV is used to accelerate the electrons. In the case of evaporating metals such as platinum a current of around 90 mA is needed on a narrow beam.

It is important to note that both thermal evaporation and electron beam evaporation are highly directional. This means that the evaporated material travels only in a straight line from the crucible until it hits the sample [100].

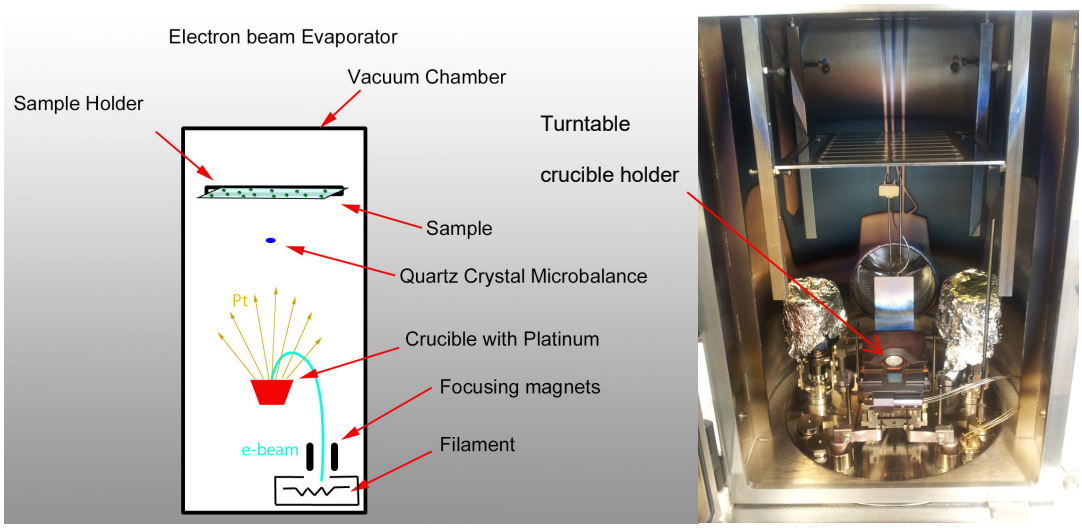

Figure 2-5 (left) Schematic of an Electron Beam Evaporator, (right) photo of the combination electron beam evaporator with two magnetrons covered with tin foil.

2.1.3.3. Sputter coating via Magnetrons

Sputter coating is a coating method that is not directional unlike the previously described methods (Section 2.1.3.1 and 2.1.3.2). Moreover, unlike thermal or E-beam coating, sputter coating does not take place under a high vacuum but rather in a low vacuum argon atmosphere (~10^{-3} mBar). In the case of sputter coating via magnetrons, electric magnets below the target generate strong magnetic fields around the target area as illustrated in Figure 2-6 (left) and these in turn cause electrons to travel along the magnetic flux near the target. Turning on the current ignites the plasma (argon plasma), i.e. the atoms are broken up into positively charged ions and negatively charged electrons, which can generally be seen as a glowing gaseous matter (see Figure 2-6 (right photo). The field lines around the magnetrons help confine the generated plasma near the magnetrons´ target keeping it away from the substrate and therefore not interfering with the generation of the thin film and heating it up. Additionally, in radio frequency (R.F.) magnetron systems the electrons produced travel further and therefore generate more argon ions, which in turn improve the argon plasma and helps the efficiency of the

sputtering process. The argon ions bombard the target gradually breaking free atoms from the target, which then travel to the substrate where they condense to form a thin film. This process is referred to as sputtering. The low vacuum argon atmosphere causes the traveling target atoms to be scattered by interactions with free argon atoms, as shown representatively in Figure 2-6 (left). This means that with increasing argon gas content (generating a lower vacuum) more interactions occur and this in turn causes more scattered sputtering results. With sputter coating the path length from target to sample is much longer than with thermal or E-beam coating (where atoms travel in a straight line) due to the scattering effect (atom trajectories are not direct (linear) but move in random scattered trajectories due to the interaction of the atoms with the argon ions). Sputter coating via magnetrons is currently regarded as one of the most effective ways to make thin films for high quality applications [101-104]. In some cases it may be desired to have a chemical reaction take place during film deposition. In such cases other gases may be introduced into the system such as oxygen, or nitrogen to produce oxides or nitrates which have similar effects as described in the plasma cleaning Section 2.1.1 [105]. In this study sputter coating was only used for coating chromium and gold films.

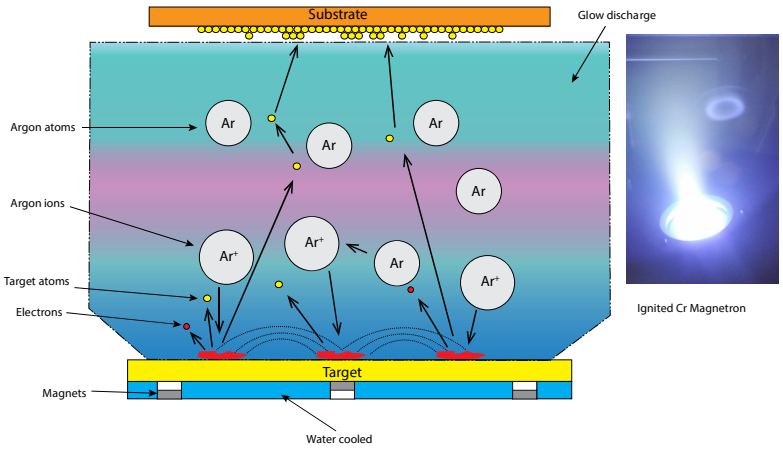

Figure 2-6 (left): Schematic of Magnetron thin film coating in Argon atmosphere (adapted from [105]); (right): Photo of ignited chromium magnetron during sputter coating.

2.1.3.4. The Quartz Crystal Microbalance for film thickness determination

Throughout this thesis it was of vital importance to determine and control the thickness of the evaporated metal layer in order to understand its effects on reaction rate and swimming velocity. The thickness can be monitored during the evaporation process using a Quartz Crystal microbalance (QCM) built into the chamber (see Figure 2-5).

It is imperative that the QCM is either very close to the substrate onto which the material is being evaporated or has been calibrated according to the position at which the deposition takes place, as otherwise the deposition thickness reported by the QCM is different than the deposition on the sample.

The principle of thickness determination by QCM uses the piezoelectric effect of a thin crystal between two electrodes. This effect means that when a mechanical strain is applied to a piezoelectric material this strain results in an electric potential or conversely, when an electric potential is applied to a piezo-material this results in a material strain. If an alternating electric field is applied this then causes the QCM to oscillate. If the acoustic wavelength of the QCM is equal to twice the combined thickness of the crystal and electrodes a standing wave condition is achieved. This means that the resonance at which the system oscillates is highly sensitive to the thickness of the crystal and its acoustic frequency and therefore any material that has been deposited on the surface of the crystal influences its resonant oscillation frequency, i.e. the resonance frequency gradually decreases with increasing thickness of the crystal. From this it is possible to calculate the mass of deposited material on the surface of the QCM using the Sauerbrey equation {2.1}, where f_0

is the resonant frequency (Hz) of the QCM, Δf is the frequency change, Δm is the mass change, A is the active crystal area (cm^2), ρ_q is the density of quartz (2.648 g/cm^3) and μ_q is the shear modulus of quartz of AT-cut crystal (2.947×10^{11} $g \cdot cm^{-1} \cdot s^{-2}$) [106].

$$\Delta f = -\frac{2 f_0^2}{A\sqrt{\rho_q \mu_\rho}} \Delta m \qquad \{2.1\}$$

In this equation the film is treated as an extension of the QCM thickness and therefore three conditions must be obeyed for accurate results: the deposited layer must be rigid, evenly distributed and finally the frequency change must be less than 2% ($\Delta f / f \leq 0.02$). This method of calculation is used by the QCM in the Edwards evaporator used in the present work. Figure 2-7 gives an illustration of the QCM and how the deposition onto the QCM affects its resonant frequency.

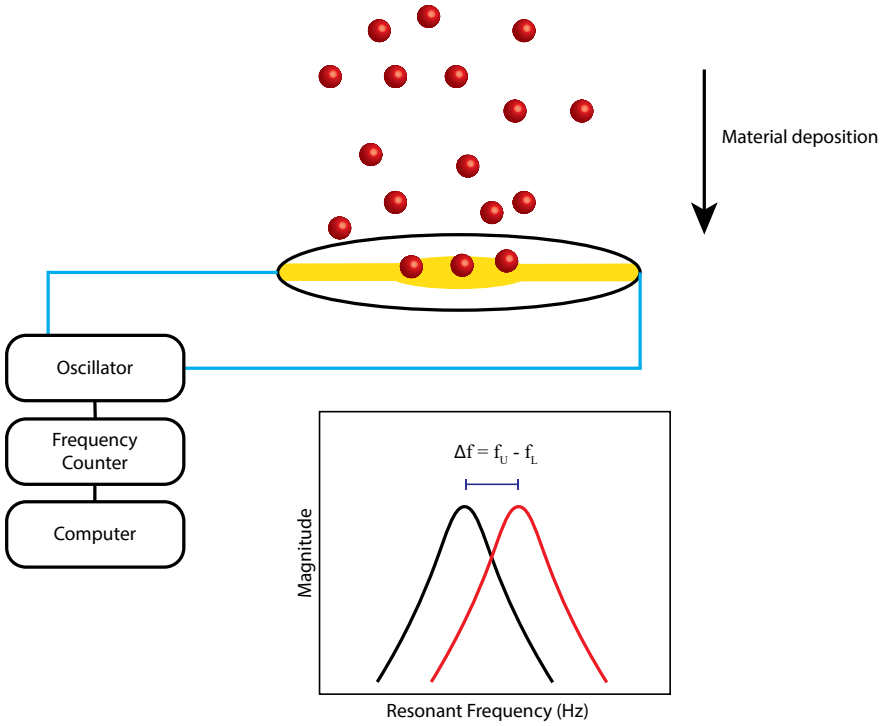

Figure 2-7 Schematic of the function of a QCM and graph showing the frequency shift Δf when the QCM crystal is loaded with material.

Analysis of the frequency changes, including the acoustic impedances of the quartz and film, is necessary for frequency shifts greater than 2%. This is called the Z-match method, and is used to calculate the change in mass as shown in formula {2.2}, where f_U is the frequency of the unloaded crystal (before deposition), f_L is the frequency of the loaded crystal, N_q is the frequency constant for AT-cut quartz crystal (1.668×10^{13} HzÅ, 35.15° inclined from the Z-axes of the crystal as shown in [107]) and Z the Z-Factor of the film material which is calculated with Eq.{2.3}, where ρ_f is the density of the film and μ_f, μ_q are the shear modulus of the film and quartz respectively.

$$\frac{\Delta m}{A} = \frac{N_q \rho_q}{\pi Z f_L} \tan^{-1}\left[Z \tan\left(\pi \frac{f_U - f_L}{f_U} \right) \right] \qquad \{2.2\}$$

$$Z = \sqrt{\frac{\rho_q \mu_q}{\rho_f \mu_f}} \qquad \{2.3\}$$

By this method, frequency changes of up to 40% shift from the unloaded QCM can be calculated, but sometimes there is a failure to calculate frequency changes of less than 40% due e.g. to short circuits of the electrodes or because lots of different materials can cause mode hopping due to excessive build-up of composite resonant modes, meaning a clean resonant frequency can no longer be obtained.

As previously stated both thermal and electron beam evaporation are highly directional and therefore it needs to be considered that the amount of evaporated material per unit area follows the inverse square law with regards to the distance between the sample and the irradiation source. Therefore any evaporation done on a flat surface with a small irradiation source will have a thickness gradient. This is discussed in detail in Chapter 3 Section 3.2.6.

2.1.4. Inkjet Printing

Inkjet printing is a technique by which a liquid material (ink) is directed in a controlled manner onto a substrate via a print head device which generates small droplets and allows printing of simple or more complex patterns. There are two major inkjet printing modes, namely continuous mode and drop-on-demand method. In pursuit of the generation of biocompatible, self-motile particles powered by enzymes, inkjet printing has been used to create differently structured particles based on silk scaffolds. The drop-on-demand method was chosen to print the inks onto silicon wafers as solutions were used in small quantities and jetted silk-based inks used in this study change structural formation after being jetted due to the sheer force acting upon the sample during jetting, thus inducing some conformational changes (see Chapter 7).

2.1.4.1. Drop-on-demand inkjet printing

Drop on demand inkjet printing allows for drops to be released only when an electrical signal is passed into the transducer as illustrated by Figure 2-8. In general the transducer is a piezoelectric material which changes its structure when being electrically charged, as previously described in Section 2.1.3.4. This structural change of the piezoelectric material alters the pressure and velocity of the fluid below and the inner shape of the print head directs it to the orifice, resulting in a drop of liquid being released [108-110]. As shown in the illustration, a drop is released for every pulse programmed into the print driver. This, coupled with a moving sample stage allows for complex patterns to be printed onto the substrate. The ink from the reservoir needs to be controlled via a pressure pump to make sure that the surface tension of the ink fluid is sufficient to stop it dribbling when there is no signal. This is generally done by means of a very slight negative pressure but

depending on the ink it may also be necessary to apply a small positive pressure especially with more viscous or high surface tension fluids. The print driver is one of the key components to generating even droplets. Generation of a certain type of oscillation to the piezo enables accurate and repetitive droplets of the ink material to be produced. The parameters for this need to be carefully chosen and calibrated to suit the ink properties which are influenced by viscosity, and the density of the liquid along with the specific print head nozzle. Furthermore, it is important to keep the surrounding temperature and humidity stable, as they can have strong impacts on the printing process.

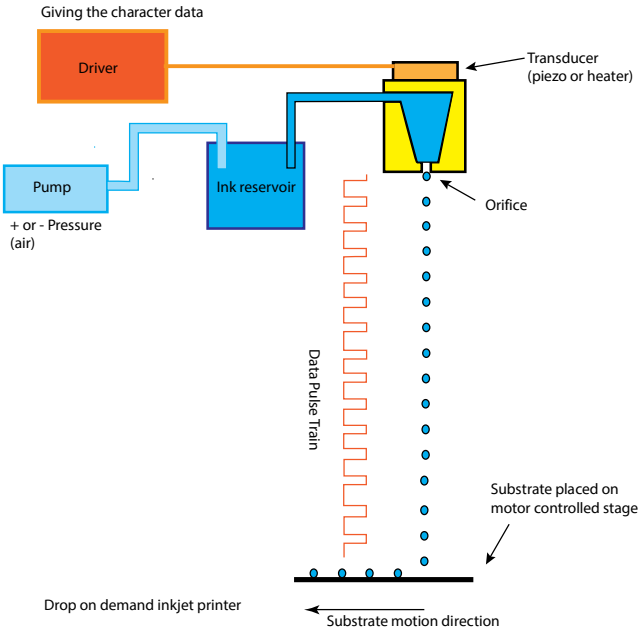

Figure 2-8 Drop on demand inkjet printing adapted from MicroFab manual.

It is possible to use inkjet printing to generate 3D structures by using a layer-by-layer (LBL) printing approach. This means that samples are generated by simply printing multiple layers, one layer on top of another, gradually generating a z-axis height of the sample. Therefore, depending on the ink used each layer may have a different height thickness. Important values to take into consideration when using this method are the spread of the droplets, because the columns formed will vary in

height if the initial droplet sizes are very different. If droplet acceleration speeds are different from sample to sample then this will also affect the column heights as the material will end up spread out further for inks that have been printed with a higher velocity. The great benefit of generating 3D structures via LBL inkjet printing is that there is no need for the high temperatures often required for other 3D printing methods and this allows the use of many different inks, in particular ones containing biological substances such as silk and enzymes. Furthermore, it is also possible to use inkjet printing to generate smooth thin films if the distance between the drops is chosen in the correct interval [111-114].

2.2. Analytical techniques

In this section I present the main analytical techniques used to characterise the experimental data presented in the following chapters.

2.2.1. UV-VIS-Spectroscopy

UV-VIS Spectroscopy is an analytical method for determining the concentration of an analyte in liquids by measuring the amount of light, at a particular wavelength, absorbed when passing through the sample in a cell (cuvette) made of glass (for visible light) or quartz (for UV spectrum). The wavelength at which a chemical absorbs light is dependent on the specific analyte. Figure 2-9 shows a schematic of the basic principle of how a spectrometer works. Light passes through a prism or commonly in more modern spectrometers a diffraction grating, and is then channelled via a pinhole through the sample in the cuvette. The light intensity is then detected by a photoresistor, which gives a readout of the intensity and is calculated into either an absorbance value or transmission value.

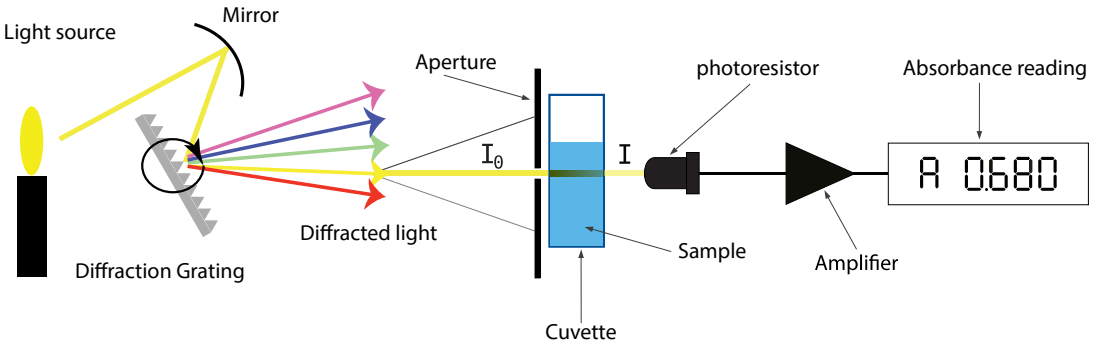

Figure 2-9 Basic schematic showing how a spectrometer works

Different wavelengths are obtained dependent on the angle at which the diffracted (diffraction grating) or refracted (prism) light reaches the aperture, as shown in Figure 2-10. It is possible to calculate the angle of the required wavelength using Eq.{2.4}, where, $\phi_{m\lambda}$ is the angle of refraction (measured against the normal), m is the order of refracted ray (where $m = 1$ is the brightest beam, as shown representative in Figure 2-10), d is the groove spacing and λ is wavelength wanted [115].

$$\phi_{m\lambda} = \arcsin\left(\frac{m\lambda}{d} - \sin\theta_i\right) \qquad \{2.4\}$$

This allows spectrometers to have a bandwidth of wavelengths generally spanning from the far UV at around 180 nm into the infrared at around 1100 nm.

It is important that the photoresistor is calibrated before each measurement, in order to have the correct reference for the initial light intensity so that the intensity drop can be measured accurately. This must be done for every wavelength as light has different energies for every wavelength and thus the photoresistor will register different baseline intensities for every band and will be more sensitive to particular wavelengths. Depending on the pattern (e.g. sawtooth as in Figure 2-10, or rectangular, or blazed) of the diffraction grating the intensities of the refracted

wavelengths will be different. All the wavelengths will be diffracted off the grating multiple times but their intensities will change as the angle widens; the light intensities are referred to as orders. The higher the order of the diffracted rays the lower the intensity and therefore the first order is highly favourable.

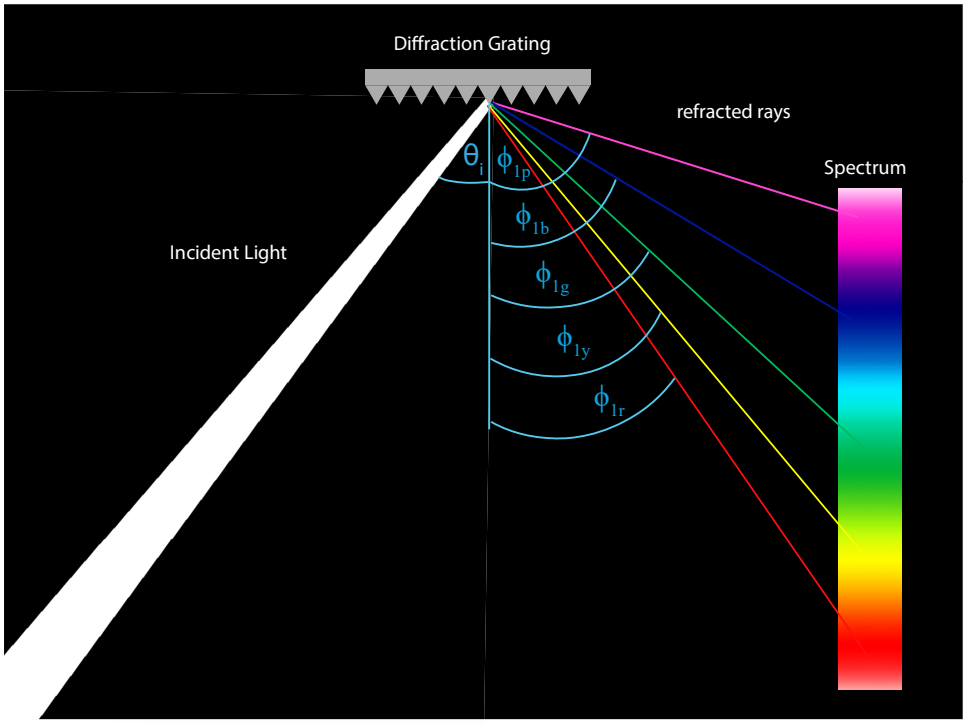

Figure 2-10 Schematic of how a diffraction grating breaks the light into its different wavelengths, this example shows a sawtooth diffraction grating. θ_i is the incident angle of the light, ϕ_1 is the first order refracted ray angle with the colour denoted as p= purple, b=blue, g=green, y=yellow, r=red.

The light absorbed by the test solution is described by the Beer-Lambert law, which is shown in Eq.{2.5}, where I is the light intensity (I_0 the initial light intensity), ε is the extinction coefficient for the current analyte, l the path length through the solution and c the concentration of the solution in mol/L. This means that the light being absorbed by the solution is proportional to the concentration of the absorbing analyte.

$$Abs(dE) = \log_{10}\frac{I_0}{I} = \varepsilon lc \qquad \{2.5\}$$

Once a suitable wavelength has been picked it is then possible to create a calibration curve by measuring the absorbance by the chemical at different concentrations. This then allows one to fit a straight line to the experimental data and to calculate the extinction coefficient for that substance at the given wavelength.

In systems where the concentration of an analyte changes over time due to a reaction taking place it is possible to determine the rate at which this reaction takes place. Such determinations are often done in biology for enzyme assays to determine the activity and lifetime of enzymes. Dependent on the system used the analyte either decreases or accumulates over a given time-frame and from this the change in concentration measured via the spectrometer allows the reaction rate to be calculated. In my studies the rate of decomposition of hydrogen peroxide has been determined in this way at $\lambda = 240$ nm.

2.2.2. Tensiometer (Wilhelmy Plate Tensiometer)

Surface tension plays a vital role in understanding interactions of self-motile particles, in particular of bubble-driven particles as investigated in Chapters 5, 6 and 7. The tensiometer enables quick measurement of surface tension for various liquids. There are a variety of different methods to measure surface tension such as the Du Noüy-Paddy method which uses a rod that is pulled out of the liquid, the Noüy Ring method, where a ring is used or, as in the present study, the Wilhelmy plate method (see Figure 2-11). The Wilhelmy plate is a thin plate that can be made of glass, filter paper or as in this study platinum in the Krüss Force Tensiometer K11 system. The plate is of known thickness (d) and length (w) and is slowly lowered onto the surface. If the material used is completely wettable then theta can

be assumed to be 0°. Roughening of materials can help with wettability [116] or alternatively literature values have to be used as correction factors for the actual material used. Prior to taking measurements it must be ensured that the plate is cleaned thoroughly, which in the case of a platinum plate can be done by allowing it to glow red for a moment in a blue flame, ensuring any organic residues have been removed. The plate is then carefully placed into the tensiometer which lowers it onto the surface of the liquid, or alternatively in some systems it may bring the sample up to the plate. When the plate touches the liquid interface a force acts upon the plate which can be correlated to the surface tension of the fluid. This force is measured, as a force dragging the plate down, by a very sensitive microbalance in the tensiometer. From this force (F) it is possible to calculate either the surface tension (γ) or the contact angle (θ) of the liquid using the Wilhelmy equation{2.5}, where θ is the contact angle and l is the wetted length which is given by Eq.{2.5}, in the case of using the Wilhelmy plate. A rough platinum plate is usually used for this as platinum has a high surface free energy which results generally in a contact angle of 0°.

$$\gamma = \frac{F}{l\cos(\theta)} \qquad \{2.5\}$$

$$l = 2w + 2d \qquad \{2.5\}$$

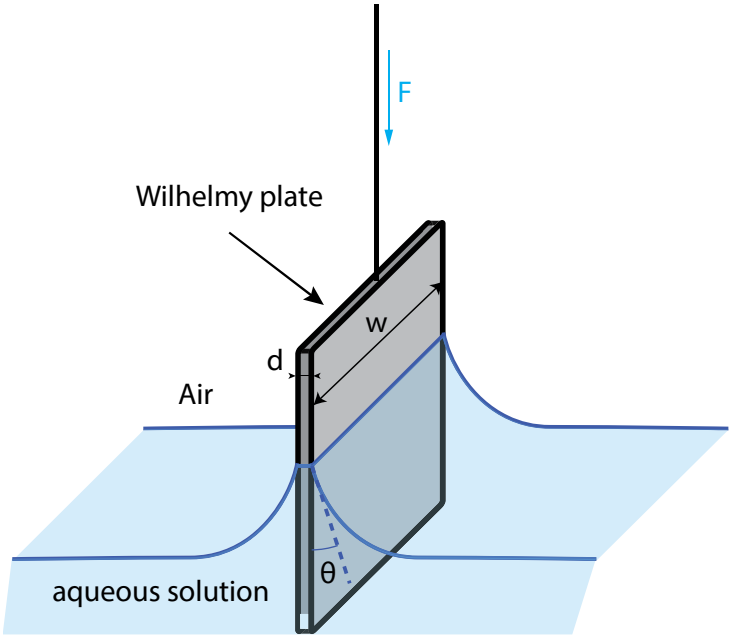

Figure 2-11 Schematic of a Wilhelmy plate being used for measuring surface tension of an aqueous solution.

Rearrangement of the Wilhelmy equation gives Eq.{2.6}, which allows calculation of the contact angle of the immersed solid. This is usually done by dynamic contact angle measurement, for which the plate is slowly immersed into and then withdrawn from the liquid. During wetting the advancing angle is determined followed by determination of the receding angle during the de-wetting process.

$$\theta = \arccos\left(\frac{F}{l \cdot \gamma}\right) \qquad \{2.6\}$$

The Du Noüy-Paddy method, using a cylindrical rod instead of the Wilhelmy plate, allows measurement of the surface tension of smaller samples but because of the much smaller wetting length this means that this method has a much smaller resolution as the resulting force measured by the tensiometer is much smaller. The wetted length is easily calculated for the rod by simply determining the circumference of the rod as shown in Eq.{2.7}.

$$l = 2\pi r \qquad \{2.7\}$$

Finally, the Noüy Ring method uses a ring which, as in the previous methods, is slowly lowered onto the liquid surface and then is raised just before the lamella gets torn from the ring (the liquid gets drawn to the ring and lifted up with the ring moving). This is the maximum force and correlates to the surface tension. In this case the wetting length is determined by the inner and outer circumference of the ring. Correction factors need to be taken into consideration as the weight of the liquid increases the measured force along with the fact that the maximum force does not occur at the same time on the inner and outer diameter of the ring. According to the Krüss tensiometer manual the best material for the ring is an alloy of Platinum-Iridium as it is optimally wettable and has a contact angle of 0°. Because of all the correction factors involved in this method one or other of the two previously described methods are generally favoured.

The Krüss Force Tensiometer K11 (as used here) measures the force multiple times until it achieves an average value with a low standard deviation which it reports as the surface tension given in mN/m. For the studies in this thesis, the Wilhelmy plate method was used to measure surface tension of solutions.

2.2.3. Contact angle

Measuring the contact angle is a method to determine the hydrophobicity of a surface to water or another liquid and is done by dropping a small drop of water, around 3-5 µl fluid, carefully onto the surface. As previously stated (Section 1.1.2 and 2.2.2) surface tension plays an important role in influencing the motion of colloids, in particular if they move between the bulk solution and air / water interface. It is also important to determine the degree of wetting of surfaces as this will generate differences with regards to the reaction rate at the surface and to

bubble detachment. Different contact angles can also be an indicator of contamination issues of the surface. By means of a tilted camera an image is taken from which the contact angle can be measured. Due to surface tension a drop is formed which has a certain contact angle (θ_C) that depends on the surface hydrophobicity and roughness as shown in Figure 2-12. θ_C is obtained by drawing a tangent from the contact points along the liquid / air interface. This means that if the liquid spreads on the surface the contact angle is small and if it stays balled up a large contact angle is measured. In the case of using water the surface is considered hydrophilic if the contact angle is below 90° and anything above it is considered hydrophobic. To increase accuracy both sides of the droplet are measured and a mean value is calculated. Super hydrophobic surfaces are those having a contact angle greater than 150°.

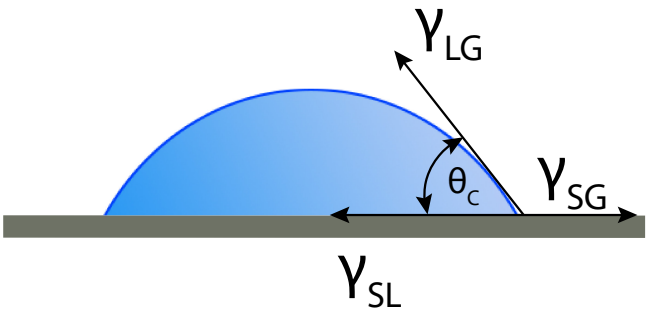

Figure 2-12 Illustration showing a water droplet (sessile) on a flat substrate for measuring the contact angle (θ_C).

In a bulk solution of e.g. pure water, each molecule is pulled in every direction by its neighbouring molecules, but in the case of molecules that are exposed to a surface, be it air or a substrate such as a silicon wafer, the molecules will become ordered so as to maintain the lowest surface free energy. This means that on a hydrophilic surface the water molecules will spread out or on a hydrophobic surface they will ball up. The effect of gravity on the droplets causes them to be slightly

skewed from an ideal spherical shape. From this the contact angle can be calculated by using Young's Eq.{2.8}, where γ_{LG},γ_{SG} and γ_{SL} give the liquid-gas, solid-gas and solid-liquid interfacial tensions, respectively [117, 118].

$$\gamma_{LG}\cos\theta_C = \gamma_{SG} - \gamma_{SL} \qquad \{2.8\}$$

2.2.4. Microscopy

Microscopy has played an essential role in my studies of self-motile particles in this thesis; it was needed for characterizing the devices (i.e. Janus, pore and microrockets) produced in this thesis as well as for recording the motion of these devices in different environments using Charged Coupled Device (CCD) cameras attached to the microscope.

2.2.4.1. Optical (Light) Microscopy

A microscope is made up of an objective lens with different magnification powers and an ocular lens (namely the eye piece one looks into) or alternatively a CCD camera for image capture, and a focus lens to allow the microscope to be focussed onto the sample being looked at. There are two main ways in which samples can be illuminated (1) using reflective light from above through the objective onto the sample (called dark-field microscopy), where contrast is due to light scattered by the sample and (2) from below going through the sample with transmitted light also referred to as bright-field microscopy (see Figure 2-13). The adjustable apertures, shown in the schematic, allow the light beam to be adjusted and the condenser lens allows focussing of the light beam onto the observed sample area. In some cases both light sources may be used simultaneously, in particular if the sample is fluorescent and filters are being used such as described in Section 2.2.4.2. In this

thesis both bright field and dark field microscopy were used depending on the sample and which generated the best images for automatic software tracking purposes.

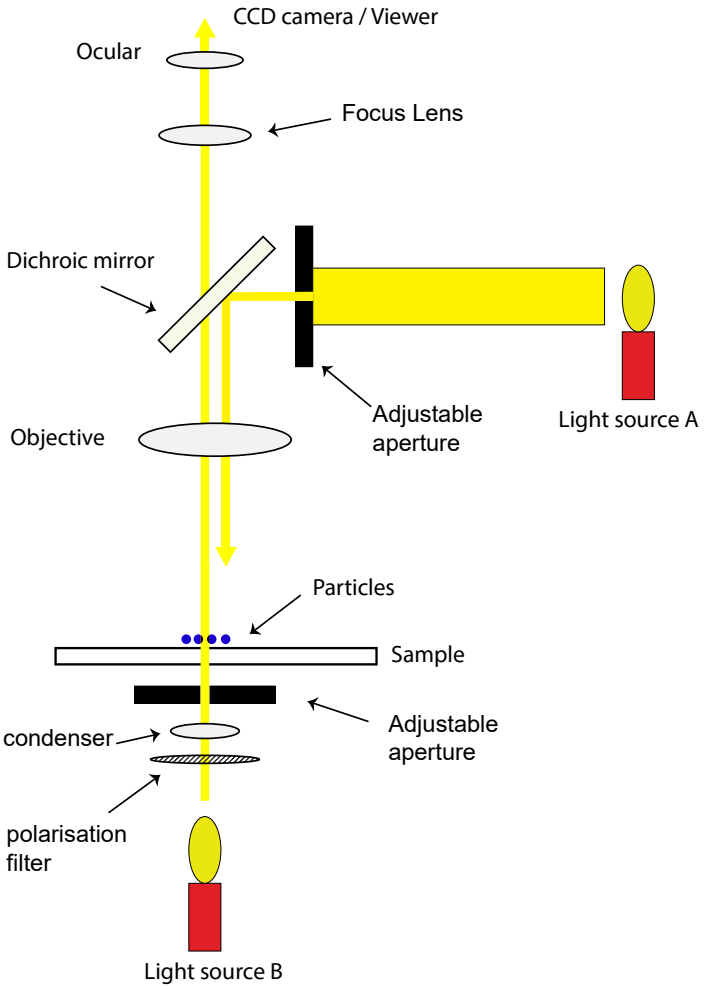

Figure 2-13 Schematic of an optical microscope with two light sources, A for reflective lighting and B for transmitted illumination.

The maximum resolution of visible light microscopy is mainly governed by the quality of the objective lens and finally by the size of the light wavelengths used i.e. the Abbe diffraction limit which is described by Eq.{2.9}, where d is the diffraction limit λ is the wavelength of the light, $n\sin\theta$ is the numerical aperture (NA) of the lens used, which in modern optics is around 1.4-1.6 meaning the Abbe limit of an optical microscope is $d = \lambda / 2.8$.

$$d = \frac{\lambda}{2n\sin\theta} \quad \{2.9\}$$

Thus, if blue light for example is used with a wavelength of 400 nm this gives a maximum resolution limit of $d = 142.9$ nm.

It is important to note that for many of the tracking experiments undertaken in this thesis samples were put into sealable quartz cuvettes with wall thicknesses of around 1 mm. Conventional objectives will not resolve good images from such cuvettes as they are only designed to compensate for the thickness of cover slips, typically 0.1-0.2 mm. However, special objectives (which have high NA's) are available with adjustable correction collars to compensate for thicker glass / quartz to ensure optimal image quality. The correction collar adjusts the central lens within the objective and therefore images are not 'skewed'; these collars were used for optical microscopy throughout this thesis.

2.2.4.2. Fluorescence Microscopy

Fluorescence microscopy is a way of enhancing optical microscopy by generating a high signal to noise ratio (generating high contrast images, as the signals received are very specific) as well as allowing indirect detection of fluorescently labelled features e.g. enzymes, that would otherwise be far below the resolution limit of an optical light microscope. The high contrast images make it particularly easy to automatically track the motion of particles via CCD camera captured images, which has been extensively used throughout this thesis. In fluorescence microscopy the light is directed through an excitation filter, which filters away any wavelengths that are not of interest, to ensure that the sample is not flooded with light (in particular the emission wavelength of the sample as this would saturate its signal

and mask its detection) at other wavelengths than those needed to excite the fluorescent substance used in the sample, called fluorophore. Flourescein isothiocynate (FITC) is an example of a fluorophore used in this study and has a peak excitation wavelength of 495 nm and an emission peak at 519 nm. This means a filter cube has to be used with the correct excitation and emission (barrier) filters, namely 450-490 nm and 515 nm cut-on long pass filter (allowing for visible light from 515nm up to the high red spectrum) respectively. Similarly the dichroic mirror has a cut-on wavelength of 500 nm and allows for the blue light to be reflected down through the objective to the observation region of the sample. This blue light then excites the fluorophore in the sample which emits light that can be detected through the dichroic mirror and emission filter which filter out any excitation wavelengths allowing detection of even very faint fluorescent signals from the sample.

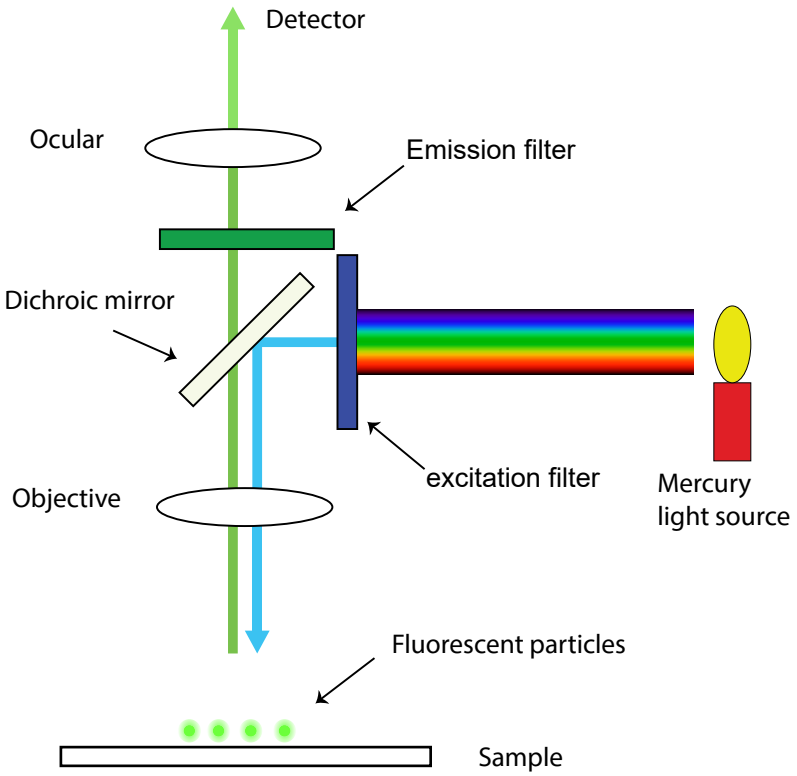

Figure 2-14 Schematic of how fluorescence microscopy works.

This means that the detectable range of the microscope is not dependent on the size of the e.g. fluorescent particles but rather the emission intensity (and CCD camera sensitivity) and therefore it is possible to visualize particles in nm size range. As previously noted, the use of fluorescently active colloids is of particular interest. It makes it possible to see the direct orientation of particles, if they have been coated with a platinum layer and therefore more information can be gathered from tracking experiments regarding the rotational diffusion coefficient of these particles [30], in addition it allows better 3D tracking of particles [92] due to the more intense signals. This method also allows the detection of enzymes that have been e.g. FITC labelled and to detect if for example they have been attached to a surface or particle.

2.2.4.3. Atomic Force Microscopy

In this thesis atomic force microscopy (AFM) was used to analyse the surface roughness of flat platinum samples on silicon wafers and also the surface on top of larger colloids i.e. 30 μm particles. It was also used to be able to measure the evaporation thickness of platinum on silicon wafers in order to verify QCM readings. This was done by masking part of the silicon wafers with TEM grids and then using ATM software to measure the step height after the grids were removed (as described in Chapter 3 Section 3.3.2).

AFM is a way of retrieving surface topography and other surface physiochemical properties of a sample with nm high resolution. As AFM scans samples in x, y and z directions, it is possible to retrieve 3D representations of the sample's surface. The basic principle of AFM is that a very sharp tip mounted on a cantilever is passed over a sample. The interaction of this cantilever with the sample's surface is

detected by a laser beam reflected off the back side of the cantilever to a position sensitive photodetector (see Figure 2-15).

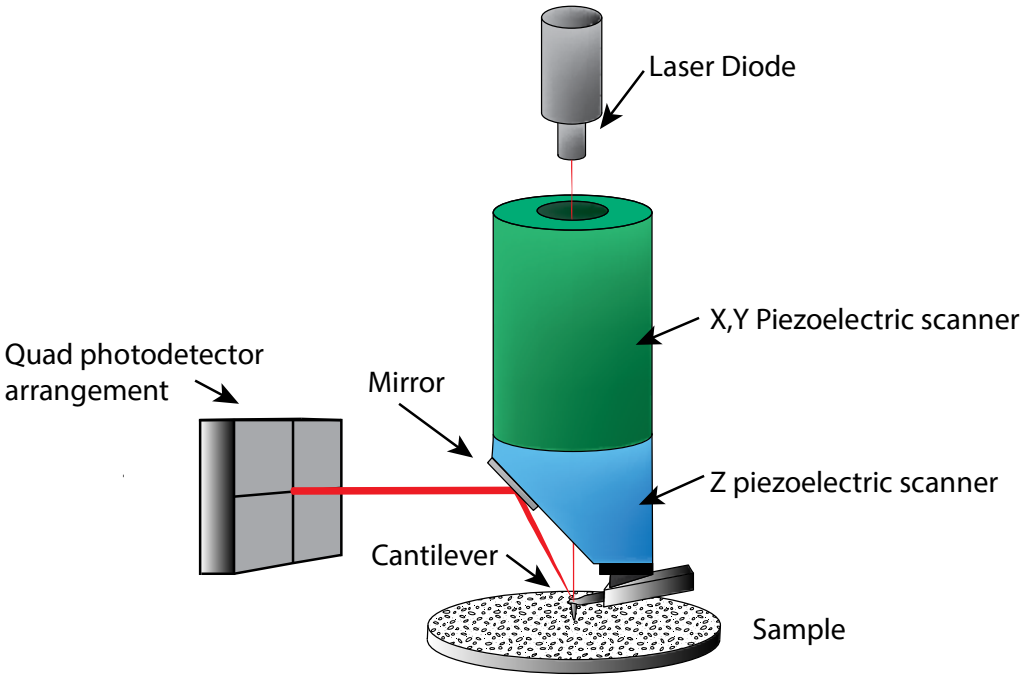

Figure 2-15 Schematic of an AFM based on the Bruckner Dimension 3000 system design.

In AFM forces are measured using the principles of Hook's Law (Eq. {2.10}), where the force (F) between the sample and the probe is dependent on the spring constant (k), which is analogous to the stiffness of the cantilever and the distance between the sample surface and the probe, where x is the cantilever's deflection.

$$F = -k \cdot x \qquad \{2.10\}$$

This means that if the spring constant of the cantilever is less than that of the surface the cantilever will bend and a deflection can be registered. For a straight shape rectangular AFM cantilever the spring constant can be calculated by Eq {2.11}, where E is Young's modulus, t is the thickness, l is the length and w the width of the cantilever [119].

$$k = \frac{Ewt^3}{4l^3} \qquad \{2.11\}$$

There are two main modes (under ambient conditions) by which a tip can be scanned across a sample, namely tapping mode (intermittent mode) and contact mode. In the case of contact mode the tip is dragged over the sample and the height differences of the sample are registered by feedback, where the laser beam is kept in the centre of the detector by movement of the Z-piezoelectric scanner (see Figure 2-15).

For tapping mode the tip is oscillated at high frequency and hits the sample's surface while scanning over the sample. It is possible to calculate the resonant frequency (f_0) of a cantilever using the simple harmonic motion Eq.{2.12}, where m_0 is the effective mass of the cantilever and k the spring constant [120].

$$f_0 = \frac{1}{2\pi}\sqrt{\frac{k}{m_0}} \qquad \{2.12\}$$

The AFM is equipped with two piezoelectric scanners as illustrated in Figure 2-15. One scanner enables the tip to move in the z-plane direction (meaning moving up and down) the other allows the tip to scan over the sample in the X and Y plane. The air cantilever holder (which was used in this study) contains a piezoelectric stack which is used to oscillate the cantilever for tapping mode operation. After a new cantilever has been loaded into the holder it is necessary to adjust the laser beam so that it is aimed onto the back of the cantilever. The closer the laser beam is to the tip-end of the cantilever the higher is the accuracy of measurement, as the deflection of the laser beam is larger the closer it is to the tip rather than the base of the cantilever (in respect to the tip displacement). As previously stated the

movement of the tip is detected by the deflection of a laser beam onto a photodiode assembly and is readjusted by a feedback loop in order to keep the beam in the same place on the photodiode, however in tapping mode this feedback loop ensures that the amplitude of the oscillation is kept constant. The z-piezo changes therefore act as a proxy for surface height at a constant force / dissipation, where the set-point (which can be manually altered) is the constant energy dissipation that is maintained. If the feedback loop is not working fast enough so that the laser beam does not stay in the correct location this information can be used as an error signal.

Tapping mode can give information regarding the vertical height of the sample as well as information regarding its elasticity. Scan speed settings along with the set-point determine how sensitively the cantilever detects the surface topography and what particular features are emphasized. Once the cantilever has successfully engaged with the sample´s surface it is important to set the gains to sensitive values. Depending on the gains the z-axis piezo adjusts faster or slower in order to keep the deflection or amplitude the same. If the gains are set too high the z-piezo may overcompensate and thus start to generate an oscillating signal and distorted images. When the tip is scanning the sample it scans the sample twice, once in each direction. This gives a trace and retrace scan signal and the more similar these signals are the better the topography images. Apart from adjustment of the gains scan speeds also have a strong influence on good measurement, however if the sample contains sudden, particularly large height changes the cantilever may not manage to cope with this. Adjusting the set-point allows for the cantilever to hit the sample with more or less force depending on the values chosen, which means that features can be more carefully observed e.g. if the cantilever hits the sample with a greater force. The two major display modes used in this thesis were (1) height

mode, which gives the height topography and can also be represented in a 3D way or a simple colour table image where in general brighter colour means greater height and (2) phase imaging. Phase imaging registers the phase lag between the signal that drives the cantilever (its oscillation) and the cantilever´s oscillation output signal. Phase imaging can be used to emphasise surface variations such as adhesion, elasticity and friction. This information is obtained simultaneously with the topography height images. Phase imaging gives a high contrast when the AFM cantilever hits sudden height differences and therefore edges are enhanced in the image.

Finally, it is important to note that over time tips will become blunt. Therefore if the features to be observed are smaller than the point of the tip, then the smallest feature that can be detected will simply be the blunt tip of the cantilever (this is also referred to as tip convolution). For this study it was believed that tapping mode was the best mode to use as tips would get blunt too fast on the hard metal surfaces being imaged if using contact mode. It was nevertheless found essential to still frequently replace the tips. One of the major benefits of AFM is that samples can be easily imaged under ambient conditions and samples do not need to be electrically conductive unlike is the case for SEM, which is described in the following section.

2.2.4.4. Scanning Electron Microscopy

The scanning electron microscope (SEM) utilises a beam of electrons to probe a sample and gathers information from the interaction of the electron beam with the sample. In this study various images were taken via SEM in order to accurately visualize the structure of particles in particular silk rockets in Chapter 7. In comparison to optical light the wavelength of electrons is much less and therefore

the abbe resolution limit (discussed previously in Section 2.2.4.1) of an electron microscope is much smaller than for optical microscopy.

It is necessary to place the samples to be analysed in a vacuum otherwise the electrons could not travel long distances and would be interrupted by collisions with spurious atoms in the air, which is comparable to the need for high vacuum during the previously described evaporation techniques in Section 2.1.3. There are some systems specifically designed for biological samples, where the samples do not have to be placed into a vacuum, these however will not be discussed here.

Figure 2-16 illustrates the basic concepts of how the SEM works. Electrons are accelerated in an electron gun and then focused onto the sample via a set of lenses. A voltage potential (acceleration voltage) is applied over the filament to generate the electrons, and it allows the electrons to pass through a small hole in the anode where the electrons can exit. The higher the voltage potential the faster the electrons will exit the anode. Typical acceleration voltages range from 1 KeV to 30 KeV. A higher acceleration voltage means that the electrons have higher energy and so for delicate samples it is possible that the sample might become damaged or even destroyed in the process of imaging, therefore this needs to be taken into account. Electrons with higher energy (increased acceleration voltage) means that the penetration depth into the sample increases.

The objective lens aperture has a similar function to the aperture on a camera. With a smaller aperture the beam width is decreased increasing the depth of focus and thus generating a sharper image but with loss of signal intensity. The condenser and objective lenses are of vital importance for SEM imaging as it is of paramount importance that the final electron-beam is as narrow as possible to give the SEM its

high resolution, in the nm range. Scanning coils allow the beam to be deflected and therefore enable the SEM to scan over the sample dependent on the settings programmed into the computer software (these settings will alter the magnetic field of the coils). If higher accuracy is needed different types of electron guns can be used such as field emission (FE) guns. It is possible to adjust various parameters in the software including the acceleration voltage, aperture size, scan size, and type of emissions to be analysed by the SEM.

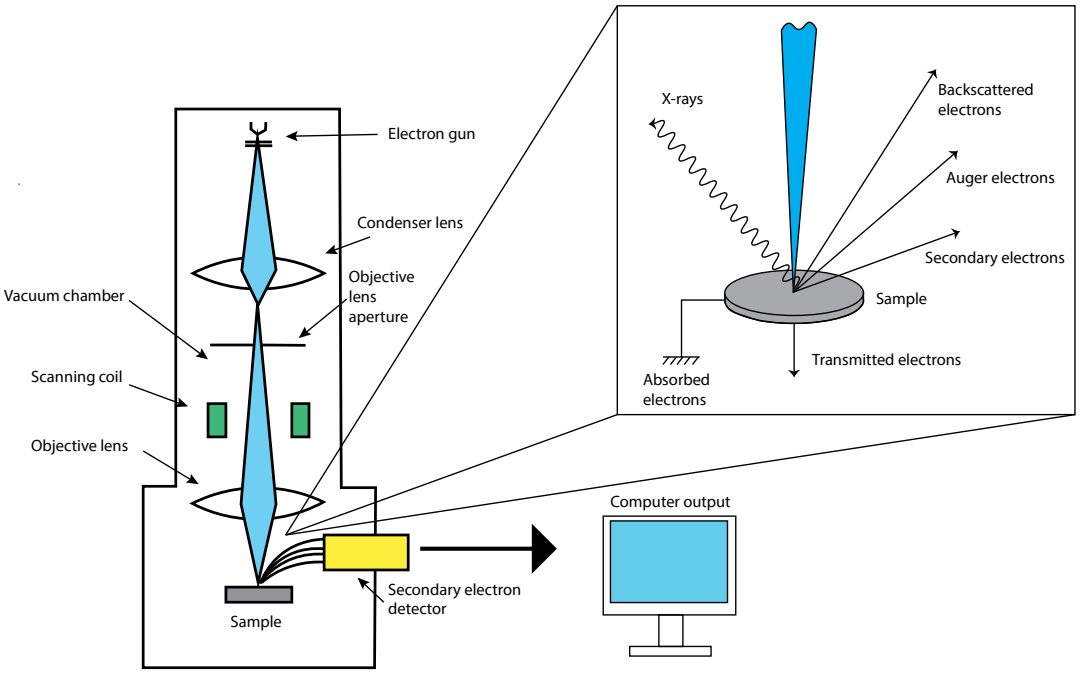

Figure 2-16 Schematic of a scanning electron microscope (SEM), the various wave emissions from the sample are shown in the inset (schematic adapted from Jeol SEM manual).

As shown in the inset of Figure 2-16 an SEM is capable of analysing a specimen via a variety of different emitted signals: such as backscattered electrons, auger electrons, secondary electrons and transmitted electrons. Further to getting topographic data, SEM can be operated in a mode so as to provide chemical information; here I have used a mode to allow characterization of the distribution of elemental platinum and chromium on spherical colloids. To achieve this, rather than collecting electrons, X-ray emissions were detected - this is also known as

Energy Dispersive X-Ray Spectroscopy (EDX). Unlike a conventional microscope, where the magnification is mostly determined by the objective used, when using an SEM the magnification is determined by the output image size on the monitor or printer and the scan size of the electron beam on the sample, i.e. the magnification is simply the display unit divided by the scan size.

Electrons that enter a sample are scattered in the sample over a distance that depends on the electron energy, density of the atoms in the sample and their atomic number. This means that for large atomic numbers and high density the scattering distance of the electrons becomes reduced.

The variety of differently emitted particles allows SEM microscopes to view samples by different methods which emphasize different key features of the sample. Looking at the secondary electrons, i.e. electrons that are produced from the emission of the valence electrons of the atoms in the sample, these electrons have only a very low energy and thus the emitted electrons will not travel long distances through the sample. Therefore only surface or very near surface atoms will emit secondary electrons which can be detected in the detector and so this method of detection is highly sensitive to the sample's surface giving it a high resolution for any topographical features.

Different to secondary electrons are backscattered electrons which are electrons that have been reflected off the sample's atoms. This means that they have a high energy and also means that they can penetrate deeply into the sample. Because these electrons are reflected by the atoms in the sample this means that the larger the atomic number of the atoms in the specimen the greater chance there is of electrons being backscattered. Therefore in areas of high atomic number the

backscattered signal is larger and the area appears brighter in the SEM image. In addition to this the direction at which the backscattered electrons pass out of the sample depends on any surface features, i.e. if the surface has some sort of irregular shape or slope then the direction of the backscattered electrons will be reflected accordingly. As a result the topography of the sample can be viewed in this manner which is known as Electron Channelling Contrast (ECC).

Because samples are bombarded with highly energetic electrons under a vacuum it is important to take into consideration the charging of the sample, as the charge will not dissipate in gas molecules like it would under normal atmospheric conditions. For conductive sample specimens this is not a problem but in the case of non-conductive samples, as were frequently used in this study, it can cause problems. Samples are sputter coated with a thin layer of gold to help prevent the accumulation of high charge on a sample that is non-conductive, and additionally giving a higher signal to noise ratio in order to show clearer surface features. However, for very high resolution SEM images gold sputtering generates gold particles that can be larger than the features to be imaged and for samples like these carbon coating is used. On the other hand, the downside to carbon coating is that it is a much more directional technique, similar to E-beam evaporation (2.1.3.2) and therefore will not cover features that go around corners. For conductive samples the charge is grounded by the stage and the problem of charging is averted. When a sample is made up of non-conductive material electrons that have been absorbed by the sample accumulate and create a negative potential. This negative potential can cause the scanning electron beam to be deflected during scanning and sudden potential releases can then cause the electron beam to move back to its original desired position. This will cause the scanned image to appear distorted (often seen

as lines of distortion). In the case of minor charging of the sample the secondary electrons can be influenced by this causing the image to appear brighter or darker in the charged area. Thus, if the sample is charged negatively then more secondary electrons are able to reach the detector (creating a higher detection efficiency for this area) which creates a greater signal for this area resulting in a brighter image. In the case of the sample becoming positively charged the secondary electrons will be deflected away from the detector thus creating a darker image. As previously stated for non-conductive samples a thin conductive layer such as gold or carbon is usually used to increase the conductivity. When using metals such as gold or platinum their high stability gives a high yield of secondary electrons and generation of a high signal resulting in better images and much better resolution of the surface structure. For very rough samples it is however important that the layer is thick enough so that there is no break in the metal film or charging may still occur. Coating via sputter coating is more favourable than thermal or electron beam coating as it is not directional as described in Section 2.1.3.

It is possible to image a non-conductive sample (with no metal film coating) without charging occurring by lowering the acceleration voltage so far that the amount of electrons flowing into the sample is the same as the amount leaving it. Further to this the amount of secondary electrons emitted from a sample increases when the acceleration voltage is reduced thus increasing the topographic sensitivity. Finally, it is possible to view a specimen without a conductive layer at a higher acceleration voltage if an SEM is run in a low vacuum mode; i.e. the vacuum is between a few tens up to 100 Pa depending on the sample being imaged (normally the vacuum would be 10^{-3} to 10^{-4} Pa). In this case the gas molecules near the electron beam in the chamber are ionized by electrons and therefore when the

positively charged ions hit the sample they neutralize any charge generated by the interactions of electrons with the sample.

2.2.4.5. Energy Dispersive X-Ray Spectroscopy analysis in an SEM

Energy Dispersive X-Ray Spectroscopy (EDX/EDS) uses the X-rays generated from samples via the electron scanning beam to detect elements present in the sample being imaged, as shown in Figure 2-16 (insert).

The incident electrons cause a variety of emissions. X-rays are created when the incident electrons cause inner shell electrons to be emitted from the atoms and outer-shell electrons move into their places. The difference in energy between the two shells the electron has moved between is released as X-Ray energy. These X-rays are called characteristic X-rays as their energies (represented by their wavelengths) are specific for each individual element. Thus it is possible to map these X-rays to individual elements that have been previously characterized. Depending on the shells in the atoms from which the electrons are emitted they are called K, L or M lines corresponding to the K, L and M shells of the atoms, see Figure 2-17 for details. The K- shell is the innermost electron shell of the atom and this means that the K – line has the highest characteristic X-Ray energy that can be emitted. Each emission line can have different emission peaks because it is possible that electrons can drop from different higher shells into the lower shell, e.g. if a K electron is removed an electron from an L shell or M shell can jump to its position so this means that there are two possible peaks in the characteristic K line for this element.

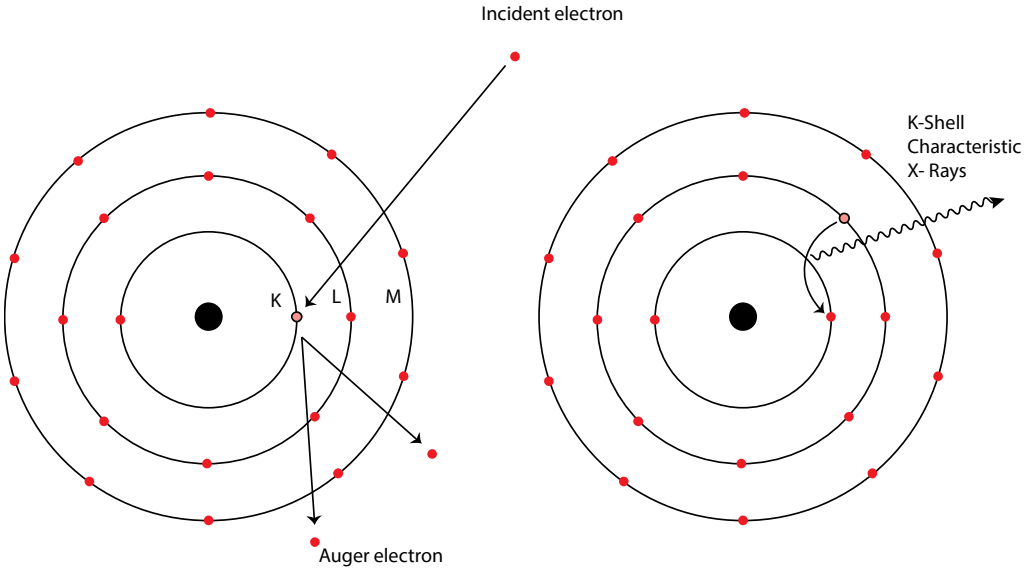

Figure 2-17 Schematic representation of the process of X-Ray emission from an Incident electron beam generating characteristic X-Rays.

On occasions where the incident electrons are decelerated by the atom´s nucleus different X-rays are emitted. These are non-specific and are described as being background X-rays, continuous – or white X-rays. When using EDS analysis in an SEM it is important to consider the fact that for heavier elements the energy required for the X-rays becomes larger. Therefore the incident electrons need a higher energy, corresponding to a higher acceleration voltage, and thus if the acceleration voltage is too low these elements will not be detected as they will not emit X-Rays. There is therefore a specific spectrum for each element which can be compared to the published data for elemental analysis. The SEM software offered by Jeol allows one to pick specific points on a sample or to map an entire sample via EDS elemental analysis. The latter process was used in some experiments in this study to verify metal coverages and zones on polystyrene colloids.

2.3. Mathematical techniques used to characterise propulsion systems

As this thesis investigates the motion of small autonomous particles it was important to be able to characterize their motion at these small length scales using various mathematical approaches. In this section the concepts of the mathematical methods which have been used throughout this work are explained and will be referenced accordingly.

2.3.1. Brownian diffusion

Understanding the type of motion particles undergo is of fundamental importance for determining if the particles are moving on their own accord (self-motile e.g. via chemical reactions) or if they are simply undergoing Brownian motion, diffusion or other flow phenomena. The diffusion coefficient (D_0) of spherical particles in a liquid is given by equation {2.13} where k_B is the Boltzmann constant, T the absolute temperature, R the radius of the particle, η the viscosity of solution and M^0 is a unit tensor of 3 × 3 elements; this is also regarded as the Stokes-Einstein diffusion coefficient for the particular particle [1]. Particles rotate randomly, where the amount of rotation is dependent on the size of the particle. This random rotation is called the rotational diffusion (τ_R^{-1}), which is given by Eq. {2.14} for spherical particles.

$$D_0 = \frac{k_B T}{(6\pi\eta R)} M^0 \qquad \{2.13\}$$

$$\tau_R^{-1} = \frac{k_B T}{(8\pi\eta R^3)} \qquad \{2.14\}$$

For these equations to hold true it is essential that the diffusion is not inhibited by forces close to a solid interface, since it is for particles that are in a bulk solution. In the case of particles that are near a wall a corrected diffusion equation D_H has to be used [121], which is given by Eq. {2.15}, where M^0 is replaced by M^H which is the hindered diffusion tensor and described by Eq. {2.16}, where Λ is given by {2.17} and h refers to the distance of the particle from the wall [122].

$$D_H = \frac{k_B T}{(6\pi\eta R)} M^H \qquad \{2.15\}$$

$$M^H = \left(1 - \frac{9}{16}\Lambda + \frac{1}{8}\Lambda^3 - \frac{45}{256}\Lambda^4 - \frac{1}{16}\Lambda^5\right)^{-1} \qquad \{2.16\}$$

$$\Lambda = \frac{R}{R+h} \qquad \{2.17\}$$

Figure 2-18 shows an example of how the diffusion coefficient of a 2 µm particle is affected by the distance from a wall. Therefore, when viewing micron-sized particles, it is very important to note the position of the particles in relation to any interfaces, such as glass surfaces, as these can affect the motion of the particles.

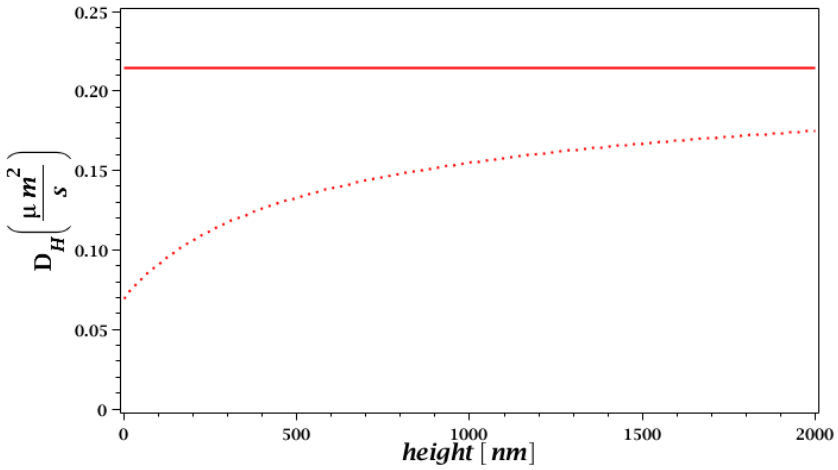

Figure 2-18 Example of a 2 µm particle's diffusion coefficient being hindered by the interference with the wall, solid line indicates unhindered diffusion coefficient.

2.3.2. Mean squared displacement analysis for propulsive Janus particles

For propulsive Janus particles, such as those described in the introduction (Section 1.1.1) the direction of the particles propulsion vector, v is dependent on its orientation and therefore this system is expected to produce trajectories that are affected by the rotational diffusion constant τ_R^{-1}. This contrasts to the case of Brownian diffusion where rotation and translation are decoupled. One can show that in this circumstance, the 2D projection of the MSD for Janus particles as a function of time, is given by Eq. {2.18} [32, 95].

$$\langle \Delta L \rangle^2 = 4D\Delta t + \frac{v^2\tau_R^2}{2}\left[\frac{2\Delta t}{\tau_R} + e^{\left(-\frac{2\Delta t}{\tau_R}\right)} - 1\right] \qquad \{2.18\}$$

Eq. {2.18} has two limiting forms.

For $\Delta t \ll \tau_R$ the first three terms of the Taylor expansion can be applied to the exponential in the 2D projection of the MSD. The terms past the third factor (x^2) in the Taylor expansion are, in the case of these limits, negligible. Therefore we can get the limit as shown in Eq. {2.19}.

$$\langle \Delta L \rangle^2 = 4D\Delta t + \frac{v^2\tau_R^2}{2}\left[\frac{2\Delta t}{\tau_R} + e^{\left(-\frac{2\Delta t}{\tau_R}\right)} - 1\right] \text{ for } \Delta t \ll \tau_R$$

$$\Rightarrow \langle \Delta L \rangle^2 = 4D\Delta t + \frac{v^2\tau_R^2}{2}\left[\frac{2\Delta t}{\tau_R} + 1 + \frac{\left(-2\Delta t/\tau_R\right)}{1!} + \frac{\left(-2\Delta t/\tau_R\right)^2}{2!} - 1\right]$$

$$\Leftrightarrow \langle \Delta L \rangle^2 = 4D\Delta t + \frac{v^2\tau_R^2}{2}\left[\frac{2\Delta t}{\tau_R} - \frac{2\Delta t}{\tau_R} + \frac{4\Delta t^2}{2\tau_R^{\,2}}\right]$$

$$\Leftrightarrow \langle \Delta L \rangle^2 = 4D\Delta t + v^2\Delta t^2 \qquad \{2.19\}$$

This limit allows one to fit the diffusion coefficient and the velocity. The fitting to the experimental data was done using the custom built LabVIEW tracking software in the later described experiments (this tracking software was initially designed and programmed by Dr J.R. Howse and Dr S. Ebbens) [95]. LabVIEW is an object-oriented, visual programming language, which allows simple programming of visual, numerical and hardware orientated programs and is used throughout this thesis to help expedite several batch analysis operations, because datasets for experiments can quickly become very large. Over short time scales, relative to the given colloids rotational time constant (2 μm particles τ_r = 6.21 s/rad^2), the enhanced displacement due to propulsion is linear and the displacement due to Brownian motion is proportional to the square root of time, which gives a curved MSD. Example Fits of Eq. {2.19} to MSD data are shown in Figure 2-19 and Figure 2-20, taken from Dunderdale et al. [95].

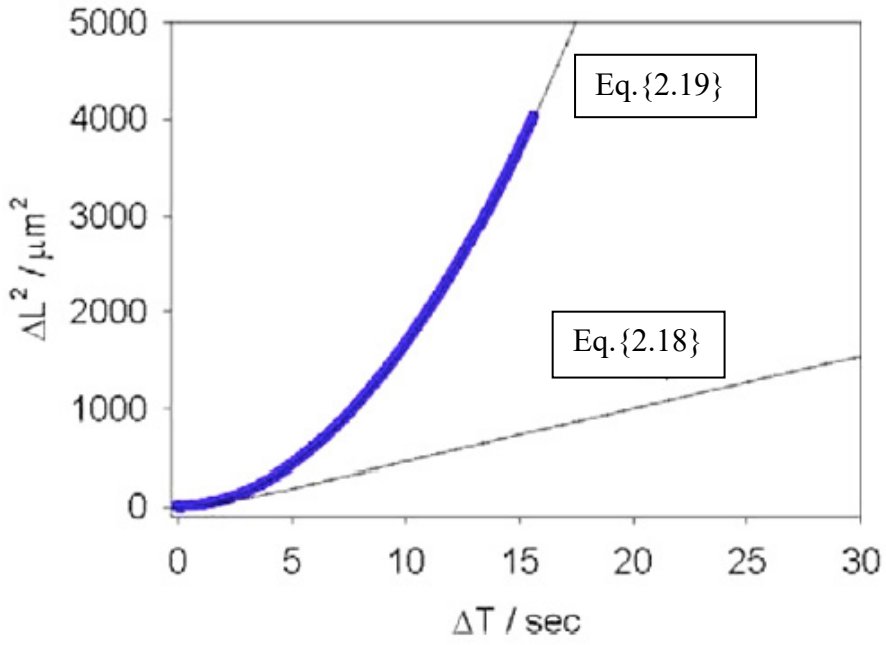

Figure 2-19 Mean-squared displacements of particles at long time intervals (dots) and plots of Eq. {2.18} and Eq. {2.19} (lines), taken from [95].

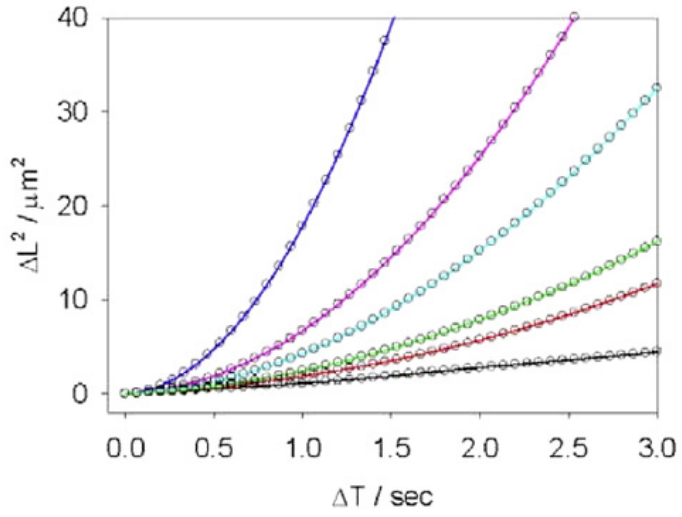

Figure 2-20 Mean-squared displacements of particles at short time intervals (dots) and fit with Eq. {2.19} taken from [95].

For longer periods of time $\Delta t \gg \tau_R$ the direction of propulsion changes due to the rotational diffusion coefficient (τ_R^{-1}). This means that the motion becomes diffusive where this diffusion is an enhanced diffusion coefficient. For this case the exponential term $e^x \Rightarrow e^{-\infty} = 0$, which means we can simplify the 2D projection of the MSD as follows and get Eq. {2.20}. In Howse, et al. [32] this limit has been given with the last factor ($-v^2\tau_R^2/2$) omitted.

$$\langle \Delta L \rangle^2 = 4D\Delta t + \frac{v^2\tau_R^2}{2}\left[\frac{2\Delta t}{\tau_R} + e^{\left(-\frac{2\Delta t}{\tau_R}\right)} - 1\right] \text{ for } \Delta t \gg \tau_R \;\Rightarrow\; e^{(-2\infty)}$$

$$\Rightarrow \langle \Delta L \rangle^2 = 4D\Delta t + \frac{v^2\tau_R^2}{2}\left[\frac{2\Delta t}{\tau_R} + e^{(-\infty)} - 1\right]$$

$$\Leftrightarrow \langle \Delta L \rangle^2 = 4D\Delta t + \frac{v^2\tau_R^2}{2}\left[\frac{2\Delta t}{\tau_R} + 0 - 1\right]$$

$$\Leftrightarrow \langle \Delta L \rangle^2 = 4D\Delta t + v^2\tau_R\Delta t - \frac{v^2\tau_R^2}{2}$$

$$\Leftrightarrow \langle \Delta L \rangle^2 = \left(4D + v^2\tau_R\right)\Delta t - \frac{v^2\tau_R^2}{2} \qquad \{2.20\}$$

The limiting form shown in Eq. {2.20} contains too many variables to resolve the equation, so it is necessary to determine the values of some of these variables. Furthermore, longer observation times of particles, increase the probability of particles moving out of the current view of the microscope [95]. For these reasons the limiting form as shown in Eq. {2.19} is used to calculate the mean squared displacement for the particles measured in the experiments in the following sections.

2.3.3. Fractal dimension

Fractal dimension can be used to help understand the trajectories of devices for which there is no obvious analytical expression for the expected MSD, such as bubble propulsive swimmers which do not have a definite link between orientation and propulsion vector orientation. Here this is used in Chapter 5 and 7 to help to gain an understanding of the relationship between catalyst distribution and directionality. This method has previously proved useful in related complex path problems such as sperm trajectories [123].

As described in my paper [74] fractal dimension D_f is a measure of the space filling properties of an object [124]. Unless the object completely fills the space it occupies, D_f will be smaller than the embedding dimension. Fractal dimension has been used to quantify a wide variety of systems, including aggregating diffusing particles and clusters [125], particle gels [126], bacterial colonies [127] and bio-polymer gels [128]. Calculating the fractal dimension of the trajectories of our bubble swimmer particles consequently provides a dimensionless number by which we can statistically compare behaviour. At sufficiently long time scales the 2D trajectory of a sphere displaying simple Brownian diffusion will have a fractal

dimension of 2, whilst the trajectory of a sphere moving in a straight line has a fractal dimension of 1. To obtain D_f we used a method described by Katz et al. for the analysis of growth paths or trails for biological cells and axons moving in 2D [129]. The fractal dimension is given by

$$D_f = \frac{\log(n)}{\log(nd/L)}, \quad \{2.21\}$$

where n is the number of trajectory segments (equivalent to the number of images in the sequence), d is the planar diameter of the trajectory and L is the path length. The planar diameter d is found by computing the maximum distance between any two points in the trajectory.

2.3.4. Persistence length

Another method to quantitatively characterize trajectories of the bubble-propelled swimmers is persistence length [74]. Persistence length is often used as a measure of the stiffness or bending properties of a polymer chain. The persistence length L_P denotes the distance along a set of chain segments where the correlation of the angle θ between segment vectors is lost; i.e. a linear set of chain segments therefore results in a larger L_p than a set of chain segments featuring loops or curves. It has been applied to a variety of systems including bio-polymers, man-made polymers [130], and in the characterisation of the trajectories of microtubules moving on a kinesin-coated surface [131]. Without normalisation persistence length will reflect both directionality and velocity.

The trajectories of bubble-propelled swimmers can be considered a chain of vectors; L_P for each trajectory was determined by first computing the average cosine angle $\langle \cos\theta \rangle$ between vectors at all separation distances L along the chain.

This was done by superimposing vectors at position j on the vector at starting position i and calculating $\cos\theta$, where $j \geq i$ and i represents all starting positions along the chain (see Figure 2-21). For the 2D trajectories a plot of $\langle\cos\theta\rangle$ against separation distance $L = \Delta L(j-i)$ has the form,

$$\langle\cos\theta\rangle = e^{-(L/2L_P)}. \qquad \{2.22\}$$

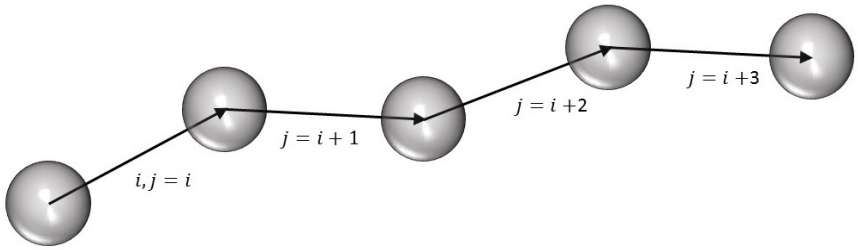

Figure 2-21: Bubble swimmer trajectories are a chain of vectors. The persistence length is found by computing the average $\boldsymbol{\cos\theta}$ between the starting vector at position $\boldsymbol{i}$ and the superimposed vectors at position $\boldsymbol{j}$, for all separation distances $\boldsymbol{L = \Delta L(j-i)}$ along the chain and all starting positions $\boldsymbol{i}$. [74]

2.3.5. Mean Squared radius of Gyration

Mean squared radius of gyration, R_g^2 calculates the average mean squared distance of each point on a trajectory from a defined central fixed point, and so reflects how compact, or spread out in space a given trajectory segment is. R_g^2 was calculated here by using Equation{2.23}, similarly to the definition which is used for polymer chain analysis.

$$R_g^2 = \frac{1}{N}\sum_{i=1}^{N}\left(r_i - r_{mean}\right)^2 \qquad \{2.23\}$$

Experimental Chapters

3. Effect of catalyst thickness, reaction rate and salt concentration on catalytic Janus particle motion

3.1. Introduction:

This chapter explores some of the fundamental behaviour of platinum powered catalytic Janus particles to establish new links between the physiochemical properties of the catalyst surface (composition and film thickness) and measured propulsion velocities. While theories have made predictions about the link between catalytic activity and propulsion velocity, these have to date not been tested [31, 132]. For platinum catalytic swimmers some factors have been identified that could produce differences in reaction rate, for example, Zhao, et al. [133] described the poisoning of platinum by sulphur-containing molecules, which cause the catalytic properties to be inhibited or even cease. In addition, a link between platinum catalyst roughness and propulsion behaviour has also been reported [9, 40] suggesting that the physical form of the platinum catalyst could also be important. However, apart from the studies mentioned, establishing quantitative links between the properties of the platinum catalytic coating, reaction rate and propulsion velocity has received little attention, and so this is the focus of the first section of this chapter, with an emphasis on platinum surface chemistry and thickness.

A second area of focus for this chapter is to determine the effect of adding salt to modify the conductivity of the swimming media. This section aims to clarify details of the propulsion mechanism for Janus particles, and is introduced with reference to mechanistic proposals for both bimetallic nanorods and Janus particles.

We recall from the introduction (Section 1.1.1.2) that bimetallic nanorods are thought to move via self-electrophoresis, and that observations of direction of motion, and intolerance for salty environments support this mechanism. [62, 134]. However, Janus particles are thought to move by self-diffusiophoresis (see Section 1.1.1.1). Various predictions have been made based on self-diffusiophoresis as the proposed mechanism for PS/Pt Janus colloids [91, 135-139] and they show good agreement with the currently reported experimental data on swimming velocity, colloidal size [31] and fuel concentration [32]. Thus single metal catalytic Janus particles would be expected to be tolerant to salt providing the particular salt does not have a "poisoning" effect on the catalysts activity. At the time of writing this thesis the effects on diffusiophoretic platinum-based swimmers has not been studied and determining salt tolerance also is of vital importance if spherical self-motile Janus-particles are to be used in applications such as drug delivery and medical microfluidics because of the high salt content in biological fluids (Section 1.2). Therefore for the first time the effects of salts on PS/Pt Janus colloids are investigated in this Chapter in conjunction with their direct effects on the catalytic reaction rate.

3.2. Methods:

3.2.1. Preparation of active colloidal samples via e-beam evaporation

Catalytically active Janus particles were prepared in two ways: platinum evaporation and chemical platinum growth. This allowed for the comparison of different platinum coating methods to see if they affected swimming velocities and salt concentration effects. For the first method PS Janus spheres were prepared, as explained in Chapter 2 Section 2.1.2, by spin coating them (well-dispersed

monolayer) onto glass slides that had previously been coated via e-beam evaporation with 20 nm chromium (Cr) (Sigma Aldrich 99.9%), onto which 15 nm of platinum was then coated via e-beam evaporation at 90 mA and 10 KeV. Chromium was used as an adhesion layer in order to measure the reaction rate of platinum coated onto glass slides after removal of the colloids which enabled a direct comparison of reaction rate to the particles velocity. A LabVIEW algorithm was used to accurately calculate the surface area that was coated in platinum. The regions where colloids had been detached from the platinum surface were negligible as colloids were sparsely coated (very few present) and therefore the measurement error in reaction rate was larger than the change due to these missing regions. Screenshots of the front panel of this program can be found in the appendix (10) Section (10.2). The Janus colloids were then re-suspended in 15% w/v H_2O_2, using a piece of moist lens tissue to act as a blade to detach the Janus colloids from the surface, and sonicated for 5 minutes, followed by further incubation at room temperature (20˚C; temperature-controlled) for 25 minutes. This solution was then diluted to 10% w/v H_2O_2 and motion pictures of the particles were taken at 30Hz with a PixeLink camera attached to a Nikon Eclipse LV100 microscope. Custom made LabVIEW vision software (as previously described in Section 2.3.2) was used to find out the x, y centre for each particle in each frame and from this data the MSD was calculated as a function of time [32, 95]. MSD vs time was used to extract the translational diffusion coefficient D and the propulsion velocity v of particles. In the case of the Janus particles described here the fitting was done for the first 0.5 seconds of the data with the theoretical rotational constants being 0.8s for 1μm, 6.2s for 2 μm, 97.1s for 5 μm and 20968.3s for 30 μm, this would mean at the longest time period fitted (0.5 s) ~983 data points were averaged.

To measure the effects of salt on the samples, suitable solutions of KNO_3 and $AgNO_3$ (Sigma Aldrich 99.9%) were gradually added to the samples, retaining a constant concentration of 10% w/v H_2O_2, with final salt concentrations in the region of 10^{-7} M to 10^{-3} M.

3.2.2. Chemically coated colloidal samples masked with chromium via e-beam evaporation

For the second method monodispersed polystyrene colloids (1 μm, 5 μm, and 30 μm in diameter) were uniformly coated with platinum via in-situ reduction of platinum salts. The coating obtained via this method was made up of 2-5 nm nanoparticles of platinum that were adhered to the surface of the colloids (custom synthesis performed by Kisker Biotech). The coated particles were spun cast onto glass slides forming a well-dispersed monolayer (Section 2.1.2) and one hemisphere was then coated with Cr via thermal evaporation (in an Edwards Evaporator 306 with a tungsten filament containing Cr pellets (Sigma Aldrich 99.9%), Section 2.1.3.1).

20 nm Pt coated slides were also masked with 2 nm and 15 nm Cr as blank measurements for reaction rates. The thin masked layer of Cr was used to ensure that the deposited chromium layer inhibited a large area of one hemisphere despite the thickness gradient caused by evaporation on the spherical colloid (this gradient is discussed in detail in Section 3.4.4). Reaction rates for the samples were measured on both the flat substrates (Pt, Pt masked with Cr and Cr) and on highly concentrated Janus particle suspensions.

3.2.3. Measurement of reaction rate of platinum decomposing hydrogen peroxide

UV-VIS spectroscopy was used in order to measure the reaction rate at which platinum decomposes hydrogen peroxide, as mentioned in the methods Section 2.2.1. After running spectral scans (see Figure 3-1 A) to ensure that there were no contaminants that could interfere with the standard wavelength used for hydrogen peroxide (240 nm) [140], a 5 point calibration was run and repeated 5 times over the course of a week to ensure consistency (Figure 3-1 B). For hydrogen peroxide an extinction coefficient of 40.18±0.46 $M^{-1}cm^{-1}$ at 240 nm was obtained, which is within 10% error of the literature reported value of 43.6 $M^{-1}cm^{-1}$[140].

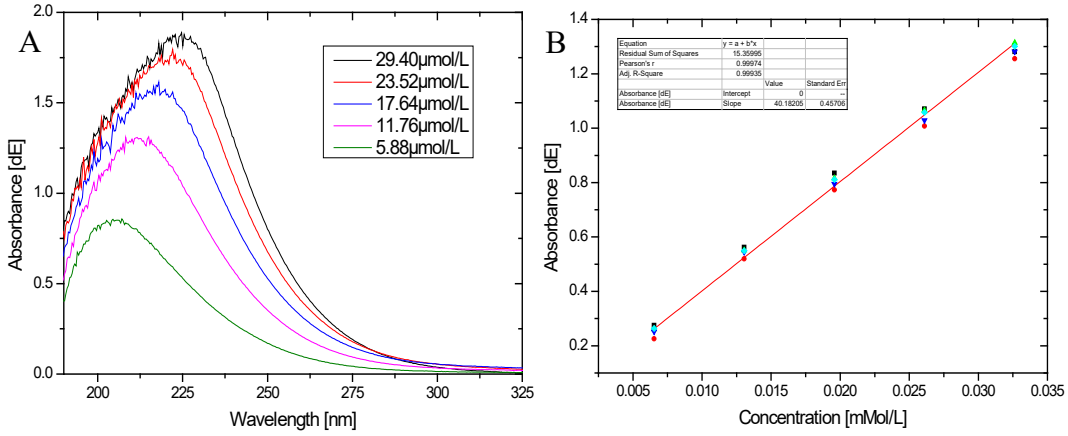

Figure 3-1 (A) Spectral sweep of the different H_2O_2 concentrations for the calibration curve. The intensity of the light follows the Beer-Lambert Law. Spectra were measured in an Ocean Optics Spectrometer USB 2000 UV-VIS-ES. (B) Hydrogen peroxide calibration curve at 240 nm. Each point was measured five times over the course of a week. The resulting extinction coefficient was 40.18±0.46 $M^{-1}cm^{-1}$.

3.2.4. Measurement of reaction rate on Pt/PS Colloids

Reaction rate measurements on particles were determined by taking consecutive 3 µl samples from the reaction vials over time, diluting these by a factor of 100 and then measuring the absorption at 240 nm in a quartz cuvette with 1cm path length.

It is important to note that measurements were done immediately, as colloids would have been still present in the samples taken (and therefore constantly degrading hydrogen peroxide). Moreover, it was important to gently agitate the mixture (especially the 5 μm and 30 μm colloid samples) during reaction rate measurement to ensure a homogenous solution and that sedimentation did not occur.

In order to calculate the surface area of the colloids, 80 μl samples were taken from each of the stock solutions used for making the samples and left to settle in a rectangular capillary tube, with the height measured using the z-axis value given by a microscope prior stage (measured manually). Several images were taken (15-25) of different areas of settled particles in the capillary tube with a Nikon LV100 microscope and PixeLink camera. These were then automatically counted with another LabVIEW program which I wrote using vision algorithms. Entering the height of the capillary tube together with the amount of images taken and a calibration coefficient (based on the specific objective and microscope used) to estimate the volume of liquid for this area allowed the particle concentration to be calculated per 1 ml of liquid. Screenshots of the LabVIEW software can be seen in the appendix (Section 10, Figure 10-14).

3.2.5. Preparation of XPS samples

XPS measurements were made on glass slides coated with Pt and treated with the different salts. The samples were left to react in a volume of 20 ml with the appropriate H_2O_2 solution (i.e. containing the particular salt to be examined). XPS data was kindly gathered in the Kroto Research Institute by Dr. Claire Hurley (Section 3.4.3).

3.2.6. Influence of the thickness of the platinum coating on reaction rate of hydrogen peroxide degradation

Platinum was coated onto glass coverslips or silicon wafers (for thickness measurements via AFM) in order to measure the reaction rate of platinum at different thicknesses. Coverslips (18×18 mm) were mounted onto a sample holder which enabled 1 cm^2 coating area on each coverslip, see Figure 3-2. Prior to evaporation of metals, the coverslips or silicon wafer substrates were placed in a Plasma-Surface System in oxygen plasma for 5 minutes.

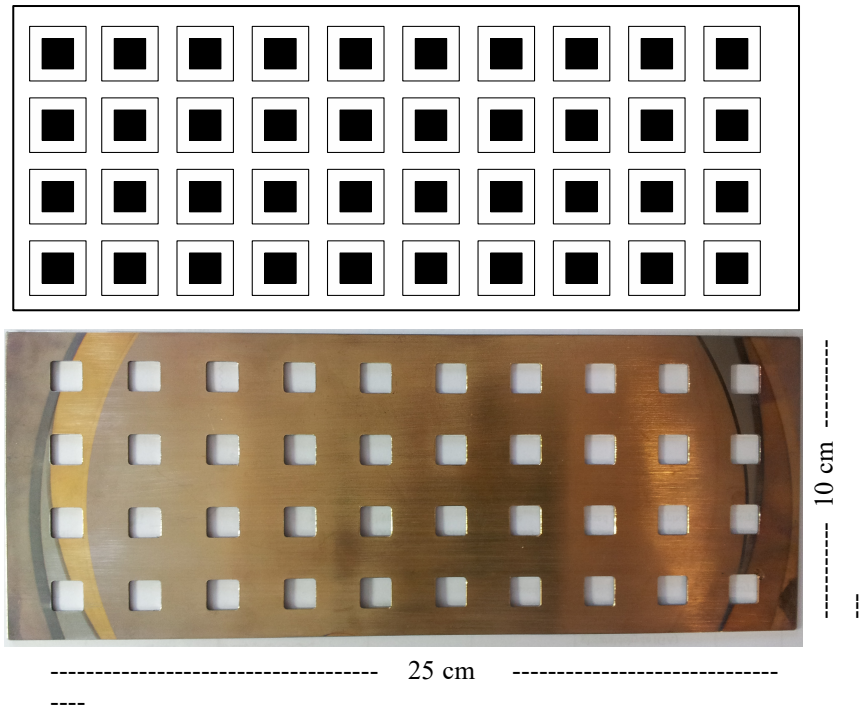

Figure 3-2 Grid for evaporation samples. The black boxes represent 1 cm^2 holes, larger boxes indicate coverslips. Lower image is a photograph of the actual grid.

For platinum layer thicknesses greater than 8 nm, it was essential that substrates initially had a thin layer (3-20 nm) of chromium (Sigma Aldrich 99.9%) coated onto their surfaces. This acted as an adhesion layer for the following platinum coating to ensure that the platinum layer did not delaminate from the substrate surface during the reaction with hydrogen peroxide [141]. Tests were made with

various samples of thinly-coated platinum (in the region of 2 to 8 nm) with and without a chromium adhesion layer to ensure that the chromium adhesion layer did not cause any electrolytic cell effects that altered the reaction rate.

Both the chromium adhesion layer and the varying thicknesses of platinum were evaporated via e-beam evaporation, as described in Section 2.1.3.2. In order to ensure the experiment was done accurately it was important to investigate how the position of the sample in the evaporator altered the thickness of platinum deposited. As previously described (see methods Section 2.1.3) thermal and e-beam evaporation are highly directional evaporation techniques. This means that the deposition amount onto a surface falls off by $1/r^2$ with increasing distance from the radiation source. Figure 3-3 shows a theoretical calculation of how the distribution of different evaporation thicknesses is affected by the distance from the centre of evaporation, over a distance of 10 cm. In the case of the Moorfield e-beam evaporator used for these samples they were held 32.5 cm above the irradiation source, which resulted in 10% less deposition at the outermost edge of the samples than at the centre. This means that a 10% variation in thickness needs to be taken into account when making thin film samples. The further the samples are away from the irradiation source the more evenly the layer is distributed but this also means that the intensity decreases rapidly and so evaporation takes longer and uses up more material. In order to account for this problem the samples were always placed in exactly the same position in the evaporator, therefore any deviation was kept to a minimum. In the case of measuring the reaction rate on colloids it was necessary to fill the entire sample holder with 16 slides, which were then all used to measure the reaction rate, as otherwise the concentration of the colloids was too

low to achieve good results. Therefore thickness variations were averaged for this experiment.

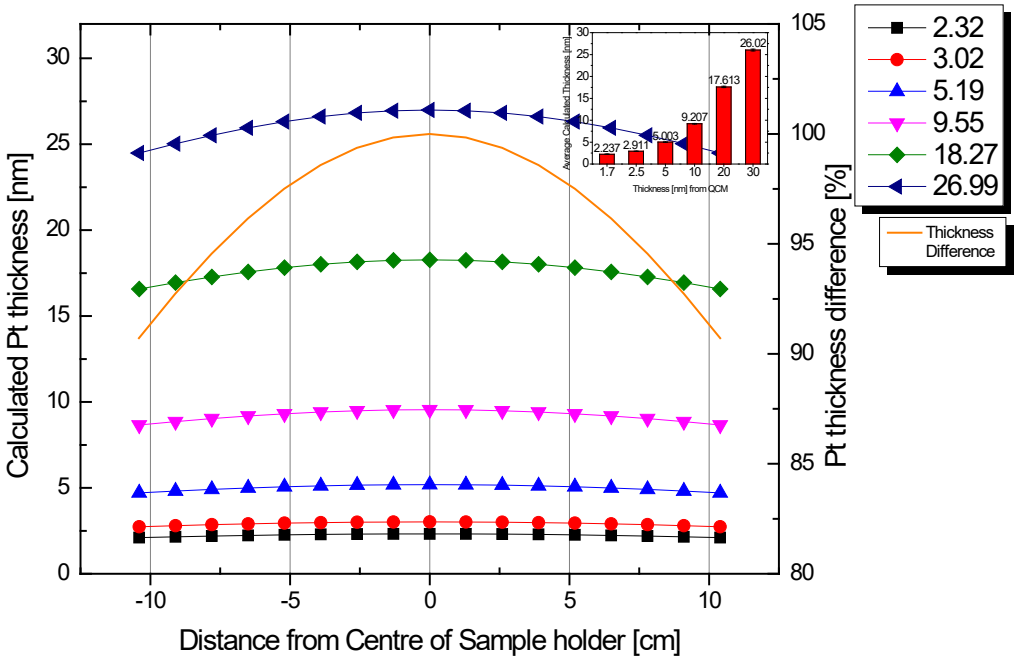

Figure 3-3 Theoretical calculation of the platinum thickness distribution over the sample holder using the inverse square law $1/r^2$ (left y-axis). Legend shows the thickness as displayed by the QCM in nm. The orange curve shows the difference in coating in [%], where the thickest sample is 100% (right y-axis). The graph insert shows the average thickness for each given QCM thickness.

3.2.7. Using a flow cell to measure the decomposition of hydrogen peroxide

The decomposition of hydrogen peroxide generates a lot of oxygen (O_2) bubbles so that a normal assay in a closed cuvette is not feasible as the bubbles would cause scattering of the light path and therefore give false readings. Due to this problem most reaction rates were measured using a quartz crystal (Hellma Analytics) flow cell with a path length of 0.1 mm. The narrow path length allows one to measure concentrations of up to 10% w/v hydrogen peroxide without going above the maximum absorbance readout of the spectrometer. In the case of samples where this method was not feasible (predominantly reaction rates measured directly on

colloidal samples), the samples were taken out of the reaction vial, 100 times diluted and measured in a d = 1 cm quartz crystal cuvette. The decomposition of hydrogen peroxide is an exothermic reaction and therefore the system needed to be temperature controlled to prevent an increase in the sample temperature, which in turn would change the reaction rate (higher reaction rate as temperature increases). In Figure 3-4 a schematic of the experimental setup is shown where the sample was placed into a temperature controlled vessel at 20°C and connected to the flow cell via tubing and a peristaltic pump. The Flowrate of the peristaltic pump was 981 ml/min which was calculated using Eq.{3.1}, where *rpm* is the set revolutions per minute of the pump (70 rpm), the tubing diameter d_{tube} was 1.42 mm and the pump's roller diameter d_{pump} was 10 cm. For reproducibility this sample flow rate was used throughout this thesis for all reaction rates done via the flow cell.

$$\text{Flow Rate [per min]} = rpm \times \pi^2 \times d_{pump} \times d_{tube} \qquad \{3.1\}$$

The sample was open to the atmosphere to keep the flowing liquid free from bubbles, which would otherwise have interfered with the readings in the spectrometer. Evaporation of solution from the sample was negligible during reaction rate measurement, because the time period was kept short (generally between 3 and 20 minutes).

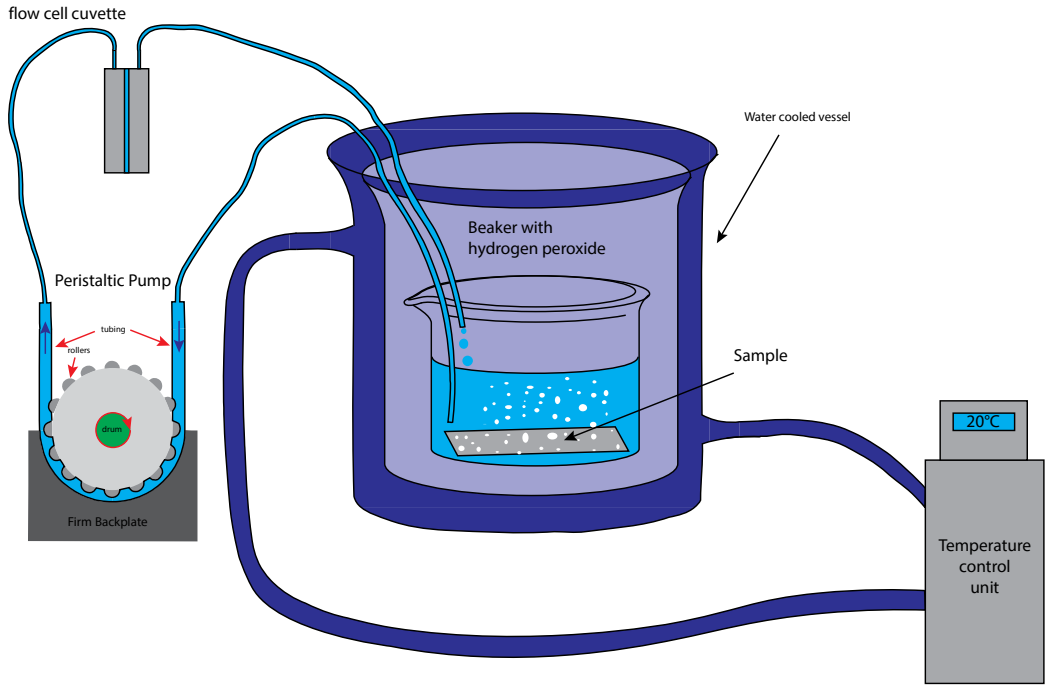

Figure 3-4 Schematic of the experimental setup for measuring temperature controlled hydrogen peroxide kinetics; the quartz flow cell is placed into a UV-VIS Spectrometer for continuous measurement over a given time.

3.2.8. Measurement of coating thickness via silicon wafer samples

Accurate measurement of deposition thickness was essential for this experiment, therefore the in-built evaporator QCM was calibrated for the varying coating thickness of the samples using AFM to measure step sizes of silicon wafer samples that had been coated with platinum at the same time as the reaction rate samples mentioned in the previous Section (3.2.6). Silicon wafers were put as close as possible to samples to ensure as little variation as possible, as shown in Figure 3-3, with an attached TEM copper grid overlaid onto the surface.

Copper grids were removed from the silicon wafer samples and the film thickness was measured by tapping mode AFM measurements on the patterned sample surface. A series of height images of the samples were recorded using a Veeco Dimension 3100 AFM platform. The images were characterized using Nanoscope Analysis software (version 1.40) by Bruker Systems, which allows one to make

relative height measurements between two steps on the sample, and were kindly done by Dr. Ehtsham U. Haq.

3.3. Preliminary Results to ensure Sample reproducibility

3.3.1. Spin Coating procedure

In order to achieve a high PS colloid coverage but well-dispersed monolayer it was found that using a spin coating program that started with a prolonged slow spin speed at 400 rpm and then finished with a high spin 2000 rpm to remove any excess solution worked well. The best solution mixture was found to contain ethanol and water in a 9:1 ratio.

3.3.2. Measurement of Silicon wafers to determine the QCM accuracy

To ensure reproducibility of results a calibration of the reported thicknesses via the QCM in the evaporator was done and a calibration curve was generated using the AFM results versus the QCM reported thicknesses. As previously stated, images were characterized using Nanoscope Analysis software to measure step height differences between uncoated and coated areas on silicon wafer substrates. Example images of the patterned samples and the measurement process can be seen below in Figure 3-5. The final results of all thickness measurements are shown in the calibration curve in Figure 3-6. These values were used to appropriately calibrate all the following data.

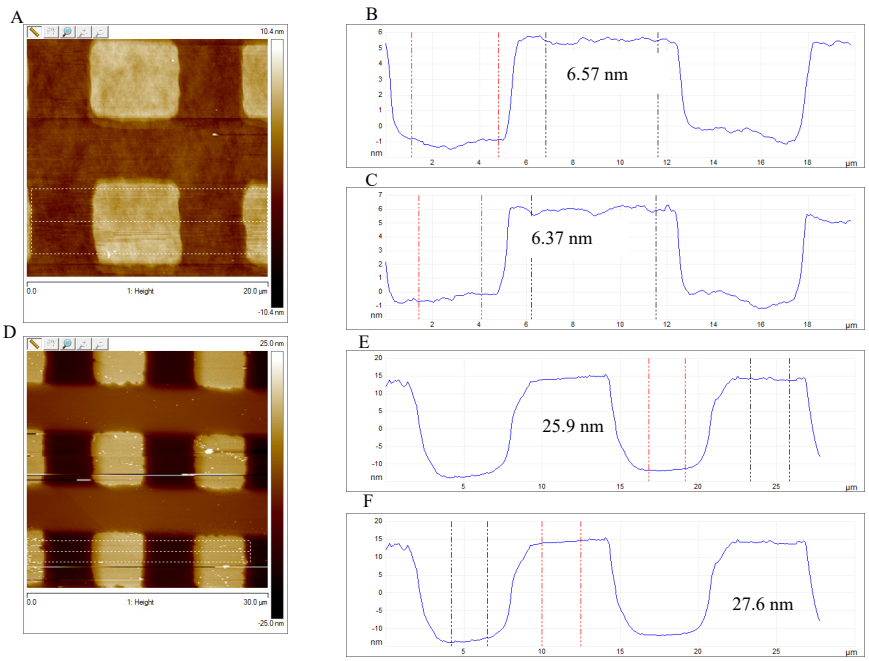

Figure 3-5 AFM images of platinum evaporated onto silicon samples, which were shadowed with TEM copper grids. Images were flattened for better peak and trough measurements. Example image of the middle (of the sample holder) 5 nm (value given by QCM) sample (A) with two measurements shown (B and C) and example image of the middle 30 nm sample (D) with two measurements shown (E and F). Images and measurements taken by Dr. Ehtsham U. Haq.

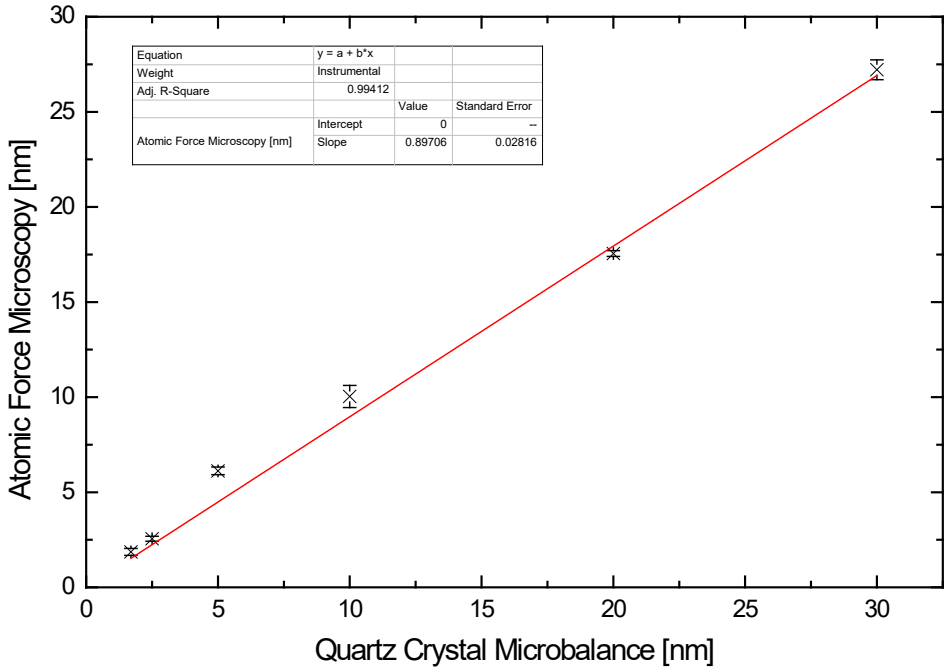

Figure 3-6 Film thickness calibration curve. QCM readings calibrated against AFM measurements. Line of best fit ($y = 0.897(\pm 0.028) \times x$).

3.3.3. Pre-treatment and standardizing a protocol for accurate reaction rate measurements

In order to be able to accurately measure reaction rates of platinum samples it was necessary to test samples that had been freshly made straight out of the evaporator, to prevent any age contamination such as thiol poisoning [133] or any other contamination of the platinum surfaces. For convenience this was done on flat surface samples. During testing it became evident that when samples were placed into hydrogen peroxide the reaction rate was initially slow and then would gradually speed up. It was ensured that this increase in reaction rate was not dure to an increase in temperature due to the exothermic reaction by means of a liquid cooling system as previously shown in Figure 3-4. This suggested that even freshly coated samples, straight out of the evaporator, had a contamination layer which was gradually removed by the catalytic reaction of the platinum surface with hydrogen peroxide, as shown in Figure 3-7. The S-curve shows the initial reaction rate (■) during which the contamination layer was gradually removed followed by a maximum reaction rate indicated by the red (■) points which follow a straight line. The fitted line in the middle section illustrates the kinetics required to calculate the reaction rate of the sample. This straight line is the maximum reaction rate at which the particular sample degraded hydrogen peroxide for the given fuel concentration, in this case 10% w/v. The later falloff (■) in reaction rate was due to fuel depletion.

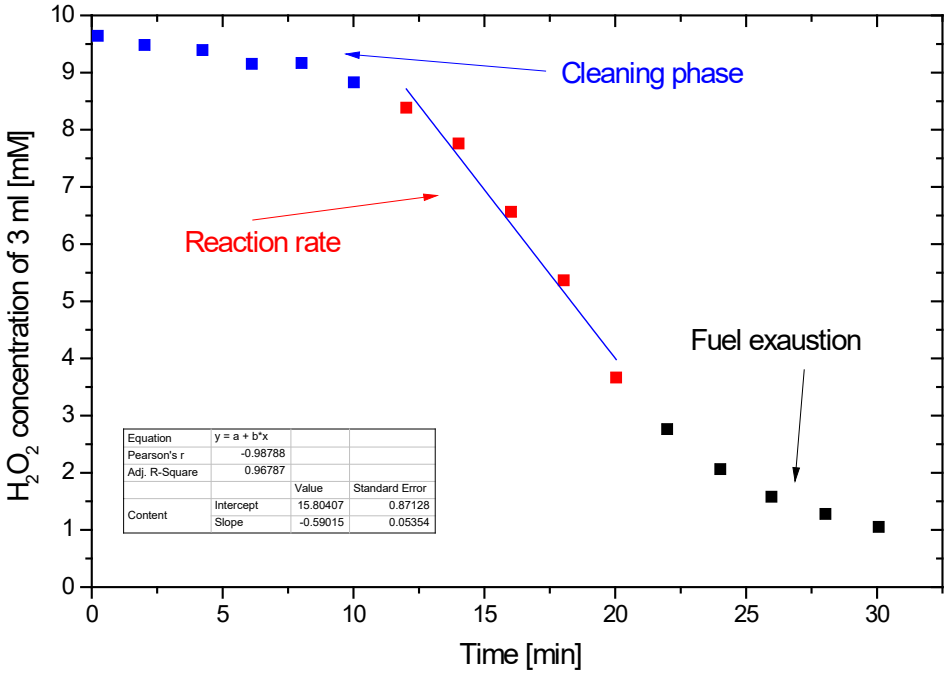

Figure 3-7 Decomposition of hydrogen peroxide on a fresh platinum sample. The fitted line indicated the region of interest in order to find the correct reaction rate at which the Pt sample decomposes H_2O_2. In the case of this sample it is (0.59±0.05) mM/min/cm^2. This sample is an example platinum sample direction taken form the evaporator after coating without incubation in H_2O_2 prior to the reported kinetics measurement.

In contrast, after samples had been incubated for 30 minutes, as described above, there was linear decomposition of hydrogen peroxide until fuel exhaustion (see Figure 3-8). It was possible to see a visual change in the detachment of oxygen bubbles from flat platinum samples after the initial cleaning phase. The bubbles appeared to be smaller and detached from the metal surface more regularly and more frequently.

Results also showed that thermally evaporated samples took longer to clean than E-beam evaporated ones, but both samples were adequately cleaned after the 30 minute incubation. These results match the previously explained advantages of E-beam evaporation over thermal evaporation in Chapter 2 Section 2.1.3.

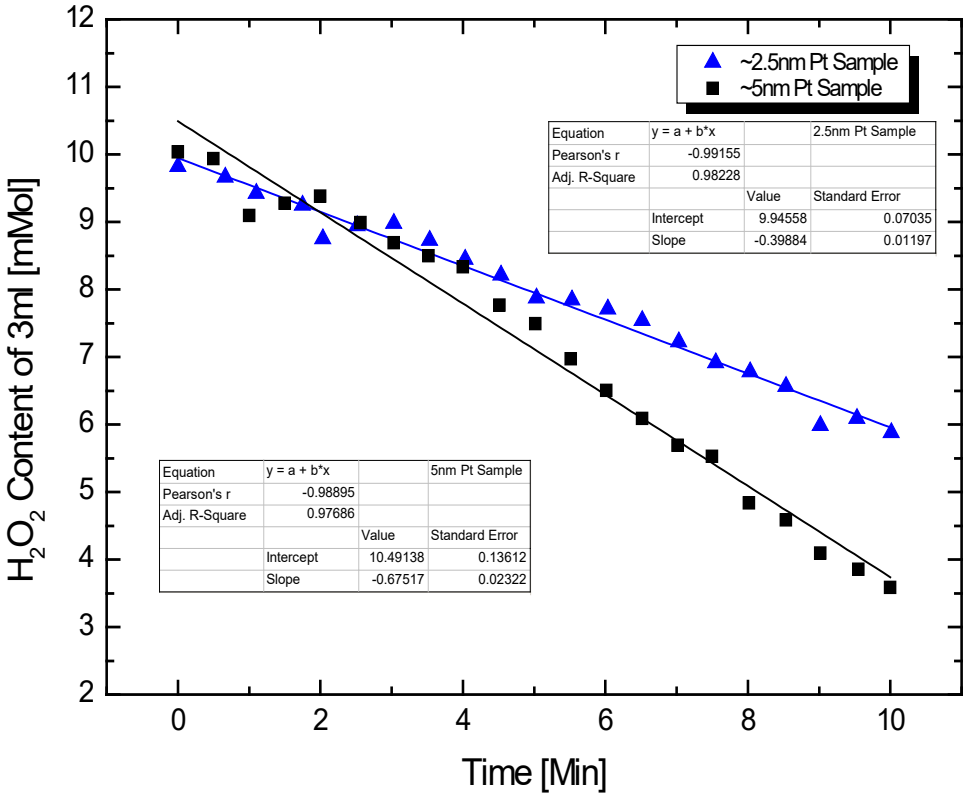

Figure 3-8 Kinetic data showing the decomposition rate of hydrogen peroxide via cleaned ▲=~2.5 nm and ■=~5 nm thick platinum. Reaction rate of 1 cm^2 Pt; ■= (0.68±0.02) mM/min/cm^2; ▲= (0.40±0.01) mM/min/cm^2.

3.3.3.1. Influence of incubation in hydrogen peroxide on hydrocarbon contamination

XPS Survey scans shown in Figure 3-9 reveal that cleaning samples in hydrogen peroxide in order to remove hydrocarbons is to a certain extent successful and helps to confirm the reason for reaction rates increasing after a previous incubation and sonication of samples in 15% w/v H_2O_2 for 30 minutes. Quantitatively it could be shown, that before and after the H_2O_2 exposure described above, the area of platinum increased from 21.7% to 40.9%, while on the other hand the carbon peak (indicator for hydrocarbons) decreased from 56.1% to 41.7%, and the initial sodium peak vanished completely. This means that more platinum surface was accessible for catalysis. It is highly probable that the cleaning of the platinum surface was indeed even greater than measured here as a couple of hours had passed before the

samples were able to be analysed in the XPS system. Li et al. [142] reports how hydrocarbon contamination increases drastically in the first three hours platinum surfaces are exposed to ambient air conditions.

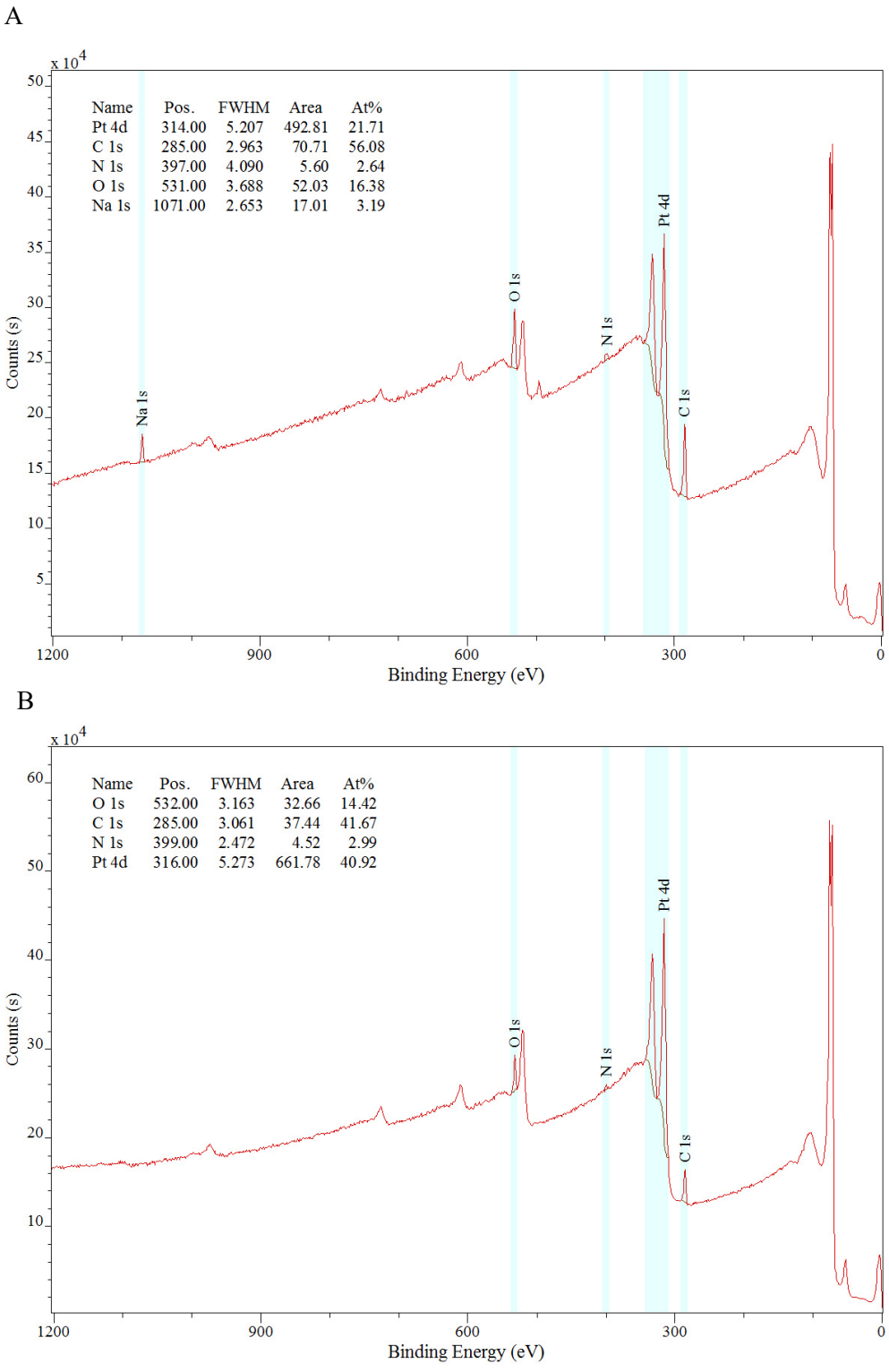

Figure 3-9 XPS survey scan of platinum coated slides before (A) and after (B) 30 min H_2O_2 incubation

From these initial preliminary results it was possible to create a much more robust protocol for pre-treatment of samples to ensure reproducible results for the following experiments. This protocol is detailed below.

Janus colloids were dispersed into a 15% w/v of hydrogen peroxide and then sonicated for 5 minutes in a sonicator bath, followed by further a 25 min unstirred incubation period at a constant temperature of 20°C. This ensured that short-term platinum surface contamination (hydrocarbons) was removed to ensure no interference with reaction rate measurements or other measurements such as particle velocity.

3.4. Results

3.4.1. How does platinum thickness affect reaction rate

The influence on reaction rate of the thickness of the deposited platinum was determined by measuring reaction rate on slides coated with varying thicknesses of platinum. Results showed that in the range between 0 and 5 nm of deposited platinum the reaction rate increased consistently with the thickness of the platinum films but showed an asymptotic relationship. Above a thickness of ~15 nm the reaction rate was close to approaching its maximum value, measured to be ~1 mM/min/cm^2 at 20 nm deposited platinum.

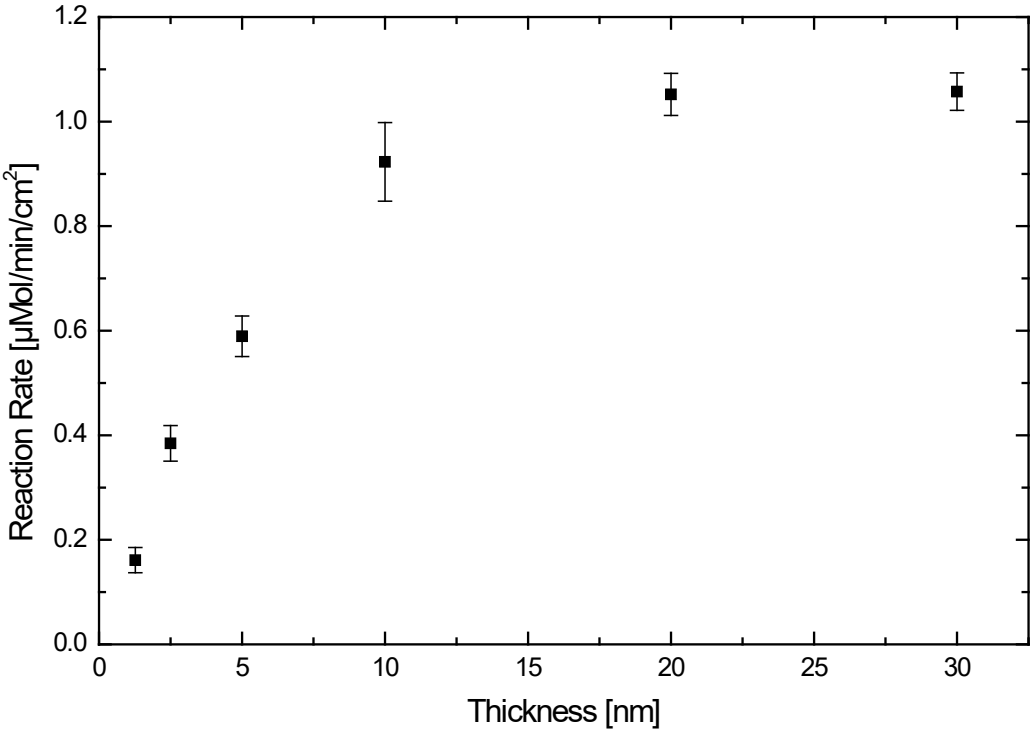

Figure 3-10 Effect of deposited platinum thickness on flat glass substrates versus Reaction Rate

The next step was to determine if altering the thickness of the platinum layer would effectively change the velocity of the Janus particles.

3.4.2. Comparison of reaction rates and velocities of Janus-particles

In Figure 3-11 trajectories are displayed as a function of platinum deposition metal thickness in 10% w/v hydrogen peroxide fuel solution. As can be clearly seen from the trajectories they moved a far longer distance over the same time period with increasing thickness of deposited platinum catalyst. The trajectory shown for 0 nm is equivalent to a particle undergoing Brownian motion with no enhanced velocity vector. As can be seen from the trajectories in Figure 3-11 (and from the corresponding MSD curves (Figure 3-12)), with increasing platinum thickness particles underwent more defined spiralling patterns.

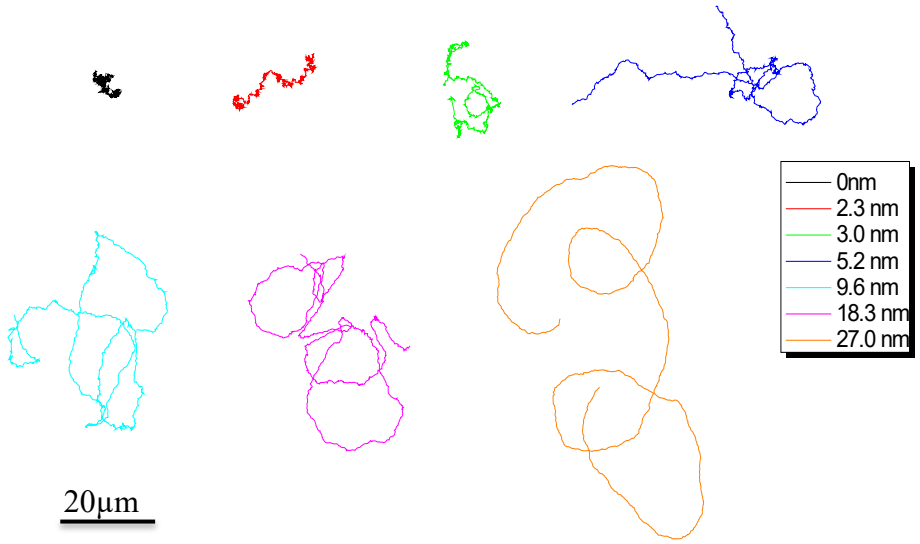

Figure 3-11 Typical trajectories of swimmers measured during the experiment. The maximum Pt thickness is indicated in the legend. All trajectories are represented for 33 seconds.

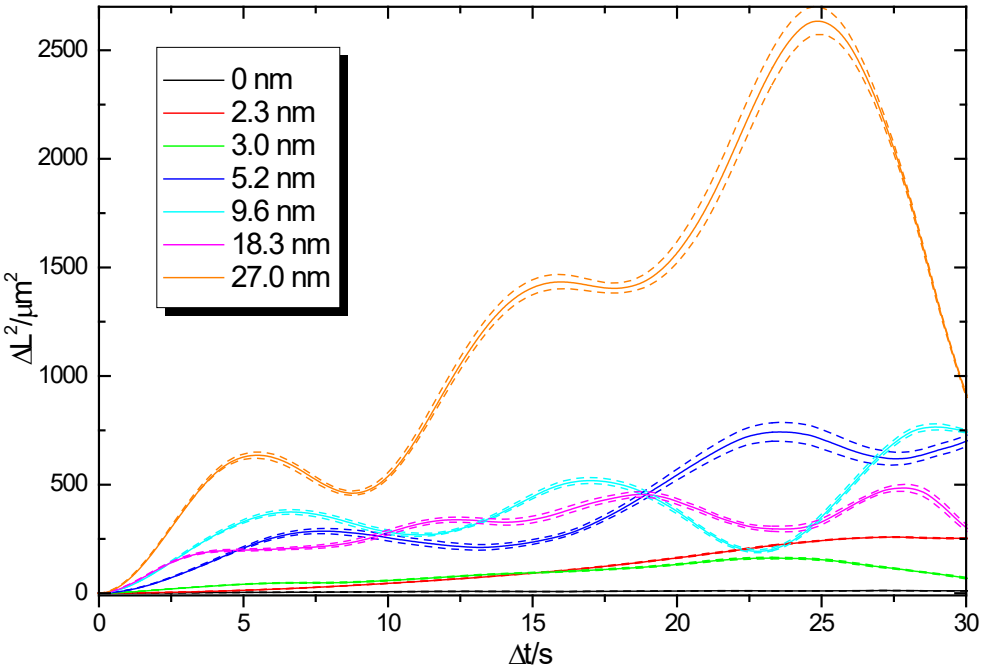

Figure 3-12 Mean Squared Displacement (MSD) as a function of time interval for the spheres as shown in Figure 3-11, corresponding to different platinum thicknesses on the spheres. Dotted lines indicate the standard deviation of the MSD.

Figure 3-12 shows the full MSD data for the previous trajectories dependent on their platinum thickness, to which Eq. {2.19} $\left(\langle \Delta L \rangle^2 = 4D\Delta t + v^2 \Delta t^2\right)$ was fitted to the first 0.5 seconds (a suitable region for 2 μm colloids), as shown in Figure 3-13.

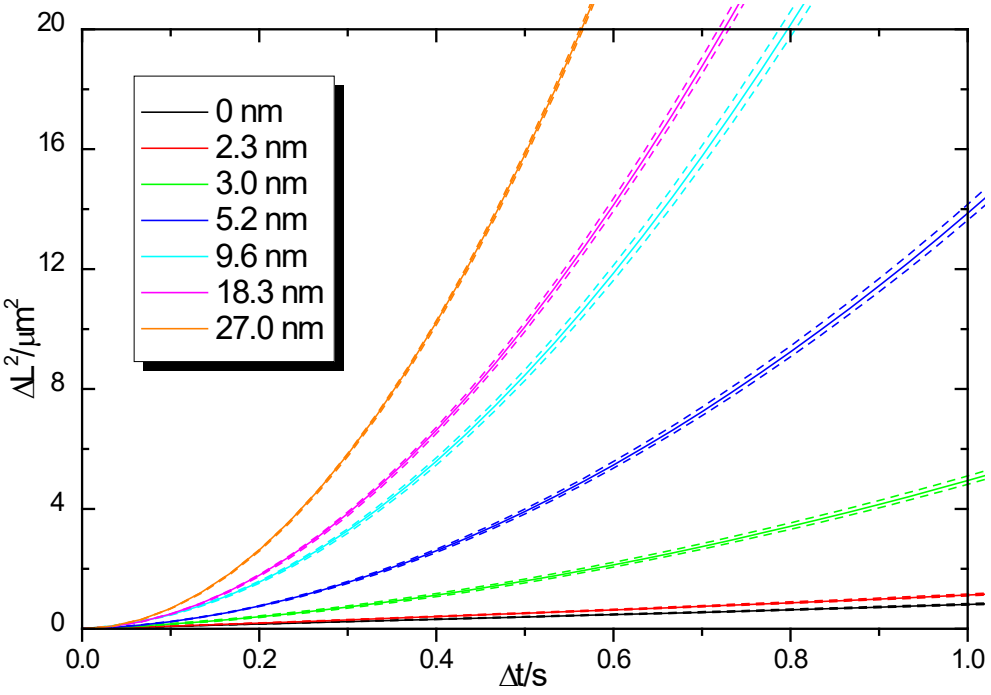

Figure 3-13 MSD of the samples showing the region of interest for fitting purposes and calculation of velocity and diffusion coefficients. Dotted lines represent the standard deviation of the MSD.

The velocity showed a very similar trend to the previously reported reaction rates as shown in Figure 3-14. The reaction rates and velocities measured are shown in Table 3.1. Furthermore, both reaction rate and velocity plotted against platinum layer thickness on a logarithmic scale showed a linear relationship as shown in Figure 3-15. The example trajectories and their MSDs as shown in Figure 3-11, Figure 3-12 and Figure 3-13 agree with the velocity increase. One can clearly see there was an increase in enhanced diffusion with increasing platinum thickness and therefore with increasing reaction rate. Plotting reaction rate against velocity of the particles gave a linear relationship, as shown in Figure 3-16. The difference in particle size due to varying thickness of the Pt layer was shown to be negligible, within error, by measuring the Brownian motion of the thinnest and thickest particles and calculating their diffusion coefficients.

Table 3.1 Reaction rates and velocities for the various platinum thicknesses.

Thickness [nm]	Reaction rate [mM/min/cm^2]	Reaction Rate [s^{-1}µm^{-2}]	Velocity [µm/s]
2	**0.20 ± 0.02**	**(1.6 ± 0.2) × 10^{10}**	**1.3 ± 0.1**
3	**0.40 ± 0.03**	**(3.9 ± 0.3) × 10^{10}**	**2.7 ± 0.2**
5	**0.60 ± 0.04**	**(5.9 ± 0.4) × 10^{10}**	**3.4 ± 0.2**
10	**0.92 ± 0.08**	**(9.3 ± 0.8) × 10^{10}**	**5.4 ± 0.2**
18	**1.05 ± 0.04**	**(10.6 ± 0.4) × 10^{10}**	**6.8 ± 0.3**
27	**1.06 ± 0.04**	**(10.6 ± 0.4) × 10^{10}**	**7.2 ± 0.3**

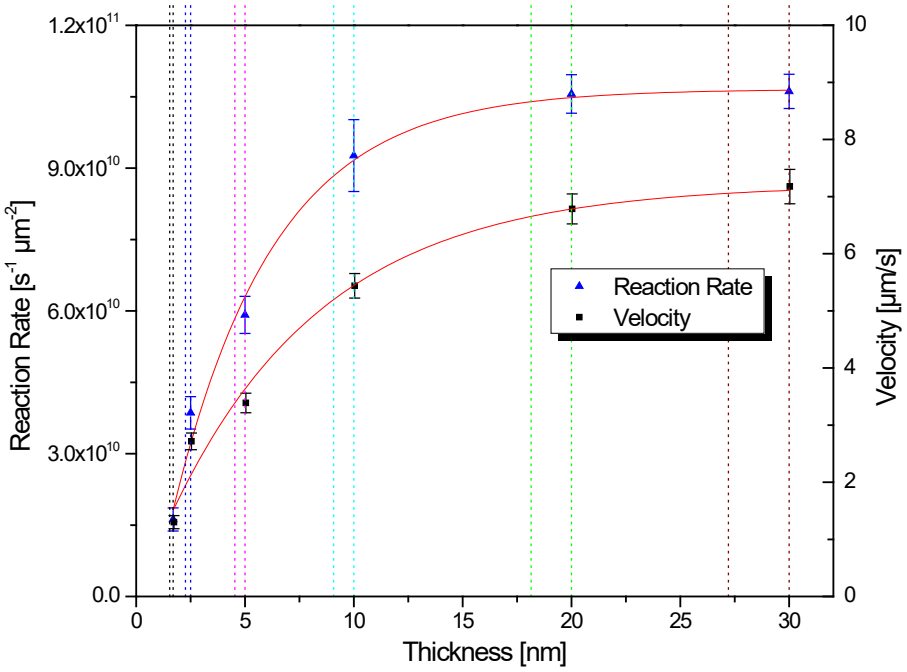

Figure 3-14 Representation of the reaction rates and velocities of the average samples against the thickness of the evaporated platinum. Dotted vertical drop lines represent the region of platinum film thickness difference over the sample holder in the evaporator (these are not error bars); maximum thickness is in the centre and tapers off towards the edges. Fitted curves (red) are to guide the eye only.

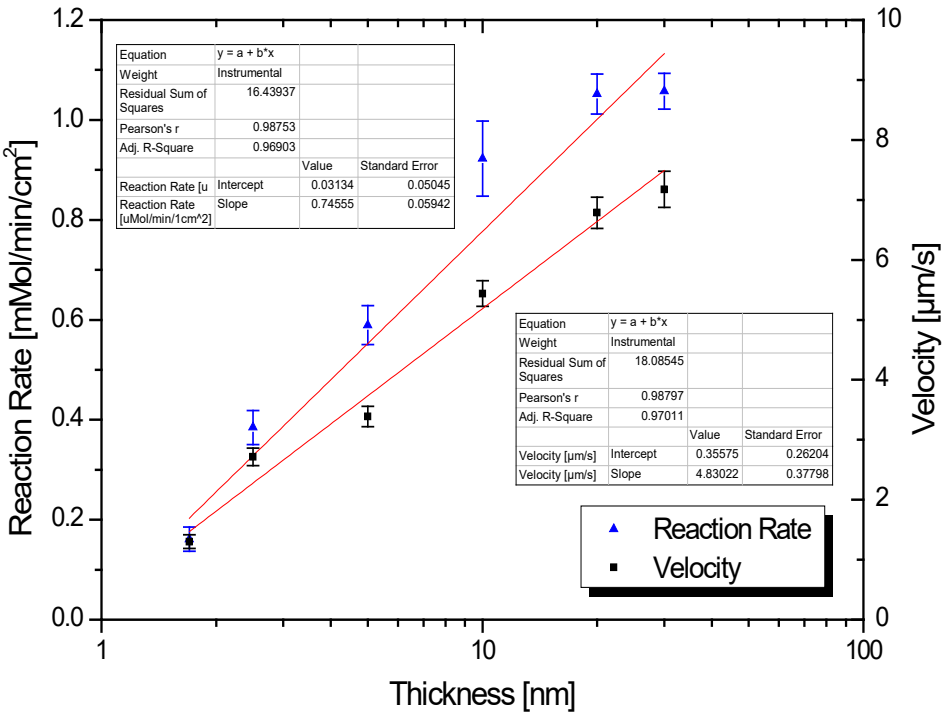

Figure 3-15 logarithmic representations of the reaction rates and velocities dependent on the platinum layer thickness. The red lines are lines of best fit and both show a very good fit.

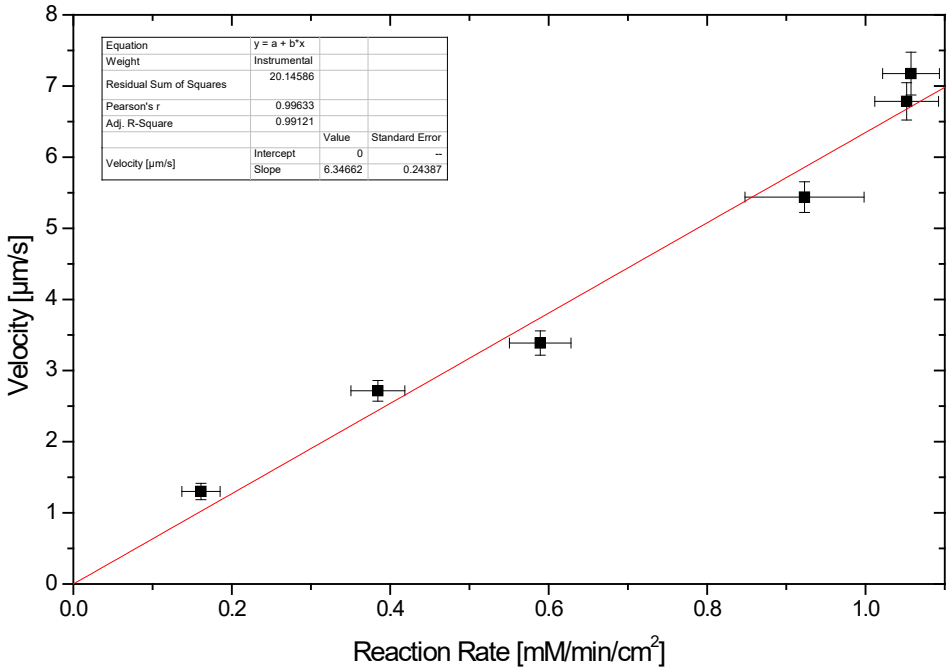

Figure 3-16 Velocity of 2 µm PS/Pt beads in relation to the reaction rate.

3.4.3. Effects of potassium nitrate and silver nitrate on the decomposition of hydrogen peroxide via platinum

Exposure of the Janus particles (via evaporation of Pt.) to 10% w/v H_2O_2 containing different concentrations of KNO_3 and $AgNO_3$ (5×10^{-7} M to 1×10^{-3} M) salts, showed there was a strong reduction in the particle velocity with increase in the concentration of either salt. Propulsion velocities reached a non-vanishing asymptotic value $v = 0.44 \pm 0.02$ μm s^{-1} at concentrations above 3×10^{-5} M, Figure 3-17. Furthermore there was a sharp change at around 10^{-6} M, depending on the initial velocity of the 'swimmers', where the velocity drastically decreased to ~3 μm/s. Velocity decrease was shown to follow a similar trend for both $AgNO_3$ and KNO_3. The diffusion coefficient data corresponds to this data and is shown in Figure 3-18. It is important to note that all this data was gained from particles that were at least 100 μm from any cuvette walls - to minimise the effect of the walls on the diffusion coefficient of the particles, as explained in Chapter 2 Section 2.3.1 with the hindered diffusion equation {2.15} and datasets were made from 25 or more particles. These results with Janus particles in low concentrations of KNO_3 are similar to those previously reported for bimetallic swimmers [62, 134]. However, the anomalous increase in velocity reported by Kagan et al. [134] with regards to $AgNO_3$ was not observed here. (Example movies of the 2 μm Janus colloids in Water (S3.1), 10% H_2O_2 (S3.2), KNO_3 10^{-6}M (S3.3) and $AgNO_3$ 10^{-6}M (S3.4) can be found in the Supportive CD).

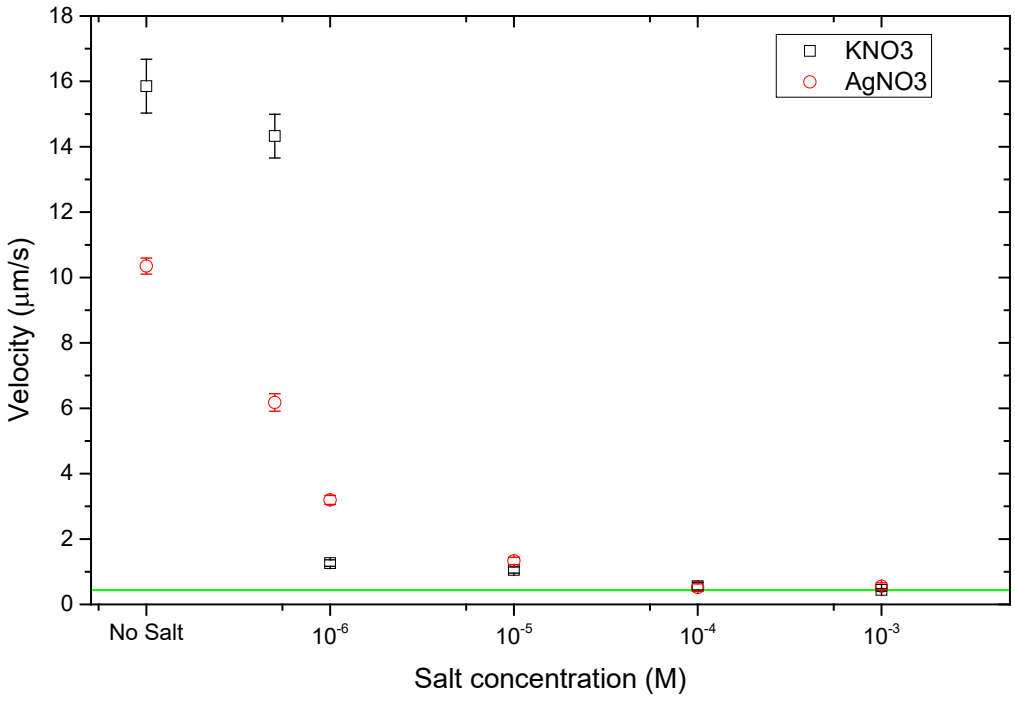

Figure 3-17 Effects of KNO_3 and $AgNO_3$ on the 'swimming' velocity of 2 µm Janus particles, the horizontal green line indicates the lowest velocity thought to be the self-diffusiophoretic component.

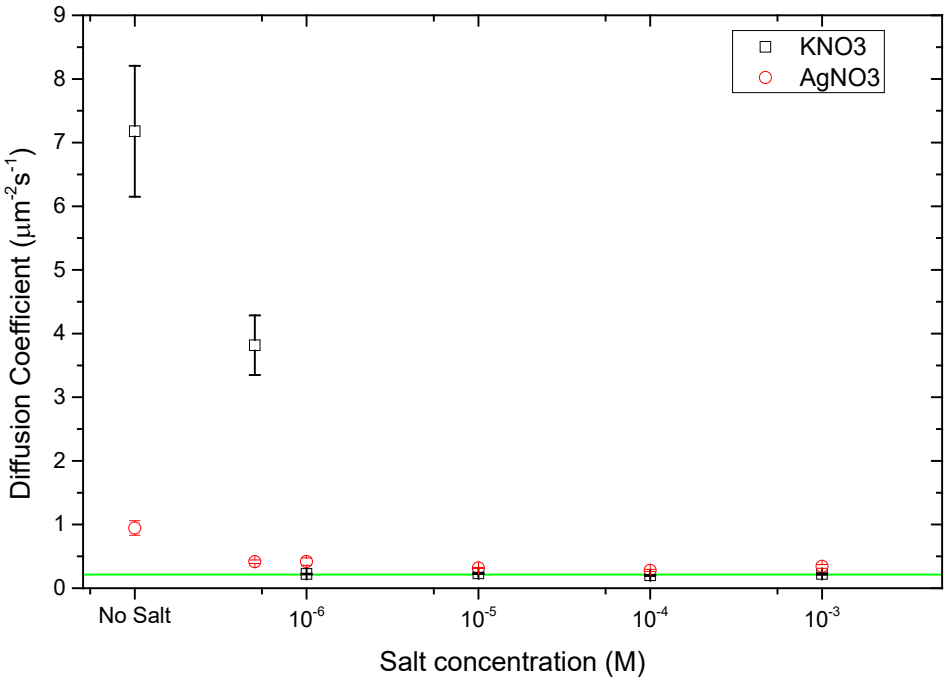

Figure 3-18 corresponding translational diffusion coefficient data to the previous data shown in Figure 3-17 as a function of salt concentration. The horizontal green line indicates the expected diffusion coefficient for particles of this size calculated using the Stokes-Einstein equation.

In order to try to understand the possible factors behind the reduction in velocity with the addition of salt, the reaction rates were then determined, Figure 3-19. Reaction rates measured on both particles and on flat surfaces showed that KNO_3 quenched the reaction rate by up to ~70%. The data also showed that the effect of the salt on the reaction rate did not follow a linear or sigmoidal relationship but rather had peaks and troughs. This observation was also previously made by Heath and Walton [143] and the peaks and troughs observed here generally match up with their reported results, however, reasons for this effect is currently unexplained. In the case of $AgNO_3$, however, the reaction rate results revealed a totally different behaviour, i.e. the reaction rate was gradually inhibited until it was barely detectable at concentrations of ~10^{-5} M or above. Tests also revealed that washing $AgNO_3$ treated slides and putting them into fresh, clean solution of 10 % H_2O_2 did not result in regained activity. When comparing the influence of salt concentration on the reaction rates measured directly on the slides, as shown in Figure 3-20, to those measured on particles, shown in Figure 3-19, the overall tendencies in both cases were the same, though the reaction rates on the colloids were much lower than those measured on the slides for an equivalent surface area.

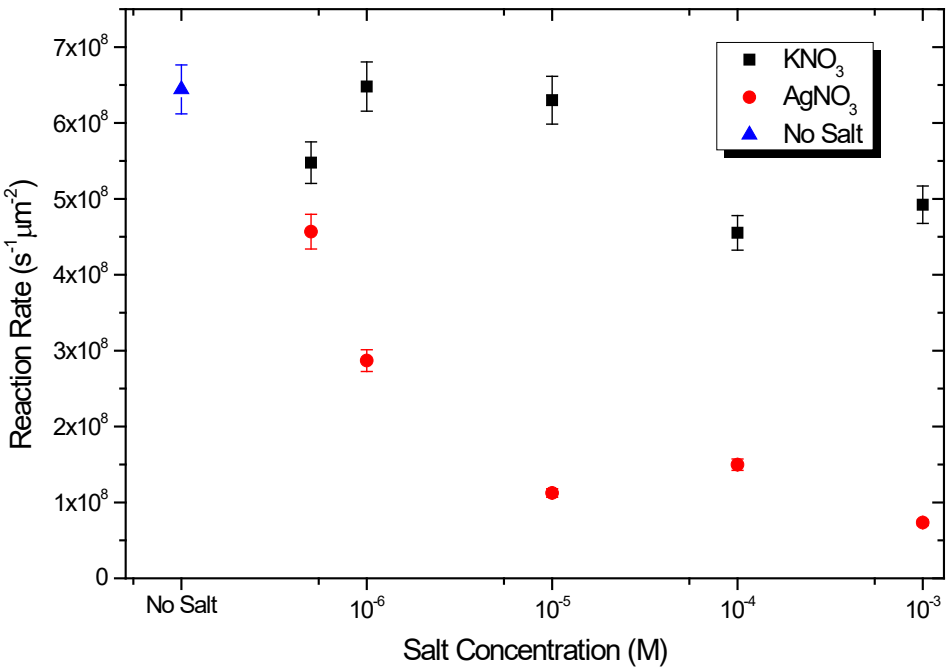

Figure 3-19 H_2O_2 decomposition rates dependent on salt concentration of KNO_3 and $AgNO_3$ measured on 2μm Janus beads with a 15 nm Pt. hemisphere

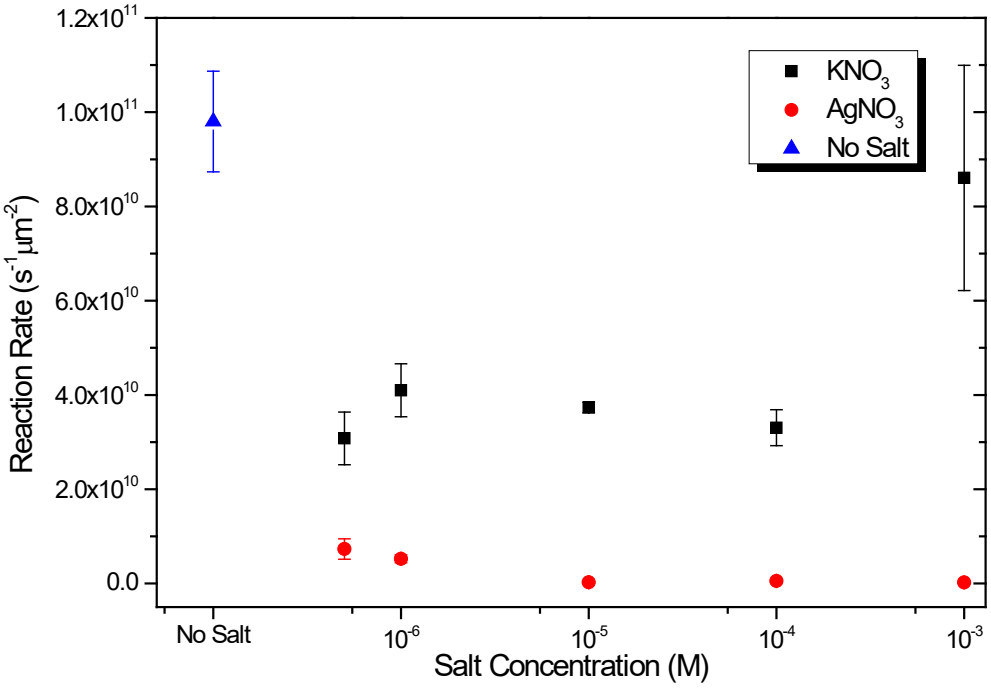

Figure 3-20 H_2O_2 decomposition rates dependent on salt concentration of KNO_3 and $AgNO_3$ on slides measured in a UV-VIS spectrometer at 240 nm.

XPS analysis of the flat surface Pt. samples reveals a fundamental difference between how $AgNO_3$ and KNO_3 affect the platinum surface. In the case of KNO_3

there does not seem to be any noticeable deposition of elemental potassium on the surface of platinum when comparing samples left to react in 10% w/v H_2O_2 (Figure 3-21) with those in 10% w/v H_2O_2 after the addition of 10^{-3} M KNO_3 (Figure 3-22).

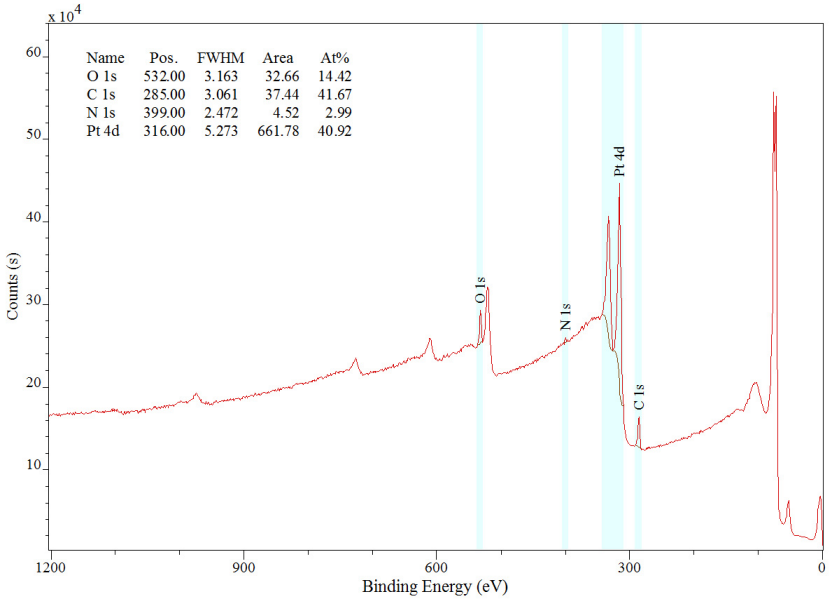

Figure 3-21 XPS survey scans of platinum coated onto glass slides with a 20 nm Cr adhesion layer incubated in 10% w/v H_2O_2 (30 min)

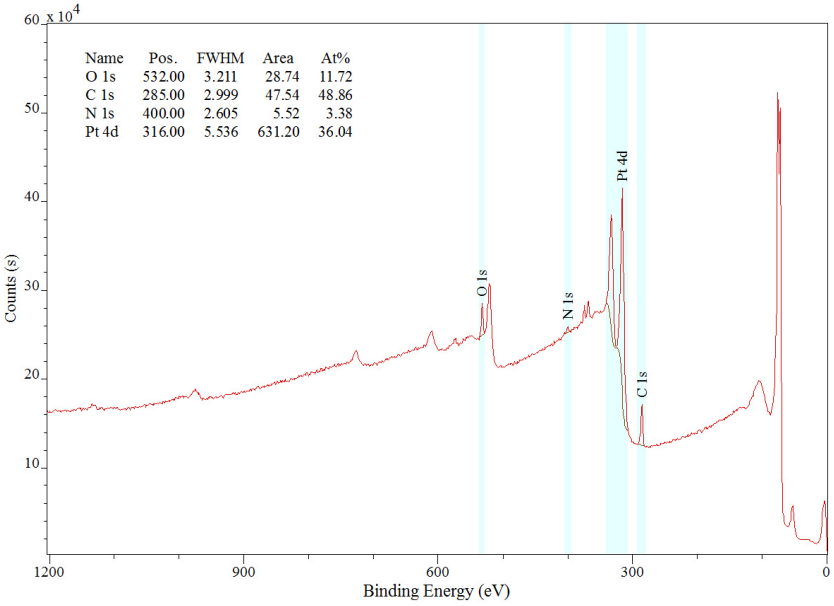

Figure 3-22 XPS survey scans of platinum coated onto glass slides with a 20 nm Cr adhesion layer. Incubated in 10% w/v H_2O_2 together with 10^{-3} M KNO_3 (30 min).

In the case of $AgNO_3$ however it is obvious that silver was actually deposited on the surface of the platinum, Figure 3-23 clearly shows the strong silver **d3** peak. The silver was mainly made up of elemental silver and silver oxide (AgO / Ag_2O), though it was not possible to characterise quantitatively how much of each silver oxide there was (see Figure 3-24). Ferraria, et al. [144] have done an extensive study on the XPS analysis of silver salts explaining the complexity of the different oxygen states of silver and their binding energy shifts. XPS data in conjunction with the velocity and reaction rate data could indicate that in fact silver was deposited in a specific area, according to the electrical field on the particles following the reaction rate gradient. In this way a more efficient, self-assembled bimetallic swimmer could have been generated and this might have negated the decrease in reactivity due to the deposited silver, which could then possibly be in-line with the observations from Kagan et al. [134].

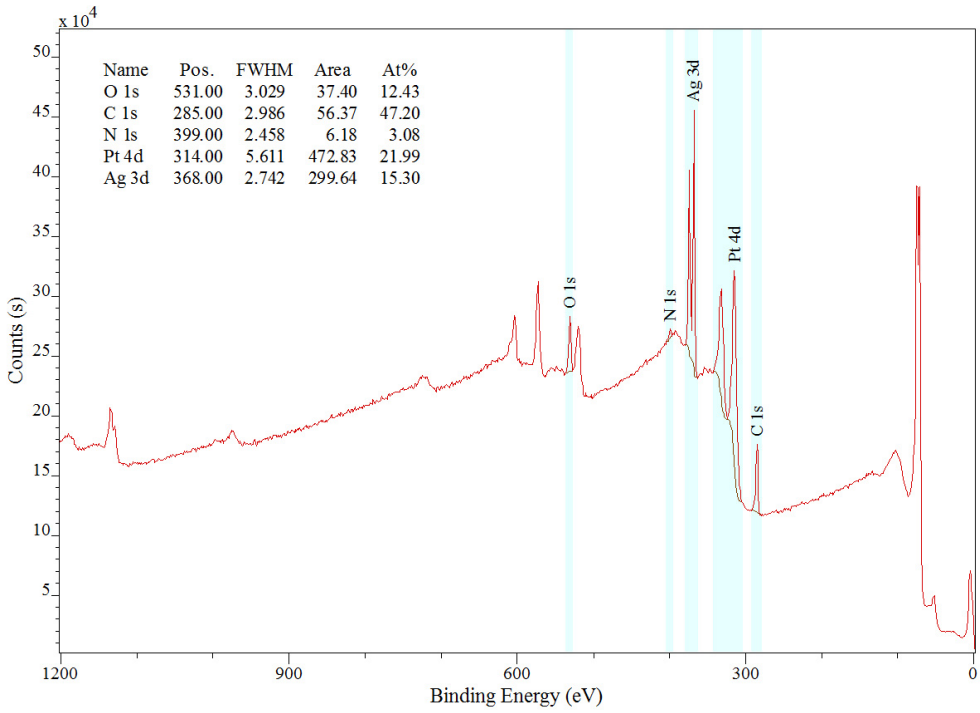

Figure 3-23 XPS Survey scans of platinum coated onto glass slides with a 20nm Cr adhesion layer. Incubated in 10% w/v H_2O_2 together with 10^{-3}M $AgNO_3$ (30min).

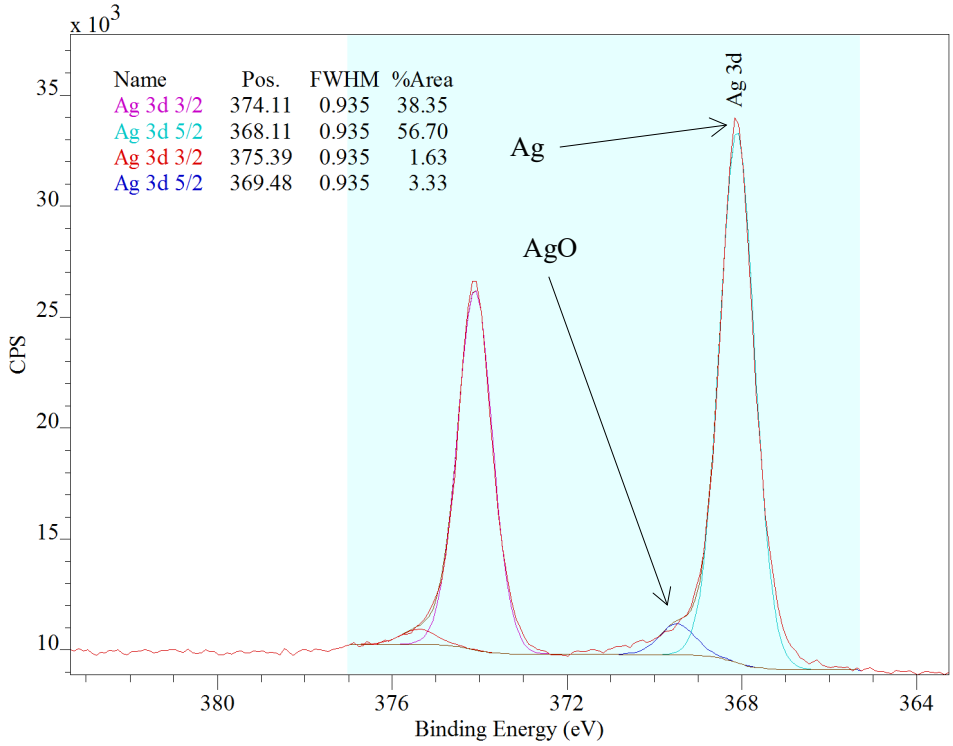

Figure 3-24 Ag-3d XPS data for Platinum treated in 10% w/v H_2O_2 with 10^{-3}M $AgNO_3$.

High resolution spectra of the platinum **4f** peaks (Figure 3-25) revealed that platinum was present in both elemental as well as oxidised form [145, 146], however there was no clear indication that the oxidation state of platinum changed after any treatment nor that any other chemical binding had taken place. This further helps to emphasize that in the case of silver nitrate the elemental silver simply deposited as a silver layer onto the surface of platinum, thus forming an inhibition layer that prevented the hydrogen peroxide molecules from coming into contact with the platinum to induce catalysis.

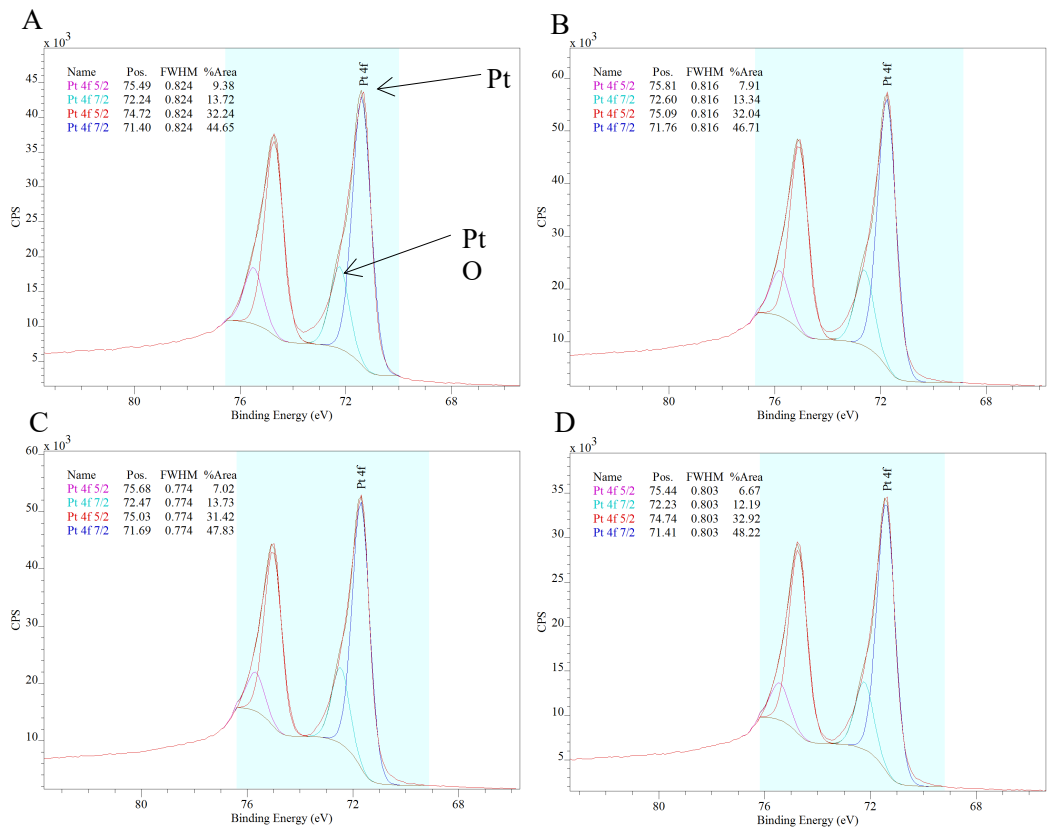

Figure 3-25 Pt-4f X-ray photoelectron spectra for (A) Untreated Pt, (B) 10% w/v H_2O_2 treated Pt, (C) 10% w/v H_2O_2 with 0.001M KNO_3 treated Pt, (D) 10% w/v H_2O_2 with 0.001M $AgNO_3$ treated Pt.

These findings are unexpected as these types of Janus particles are thought to be self-diffusiophoretic, a model that does not suggest any implicit salt dependency for propulsion velocity, other than via any accompanying reduction in reaction rate, which the data above shows is not significant enough to explain the dramatic velocity reduction observed. This is an indicator that there may be electrostatic interactions involved in the propulsion mechanism which are screened by salt, thereby inhibiting the motion. Furthermore, the fact that the Janus particles end up with a minimum velocity rather than no velocity indicates that particles might have two contributions to their motion, a self-diffusiophoretic component and an additional component which is affected by the salt.

A possible explanation of this behaviour, resulting from a collaboration with Prof. Golestanian from Oxford University, has been recently proposed in our joint publication "Electrokinetic effects in catalytic platinum-insulator Janus swimmers" [147]. As shown in Figure 3-26(b) analysis of the details of the reaction pathways for the decomposition of hydrogen peroxide shows there are two reaction rate loops. It was proposed that the reaction rate loop α contains the uncharged species which are responsible for the diffusiophoretic motion of the particles, whereas the γ loop is responsible for the charged intermediates which are affected by salt concentrations.

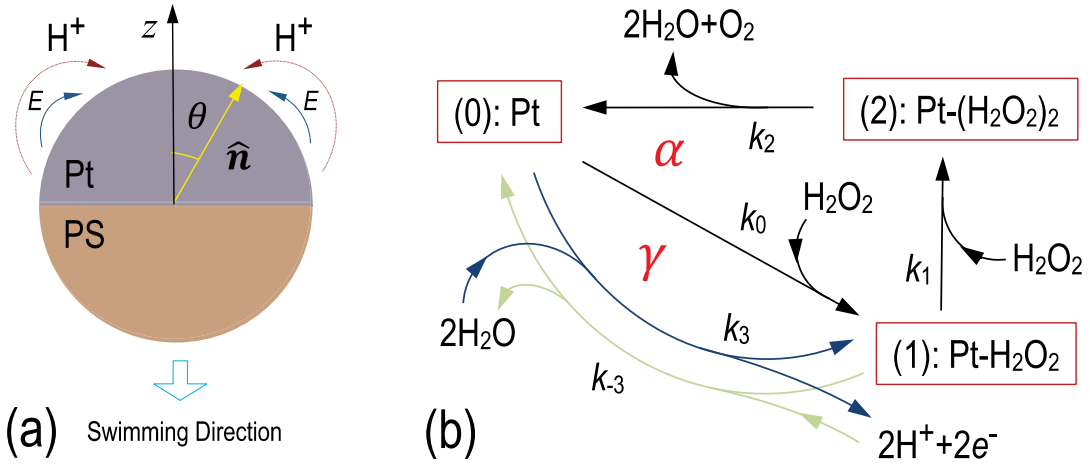

Figure 3-26 (a) A half Pt-coated polystyrene (PS) Janus sphere showing the direction of flow of ions and the electric field. (b) The catalytic reaction scheme showing the competing reactions which have the topological structure of two coupled loops [148]. Loop α is the main non-equilibrium cycle that involves only uncharged species, and loop γ is linked to the production of charged intermediates H^+, e^- taken from [147].

This analysis produced a mechanism that could be affected by salt-concentration, but in order for salts to contribute to the motion of the particle, it is also necessary for there to be gradient in the rate of production of these ionic species across the catalytic hemisphere to produce an associated fluid flow (Figure 3-26a). As discussed above, a clear link between platinum thickness and reaction rate has been established, so the remainder of this chapter considers whether a gradient in

platinum thickness across the catalytic hemisphere could be producing the electrokinetic contribution to propulsion that is quenched by the addition of salt.

3.4.4. Measuring reaction rate on flat thin film platinum versus reaction rate measurement on particles

The previously discussed experiments demonstrated how the decomposition rate of H_2O_2 via Pt is dependent on the thickness of the Pt layer (Figure 3-14), so it is now important to look closely at how the deposition of platinum in a thermal or e-beam evaporator results in a platinum layer that is not homogenously thick over the Janus cap of a spherical particle.

Thermal and e-beam evaporation techniques are highly directional methods (see methods Section 2.1.3) so that evaporation onto a curved surface such as the surface of a spherical colloid, as used here, will generate a gradient in thickness which can be described by Eq.{3.2}, where I_0 is the initial intensity of the deposition beam over the evaporation period, i.e. 20 nm deposition, I_s is the actual deposition thickness measured radially for the specific angle (θ_i) on the sphere as shown in Figure 3-27. This means that the actual deposition amount at the equator of the sphere ($\theta_i = \pm 90°$) is 0 nm and 20 nm at the pole ($\theta_i = 0°$).

$$I_S = I_0 \cos\left(\theta_i\right) \qquad \{3.2\}$$

The same approach for calculating the thickness distribution on a spherical colloid was used in Archer et al. [90].

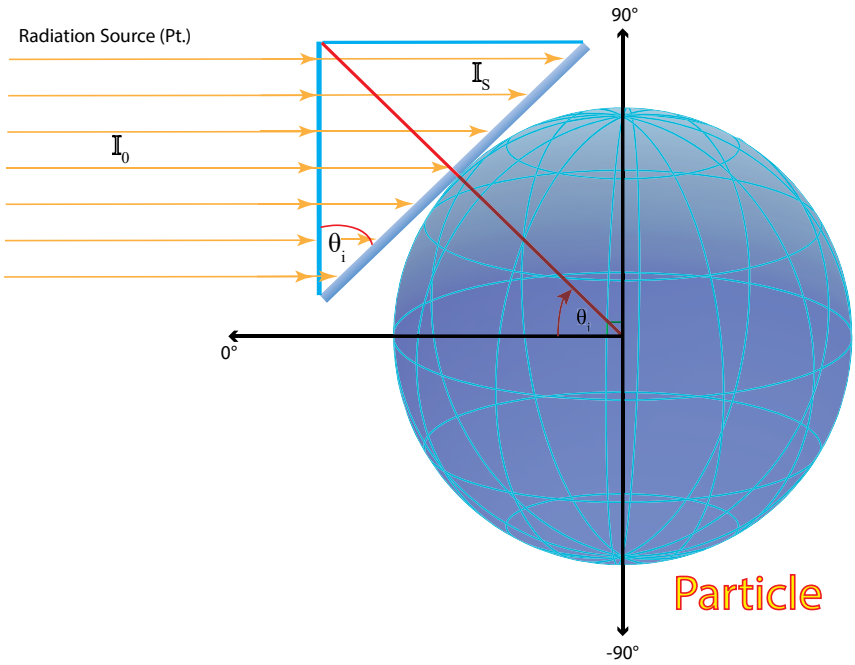

Figure 3-27 Schematic showing an example angle of deposition for a spherical particle demonstrating how the intensity is dependent on the angle of incidence θ_i.

The thickness gradient helps explain the variation in reaction rates for slides and reaction rates measured directly on particles. As previously mentioned and shown in Figure 3-14 the thickness dependent reaction rate plateaued in the region of 15 nm. Therefore, considering the surface area on a flat surface compared to that on a spherical colloid, the reaction rate of the colloid will fall off drastically because the equator regions will always have a very thin coating in comparison to the pole (see Figure 3-28). This means that the overall reaction rate of an evaporated platinum cap on a spherical particle will always be lower than for the same surface area of a flat substrate.

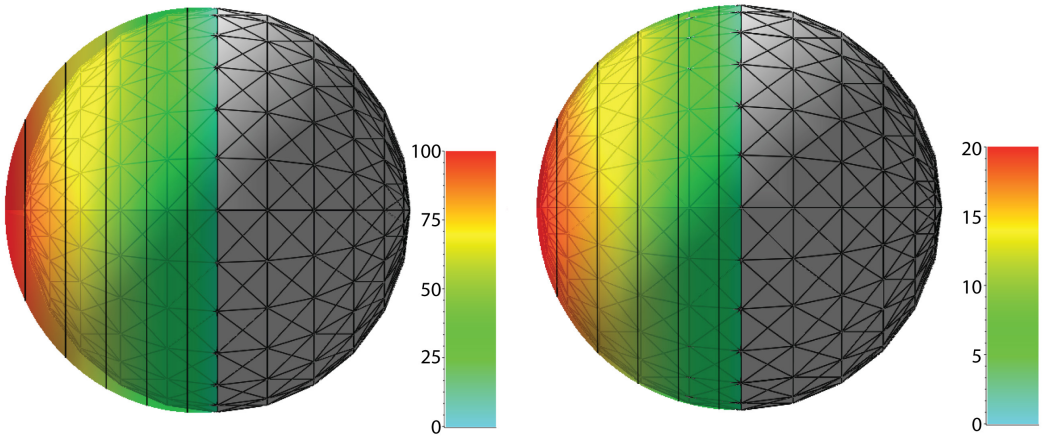

Figure 3-28 3D plots of two coated polystyrene spheres (R=1 μm) showing evaporated thickness distribution (indicated by the coloured in region) as it appears on the colloid (grey); (left) equivalent of 100 nm of metal coating, (right) 20 nm, colour bars given in nm.

Knowing that the thickness of Pt affects the reaction rate, it implies that a Janus colloid made via thermal or E-beam evaporation will have a surface reaction rate gradient. This in turn will not allow for simple diffusiophoretic behaviour as was initially modelled for a uniformly active Janus sphere [30, 135], but suggests that a combination of electrokinetic motion driven by a reaction rate gradient and diffusiophoretic behaviour may be the propulsion mechanism. Using the previously described calculations the reaction rate at a given angle on the colloid can be estimated from the thickness data reported in Table 3.1, which gives an exponential relationship as shown in Figure 3-29 with a high correlation of $R^2 = 0.99$. Here the maximum thickness (at the pole) is 26.99 nm.

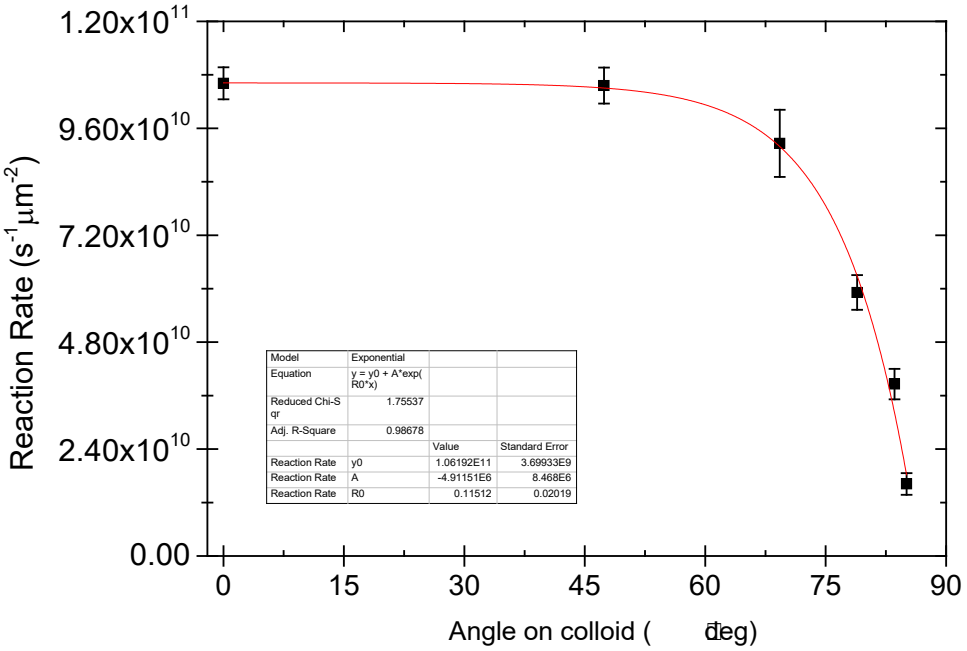

Figure 3-29 H_2O_2 decomposition rate (via Pt) on a spherical colloid as a function of angle, where 0° represents the pole and 90° the equator. Here the highest reactivity is representative of 27 nm of platinum thickness and the lowest 2.3 nm, Reaction rates are taken from actual experimental data and therefore errors are experimental errors.

Based on this finding that a gradient in reactivity appears to be driving a major component of observed propulsion velocity, one final experiment was performed to compare velocities and diffusion coefficients of colloids with a homogenous platinum layer containing no reaction rate gradient to ones with a reaction rate gradient: as the homogenous reaction rate particles should only undergo self-diffusiophoresis.

3.4.5. Comparison of chemically coated platinum particles masked with chromium to e-beam generated ones

As shown in Figure 3-30 and Figure 3-31 both 1 µm and 5 µm particles showed a slight increase in velocity when H_2O_2 concentrations were increased. Unexpectedly however, there was no notable difference between chromium masked and unmasked particles, therefore the chemically platinum coated, chromium masked

colloids do not seem to fit the normal model of propulsion accepted for Janus 'swimmers'. It was also observed that, in particular, fully platinum coated particles seemed to cause increasing turbulence or convection-like flows that made it hard to analyse data accurately and it is possible that they were actually acting like miniature pumps [62, 149, 150]. This behaviour will be discussed in more detail in Chapter 4 where different concentrations of these particles are analysed and their behaviour with increased crowding is investigated using different analytical techniques to characterize their behaviour.

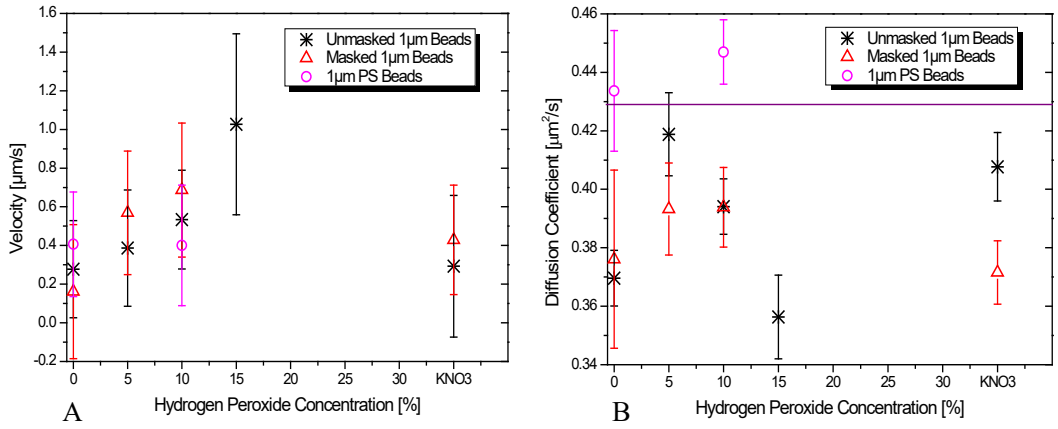

Figure 3-30 Velocities and diffusion coefficients as a function of hydrogen peroxide concentration (w/v) of fully coated 1 µm Pt colloids masked with 15 nm Cr on one hemisphere, and unmasked particles. O denotes pure uncoated polystyrene (PS) particles.

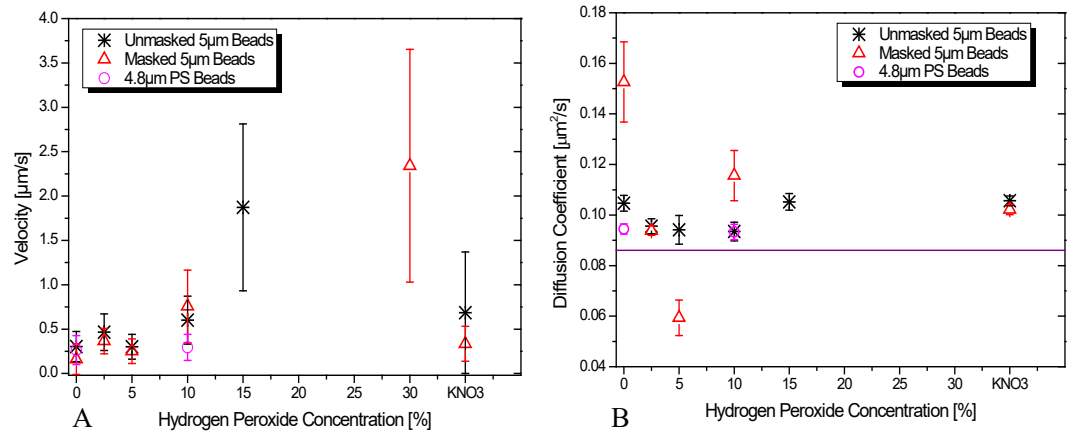

Figure 3-31 Velocities and diffusion coefficients as a function of H_2O_2 concentration (w/v) of fully coated 5 µm Pt. colloids masked with 15 nm Cr on one hemisphere, and unmasked particles. O denotes pure uncoated polystyrene (PS) particles.

Measurements of reaction rates directly on the 1 μm and 5 μm colloids (see Figure 3-32) showed that colloids that had been chemically coated with Pt could achieve much higher reaction rates per cm^2 than colloids where Pt was deposited via e-beam or thermal evaporation. This data is compatible with an effect of the gradient of platinum on the surface of the E-beam coated colloid as discussed in Section 3.4.2 of this chapter, compared to the chemically coated particles (as schematically shown in section 1.5b) which are expected to have a homogenous thickness and a rougher surface structure to evaporated samples.

This would mean if the previously described colloids, which were made via E-beam evaporation, were simply undergoing self-diffusiophoresis then these chemically coated particles, when given Janus structure, should show greater velocities. Figure 3-30 and Figure 3-31 show that this was not the case, for there was no definite difference between masked (Janus - PS/Pt/Cr, schematic section 1.5c) and unmasked (symmetrical - PS/Pt, schematic section 1.5b) chemically coated particles. The velocities obtained for both masked and unmasked particles were of the order of ~0.6 μm/s for 1 μm particles and ~0.8 μm/s for 5 μm particles.

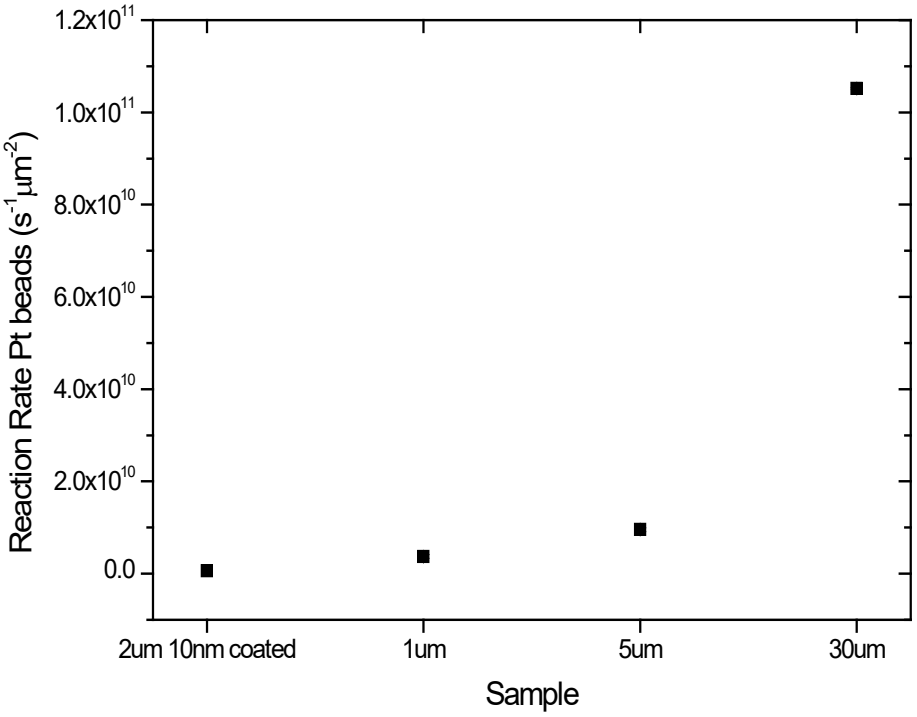

Figure 3-32 Reaction rate comparison of polystyrene beads chemically fully coated with Pt.

30 µm particles have not been further analysed in this chapter as their propulsion mechanism was via bubble propulsion and not self-diffusiophoresis or self-electrophoresis and this mechanism is discussed in detail in the next Chapter (4).

3.5. Discussion

3.5.1. Reaction rate

The good correlation observed for the velocity versus the reaction rate in this chapter (Figure 3-16) corresponds to and appears to confirm the theoretical data described in Ebbens, et al. [31]. Figure 3-33 shows the three scaling regimes expected for different situations of swimmers being affected by hydrogen peroxide fuel concentration or the difference in the size of the particles themselves. Because there are two different reaction rate constants used in the theoretical treatment it is difficult to tell which reaction rate to put into the equations, furthermore it is currently not possible to measure these independently and the reaction rate obtained

in the experimental results is not obviously converted into these parameters. However, as one rate is the limiting reaction rate, which will control the speed of the other, one may reasonably assume the same rate for both.

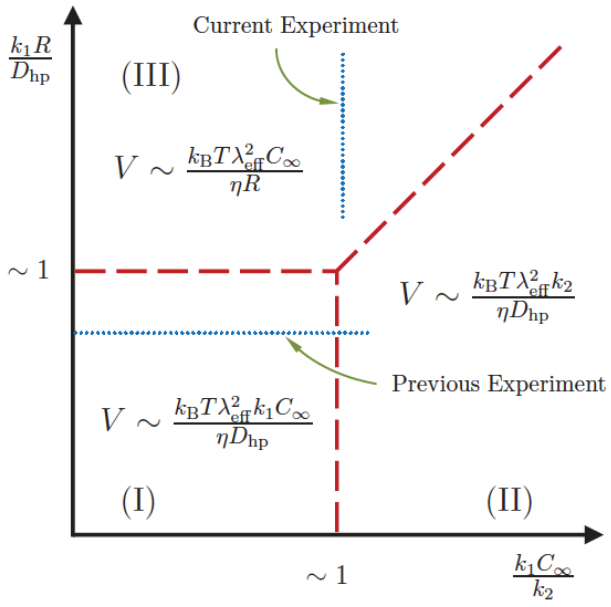

Figure 3-33 Three different scaling regimes as described in Ebbens, et al. [31] for the swimming velocity as a function of the size and fuel concentrations. The dashed lines indicate the experiments described in the paper for the particle size dependency and the concentration dependency as described in Howse, et al. [32]

From Eq. {1.2} we can see that the velocity of a particle is assumed to have a linear relationship to the reaction rate *k*. This agrees with my results as shown in Figure 3-16. It is thought that the current experiment based on difference in reaction rate will fall into regimes I and II as these have linear reaction rate dependencies in their equations, whereas regime III does not. In order to map all the regime regions fully it would be necessary to test different fuel concentrations and particle sizes so it is possible to tell if these different regimes and sudden changes where the velocity stops being dependent on the particle size or fuel concentration or the reaction rate really exist.

Different velocities have been previously reported for Janus-particles of the same size. For example 2 μm spherical Janus-particles were reported to swim at an average of 3.4 μm/s in 5% w/v H_2O_2 [30], 3.1 μm/s [32] and 9 μm/s in 10% w/v H_2O_2 [31]. The reason for the differences might be uneven coatings of platinum on the beads or uneven thickness distributions, or different reaction rates causing different speeds, since my experimental results showed that both the reaction rate and the velocity increased with increasing thickness of platinum (see Figure 3-14). The work in this chapter points at a way to achieve better control and reproducibility for Janus particle swimmers, which will benefit future systematic parametric investigations.

The platinum thickness experiment shows that there is an asymptotic relationship between platinum layer thickness and reaction rate. Above ~15 nm Pt there is not much increase in reaction rate anymore. One would assume from this that layers above 15 nm of deposited platinum would most likely have the same properties as bulk platinum. In Suzuki, et al. [151] it is reported that 10 nm of Pt has the same lattice constant (0.03926 nm) as bulk Pt. This would indicate that in the case of lower thicknesses the film may have defects in the metal lattice which could be the reason for the high increase in reaction rate, as the whole surface is not as densely packed with platinum atoms as it could be. However, above 10 nm one would expect there to be no further change in reaction rate. In the event this did not really hold true until around 15-20 nm. This could indicate that either this does not apply for E-beam evaporation of Pt and the lattice constants are the same at a greater film thickness (than 10 nm), or not only the Pt surface atoms interact with the H_2O_2 molecules but also the underlying layers to a certain extent. AFM measurements made on different sample thicknesses' of Pt as previously shown in Figure 3-5 did

not indicate any major differences in surface roughness with changing coating thickness. SEM images presented by Wang et al. [9] do indicate that a 10 nm E-beam platinum deposition onto colloids does not contain any notable defects and is not as rough as platinum deposited via chemical synthesis routes.

The strong reaction rate change between 2.5 nm and 10 nm film thickness, in conjunction with the small difference over the sample holder (Figure 3-3) at thin thicknesses but large difference at high thicknesses (see Figure 3-14), shows that there is a region between ~5 nm and ~10 nm where the largest changes in reaction rate occur over the sample holder as described in Section 3.2.6. As the theoretical calculation of Figure 3-3 shows, the percentage error of amount deposited over the sample holder does not change but of course the difference in thickness changes. This may be one of the reasons why past experiments showed a large difference in swim speeds since swimmers were made using mainly 5 nm to 10 nm thick platinum coatings; i.e. the reaction rates of the swimmers could have been different due to variations in coating thickness over the sample holder in the evaporator. The vertical dotted lines in Figure 3-14 emphasize these regions of error. To improve the reproducibility of results in the future it might therefore be advisable to use a minimum coating thickness of 15 to 20 nm of platinum. This way the produced samples would be less likely to be susceptible to velocity change due to varying thickness of platinum over the selection of samples on the holder in the evaporator.

3.5.2. Self-Diffusiophoresis or Self-electrophoresis - The proposed model

The results with spherical Janus particles clearly show that particles made with highly directional evaporation methods such as E-beam and thermal evaporation are highly sensitive to salt concentrations. Previously these particles were thought to

only undergo self-diffusiophoresis, but the model of self-diffusiophoresis does not allow for any salt-influencing effects on the motion of the particles. As was demonstrated in Section 3.4.4 during directional evaporation onto spherical particles the material is deposited at different thicknesses over the particles, where the thickest deposition is on the surface orthogonal to the beam as shown in Figure 3-28. As previously indicated the reaction rates vary monotonically on the surface of the colloid with a maximum reaction rate at $\theta = 0°$ and a minimum at $\theta = 90°$. The uncharged species can diffuse freely in the solution whereas the charged species diffuse according to the electric potential in the near proximity of the colloid as shown in the schematic Figure 3-26(a). This therefore leads to a self-generated electrical field over the hemisphere of the colloid.

Comparing the effects of salts with different chemical composition: KNO_3 and $AgNO_3$, the results clearly showed that there are two different effects taking place. Measuring reaction rate directly on flat platinum surfaces in 10% w/v H_2O_2 with different salt concentrations showed that KNO_3, quenches the reaction rate to around 70% the original values with varying peaks and troughs an effect that was previously reported by Heath and Walton [143], whereas $AgNO_3$ poisons the platinum surface with elemental silver deposits, which cannot be removed by cleaning and diminish the reaction rate dramatically. The electrochemical deposition of salt by using H_2O_2 and $AgNO_3$ via electrodes is a known deposition technique [152] and therefore it is highly possible that electron flows across the platinum catalyst enable this deposition to take place here.

Based on reaction rates alone, the velocities for Janus swimmers in the two salts should differ considerably. However this is not the case. It may be hypothesized that in fact the swimmers become more efficient with silver deposits, comparable to

the Au/Pt bimetallic nanorods in Kagan et al.[134], which showed an increase in velocity in silver solution it therefore might be interesting to run an XPS analysis on Au/Pt nanorods to see if any elemental silver was deposited onto one side of the nanorod, as there might be a link between the proton flow and the silver deposition onto the metal. If so, this could mean that initially silver deposited on the Janus particles in a way which did not cover the platinum layer fully but generated a bimetallic particle (a particle containing Platinum exposed surfaces and silver exposed surfaces).

3.6. Conclusions

Depositing different thicknesses (between 2.5 and 20 nm) of the platinum catalyst via evaporation onto planar substrates showed that the decomposition rate of hydrogen peroxide increased with thickness (Figure 3-10). This is an interesting finding in its own right, and does not have an obvious explanation, and may provide a route to establish gradients of reactivity that could be used for pumping systems, and also provide a novel indirect method for film thickness measurement. A corollary of this observation is that a reaction gradient is also predicated across the surface of Janus particles prepared by metal evaporation as these show thickness variations due to the deposition process (Figure 3-28). It was also shown that non-conductive, self-motile Janus particles are salt dependent and slow down dramatically on the addition of salt. Moreover, although the reaction rate dependencies of potassium nitrate and silver nitrate are different, the swimmers show a similar salt concentration versus velocity profile for both salts (Figure 3-17). These observations suggest that salts are affecting the propulsion mechanism for Janus spheres in a way not solely related to hydrogen peroxide decomposition rate. A model was proposed to account for these observations,

which shows how an electrokinetic mechanism that would be affected by electrostatic screening can exist for spherical catalytic swimmers if there is a gradient of surface catalytic activity, and the experiments in this chapter have shown that this does exist. To further verify the importance of a reaction rate gradient to enable rapid propulsion for Janus catalytic spheres, the case where the catalyst was deposited without obvious thickness variations, using a chemical coating was also investigated. Both symmetrically active and Janus particles show similar velocities within error, and these are significantly lower than that observed for the evaporatively prepared Janus particle, suggesting that a reactivity gradient is a requirement for significant propulsion. Consequently the results in this chapter have fundamentally modified the mechanistic understanding for the widely studied catalytic Janus particle system. This chapter has also shown that ensuring the surface cleanliness of the platinum catalyst is important to produce consistent reaction rates and propulsion velocities, and has proposed a protocol to achieve this.

4. Convective motion onset for high volume fractions of catalytic active colloids

4.1. Introduction

The final section of Chapter 3 established that colloids symmetrically coated with platinum catalyst do not produce appreciable propulsion velocities when measured in isolation at low volume fractions, despite reaction rate measurements showing that they were producing an appreciable hydrogen peroxide decomposition rate. This was as expected because of the absence of both a surface reactivity gradient and a Janus structure, factors that have been established to be necessary for rapid phoretic propulsion. However there were indications that at higher volume fractions, some flow like behaviours were observed. As Dunderdale et al. [95] points out, in order to be able to accurately measure velocities via MSD it is important that the colloids do not interact with each other or undergo random turbulences, such as convective flows [95], which could influence the measured trajectories of other micromotors and thus generate inaccurate results. At this point one may ask: what exactly is convective flow? It is a flow which arises when a liquid has a non-equilibrium state (e.g. concentration gradient) and therefore the arising flow compensates for this. It is important to note that convective flow is a flow which is always circular if one considers the whole observation chamber as overall the same amount of liquid needs to be maintained in all locations. When viewing samples under the microscope however, observations are in general carried out over a limited field of view, which means that often the convective currents appear linear in the region of interest. Thus colloids carried along with the convective flow patterns will often exhibit linear motion totally unaffected by any Brownian rotational effects. As previously explained in Section 2.3.2 this means

that calculating MSD over long time periods for these trajectories will give a constantly increasing MSD, whereas particles undergoing phoretic self-propulsion and Brownian rotation will eventually become diffusive over longer timescales [95]. In addition, convective flow velocities are often constant providing there are not multiple convective flows converging upon each other. There are various ways of inducing convective flow, but predominantly it arises due to temperature gradients, which cause the liquid to have different densities and thus convective flow tries to even out these differences [153]. Gravity can also induce convective flow by generating a pressure difference in a microfluidic cell as described in Morier et al. [154], or by the sedimentation of colloids as described in Hamid et al. [155].

In a recent study, ways to remove the convective flow vector (advection) from diffusion coefficients of colloids in shear flow were investigated [156]. Another recent publication using covalently immobilised catalase attached via gold to the flat surface of a lab-on-a-chip based application showed that catalytically active areas can cause pumping effects [150] due to a concentration gradient that forms in the surrounding bulk solution when a catalytic reaction takes place such as the decomposition of hydrogen peroxide into oxygen and water. We can regard pumping as a forced convection effect. The main difference between pumping and convection lies in the fact that convection is a flow that always attempts to compensate for any *non-equilibrium* states, whereas pumping uses an external force or power to generate a motion of the liquid. Kline et al. [149] show that electroosmotic flow, generated by oxidation of H_2O_2 causing protons to migrate from a gold anode to a silver cathode, can create a convective flow along the gold surface, as shown in Figure 4-1.

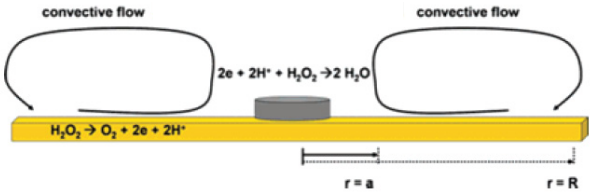

Figure 4-1 Protons (H+) generated by oxidation of H_2O_2 migrate from the anode (gold) to cathode (silver, centre), generating electroosmotic flow. This flow creates a convection roll that sweeps tracer particles inward along the gold surface. The convection roll extends from r = a (near the silver) to r = R, taken from [149].

It has been observed in microbiology that convective flows can be generated by bacteria in bacterial suspensions [157-159].

Following on from these pumping effects one can hypothesize that the concentration of active colloids in the fuel solution might generate localised concentration gradients which in turn will cause a non-equilibrium state of the bulk solution which will undergo convectional flow in order to equalise the concentration gradients. Homogeneously catalytically active micromotors could therefore be seen as small mobile pumps that are capable of generating localised concentration gradients and as they are not attached to any surface they are able to move in the solution and are carried along with flow. In conclusion: convective flow patterns might occur that are dependent on the concentration of the micromotors and their reactivity. The micromotor concentration may also influence the accuracy of velocity measurements of Janus or symmetrical spheres or other similar self-motile particles, as these measurements will most likely be inaccurate if micromotor volume fractions are near concentrations where convection flow is about to happen. Until now, the relationship between catalytically active colloid concentration and convective flow patterns and the emanating velocities has not been investigated. One theoretical analysis by R. Golestanian [160] for symmetrical catalytically active particles predicted an anomalous diffusive effect at very short

time scales that would produce a ~$t^{3/2}$ MSD versus time evolution (Figure 4-2). In this context the studies in this chapter aim to gain better experimental understanding of these effects.

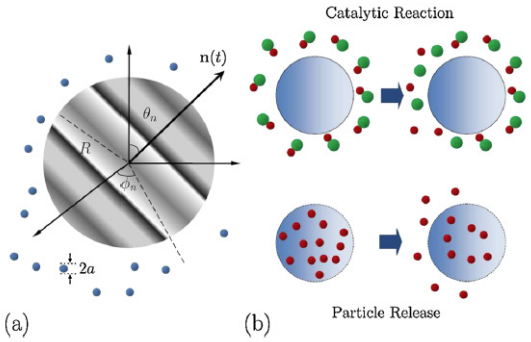

Figure 4-2 (a) Schematics of an instantaneous configuration of an axially symmetric surface-active spherical colloid. (b) The model could correspond to a chemical reaction catalysed on the surface with the simplifying assumption that one of the product particles is very similar to the substrate, or a container that releases particles through channels, taken from [160].

4.2. Influence of volume fraction on the motion of spherical homogeneously active, chemically-coated Pt/PS colloids

4.2.1. Methods

4.2.1.1. Particle preparation

Monodispersed polystyrene colloids 1 µm and 5 µm in diameter were uniformly coated with platinum via in-situ reduction of platinum salts. The coating obtained by this method was made up of 2-5nm nanoparticles of platinum that were adhered to the surface of the colloids. This synthesis was performed by Kisker Biotech. The colloids were then suspended in water as stock suspensions, as previously reported in Chapter 3.

4.2.1.2. Counting of particles

For this experiment to succeed it was extremely important to have an accurate estimate of the particle concentration within a sample. This was achieved by firstly generating stock suspensions of 1 and 5 μm particles in water. The numbers of particles in the stock solutions were then counted using optical microscopy by means of rectangular capillary tubes into which some of the homogenously dispersed stock suspensions were placed. The ends of the capillary tubes were then sealed off and their inner height was measured using a Prior electronic microscope stage, which gives out z-axes height readings (in μm). This was necessary as every capillary tube turned out to have a different inner height. The capillary tubes were then left between 30 minutes to 1 hour in order for the colloids to settle to the bottom of the tube. Once it was verified that the bulk of the particles had settled to the bottom and showed a uniform distribution (estimated visually by scanning the capillary under the microscope) over the capillary tube a large number of images were taken of the particles (20 to 30), see Figure 4-3. The particles in the images were then counted in a custom-written LabVIEW program (shown in Appendix 10.7), which allowed colloids to be recognized while ignoring larger or smaller dirt particles as well as splitting-up touching particles into two or more separate particles. As the process was not totally error free, as can be seen from Figure 4-3, the images were verified and any counting errors that were made corrected manually to ensure accurate counting (by cross comparison of threshold images and original images, Figure 4-3).

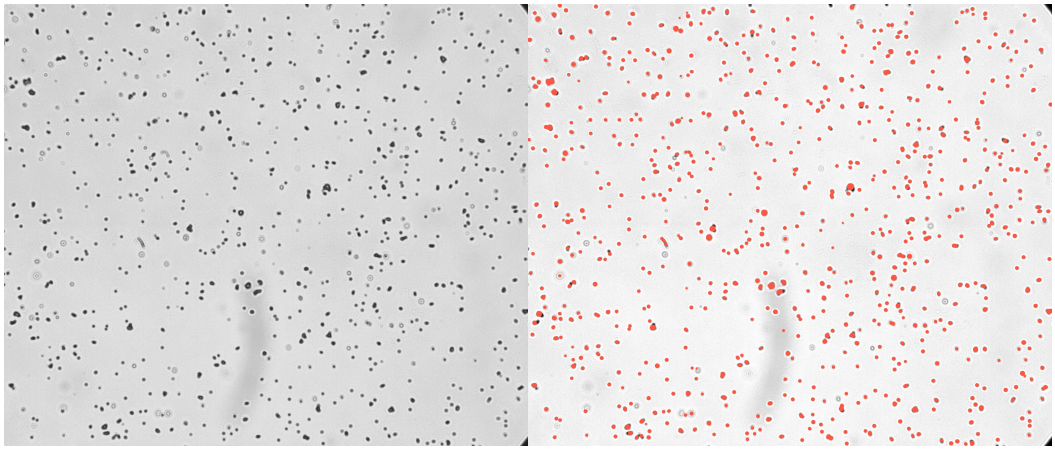

Figure 4-3 Microscope image showing settled 1 µm homogeneously Pt.-coated PS colloids at the bottom of a capillary, (left) raw image, (right) image with counter particle overlays.

In order to calculate the particle concentration estimated per 1 ml of stock suspension the particles were counted for a given image area, the image area was then multiplied by the capillary height giving the total volume for the counted particles in that particular image, with the help of the previously taken pixel calibration images along with the capillary height data of the particular capillary. This was done for all images and added together and calculated up to 1 ml of stock suspension.

For the 1 µm stock suspension it was necessary to dilute the stock suspension in order for the resulting sample not to be too crowded with particles for accurate counting; the particle count was later corrected for the dilution factor used. Because the colloids settled to the bottom of the bulk solution it was imperative that during the dilution process the samples were first sonicated and then constantly stirred until the process was completed and the sample was pipetted into the capillary tubes.

The volume fraction number φ for 1 and 5 µm spherical colloids was calculated using the following formula:

$$\phi = \frac{4}{3}\pi a^3 \left(\frac{N}{V}\right), \qquad \{4.1\}$$

where a is the colloids radius, N is the number of spherical colloids in the given volume V [161].

4.2.1.3. Preparation of Samples and capture of image data

During this experiment it became apparent that in particular the 5 μm particles had a tendency to settle very rapidly. It was therefore necessary to sonicate and vortex the samples constantly to ensure homogenous suspensions of the colloids. As a dilution series was taken from the stock solution it was imperative that the sample was vortexed seconds before samples were taken from the stock solution to ensure accurate dilutions. Several dilutions were then taken from each of the stock suspensions and measured in a 1 mm quartz cuvette under an optical microscope (Nikon Eclipse LV100) with an Andor CCD camera. Movies of at least 1000 frames were taken at a framerate of 33 fps. The movies were then tracked with the previously mentioned LabVIEW tracking software and the MSD, mean squared gyration, fractal dimension, and persistence lengths were calculated using the custom built LabVIEW analyser software mentioned in Chapter 4 Section 5.2.4.

4.2.1.4. Trajectory analysis

MSD Trajectory Analysis was done as described in Sections 2.3.2 and 3.2.1, whereas fractal dimension and persistence length and mean squared gyration analysis was done as described in Sections 2.3.3, 2.3.4 and 2.3.5 respectively, implementing custom written LabVIEW Algorithms.

4.2.2. Results and discussion

After placing either 1 μm or 5 μm platinum coated PS colloids in 10% hydrogen peroxide fuel solution, no visible bubbles were formed on the surfaces of the colloids (unlike the 30 μm Pt/PS colloids investigated in Chapter 5 and 6). However it was obvious that at higher colloid concentrations (above ~5.85 x 10^3 particles/ml (1 μm) (φ_1 = 3.06 x 10^{-9})) and ~3.34 x 10^3 particles/ml (5 μm)(φ_5 = 2.19 x 10^{-7})) rapid formation of oxygen bubbles was present in the bulk solution, where oxygen levels reached critical saturation levels, and on the surface edges of the quartz cuvette, where it seemed most of the bubbles would nucleate on the glass walls of the cuvettes and gradually grow in size. This rapid formation of bubbles made it necessary to invert the cuvettes between each video take, as otherwise the bubbles forming on the top of the cell made it hard to focus onto any colloids. It was then essential to wait at least 20 to 30 seconds to ensure any residual flow from inverting the cuvette had subsided before a new movie could be taken. For high volume fractions it was possible to track multiple particles per movie in a region of interest, while at lower concentrations in general only one particle per movie was possible. Reaction rates for the 1 μm particles under consideration were ~3.7x10^9 $s^{-1}\mu m^{-2}$ and ~9.5x10^9 $s^{-1}\mu m^{-2}$ for 5 μm colloids (see Chapter 3 Section 3.4.5) which means the reaction rate of 5 μm colloids is ~2.6 times higher than for 1 μm particles. Figure 4-4 shows that the trajectories for 1 and 5 μm colloids in water seemed to be very similar, where both types of particles only appeared to be undergoing Brownian motion. The numbers in Figure 4-4 refer to the particle concentrations / volume fractions in Table 4.1 (for 1 μm) and Table 4.2 (for 5 μm). When 10% w/v hydrogen peroxide was introduced into the system, trajectory data showed that at low particle concentrations (below φ_1 = 1.23 x 10^{-8}, φ_5 = 6.13 x 10^{-7})

there was little difference between water and hydrogen peroxide data for both 1 and 5 μm particles. At higher volume fractions (φ_1 = 2.45 x 10^{-8}, 4.68 x 10^4/ml, 1 μm particles) however a flow-effect, which can be compared to convective flow, seemed to contribute to the motion of both 1 μm and 5 μm particles, as the trajectories showed drift, and also the particles clearly moved further in a given time period. Comparing this convective effect for 5 μm versus 1 μm catalytically active particles the 5 μm particles seem to show these flow-effects at a much lower particle concentration (φ_5 = 7.66 x 10^{-7}, 1.17 x 10^4 particles/ml) than 1 μm catalytically active particles. This difference between 1 and 5 μm particles is most likely due to each particle having a larger surface area and reactivity and thus generating a greater difference in concentration gradient in the near proximity of each colloid. (Representative movies of 1 and 5 μm colloids in H_2O_2 and Water at high and low volume fractions can be found on the Supportive CD, Movies S4.1-8).

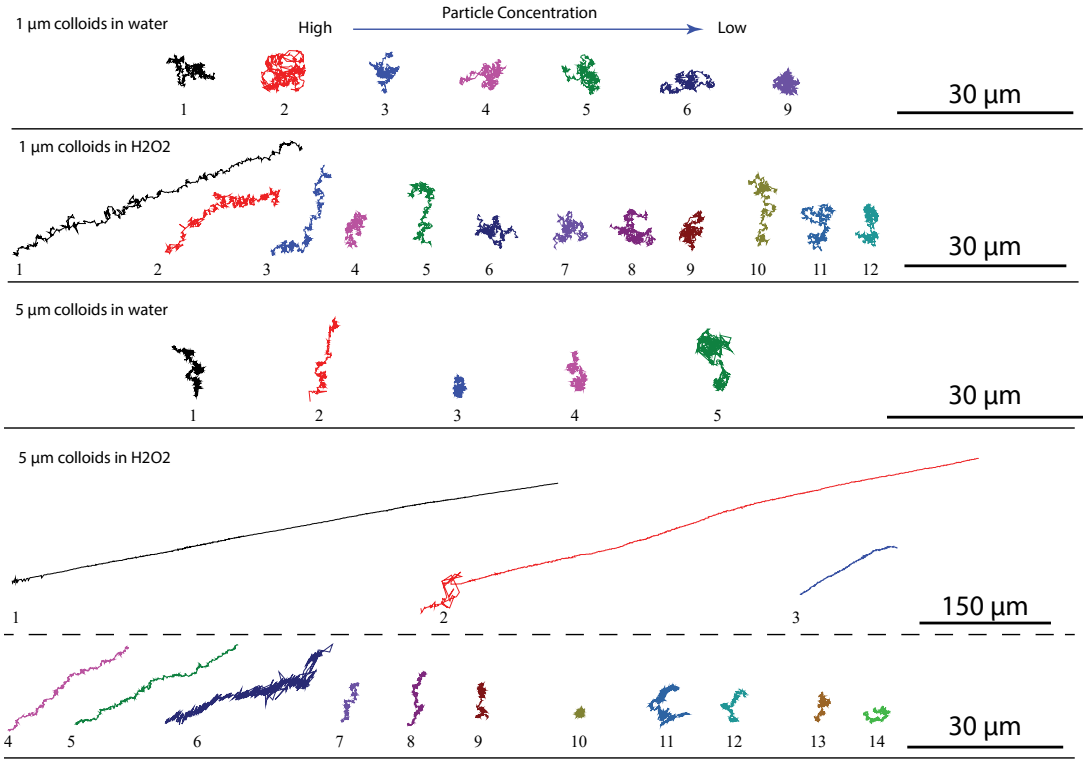

Figure 4-4 Representative trajectory data of 1 and 5 µm colloids at varying particle concentrations in water and 10 % w/v hydrogen peroxide particle concentrations and equivalent volume fractions are shown in Table 4.1 (1 µm) and Table 4.2 (5µm), Representative movies of 1 and 5 µm colloids in H_2O_2 and Water at high and low volume fractions can be found on the Supportive CD, Movies S4.1-8.

In order to be able to distinguish and understand these initial trajectory observations better the following more detailed data analysis methods were used.

Table 4.1 particle concentrations for 1 µm colloids given in particles per 1 ml and volume fraction φ_1.

	1 µm [N/ml] (water)	φ_{1w}	1 µm [N/ml] (H_2O_2)	φ_1
1	1.50×10^{6}	7.87×10^{-7}	1.86×10^{6}	9.76×10^{-7}
2	7.52×10^{5}	3.94×10^{-7}	9.32×10^{5}	4.88×10^{-7}
3	4.68×10^{5}	2.45×10^{-7}	4.68×10^{5}	2.45×10^{-7}
4	1.87×10^{5}	9.81×10^{-8}	1.87×10^{5}	9.81×10^{-8}
5	4.68×10^{4}	2.45×10^{-8}	4.68×10^{4}	2.45×10^{-8}
6	2.34×10^{4}	1.23×10^{-8}	2.34×10^{4}	1.23×10^{-8}
7	1.56×10^{4}	8.17×10^{-9}	1.56×10^{4}	8.17×10^{-9}
8	1.17×10^{4}	6.13×10^{-9}	1.17×10^{4}	6.13×10^{-9}
9	9.37×10^{3}	4.90×10^{-9}	9.37×10^{3}	4.90×10^{-9}
10	5.85×10^{3}	3.06×10^{-9}	5.85×10^{3}	3.06×10^{-9}
11	4.68×10^{3}	2.45×10^{-9}	4.68×10^{3}	2.45×10^{-9}
12	3.90×10^{3}	2.04×10^{-9}	3.90×10^{3}	2.04×10^{-9}

Table 4.2 particle concentrations for 5 µm colloids given in particles per 1 ml and volume fraction φ_5

	5 µm [N/ml] (water)	φ_{5w}	5 µm [N/ml] (H_2O_2)	φ_5
1	2.32×10^6	1.52×10^{-4}	4.68×10^5	3.06×10^{-5}
2	1.16×10^6	7.60×10^{-5}	1.87×10^5	1.23×10^{-5}
3	5.81×10^5	3.80×10^{-5}	4.68×10^4	3.06×10^{-6}
4	2.34×10^5	1.53×10^{-5}	2.34×10^4	1.53×10^{-6}
5	2.93×10^4	1.92×10^{-6}	1.56×10^4	1.02×10^{-6}
6			1.17×10^4	7.66×10^{-7}
7			9.37×10^3	6.13×10^{-7}
8			7.80×10^3	5.11×10^{-7}
9			6.69×10^3	4.38×10^{-7}
10			5.85×10^3	3.83×10^{-7}
11			5.20×10^3	3.41×10^{-7}
12			4.68×10^3	3.06×10^{-7}
13			3.34×10^3	2.19×10^{-7}
14			9.37×10^2	6.13×10^{-8}

Comparison of MSD plots of 1 µm (Figure 4-5 A and B), and 5 µm (Figure 4-6 A and B) colloids in water at high and low volume fractions revealed Brownian motion like behaviour for all plots. If we compare the MSD plots for both short (insets) and long times we get a linear relationship for short times whereas the MSD becomes diffusive for long periods of time which is to be expected for Brownian motion [95]. However comparing the MSD plots for high and low volume fractions in 10% hydrogen peroxide fuel solution results clearly show that both 1 µm (Figure 4-5 C) and 5 µm (Figure 4-6 C) colloids showed Brownian motion behaviour at low volume fractions, but at high volume fractions this changed and became ballistic motion behaviour. This indicates an effect of convective flow as for both long times (1 µm Figure 4-5 D and 5 µm Figure 4-6 D) and short times (insets) there was a constant increase in ΔL^2. In comparison to Janus propulsion the MSD plots should become gradually diffusive over long periods of time as the rotational diffusion coefficients of Janus particles is coupled to their motion and therefore affects their trajectories. As can be clearly seen from the representative plots this is not the case and therefore this propulsion mechanism is not taking place here. So it is not

surprising as each individual colloid is not expected to develop an orientation linked propulsion velocity due to proximity to neighbouring active colloids.

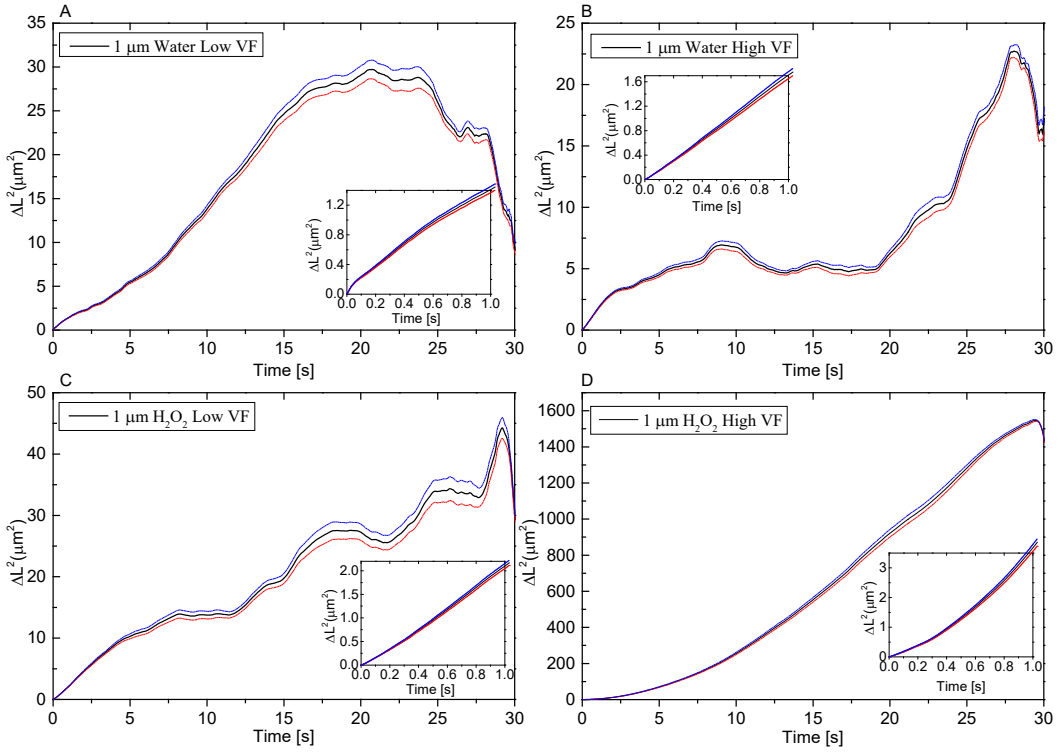

Figure 4-5 Representative MSD plots of 1 µm colloids in Water and Hydrogen peroxide (10% w/v) at Low and High volume fractions; A $\varphi = 2.04 \times 10^{-9}$, B $\varphi = 7.87 \times 10^{-7}$, C $\varphi = 2.04 \times 10^{-9}$, D $\varphi = 9.76 \times 10^{-7}$. Insets are the same MSD's represented for the initial first second.

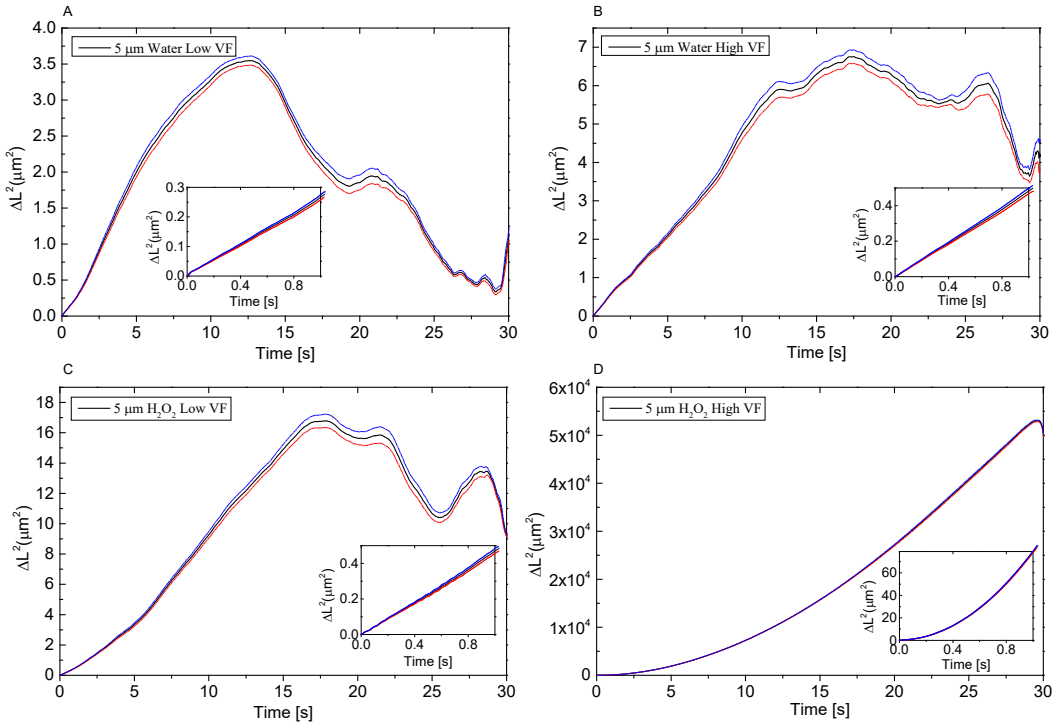

Figure 4-6 Representative MSD plots of 5 µm colloids in Water and Hydrogen peroxide (10% w/v) at Low and High volume fractions; A $\varphi = 1.92 \times 10^{-6}$, B $\varphi = 1.52 \times 10^{-4}$, C $\varphi = 6.13 \times 10^{-8}$, D $\varphi = 3.06 \times 10^{-5}$. Insets are the same MSD's represented for the initial first second.

At this point it is important to note that it was observed that colloids in the bottom half of the cell moved in the opposite direction to colloids near the top of the cell. In addition to this particles near the edges of the cell could be seen moving either upwards or downwards, thus giving a full circular motion loop.

MSD fitted velocity data as shown in Figure 4-7 showed there was a distinct difference between the behaviour of the 1 µm and 5 µm volume fractions (in 10% H_2O_2): no obvious velocity increase could be detected for 1 µm colloids until at least volume fractions of $\varphi_1 = 9.81 \times 10^{-8}$ (1.87×10^5 particles/ml) however for 5 µm colloids the velocity increase was observed at a much lower volume fractions of $\varphi_5 = 7.66 \times 10^{-7}$ (1.17×10^4 particles/ml) and above which agrees with the previously described observations of the trajectories. As seen in Figure 4-7 A initially 1 µm colloids showed a drift velocity of between 0.4 and 0.7 µm/s for lower volume

fractions increasing to 1.6 μm/s for the highest volume fraction measured. In contrast, the 5 μm particles showed an initial velocity oscillation between 0.2 and 0.5 μm/s at the low volume fractions and then with increase in volume fraction above $\varphi_5 = 7.66 \times 10^{-7}$ (1.17×10^4 particles/ml) showed a strong increase in velocity reaching maximum values of 12 μm/s. The large variance in the data could be a result of the need to invert the cuvettes frequently and if this was not done frequently enough or if the sample had not settled properly and particles were still undergoing slight motion after the inversions this might have led to inaccuracy in the recorded data. Further to this it is important to note that 5 μm colloids had a tendency to settle to the bottom of the cuvettes more rapidly than 1 μm. In conjunction with this Lattuada et al. [162] find that colloidal swarms settle faster than isolated particles, which could add to the increasing errors at higher concentrations. Blank data of colloids measured in water show that the average velocity measured was in the region of 0.2 to 0.6 μm/s for all concentrations of 1 μm particles. Measurements of 5 μm colloids in water showed that the velocity was between 0.2 and 0.4 μm/s, and there seemed to be an indication that at high concentrations the velocity decreased slightly. One reason for this might be that as particle concentration increases the Brownian motion of a particle is hindered by neighbour particles in a similar way as it would be if a particle was near a wall [121]. Ghosh et al. [163] finding, that diffusive behaviour of colloids confined in microcylinders become more hindered at higher volume fractions could be related to this change in velocity.

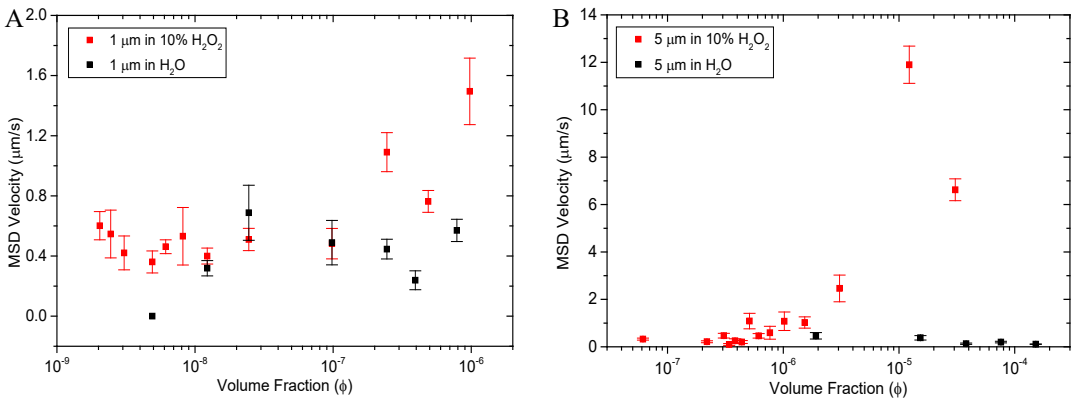

Figure 4-7 mean velocities calculated via MSD (0.5s fitting) of chemically fully coated PS colloids (A) 1 µm (B) 5 µm at different particle concentrations in 10% H_2O_2 fuel and water for the duration of 30 seconds.

Comparison of the average distance that 1 µm and 5 µm particles travelled over 15 seconds in 10% H_2O_2 (shown in Figure 4-8), from the initial tracking point to the position at 15 seconds, shows that the 1 µm micromotors travelled similar average distances (~5 µm) at all concentrations up to a volume fraction of $\varphi 1 = 9.81 \times 10^{-8}$ (1.87×10^5 particles/ml), but above this the distance travelled increased markedly up to around 30 µm at $\varphi 1 = 9.76 \times 10^{-7}$ (1.86 x 106 particles/ml). 5 µm particle data (Figure 4-8 B) shows an increase, possibly stepwise, in distance travelled initially starting at a similar value of 5 µm then at volume fractions above $\varphi 5 = 5.11 \times 10^{-7}$ (7.80×10^3 particles/ml) 20 µm and finally at $\varphi 5 = 3.06 \times 10^{-5}$ (4.68×10^5 particles/ml) up to a distance of ~160 µm from the origin. In contrast, when in water the data for both the 1 µm and 5 µm colloids shows that the average distance travelled stays consistently around 5 µm over the complete range of volume fractions.

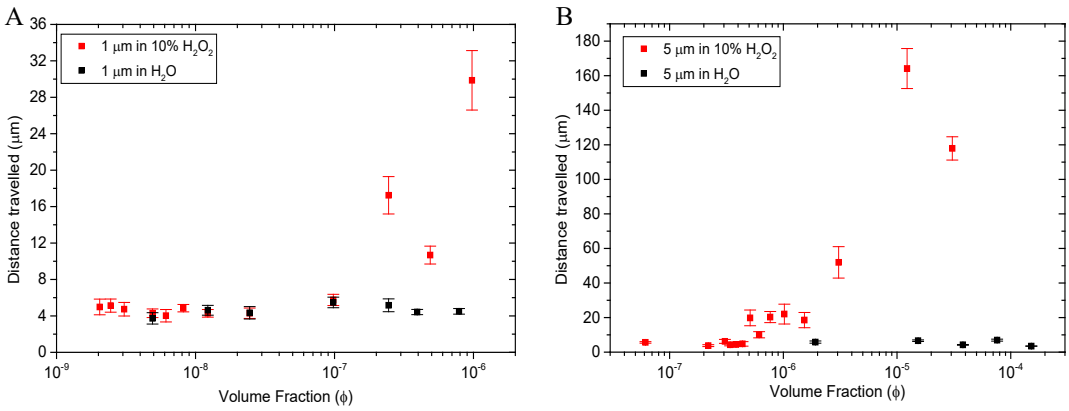

Figure 4-8 Mean distance travelled after 15 seconds of chemically fully coated PS colloids (A) 1 µm (B) 5 µm at different particle concentrations in 10% H_2O_2 fuel and water.

The mean squared Gyration data (shown in Figure 4-9) for 1 µm and 5 µm colloids agrees in general with the previously described data, and values of more than 100 μm^2 were only measured for 1 µm colloids at volume fractions above $\varphi_1 = 9.81 \times 10^{-8}$ (1.87×10^5 particles/ml). The data at lower volume fractions were seen to be similar for both water and hydrogen peroxide. 5 µm particle data showed that there was more variation present even for the particles measured in water but data showed a similar, possibly stepwise, increase with particle concentration as seen in the distance travelled data starting at volume fractions above $\varphi_5 = 4.38 \times 10^{-7}$ (6.69×10^3 particles/ml). As the mean squared Gyration increased rapidly for 5 µm particles a log scale was used to display the data more efficiently.

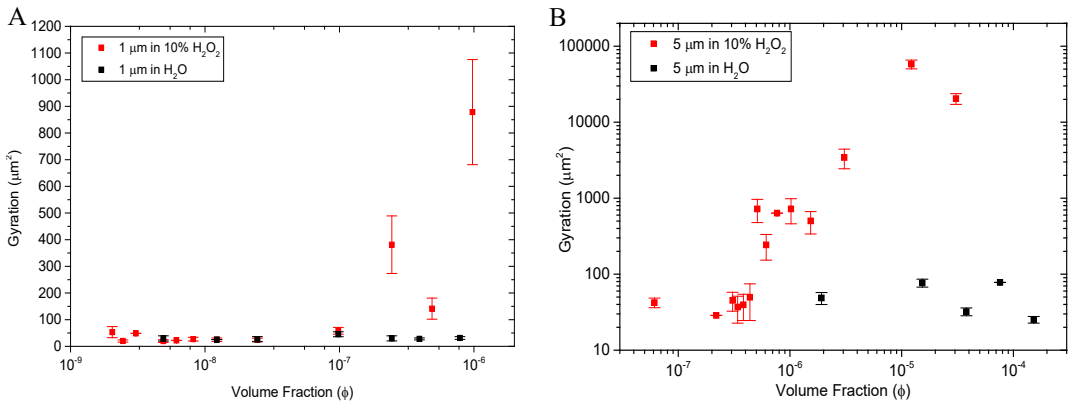

Figure 4-9 Mean squared Gyration of chemically fully coated PS colloids (A) 1 µm (B) 5 µm at different particle concentrations in 10% H_2O_2 fuel and water for the duration of 30 seconds.

Persistence length data (Figure 4-10) and fractal dimension (Figure 4-11) showed similar behaviour. Thus, the persistence length oscillated between 0.05 and 0.065 µm initially for 1 µm particles and jumped suddenly to 0.082 µm at $4.7x10^5$ particles/ml (Figure 4-10 A). It could be argued that in this case the increase in persistence length was not stepwise but increased gradually with increasing concentrations. For 5 µm micromotors the persistence length remained around 0.04 µm initially and then showed an increase at volume fractions above $\varphi_5 = 5.11 \times 10^{-7}$ (7.80×10^3 particles/ml) reaching a value of ~100 µm at $\varphi_5 = 3.06 \times 10^{-5}$ (4.68×10^5 particles/ml); the data pattern resembled that previously seen in the Gyration, velocity and distance data.

Water data for the 1 µm particles showed a slight increase in persistence length at very high volume fractions; however volume fraction had no influence on persistence length of the 5 um particles in water, which oscillated between 0.05 and 0.1 µm similar to the low particle concentration value in hydrogen peroxide.

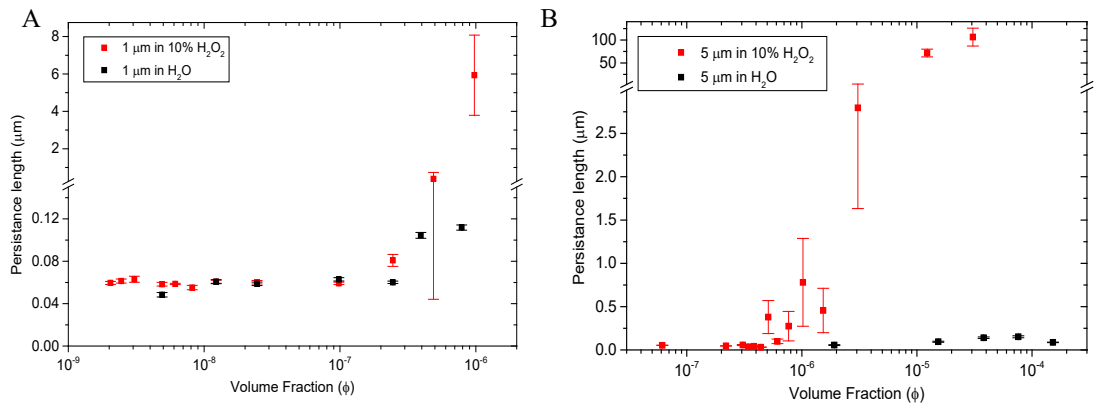

Figure 4-10 Mean persistence lengths of chemically fully coated PS colloids (A) 1 µm (B) 5 µm at different particle concentrations in 10% H_2O_2 fuel and water for the duration of 30 seconds.

Fractal dimension of 1 µm particles in H_2O_2 was relatively constant over a wide volume fraction range until it drastically decreased at $\varphi_1 = 2.45 \times 10^{-7}$ (4.68×10^5 particles/ml) (see Figure 4-11 A), which is in agreement with the previously described data. Water data over the whole range of volume fractions showed fractal dimension values of 1.4 to 1.6, which was the same as for 1 µm particles in hydrogen peroxide at the lower volume fractions. On the other hand, 5 µm colloids (Figure 4-11 B) showed initially a high variance in fractal dimension between 1.3 and 1.7, which was followed by a sharp decrease in fractal dimension, which would be expected for trajectories becoming more linear due to the colloids being carried along by convective flow effects. The variation at low volume fractions could be due to the rapid sedimentation of the 5 µm colloids and the problems of large amounts of oxygen being generated having a more dominant effect at stages when less convective flow effects are taking place.

The initial fractal dimension values for both 1 µm and 5 µm particles are near the Brownian motion values measured for these colloids at around 1.4 to 1.7. At the highest measured volume fractions in hydrogen peroxide fuel the fractal dimension drops down to 1.1 for 1 µm and 5 µm colloids, indicating highly linear pathways

analogous to strong convective flows. Fractal dimension data for 5 µm colloids measured in water seemed to show an interesting trend that at very high volume fractions above φ_{5w} = 3.80 x 10^{-5} (5.81 x 10^{5} particles/ml) the fractal dimension also decreases. This could be linked to the previous observations that the velocity decreases slightly at very high particle concentrations and the Brownian motion of these particles is hindered by their neighbouring particle population [163].

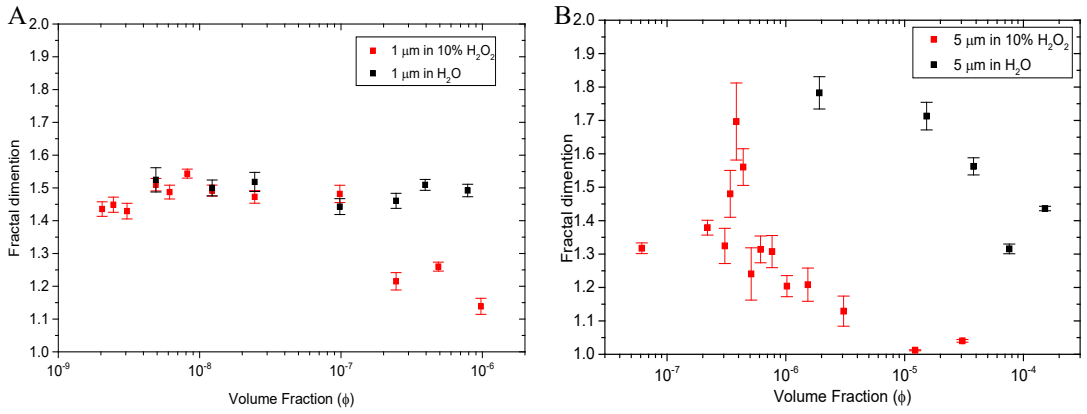

Figure 4-11 Fractal Dimension of chemically fully coated PS colloids (A) 1 µm (B) 5 µm at different particle concentrations in 10% H_2O_2 fuel and water for the duration of 30 seconds.

4.2.2.1. Influence of surface area of active platinum on micromotor flow effects

The reactivity of a micromotor is governed by the area of its reactive (platinum) surface [74, 147]; therefore it could be hypothesized that the amount of catalytically active surface area available in a certain fuel volume would cause similar pumping and flow-effects regardless of particle size. It is for this reason that the previously displayed data has now been plotted against the platinum surface area rather than the colloid concentration. In this way it is also possible to directly relate 1 µm and 5 µm colloids in the same dataset. It is however important to note that the reaction rate of 5 µm colloids is 2.7 times greater than that for 1 µm colloids

The mean velocities calculated via MSD showed a velocity increase at surface area concentrations above 2.5 mm^2/ml, moreover the 5 µm and 1 µm data matched well (See Figure 110 A). Water data showed relatively constant mean velocity of both 1 µm and 5 µm particles across all concentrations, with only minor fluctuations emphasizing the fact that fuel solution is needed for there to be an increase in velocity. In comparison volume fraction data that takes the total volume of the colloids rather than just the surface area into account shifts the data points of 1 µm colloids further down the scale suggesting that the volume fractions measured for 1 µm colloids might be more towards the edge of the velocity increase.

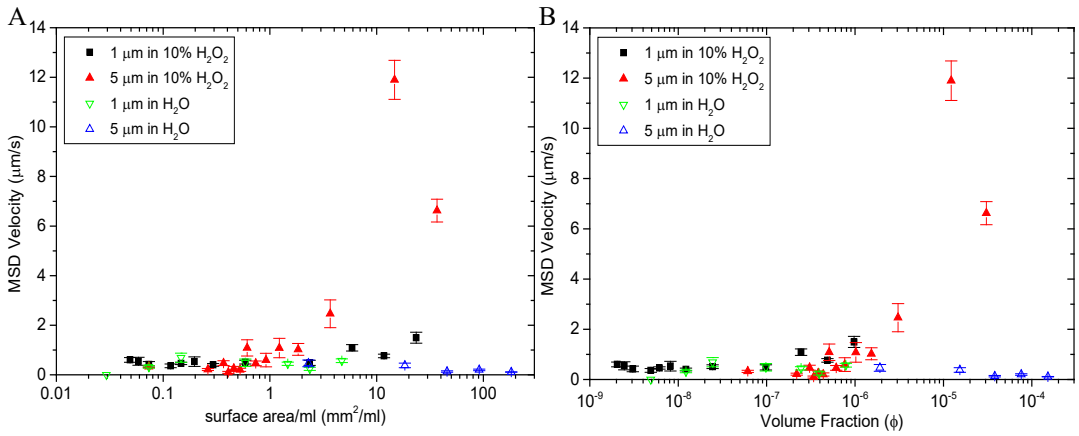

Figure 4-12 Influence of the Platinum Surface area per ml hydrogen peroxide fuel solution (10% w/v) on the mean velocity calculated via MSD (0.5s fitting) of 1 µm and 5 µm colloids.

Comparison of the average distance travelled from the initial position to the position at 15 seconds for the particles (see Figure 4-13 A) shows close agreement for the 1 µm and 5 µm particles for all values up to 10 mm^2/ml. There was a similar trend to that observed for mean velocity, indicating a strong relationship between the active surface area and the distance travelled which would be expected as the velocity data showed this similar increase. The data indicated that the increase might be of a stepwise nature where certain threshold values need to be reached in order for flow to occur (in this case at least ~2.3 mm^2 Pt surface area / ml) but it is

possible that experimental errors can be responsible for this and in fact the increase is more gradual. Volume fraction comparison data shown in Figure 4-13 B illustrates that the 1 µm data might need to be shifted down slightly and in this case it makes the discrepancies between 1 and 5 µm colloids vanish.

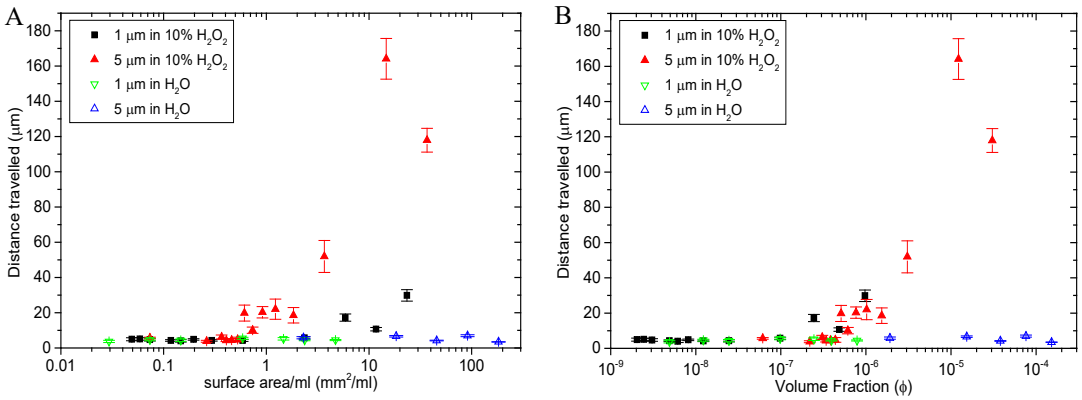

Figure 4-13 Influence of the (A) Platinum Surface area per ml hydrogen peroxide fuel solution (10% w/v) and Volume Fraction (B) on the average distance travelled after 15 seconds of 1 µm and 5 µm colloids.

Mean squared Gyration data emphasises the convective flow effects and shows that above 2.3 mm^2 /ml flow effects occur, however the data does not clearly show a gradual increase but does show strong variation in the data, which could indicate that the flow effects are more random than controlled. Nevertheless it can still be argued that the mean squared Gyration values do increase at higher surface area concentration, which is in general agreement with all the previously described data. Mean squared Gyration also shows the strong difference between blank water data and the influence fuel solution has on the flow effects seen. Finally, comparing the 1 µm and 5 µm data it is evident that both datasets complement each other. Overlapping of data once again is more defined in the Volume fraction comparison rather than the surface area, however if we consider the slightly lower reaction rate for 1 µm colloids this will most likely account for this discrepancy.

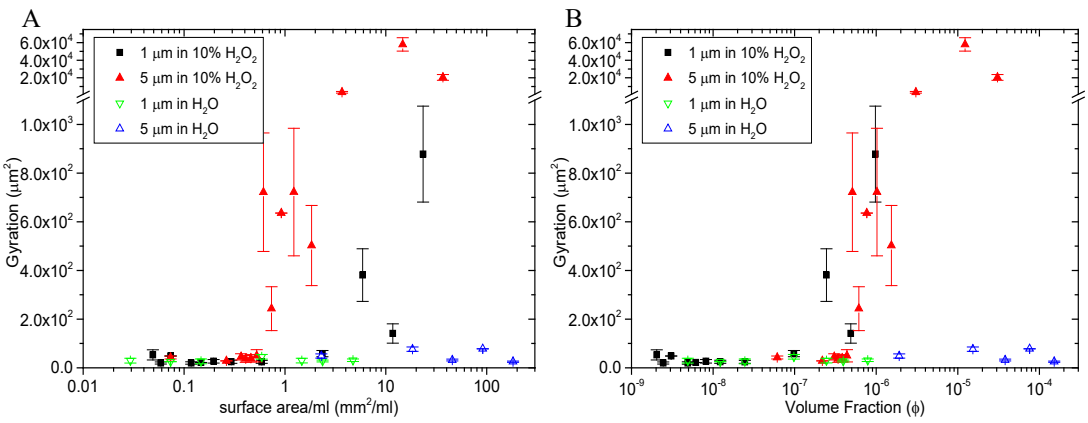

Figure 4-14 Influence of the Platinum Surface area per ml hydrogen peroxide fuel solution (10% w/v) on the mean squared radius of Gyration of 1 µm and 5 µm colloids for the duration of 30 seconds.

Similarly, it could be shown that, as the active platinum surface area was raised above ~2.3 mm^2/ml of fuel solution, there was an increase in persistence length (Figure 4-15) and a fall in fractal dimension (Figure 4-16). The data however also reveals that persistence length is dependent on the particle size as Brownian motion presents a larger influence on the 1 µm particle than on the 5 µm particles and therefore even though persistence length increased it was more gradual for the 1 µm particles than for the 5 µm particles. Comparison of persistence length for particles measured in water showed no increase or decrease in persistence length within error for both 1 µm and 5 µm particles. The persistence length was however seen to be slightly larger in general for 5 µm particles than 1 µm particles which would be due to the larger contribution of Brownian motion on these smaller particles in addition to the lower reactivity of 1 µm colloids. Volume fraction comparison of 1 and 5 µm colloids overlaps here perfectly (Figure 4-16 B).

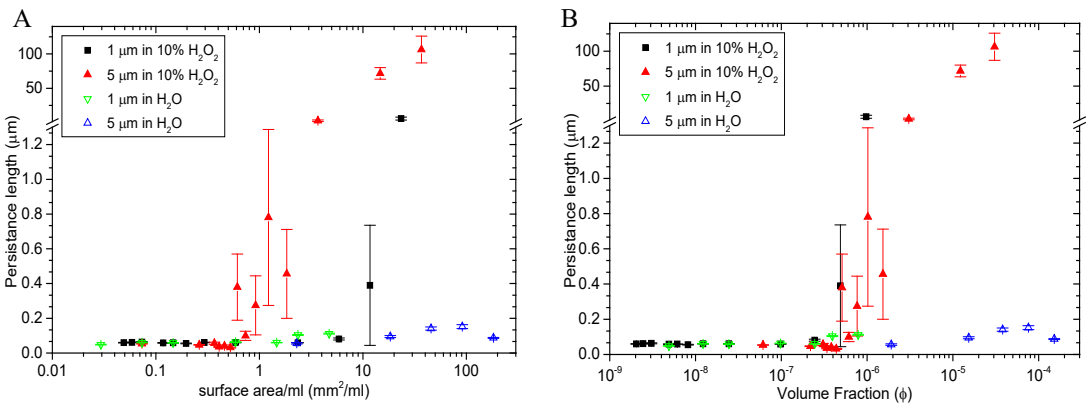

Figure 4-15 Influence of the Platinum Surface area per ml hydrogen peroxide fuel solution (10% w/v) on the average persistence length of 1 µm and 5 µm colloids for the duration of 30 seconds.

There seems to be a strong relation between fractal dimension and platinum surface area (see Figure 4-16 A), such that increasing active platinum surface area causes a gradual decrease in fractal dimension. However, there is also a decrease in fractal dimension at very high particle concentrations in water, perhaps due to the reasons suggested earlier. Fractal dimension data indicates that near to the threshold region of 2.3 mm^2 / ml the data variability is at its strongest. This indicates that the system is possibly switching between flow effects and no major flow effects. Once again here the volume fraction comparison data shows better overlapping of data points for 1 and 5 µm colloids (Figure 4-16 B).

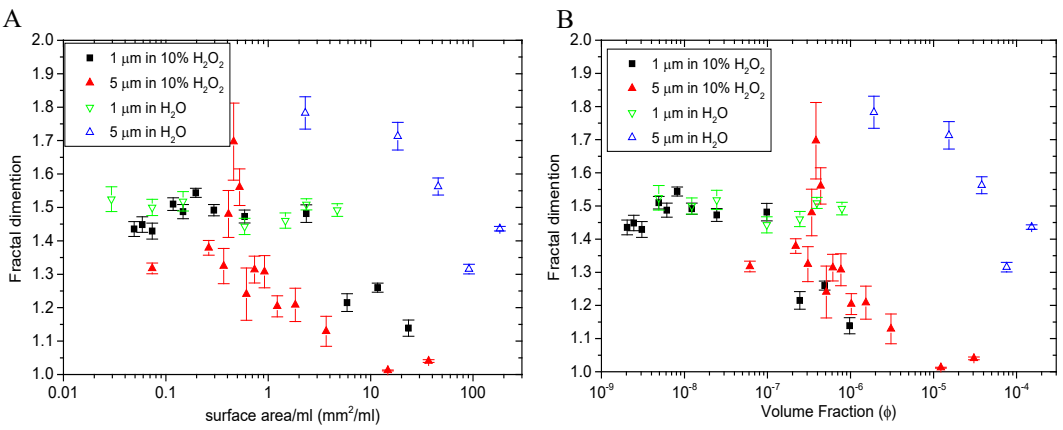

Figure 4-16 Influence of the (A) Platinum Surface area per ml hydrogen peroxide fuel solution (10% w/v) and (B) Volume Fraction on the average fractal dimension of 1 µm and 5 µm colloids for the duration of 30 seconds.

Finally it is important that although the comparison volume fraction data shown in this section does display a better overlapping of data for 1 and 5 µm particles this does not take the surface area and reactivity into account. Therefore to take this into account, the MSD fitted velocity data (previously presented in Figure 4-7) were normalised for reaction rate differences between 1 and 5 µm colloids by multiplying the hydrogen peroxide velocity data for 1 µm colloids by 2.7 (the difference in reactivity). It could then clearly be seen that the data shifts in favour of the 1 µm colloids and thus probably gives a more accurate representation of the real experimental data, see Figure 4-17. This comparison shows that it is important to also take the reactivity together with the colloid size and active surface area into account when comparing different sized colloids.

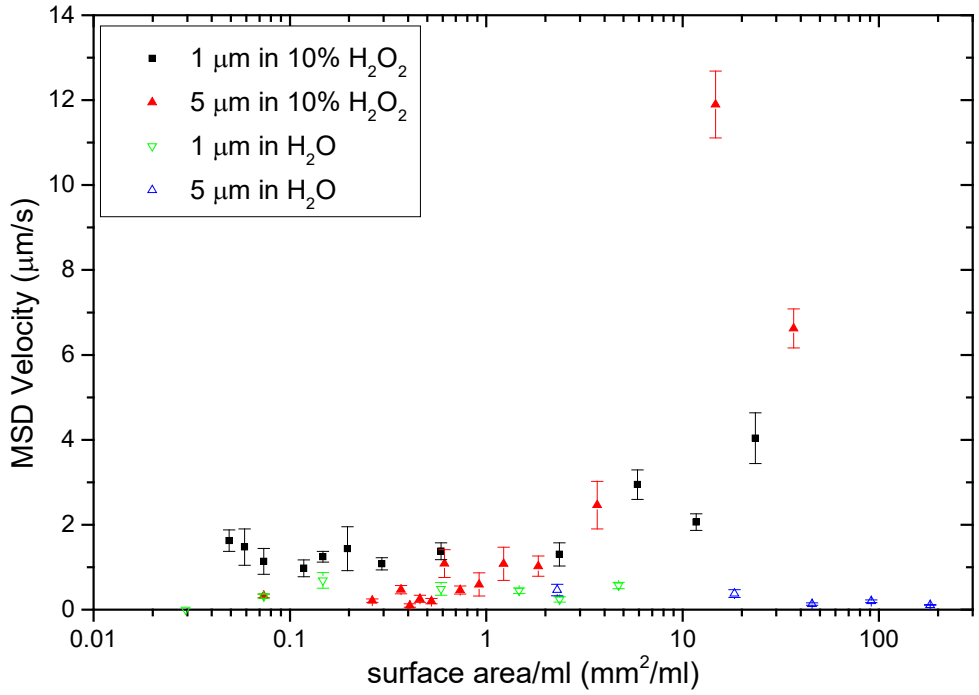

Figure 4-17 Influence of the Platinum Surface area per ml hydrogen peroxide fuel solution (10% w/v) on the mean velocity calculated via MSD (0.5s fitting) normalised for reaction rate difference of 1 µm to 5 µm colloids, data for 1 µm colloids has been multiplied by 2.7.

4.2.3. Conclusions

The experimental data shows that there seems to be a relationship between the colloidal volume fraction of chemically active particles and their reactivity generating local concentration gradients and thus non-equilibrium conditions in the solutions, which induce pumping / flow effects that cause the colloids to drift along with the surrounding bulk solution. The increase in these drift and flow motions can be best distinguished by looking at the persistence length, fractal dimension and mean squared gyration of the particles because an enhanced drifting motion causes the particles to increase their persistence length due to pathways becoming more linear and the random walk due to the Brownian motion of the particles becoming less dominant. In a similar way the fractal dimension of these particles is reduced and the mean squared radius of gyration is increased. Another analytical method

which gives reliable results is the measurement how far the particles have travelled in a given timeframe (in the case here after 15 seconds). Velocity data calculated via MSD does in general agree to the other data sets but effects are not as strongly represented and variation can be sometimes larger.

It is however important to also look at the MSD curves for these colloids in order to be able to clearly distinguish between convective flows and self-motile propulsions as previously described in Dunderdale et al. [95]. The comparison of different sized particles by looking at the overall catalytically active surface area of these samples indicates strongly that the main flow-effect is caused by how much catalytically active surface area there is within a certain volume. However the smaller the colloidal particles are, the more their drift motion is also influenced by a growing contribution of Brownian motion. This is most noticeable when looking at the persistence lengths and fractal dimension values for these particles. In particular the surface area data normalised for the differences in reaction rate between 1 and 5 μm colloids makes it clear the reactivity of the surface area is key to establishing the correct volume fractions dependent on the particle size. Using surface area together with reaction rate seems to be by far the best way to compare different size particles to each other.

This experiment gives a good indication at which volume fractions it is advisable to measure Janus particles undergoing enhanced motion to ensure that no collective behaviour influences their autonomous motion and increases false velocity readings. In the present study the data gathered indicate that samples should have a surface area smaller than 2.3 mm^2/ml of fuel solution (assuming the fuel is 10% H_2O_2 and the reaction rate is similar to that of these colloids).

At low volume fractions, the behaviour of the symmetrical catalytically active colloids considered here resembles pure Brownian motion, with a MSD that scales linearly with time, within the limits of the experimental resolution. It was not possible to discern the previously predicted model of anomalous diffusion of symmetrically active colloids in this scenario, probably due to the very fast timescale over which this effect would be observed for the relatively small particle sizes considered here [160].

4.2.4. Future work

It might be very useful to repeat this experiment with different volume fractions of Janus particles (1 and 5 um size) to determine how much the swimming behaviour of these particles affects the pumping and flow effects caused by high fractions and how this is related to the platinum surface area per ml. Due to time constraints it was not done here.

Additionally, it would also be interesting to see how different amounts of platinum coating (which affects the overall platinum reactivity) affect the flow effects at different concentrations when the reactivity is different per surface area unit. As the results obtained here clearly indicate that reactivity in particular plays a vital role in fully understanding these effects.

As a further point, we have shown that in order to look for anomalous diffusion phenomena for symmetrically active colloids it will be necessary to ensure volume fractions are controlled to avoid convection.

5. Controlling the directionality of bubble propulsive micromotors via catalyst distribution

5.1. Introduction

There are currently a range of preparation methods, catalytic distributions and reactions for achieving bubble-propelled motion. In particular, bubble-propulsion via complex geometries of rolled up tubes ('microjets'), usually with the catalyst present on the inside of the tubes, have received intensive research attention [26] (see Section 1.1.2).

This contrasts with phoretic particles (see Section 1.1.1 and Chapter 3) where oxygen bubbles from decomposed H_2O_2 nucleate randomly in the bulk solution and do not exert any obvious propulsive forces on the particles [9]. It has not previously been attempted to quantitatively describe the trajectory behaviour of bubble swimmers, but there are numerous examples, which were reported in Section 1.1.2 of the introduction, in which qualitative reports of trajectories have been made suggesting different behaviour for bubble propulsion swimmers than for phoretic swimmers. The examples presented previously for bubble-propelled micromotors (Section 1.1.2) illustrate that micromotors show huge promise for use for a variety of applications. If these devices are to be further developed and enhanced, it is clear that a better understanding of the relationship between the catalytic distribution and directionality of motion needs to be made. This chapter looks into possible ways of systematically characterising the different trajectory behaviours other than by the well-known MSD model for phoretic micromotors, which has allowed a better understanding of the relationship of the Janus catalytic distribution to the Brownian rotational diffusion coefficient [32, 147, 164] (Section 2.3.2).

As described extensively in Chapter 3, this asymmetrical relationship to promote the propulsion of phoretic devices has allowed MSD data to be fitted to the Brownian diffusion parameter and rotational and translational velocities [31, 95]. However, the coupling effect has been used in order to determine if particles are undergoing phoretic motion or bubble propulsion as the MSD plots deviate from the expected predictions if bubble propulsion is present [63, 165].

It is for this reason that various other methods are investigated in this chapter to see if or how they may possibly help to characterise trajectories in order to distinguish between the motions of various systems. One such method applied here is **persistence length** (see Chapter 2.3.4 for details), which has been used to understand stochastic motion of protein motor microtubules [131]. In addition, **mean squared gyration** and **fractal dimension** (see Chapter 2.3.3 for details) are also used to give further characterisation. These methods allow one to determine differences in the trajectories of the three geometries investigated in this chapter, namely symmetrical catalytic distribution, Janus and pore-type particles (as previously shown in section 1.5). Finally, a theoretical simplistic stochastic model [74] is described to help illustrate and emphasize the suspected reasons why bubble-propelled micromotors undergo such highly random behaviour. The theoretically produced trajectories from this model further illustrate the possibilities of the three characterisation methods investigated allowing direct comparison of the theoretical data with real experimental data.

5.2. Methods

5.2.1. Particle preparation - different amounts of exposed platinum surfaces

Monodispersed polystyrene colloids 30μm in diameter were uniformly coated with platinum via in-situ reduction of platinum salts. The coating obtained via this method was made up of 2-5nm nanoparticles (reported by Kisker) of platinum that were adhered to the surface of the colloids. This synthesis was performed by Kisker Biotech.

In order to mask part of the reactive surface of these particles, colloids were suspended in ethanol solution (99.8% Sigma-Aldrich) and spun cast (Laurell Technologies Spin coater) onto oxygen plasma pre-cleaned glass slides (Section 2.1.1). The spin coating process is explained in detail in Chapter 2 Section 2.1.2. Volume fractions and coating conditions were chosen to ensure that the colloids were separate and not touching (this was verified with optical microscopy), because this could cause shadowing effects during masking (in particular with regards to sputter coated samples). The colloid covered glass slides were then coated with chromium: (a) via electron-beam induced thermal evaporation to produce Janus particles due to the directionality of the evaporation (Section 2.1.3.2) or (b) with sputter coating via magnetrons (Section 2.1.3.3) at $5.7x10^{-3}$ mBar in argon atmosphere (Moorfield combination e-Beam/sputter coater), which coated the particles on more than just one hemisphere (but not fully due to shadowing of the substrate) because this method of evaporation is not directional, as represented schematically in Figure 5-1.

A layer of 300 nm of Cr (99.95% Sigma-Aldrich) was coated onto the particles using these methods, monitored using a QCM, in near proximity to the colloids.

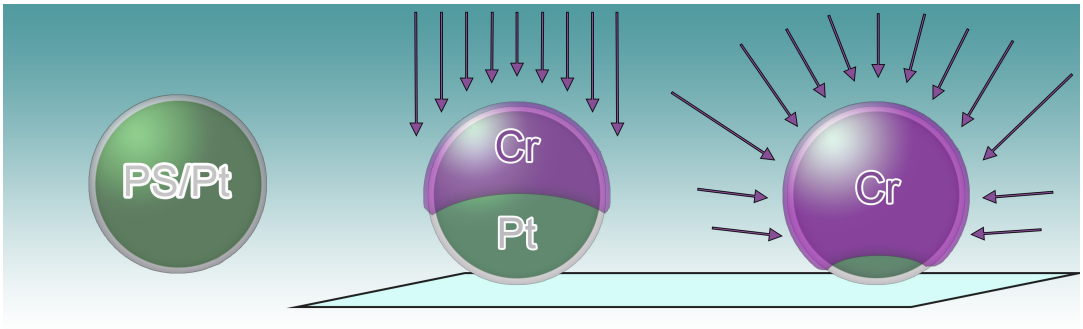

Figure 5-1 Schematic of polystyrene particles fully chemically coated with platinum (left) and then coated via E-beam (middle) or sputtering magnetron sputter coating (right) with chromium onto the surface to achieve Janus or particles with a small circular region of exposed platinum. Arrows indicate the direction of chromium coating and the blue surface indicates the glass substrate the colloids were attached to.

5.2.2. Energy-Dispersive X-Ray Spectroscopy

In order to characterise the e-beam and sputter chromium coated, platinum nanoparticle covered PS colloids from different angles; the colloids were detached from their original substrates using a dry piece of lens tissue by wiping this carefully over the glass slide and then subsequently wiping the colloid covered tissue carefully over an SEM carbon sticky pad. In this way high contrast images for the colloids versus the background were ensured and good secure attachment of the colloids to the substrate was achieved. Because the colloids are spheres these were then, in general, imaged under low vacuum conditions at ~50 Pa to ensure charging did not occur. EDS imaging was performed using a JEOL JSM-6010LA SEM system at an acceleration voltage of 15 to 18 KeV over a period of 40 minutes per scan (size 512x512 pixel). The imaging process is described in detail in the methods Chapter 2 Section 2.2.4.4-5.

5.2.3. Video Microscopy

The 30 μm diameter size of the particles considered here allowed them to be imaged in a petri dish with a diameter of 3 cm and ~1 cm volume depth that was illuminated with a powerful cold white (BridgeLUX) LED light source from a ~45° side angle. This angle ensured that the bubbles produced from the particles left a bright reflection in the imaging camera, which helped to achieve subsequent automatic position tracking. A long distance macro lens was directly mounted onto a PixeLink camera and 1000 frame long movies were taken at a frame rate of 25 frames per second. During the experiment it was ensured that the room temperature (20°C) was carefully monitored and air movement and vibrations were kept to a minimum to minimize surface flow effects. The experimental setup is shown in a photograph in Figure 5-2.

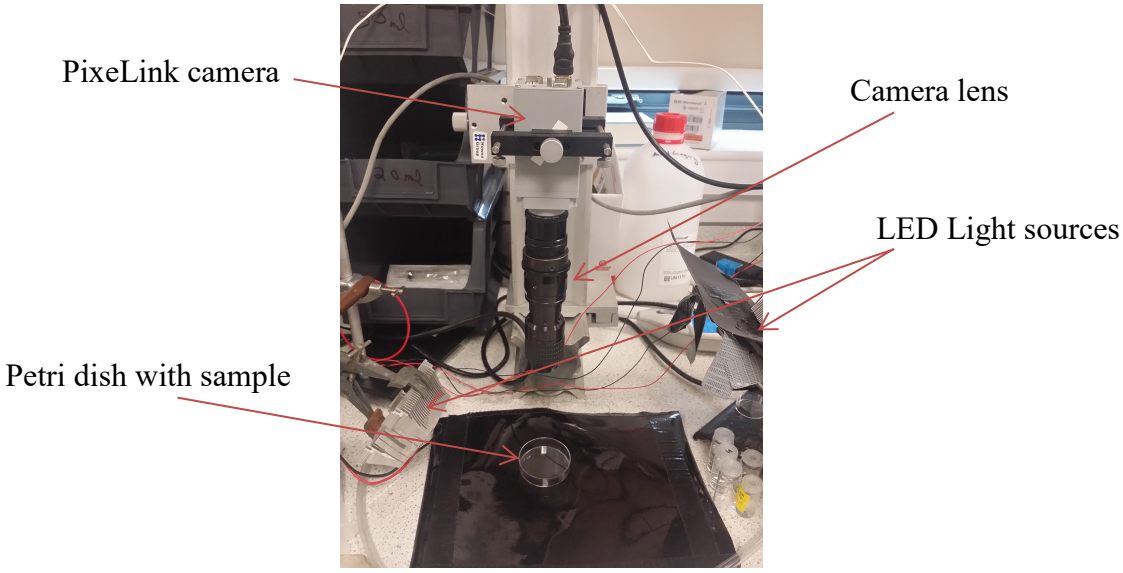

Figure 5-2 Photograph of the experimental imaging setup for bubble propelled 30 μm colloids. A PixeLink camera can be seen mounted on X-rail viewing down upon a petri dish containing the fuel and swimmers.

In order to be able to track the position of the particles during these videos it was necessary to run an image subtraction routine implemented using custom LabVIEW (National Instruments) image analysis algorithms, where successive images were

subtracted. This image processing technique allowed for bubbles still attached to the colloid (the latest bubbles) to be isolated from those already detached from the colloid and not contributing to propulsion anymore, which therefore allowed tracking of the colloid rather than floating bubbles. Some screenshots of the 'front panel' of the program and the code can be seen in the appendix 10 Section 10.3.

This bubble was then used to track the motion of the particles using the same custom built, multi particle tracking algorithm written in LabVIEW, (see Chapter 3), which generates 2D x, y trajectory data as a function of time, for each particle present in a given video sequence.

5.2.4. Trajectory Analysis

Before trajectory analysis, simple algorithms were applied to ensure tracks of particles were at least 15 seconds long and any falsely tracked particles were binned (e.g. not moving). Average instantaneous velocities were calculated for each trajectory passing these criteria by calculating the instantaneous velocity on a frame-by-frame basis and averaging this over the whole trajectory. The fractal dimension (as described in Chapter 2 Section 2.3.3), mean radius of gyration and persistence lengths (Section 2.3.4) of the trajectories were also calculated using custom algorithms. Prior to fractal dimension and persistence length determination, a Savitzky-Golay smoothing algorithm was performed in LabVIEW, with a setting of 5 side-points (k). This filter performs the piece-by-piece fitting of a polynomial to the data using least squares minimization, where the fitting window has a length of ($2k+1$). The Levenburg-Marqaudt function in LabVIEW was used to fit Equation {2.22} to the experimental data to find the persistence length, L_P, as described in Section 2.3.4.

Where the trajectory contained loops, the plot of $\langle \cos\theta \rangle$ displayed a sinusoidal pattern, consequently the fitting of Equation {2.22} was applied to the early exponential decay curve ($L \leq 1$ mm). Binning and averaging of the $\cos\theta$ data to find L_P relies on the trajectory chain segments having equal step sizes ΔL (see Figure 2-21). To ensure that this was the case the linear interpolation function in LabVIEW was applied to add an additional 20 points between the smoothed trajectory points. Then points ΔL apart were selected from the interpolated data to produce trajectories where the vectors were of equal length. ΔL was chosen to be sufficiently small so as to reproduce the smoothed trajectories, see Figure 5-12(B). Typically this would be $\Delta L = L_c/10000$, where L_c is the trajectory contour length [74]. All trajectory analysis was programmed in LabVIEW with the help of Dr. A. Campbell.

5.2.5. 2D Stochastic Model:

The algorithm to generate model bubble release trajectories was implemented using LabVIEW with the help of Dr. S. Ebbens. It is important to note that this algorithm only considers a 2D case, but this actually represents the way the experimental data was gathered, i.e. in 2D, as viewing of the particles was done from above down. The only variable in the algorithm that controls the resulting trajectories is the arc angle θ, which limits the range of angles over which translations can occur. Each trajectory step was generated as follows: firstly a LabVIEW in built random number generator was used to generate a new bubble release angle, ξ such that $-\theta/2 \leq \xi \leq \theta/2$. This angle was then added to the current colloidal orientation angle, φ (φ defines the orientation of the active portion of the colloid, and bisects the arc angle) to determine the angular position of the new bubble release event,

$\alpha = \phi + \xi$. A unit length translation orientated in the opposite direction to α was then applied to the current colloidal x, y coordinates (i.e. $x' = x - \Delta x$, where $\Delta x = \cos\alpha$; and $y' = y - \Delta y$, where $\Delta y = \sin\alpha$). Finally, the new orientation of the active patch was updated according to: $\phi' = \alpha$. This last stage re-orients the particles bubble-producing region to be aligned with the randomly chosen bubble release position and was used in the algorithm as a crude proxy for the torques that bubble detachment might have generated. This model has also been described in Gregory et al. [74]

5.3. Results and Discussion

5.3.1. Masking catalytic active platinum layer

All colloids were initially chemically coated with platinum nanoparticles and were then masked using chromium, which demonstrated a good inhibition of activity of the platinum surface. Initial hydrogen peroxide decomposition rate tests done on 20 nm of e-beam evaporated platinum on glass substrates showed that when this was then coated with a 5 nm chromium layer there was a H_2O_2 decomposition rate constant of $5.97 \cdot 10^8$ $s^{-1}\mu m^{-2}$ which was 150 times slower than the decomposition rate with the pure platinum layer (rate of $9.26 \cdot 10^{10}$ $s^{-1}\mu m^{-2}$).

In order to verify that the colloids had the right amount of inhibiting chromium layer, as represented schematically in Figure 5-1, the structures were verified using SEM and EDS to show the distributions of chromium and platinum on the polystyrene coated colloids (See Figure 5-3 and Figure 5-4).

In order to see particles in different orientations the particles were transferred from the glass substrate slides onto SEM carbon sticky pads via lens tissue (see Section

4.3.2). Figure 5-3 shows the three different types of particles that were later analysed in this experiment. It can be clearly seen in Figure 5-3(a) that the colloid was evenly coated with platinum nanoparticles over the entire sphere (unmasked), whereas in Figure 5-3 (b) only half of the particle was coated with chromium, with the amount of chromium tapering off towards the equator of the particle (masked). The red lines indicate the cut off regions. Figure 5-3 (c) and Figure 5-4 show the chromium coverage of four different particles after the sputter coating process. It can be clearly seen that the chromium coverage was much greater than for the Janus particles generated via E-beam coating.

Statistical analysis over several EDS images revealed that the mean circular pore diameter was 23 ± 2 μm, corresponding to 19 ± 5% exposed catalytic surface. This was represented by an arc angle of 68 ± 19^0 in the theoretical simple stochastic model described in Section (5.2.5).

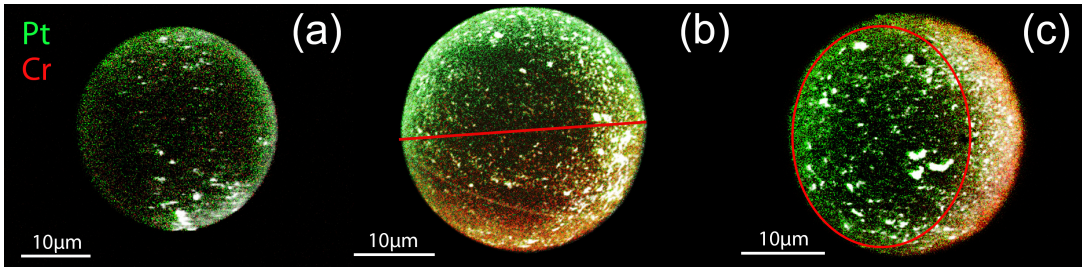

Figure 5-3 Overlaid Energy Dispersive X-ray Spectroscopy (EDS) images for Pt. peak intensity (Green: energy range 1.93-2.17 eV) and Cr peak intensity (Red: energy range 5.24-5.58 eV) distribution for typical platinum coated polystyrene colloids: (a) Unmasked (b) masked by Cr evaporation (c) masked by Cr sputter coating. Red line indicates approximate boundary between the catalytically active and masked regions.

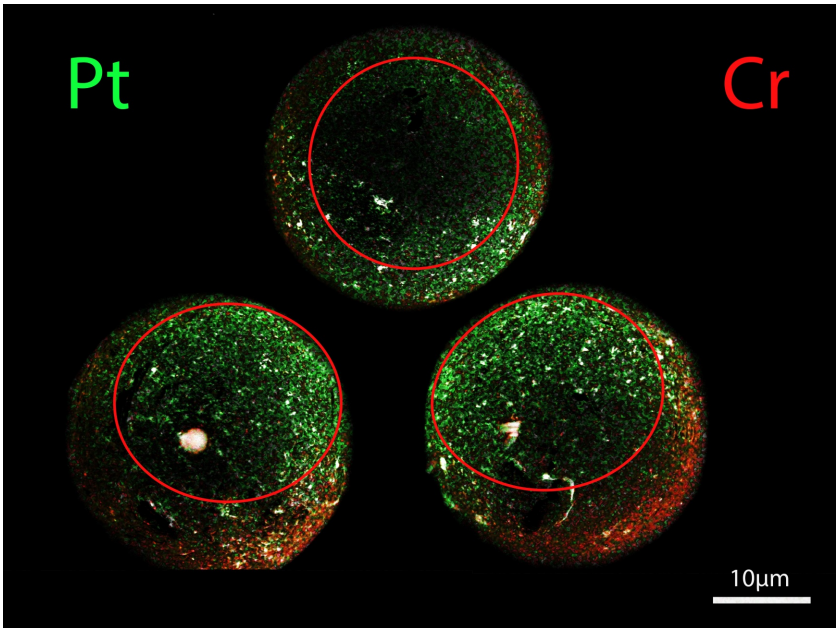

Figure 5-4 Additional Overlaid Energy Dispersive X-ray Spectroscopy (EDS) images for Pt peak intensity (Green: energy range 1.93-2.17 eV) and Cr peak intensity (Red: energy range 5.24-5.58 eV) distribution for differently oriented chromium sputter coated platinum coated polystyrene colloids.

5.3.2. Propulsion behaviour

5.3.2.1. Effects of fuel concentration on fully Platinum coated 30µm PS colloidal 'swimmers'

The effect of H_2O_2 fuel concentration on the 'swimming' behaviour of unmodified chemically coated platinum PS particles (fully active) was investigated next. The trajectories of 30 µm particles did not show any notable differences when placed in 1%, 2%, 3%, 5%, 7% or 10% H_2O_2 solutions, as shown in Figure 5-5. Mean instantaneous velocities ranged from 1.4-1.8 mm/s, with maximum propulsion velocities observed at 2% w/v fuel. Increasing the fuel concentration above 2% resulted in a gradual reduction in velocity as the concentration increased, as shown in Figure 5-6 (A). Reaction Rate experiments showed that the rate of H_2O_2 decomposition by platinum continued to increase in the range 2-10%. Therefore these results indicate that the bubble propulsion mechanism did not benefit from this increase in the rate of gas generation.

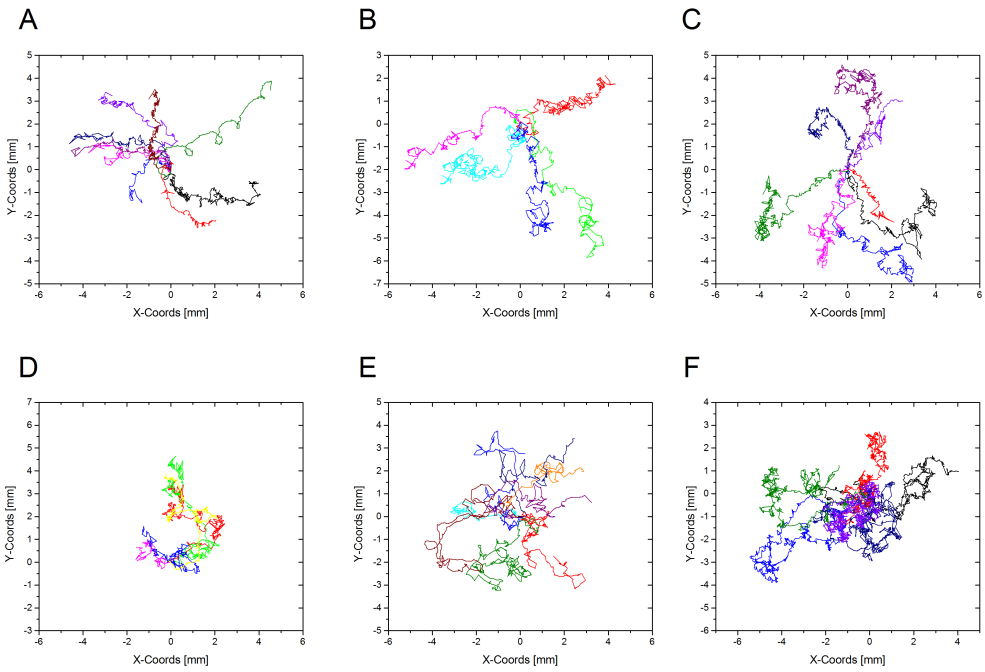

Figure 5-5 Trajectory plots of uncoated symmetrically active 30 µm particles in different hydrogen peroxide concentrations (A) 1%, (B) 2%, (C) 3%, (D) 5%, (E) 7% and (F) 10%.

Micromotors were also tested in 10% v/w H_2O_2 after the addition of 0.1M KNO_3 salt. It was observed that the addition of this high concentration of KNO_3 did not alter the instantaneous velocities of any of the three particles (symmetrical, Janus and pore) to any notable extent despite a reduction in reaction rate of around 70% of the initial value (see Chapter 3). This means that these micromotors show a strong salt tolerance.

Persistence length shown in Figure 5-6 (B) indicates that there may be a difference to the trajectories at higher H_2O_2 concentrations, where the trajectories might have been less persistent, but the data does not reveal this clearly. Mean squared gyration analysis (Figure 5-6 (C)) indicates that as the fuel concentration increased the mean squared gyrations fell gradually, but only very slightly, starting at 5.60 ± 0.56 mm^2 and decreasing to 3.42 ± 0.83 mm^2. There was one discrepant value: a very high value of 12.24 ± 1.92 mm^2 was observed at 3% w/v H_2O_2. The fractal dimension

analysis (Figure 5-6 (D)) of this data indicates a tendency for particles to have a higher fractal dimension at higher H_2O_2 concentrations. This, together with the persistence length and mean squared gyration data could mean that trajectories underwent a very slightly more random trajectory pattern at higher fuel concentrations, perhaps because bubbles were produced more frequently at random locations.

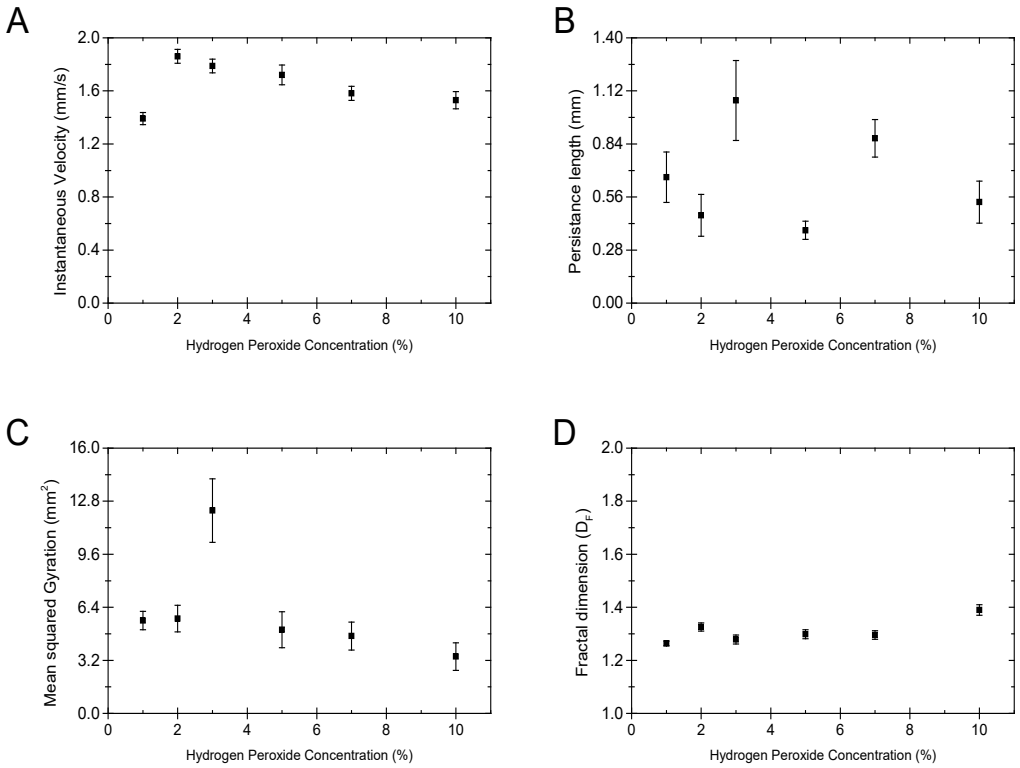

Figure 5-6 (A) Averaged mean instantanous velocites of symmetrically active 30 µm PS particles coated with Platinum; (B) Persistance length dependant on fuel concentration; (C) Mean Squared Gyration dependant on fuel concentration; (D) Fractal dimension dependant on fuel concentration

Looking at the mean distance travelled over a time interval of 15 seconds as shown in Figure 5-7 (A) (essentially drawing a straight line from the start to the end point) there is also an indication that at fuel concentrations of 3% up to 10% the trajectories travel a smaller distance, which would agree with the fractal dimension and persistence length data indicating that the trajectory paths become more chaotic.

As each particle has its own path length (contour length (L_C)) it becomes apparent that data might be skewed due to changes in path length when averaging the data of multiple trajectories, such that the varying path lengths are not taken into account when analysing the individual persistence length for each trajectory. Therefore, in order to normalize the data for L_C the persistence length was divided by the path length as shown in Figure 5-7 (B). Normalized persistence length data Figure 5-7 (B) indicates that there might not be any clear relationship between normalised persistence length and fuel concentration between 1% and 10%.

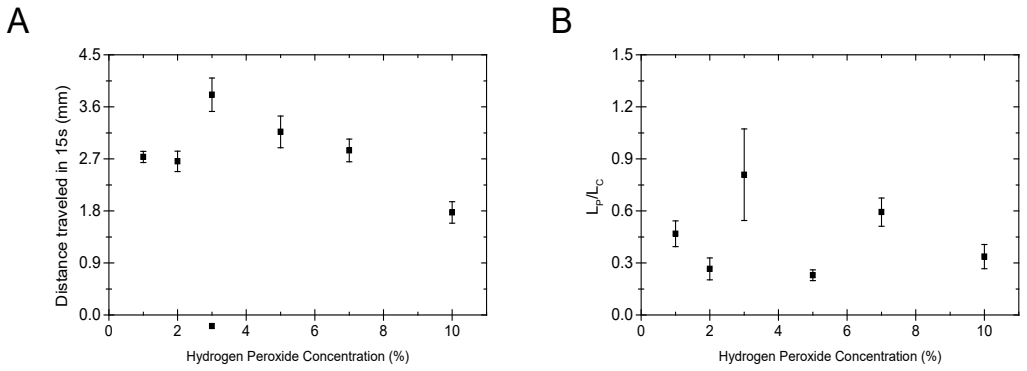

Figure 5-7 Averaged mean instantanous velocites of symmetrically active 30 µm PS particles coated with Platinum; (B) Influence of fuel concentration on Persistance length; (C) Influence of fuel concentration on mean squared gyration; (D) Influence of fuel concentration on Fractal dimension.

These results therefore indicate that 30 µm particles seemed to average around the same instantaneous velocities in concentrations of hydrogen peroxide between 1% and 10% but their trajectories seemed to undergo less persistent paths with increasing fuel concentrations. There are indications that particles might have travelled the furthest distance at 3% H_2O_2 and slightly smaller distances at increasing fuel concentrations in the region of 3% to 10%. However at concentrations of 1% and 2 % the distance travelled is similar to the value for 7% fuel concentration which roughly matches the trend for the instantaneous velocities. This indicates that at higher fuel concentrations the propulsion direction changed

more frequently thus causing the overall trajectories to become slightly more diffusive.

The maximum velocity observed here can be compared to that of similarly sized titanium masked (water driven (Ga/Al)) swimmers, which were reported by Wang et al. [55] to have velocities of 3 mm/s. A key difference to water driven (Ga/Al)) micromotors however was that the micromotors reported here do not need any additional surfactant added into the fuel solutions, whereas the Ga/Al micromotors needed Triton X 100 added to the bulk solution to enable motion. Elsewhere, velocities for micro swimming devices such as nanotube swimmers were reported to be 12 μm/s to 500 μm/s [16, 52, 67-69, 72, 73, 166-168], while peak velocities for these type of microswimmers were reported by Wang at al. to be 980 μm/s for PANI/Pt microjets [71] and 1410 μm/s for PEDOT/Pt microjets [70]. For all these micromotors however the addition of surfactant was necessary to induce motion.

5.3.2.2. Influence of masking the micromotors

All three catalytically active colloid samples, i.e. symmetric, Janus and pore particles, were dispersed in Petri dishes containing 10% w/v H_2O_2 and their motion was monitored and recorded using video microscopy. It had to be ensured that there was no air movement and the temperature of the room was kept constant (22°C). Once the samples were placed into the fuel solution, bubbles could be seen to issue from the colloids surfaces, and cause them to undergo enhanced motion. Symmetrical (fully active) particles ‘swam’ both in the bulk solution and at the air / liquid interface. The previously described image analysis via LabVIEW Vision modules was used to extract x, y coordinates for individual colloids of each type as

a function of time. From this data it was possible to analyse the trajectories of these particles by the previously described analytical techniques.

Figure 5-8 shows typical instantaneous velocities as a function of time for the three different active colloid structures in 10% w/v hydrogen peroxide solutions. From this it can be clearly seen that the motion proceeds via a stop-start mechanism, reflecting the bubble growth and burst process occurring at the catalytically active surfaces. This mechanism is described in detail in Manjare et.al. [34].

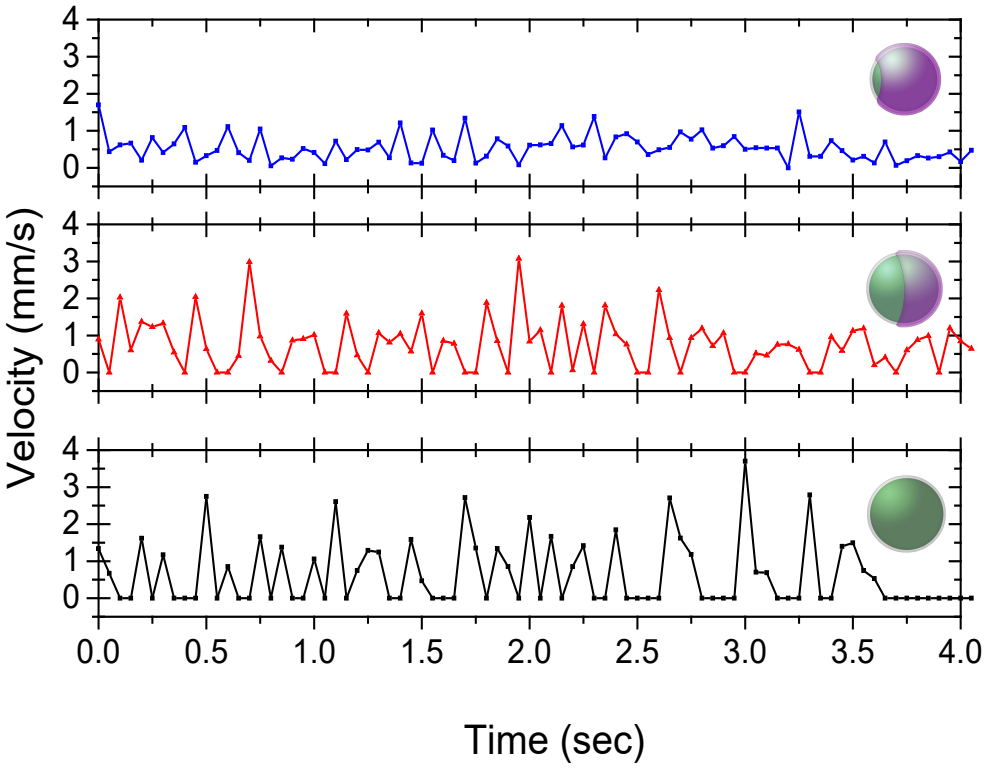

Figure 5-8 Example instantaneous velocities (v) against time for typical pore, Janus and symmetrical activity catalytic colloids.

When qualitatively comparing the instantaneous velocities of the three different types of particles shown in Figure 5-8, there is an indication that particles with a pore activity undergo slightly more smoothed and less extreme peak and stop

motion than Janus or symmetrical particles. For the Janus particles it seems that there is less stopping motion than for the symmetrical particles (Figure 5-8).

Figure 5-9 shows a comparison of the mean instantaneous velocities dependent on the particle structure. Instantaneous velocities of the unmodified particles and Janus particles are very similar at 1.56 ± 0.06 mm/s and 1.33 ± 0.08 mm/s however the mean velocity for pore particles was slower, averaging 0.42 ± 0.03 mm/s. The small reduction in velocity of Janus particles compared to the symmetrical particles indicates that the generation of bubbles is converted into motion more efficiently by Janus particles, suggesting that control of the catalyst distribution is a desirable feature. The pore shaped activity colloids exhibited a quarter of the velocity of symmetrical particles, which is most likely explained by the reduction in surface activity, since on average the pore particles were shown to have total surface activity of 19% of the colloid's surface. Example movies can be found on the Supportive CD for symmetrical (S3.1), Janus (S3.2) and pore (S3.3).

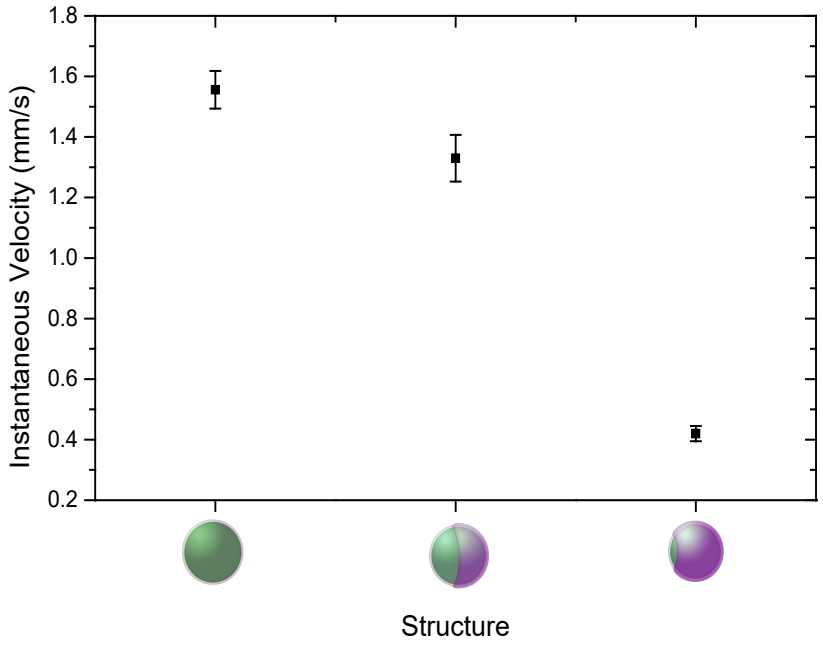

Figure 5-9 Mean instantaneous velocity as function of structure (10% w/v H_2O_2; data from 33 symmetrical, 63 Janus, and 246 pore particles), Supportive CD for movies for symmetrical (S3.1), Janus (S3.2) and pore (S3.3).

Observations of unmasked symmetrical active particles showed that they switched back and forth between the bulk and air / water interface, whereas a much higher proportion of masked particles could be seen swimming at the air / water interface, with particles only occasionally moving into the bulk solution. Janus and pore particles both had particles moving in the bulk solution and at the interface but as the overall activity was qualitatively less it seemed that more particles appeared to be locked in at the air / liquid interface and did not break free into the bulk solution.

Previous studies have also reported changes in vertical height within a fluid volume for bubble generating devices, which have been explained by buoyancy changes due to surface attached bubbles growing [56, 169].

Assuming gravity is negligible it was possible to calculate the particle detachment energy required for these particles to leave the air / liquid interface (γ_{aw}): for a particle radius of a = 15 μm calculated with equation {5.1} gives a detachment energy of $E = 1.3 \cdot 10^{10}\, kT$, where θ represents the contact angle. Considering this factor only, the particles should not be able to detach from the interface.

$$E = \pi \cdot a^2 \cdot \gamma_{aw} \cdot \left(1 - \cos\theta\right)^2 \qquad \{5.1\}$$

In reality however it appears that a combination of contributions from gravity, meniscus pinning effects and the generation of the bubbles, which may cause additional disturbance to the surface tension in close proximity of the particles, can cause detachment of the particles from the air / liquid interface into the bulk solution.

It has been previously reported that symmetrically active devices undergoing bubble propulsion were seen to rise to the air / water interface because of increased

buoyancy resulting from bubbles attached to the particles surface; these particles would then either stay at the interface or sink back into the bulk solution after the attached bubbles burst or were released [169]. Taking this together with the present results it can be assumed that introducing asymmetry and decreasing the overall activity of the particles enhanced the residence time at the air / water interface. The mechanism for this is however unknown.

After taking into account the velocities of the differently coated particles it was possible to compare the resulting trajectories of symmetrical, Janus and pore particles and an attempt was made to analyse if there were any differences with regards to how the directionality of these particles correlated to the catalyst distribution. In Figure 5-10 example trajectories of the three different geometries are displayed (Left to right: symmetrical, Janus, pore activity). Comparing these trajectories visually it is noticeable that the three different geometries showed distinctively different trajectories. There are some example movies of the three different geometries in the supporting information CD (Movies S5.1-3).

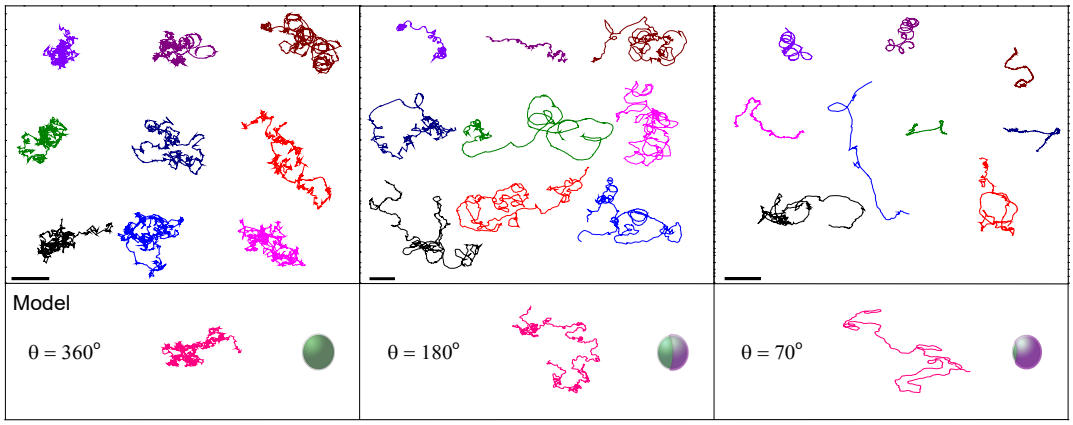

Figure 5-10 Example trajectories (40 second duration) for typical bubble propulsive colloids recorded in 10 % w/v H_2O_2 (Left to Right: symmetrical activity, Janus activity and pore activity). Lower box: trajectories produced using a simple 2D model (See Figure 5-11) with arc angle chosen to match the geometry of the colloids as determined by EDS (See Figure 5-3, Figure 5-4), scale bars 2 mm [74].

One surprizing feature of these bubble-propelled swimmers was that for all three geometries there appeared to be some particles that underwent rotational behaviour despite not having any obvious asymmetry which is known to generate strongly rotating particles as shown in Archer et al. [90]. The masking of the particles did not seem to change the frequency of this phenomenon. A possible reason may be that certain positions on the catalytically active surface of some of the particles may be more favourable than others for the release of bubbles, e.g. an area with a slightly larger platinum nanoparticle.

Even though symmetrically active particles were shown to have the highest mean instantaneous velocities, the resulting trajectories showed frequent abrupt changes in direction with the result that the overall displacement of the particles over time was smaller than that of asymmetrically active particles.

Janus particles showed fewer abrupt changes which gave rise to smoother trajectories along with larger displacements from the origin. Several trajectories showed frequent sections with paths as long as 2 mm without directional changes. In a similar way pore particles exhibited these same but enhanced features so that the increased trajectory directionality showed sections of ~5mm before a change in direction was seen. It is important to note that for particles that underwent spiral trajectories this was not the case. Similarly to Janus particles, pore particles moved further away from the origin (in the same amount of time) even though the velocity of the particles was significantly slower.

5.3.2.3. Simple Stochastic Bubble Release model

It was attempted to produce a simple theoretical simulation model which would demonstrate the random behaviour displayed by the differently active spherical

bubble-propelled micromotors in the experiments. Figure 5-11 shows an illustration of the basic simplistic stochastic 2D model of motion due to bubble propulsion on a symmetrically coated particle (Figure 5-11a) and on a masked particle with an exposed catalytically active pore of angle θ (Figure 5-11b). This model was programmed into LabVIEW as described in Section 5.2.5 and was run with varying arc angles (θ) representing the varying catalytic activities on the particles.

As shown in Figure 5-11 this model builds on the basis that bubble release occurs at a random location on the active surface of the particle. The model assumes that the active surface is totally homogenous and that only one bubble is formed at a time, and at a regular rate. The model does not take into account that velocity changes due to diminished reactivity, but this means that data gained from the model does not need to be corrected for this velocity change unlike with the real experimental data. The model causes the particles to move in the opposite direction to where the bubble was produced.

As the catalytic arc angle available for bubble generation is reduced, the possible directions of motion available to a device starting with an arbitrary orientation are consequently also reduced, Figure 5-11b. However, this alone does not allow for any re-orientation with time of the partially catalytically active model bubble swimmers. It is highly probable that in the case of a bubble growing and being released from the surface of a particle near the edge of the arc, the released bubble will not only thrust the particle in the opposite direction but also exert a torque onto the particle causing it to rotate. Based on this the model attempts to estimate the torque exerted by the bubble by simply realigning the active pore centre to the previous bubble release location. In the case of symmetrical particles this realignment has no effect; however, for devices with a partial arc, re-orientation

from an initial arbitrary starting alignment now occurs if stochastic bubble release occurs away from the mid-point of the arc, Figure 5-11b.

A typical example trajectory for each type of platinum coverage (symmetrical, Janus and pore) is shown below the real trajectories in Figure 5-10, where the arc angle chosen for the pore particles was calculated using the EDS analysis given by the EDS characterization of the particles. Qualitatively the trajectories showed similar behaviour to those of the experimental data. Therefore it is evident that restricting the available catalytic surface area can increase directionality of spherical bubble swimmers.

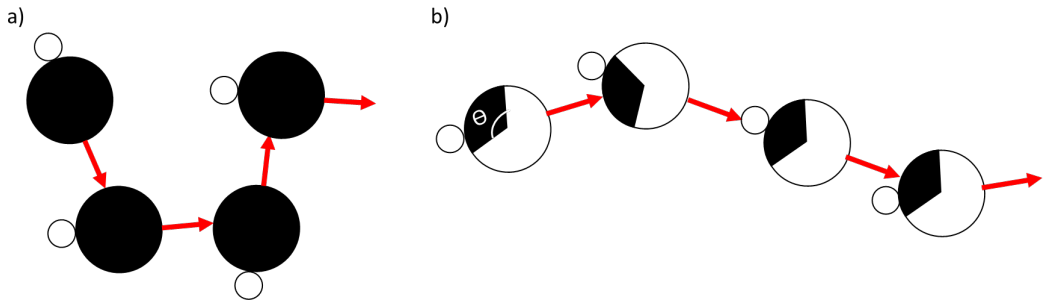

Figure 5-11: Stochastic model for bubble release: a) symmetrically coated particle – bubble release occurs at a random position on the perimeter of the particle (indicated by the smaller open circle), resulting in translation away from the detachment point b) asymmetrical particle with patch defined by arc angle, Θ: motion proceeds as in a), but bubble release also produces a torque which is modelled by aligning the catalytic patch with the previous bubble release position. This has the effect of producing increased orientation changes for bubble release at the edges of the arc, and no change for bubble release that is centred within the catalytic arc perimeter, taken from [74].

It must be noted that the microscopic observations made are insufficiently clear to reveal the actual distribution of bubble release positions, and so I based this model on the assumption of stochastic bubble distribution over the catalytically active section. If instead, bubble release showed a preference for certain positions at the active surface then an increased persistence of motion would correspondingly be produced.

5.3.2.4. Quantitative analysis for bubble swimmer trajectories

The described trajectories show how masking catalytic reactivity of spherical bubble-propelled micromotors does indeed change propulsion trajectories but analysis of these trajectories is more difficult than e.g. for diffusiophoretic swimmers as no defined methods have been established for the characterisation of bubble-propelled trajectories. Therefore an attempt was made to apply various different path analysis methods which have been used for other complex trajectory applications such as sperm trajectories [123] and protein motor transport [131]. Fractal dimension, radius of gyration and persistence length were applied to trajectory data to allow for better characterisation. All methods were programmed into LabVIEW and trajectory data was imported and analysed after being binned for data that did not leave trajectories long enough for proper analysis.

Fractal dimension D_f is a useful method to quantify a large variety of systems which include diffusing, aggregating particles and clusters [125], bacterial colonies [127] particle gels [126] and bio-polymer gels [128]. The basic concepts of fractal dimension are described in the methods Chapter 2 Section 2.3.3. Thus calculating the fractal dimension of the bubble swimmer trajectories gives a number which allows the different trajectories to be quantified statistically. If the projected 2D trajectories of these bubble 'swimmers' display a fractal dimension of 2 the particle is undergoing simple Brownian motion, whereas for a straight line trajectory the fractal dimension would be 1.

However, simple application of the fractal dimension method (Section 2.3.3) to the experimental data was not directly possible, as extracted trajectories contained random fluctuations due to the tracking of bubbles formed on the swimmers rather than the swimmer particles directly (tracking method described in Section 5.2.3).

By simple smoothing of the data it was possible to remove these fluctuations, which would have otherwise inflated D_f, and the main trajectory of the particle was then followed. The smoothing was done in LabVIEW using a Savitzky-Golay smoothing algorithm, which uses a piece-by-piece fitting of a polynomial to the data via least squares minimization. An example trajectory before (A) and after (B) smoothing is shown in Figure 5-12.

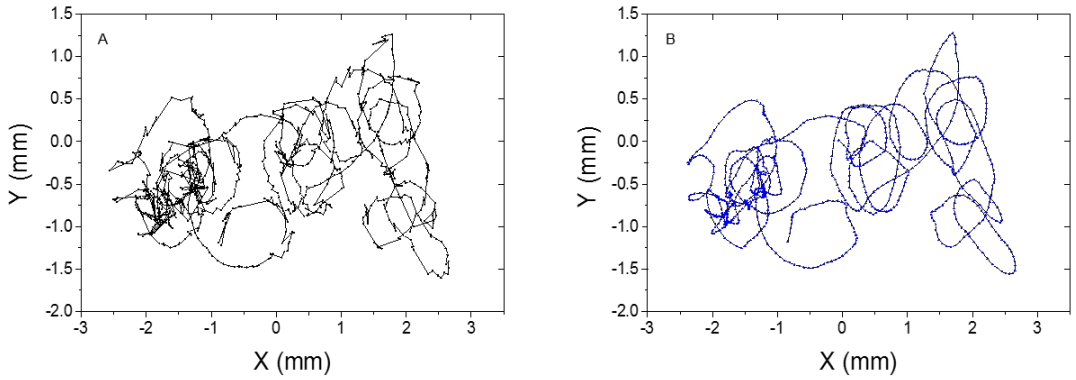

Figure 5-12: Example of trajectory smoothing performed to allow fractal analysis: (A) Original trajectory. (B) Trajectory smoothed using Savitzky-Golay smoothing filter.

Figure 5-13 (A) shows the averaged calculated fractal dimensions for the three geometries. As can be clearly seen, when the catalytic active area is decreased the fractal dimension goes gradually down from initially 1.40 (symmetrical) to 1.32 for Janus particles and 1.19 for pore particles. These results show that modifying the catalytically active area on a spherical colloid can indeed alter the trajectory in such a way as to generate trajectory paths which are less recursive. This is beneficial for transport applications and generates devices that are more effective. The biggest advantage of using fractal analysis is that the quantitative output is dimensionless and therefore a variety of different systems produced at different time and length scales can be directly compared. For example, the fractal dimension observed for the Janus swimmers in this study is very similar to the fractal dimension of 1.3 reported for self-motile sperm [123].

The other two analytical methods, mean squared gyration and persistence length, both report length scales and therefore without normalisation take both propulsion velocity and directionality into account.

Mean squared radius of gyration, as described in Section 2.3.5, R_g^2 was calculated here by using equation{2.23}. In the case of the trajectories analysed here r_{mean} is taken to be the unweighted mean x, y coordinate for the trajectory segment. As can be seen from Figure 5-13 (B) the mean squared radius of gyration values were higher for Janus and pore particles than for symmetrical particles.

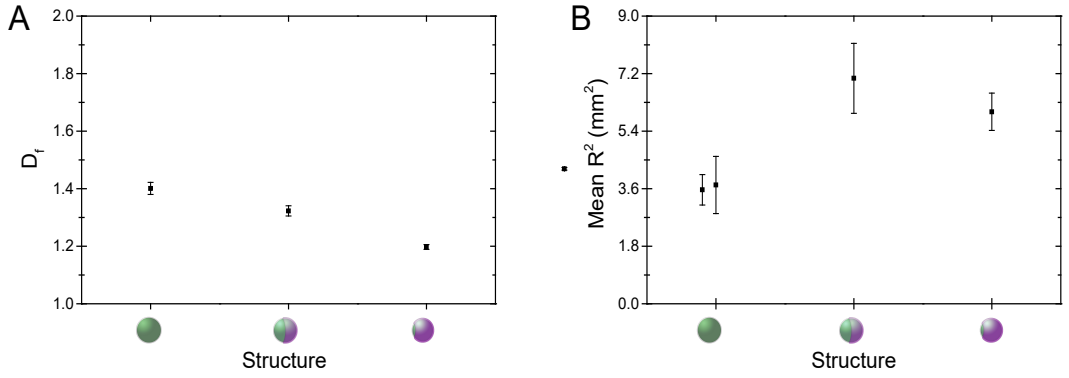

Figure 5-13 Results of trajectory analysis for bubble swimmers (A) Fractal dimension [D_f] (B) Mean squared radius of gyration [R^2].

The slightly lower gyration shown for the pore particles versus the Janus particles is due to the fact that the particles move much more slowly. When comparing trajectories of a fixed duration a larger mean squared gyration value indicates that a trajectory has extended over a larger region of space. This indicates that the trajectories are of a more directed, straighter form and therefore produce a faster transport. As previously shown in Figure 5-9 the asymmetrical swimmers had a lower propulsion velocity, in particular the pore particles, but despite this the mean squared gyration values were higher for both types of asymmetrical particles compared to symmetrical ones. This provides further evidence that a more defined

catalytic activity area results in an increased directionality and therefore achieves a greater distance from the origin.

As a final analytical method **persistence length** was used to characterise the trajectories of the spherical bubble swimmers. The basic concept of this analytical approach is explained in the methods Chapter 2 Section 2.3.4. This method is widely used to measure the stiffness and bending properties of polymer chains [130], where the persistence length L_P is a measure for length at which the correlation of the angle θ between the segment vectors is lost. This means that a linear set of chain segments will result in a larger persistence length value than a set of chain segments with loops and curves. Similarly to mean squared gyration this analysis method also reflects both velocity and directionality.

Trajectories extracted by the image analysis of the micromotors allow one to generate a chain of vectors. In the normal application fields of persistence length analysis the length between the chain vectors is equal and therefore persistence length L_P can be simply calculated by determining the average cosine angle $\langle \cos\theta \rangle$ between vectors at all separation distances L along the chain. As shown previously in Figure 2-21 this was done by superimposing vectors at position j on the vector at starting position i and calculating $\cos\theta$, where $j \geq i$ and i represents all starting positions along the chain. For the present 2D trajectories a plot of $\langle \cos\theta \rangle$ against separation distance $L = \Delta L(j - i)$ has the form, $\langle \cos\theta \rangle = e^{-(L/2L_P)}$.

As particles were tracked via optical microscopy the tracks had a given frame rate which means that the distance between two trajectory points was dependent on the velocity of the particle. As previously shown the instantaneous velocities of the bubble swimmers were not the same throughout a trajectory but rather showed a

start-stop motion (Figure 5-8). Therefore, there must be a great difference in the length between the chain vectors resulting from the track points so that it would be impossible to get an accurate persistence length measurement simply by using the above mentioned calculation. In order to be able to gain equal lengths between the chain vectors it was essential to re-grid the trajectory data. To achieve this inbuilt LabVIEW interpolation functions were used to generate additional points between each trajectory point small enough to allow for even spacing over the entire track, thereafter the persistence length was calculated as described.

The results of the persistence length analysis support those of the previous methods and show there was an increase in directionality for Janus and pore particles, with an increase in persistence length from 0.5 mm for symmetrical particles to 1.1 mm for Janus particles and even greater for pore particles at an L_P of 1.4 mm despite the decreasing velocity of the particles as shown in Figure 5-14(A). In an attempt to normalise the effects caused by decrease in velocity of the particles, the persistence length L_P was divided by the trajectory length (contour length L_C), as shown in Figure 5-14(B). These results show that the persistence length of pore-shaped particles normalised for velocity is ~10 times greater than that of symmetrical ones and 5 times greater than for Janus particles. All these analytical methods clearly reveal that altering the catalytic activity site can statistically increase directionality and therefore also efficiency of spherical bubble-propelled micromotors. They have proven to be useful methods for the analysis of a wide variety of trajectories.

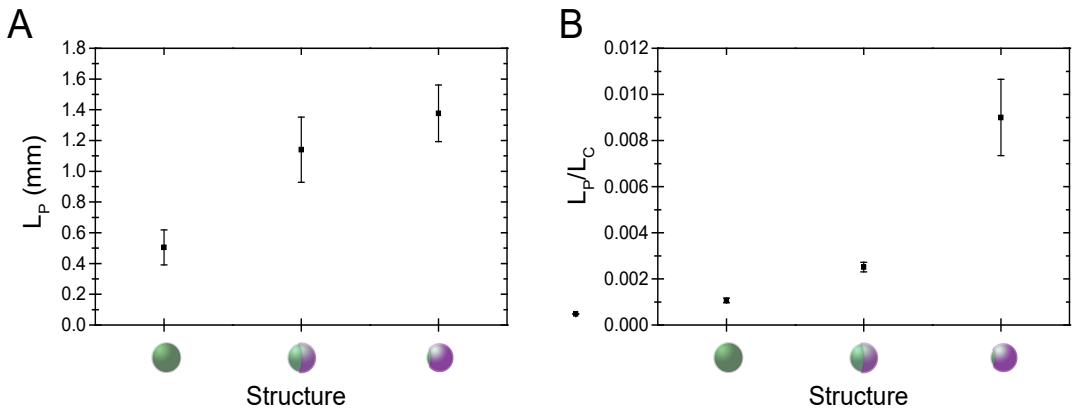

Figure 5-14 Results of trajectory analysis for bubble swimmers (A) Persistence length [L_P] (B) shows values normalised to total path length [L_C].

In a further attempt to characterise the system, the trajectories resulting from this model were also analysed for fractal dimension and persistence length using the simple stochastic model described previously in Section 5.3.2.3. The fractal dimension data reproduced the decrease in fractal dimension with reducing pore arc observed experimentally as shown in Figure 5-15 (A). The persistence length calculated for these trajectories also showed a similar behaviour to the experimental data, i.e. the persistence length increased with decreasing pore size; here the model data does not need to be corrected for decreasing velocity as the velocity for all particles was modelled to be the same (see Figure 5-15 (B)). These results show that is it indeed possible to gain more control for bubble swimmers by localizing the bubble generation sites, creating more controlled motion for particles coated with unreactive chromium.

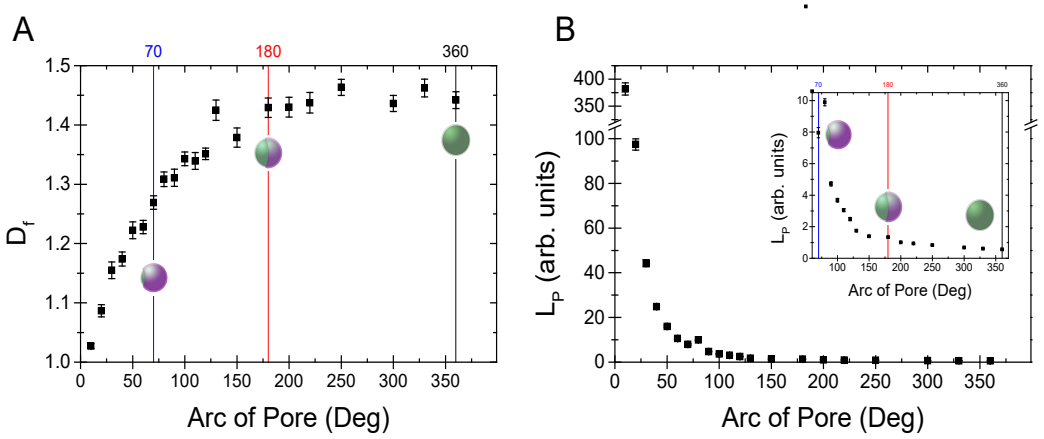

Figure 5-15: Trajectory analysis for model data generated for different exposed catalytic surface coverages. (A) Fractal dimension, (B) persistence length, inset shows enlarged region between the arc angle of 60° and 360°. Vertical lines show region of experimental data.

In order to clearly show that the motion of the bubble-propelled motors is not coupled to their Brownian rotational diffusion constant, it is illustrative to calculate their expected persistence length when assuming that device orientation determines translational thrust direction and the body of the swimming device is solely re-orientated by Brownian rotational diffusion. Under these circumstances the persistence length would be generated from the rotational diffusion time constant (2100 seconds for a 30µm spherical particle) and the propulsion velocity which would equate to a persistence length of 8.4 metres. From this calculation it becomes apparent that the observed behaviour is far from as persistent as this, even for pore particles which in comparison only achieve 0.015% of this persistence. On the other hand phoretic Janus swimmers show a well-defined link between motion direction and rotational diffusion coefficient. Thus a phoretic Janus swimmer of 5 µm diameter and a propulsion velocity of around 5 µm/s would be expected to have a persistence length of ~0.5 mm, which indeed agrees with experimental trajectories [31]. This velocity is only around 1% of the propulsion velocity

measured for bubble swimmers but the resulting persistence length emphasises how much more chaotic the propulsion behaviour of bubble swimmers is in comparison to phoretic swimmers, even though the catalytic active centre is focused more than with the pore particles.

The major loss of directionality for bubble propulsive devices is likely to be at least partially dependent on one or both of the following two factors: increased particle rotation due to the bubble propulsion process (i.e. driven rotations) and the low correlation between the device orientation and propulsion direction. In order to understand these problems better it could be important to use higher resolution imaging together with high frame rate capture.

The experimental data together with the simple stochastic model reveal that it is possible to tune the trajectory behaviour by confining the catalytic active area thus increasing directionality of the devices. The model gives an indication how much the catalytic activity has to be confined in order to achieve the desired directionality behaviour, as shown in Figure 5-15. The increased directionality is achieved because confining the area of activity to a pore increases the chances of bubbles being produced in a smaller more localised area. Therefore, the random rotational torques generated by bubbles further from the centre of activity are smaller and bubble generation is more likely to occur closer to the centre of activity.

5.4. Conclusions

The influence of the catalytic distribution on the surface of spherical bubble swimmers on their trajectories has been investigated using novel analytical techniques to the field of bubble swimmers to help characterise the change in trajectory behaviour. A simple symmetrically active spherical colloid showed

velocities of 1.8 mm/s in fuel solutions, but the trajectories of these particles showed frequent abrupt changes in direction. In comparison trajectories of Janus particles showed a slightly reduced propulsion velocity but the resulting trajectories were seen to be more directional and the instantaneous velocities over time also showed a smoother pattern. Constraining the activity further to a smaller pore further increased this behaviour but strongly reduced propulsion velocity.

In order to be able to quantitatively compare the trajectories of the three different geometries (symmetrical, Janus and pore) three different analytical techniques (fractal dimension, mean squared gyration and persistence length) were applied in order to analyse the trajectory data, where initial raw data had to be smoothed and in the case of persistence length re-gridded to equal time frames. The data clearly shows how these three methods can be used to define the characteristics of bubble-propelled micromotors to show differences in their directionality. All three methods were in agreement that constraining catalytic activity on spherical bubble swimmers generated more directional trajectories, i.e. the fractal dimension of the trajectories decreased, which significantly increased persistence length and increased the extent of the radius of gyration. It is clear however, when comparing bubble-propelled spherical micromotors to phoretic micromotors, that the latter produce less random motion and are governed by their Brownian rotational diffusion coefficients. In contrast, the bubble-propelled swimmers are governed by the sites of random nucleation of bubbles produced on the catalytic surface causing a high degree of randomisation to their trajectories not influenced by Brownian rotation. The simple stochastic model demonstrated in this chapter illustrates how the random nucleation sites of the bubbles can affect the random behaviours of the swimmers and how it is

possible to successfully minimise the randomisation effects by confining the catalytically active area.

This study has illustrated how it is possible to utilise different analytical methods in order to characterise trajectory behaviour which cannot be assessed properly by the well-known MSD model. This is of particular interest for research on bubble swimmer devices as currently there are no generally accepted models / methods to properly characterise their trajectories apart from by qualitative observations. It is thought that the techniques used here might also help one to compare different systems including biological swimmers at different length scales. Furthermore, the ability to understand and characterise trajectories better should aid comparative study of the efficiency of the different devices.

5.5. Future Work

It might be interesting to see how increasing hydrogen peroxide concentration affects the motion of Janus and pore coated particles, to see if the same decline in velocity occurs for these particles as with symmetrically unmasked particles.

An enhancement for the model might be to take the change in reactivity with decreasing pore size into consideration, this way it may be possible to achieve realistic values rather than arbitrary values.

6. Micromotors in biological fluids

6.1. Introduction

There have been various examples of micromotors that are capable of swimming in complex media such as simulated blood, serum [28, 71] and seawater after the addition of fuel, generally hydrogen peroxide. However, lowering surface tension has been reported to be a key factor in achieving motion of tube-like 'swimmers' [53, 67, 68] and consequently there are no reports of autonomous swimmers moving in biological solutions, such as human serum without the addition of surfactant [53, 67, 68]. It is clear that a reliance on this additive is undesirable. As the spherical symmetrical bubble-propelled swimmers used in Chapter 5 did not need the addition of surfactant in water this chapter assesses the potential for these devices to also operate within serum.

The reasons why bubble propelled swimmers do not 'swim' in biological fluids such as serum, without the addition of surfactant (e.g. SDS) is not fully understood. In many cases it has been assumed by extrapolation, that because bubble propulsion in water required surfactant to reduce surface tension, the surfactant is required for the same reason within biofluids. However this analysis does not take into account any interactions the surfactants have on the proteins or other molecules in the solutions. It has been shown that SDS in fact causes the unfolding of proteins contained in the serum solution [170]. It is therefore important to note that to date, none of these interactions of surfactants with human serum for example, have been considered or discussed in any current active colloidal papers so far as I know.

6.2. Methods

6.2.1. Particle Preparation:

Polystyrene (PS) colloids (30 μm diameter) were uniformly chemically coated with platinum nanoparticles (2-5 nm diameter) by platinum salt reduction to serve as the symmetrical bubble propulsive devices used in this study (the same devices as used in Chapter 4 and displayed Schematically in Section 1.5 b).

Particles were then placed in a Petri dish of 3 cm diameter and ~ 1 cm depth which contained the various test solutions using hydrogen peroxide as a fuel source, under a controlled room temperature of 20°C and with air movement kept to a minimum.

6.2.2. Video Microscopy and Trajectory Analysis

This analysis was done in the same way as in Chapter 4.

6.2.3. Reaction Rate Measurements

Reaction rate measurements were done on glass slides, which were coated with a 20 nm chromium adhesion layer followed by 20 nm platinum via E-beam metal evaporation. A Moorfield E-beam coater as described in Section 2.1.3.2 was used. The reaction rates were measured at 280 nm in a Jenaway UV-VIS 6305 Spectrometer using a Hellma Analytics 0.01 mm path length Quartz crystal flow cell and 20 ml of sample volume which was kept under constant temperature control at room temperature (22°C) as previously described in Chapter 3 Section 3.2.7. Samples were initially incubated in 15% v/w H_2O_2 for 30 minutes in order to clean off any hydrocarbons left behind after the evaporation step, since they could affect the reaction rate measurements. Each sample was then first measured in 10% v/w H_2O_2 followed by the specific sample solution (e.g. 2% serum with H_2O_2) and

then finally measured again in 10% v/w H_2O_2. Each kinetic measurement was done for 10 minutes after which the reaction rate was determined.

6.2.4. Surface tension measurements

In order to measure the surface tension of samples, 10 ml of sample was needed. For these experiments the tensiometer used a platinum Wilhelmy plate and it was therefore not possible to measure the surface tension directly in hydrogen peroxide solutions, as this would have caused the hydrogen peroxide to decompose into oxygen and water. In order to avoid this, equivalent solutions were made for surface tension analysis which contained only water in place of hydrogen peroxide and the particular salts and surfactants in the same concentrations. Chapter 2 Section 2.2.2 described surface tension techniques in detail.

6.2.5. Attachment of PEG_{3000} to platinum surface

It was attempted to mask the platinum surface area with a monolayer of Thiol-PEG_{3000} (methyl ether thiol MW 3000). Samples were incubated in 100 mM Thiol PEG_{3000} solution for 48 hours and then washed 5 times with deionised water.

6.3. Results and Discussion

6.3.1. Salt Effect

To start to assess the biocompatibility of the spherical catalytic swimming devices introduced in Chapter 5, motion within salt containing aqueous solutions was investigated. As has been discussed above, a key factor for biocompatibility is tolerance to high ionic strength solutions. Therefore the effect of adding 0.1 M KNO_3 to H_2O_2 fuel solution (10 %) on the instantaneous velocities of symmetrical and Janus colloids (from Chapter 5) was investigated. In the case of symmetrically

active bubble-propelled particles in H_2O_2 fuel and fuel doped with 0.1 M KNO_3 both gave velocities of ~ 1.5 mm/s, as shown in Table 6.1. For Janus colloids however there was a velocity decrease of nearly 50% in 0.1 M KNO_3, from initially ~1.4 mm/s down to ~0.8 mm/s. This velocity decrease could be due to the previous finding in Chapter 3; that KNO_3 decreases the reaction rate to around 70%. No notable difference in velocity measured for symmetrical colloids may be due to the larger overall activity surface area of the colloids and therefore them not being as sensitive to the 70% reaction rate decrease.

Table 6.1 Instantaneous velocity measurements of 30 μm symmetrical and Janus PS/Pt colloids in 10% H_2O_2 with and without KNO_3

Particle type	H_2O_2 [% w/v]	KNO_3 [M]	Instantaneous Velocity [mm/s]
Symmetrical	10	0	1.53 ± 0.06
Symmetrical	10	0.1	1.56 ± 0.03
Janus	10	0	1.42 ± 0.08
Janus	10	0.1	0.76 ± 0.03

6.3.2. Swimming in human serum and blood

Having established that the simple spherical bubble propulsive devices are tolerant to salt, and do not require surfactants to produce motion in water, they were tested in biofluids, solely doped with hydrogen peroxide fuel. Placing 30 μm symmetrically coated Pt/PS colloids in varying concentrations of human serum, containing hydrogen peroxide as a fuel solution, showed that motion of the colloids ceased after a brief time, with the vast majority of particles settling to the bottom of the petri dish (or in some cases some being stuck at the air / liquid interface). Figure 6-1 shows an image sequence with representative tracks of micromotors swimming in 10% Human serum with 3% H_2O_2 fuel added. The particles undergoing motion were examined just after being placed in the solution. Black arrows indicate a few

particles that have stopped bubbling (after being in the solution for ~3 min) and have started to sink to the bottom of the petri dish (motion generally stopped after 1-5 minutes). Figure 6-2 shows some example tracks for particles in 1% Serum with 10% H_2O_2. In this case particles continued their motion for up to ~15 minutes with the occasional particle having even longer durations of propulsive motion. Finally, Figure 6-3 shows a track for a particle swimming in 10% serum and 3% H_2O_2 with the addition of 1% SDS. Here even after long observation times; ~1 hour, motion could still be detected. It is however important to note that even though all colloids seemed to retain their activity, a large proportion of colloids got stuck at the edges of the petri dish at the liquid meniscus and also then motion of colloids was slightly different, micromotors tended to drop to the bottom of the petri dish and spend less time swimming in the bulk solution or surface. This is most likely due to the decrease in surface tension due to SDS and the micromotors having a large mass. SDS might also affect how long the bubbles stay attached to the micromotor surface and thus the increased buoyancy effect of attached bubbles might be less if they detach earlier or burst earlier. Example movies can be found on the accompanying CD.

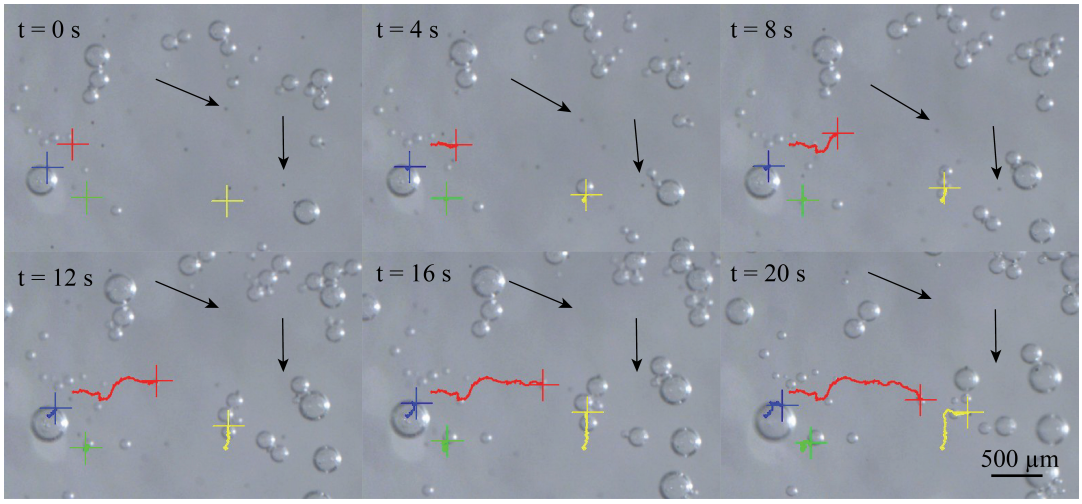

Figure 6-1 Example image captures of 30 µm symmetrical PS/PT colloids in 10% Human Serum and 3 % H_2O_2 without the addition of surfactants, Coloured lines and crosses (red, yellow, green and blue) indicate particle trajectories. Black arrows indicate inactive particles that sink to the bottom of the petri dish over time (CD Chapter 6 Movie S6.1).

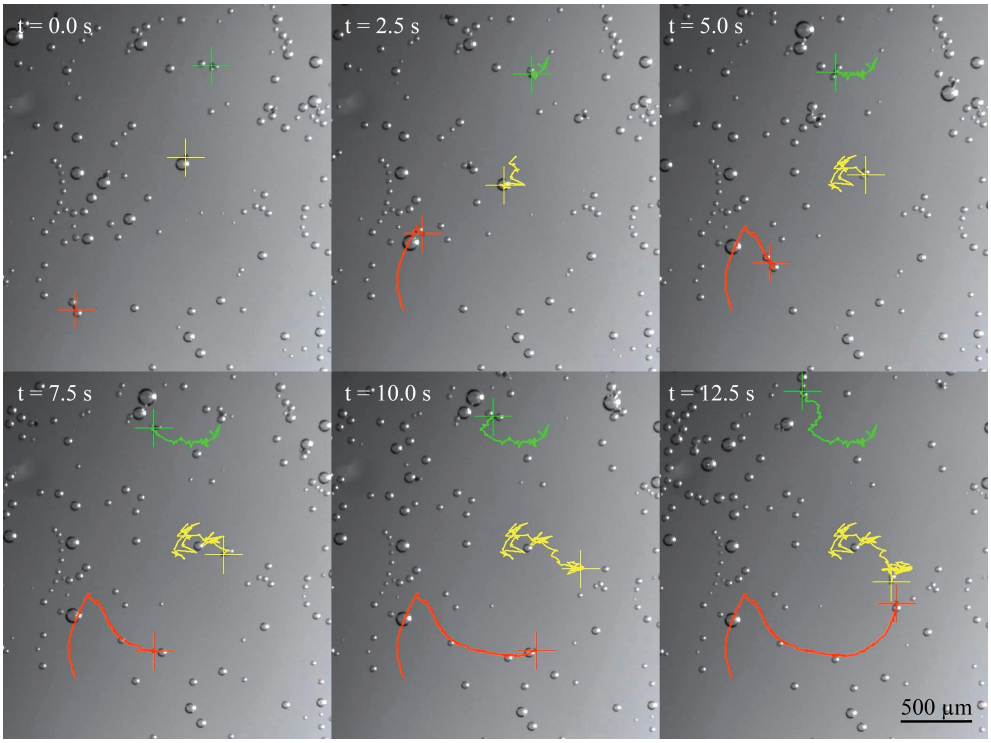

Figure 6-2 Example image captures of 30 µm symmetrical PS/PT colloids in 1% Human Serum and 10 % H_2O_2 without the addition of surfactant, coloured lines and crosses (red, yellow and green) indicate particle trajectories (CD Chapter 6 Movie S6.2).

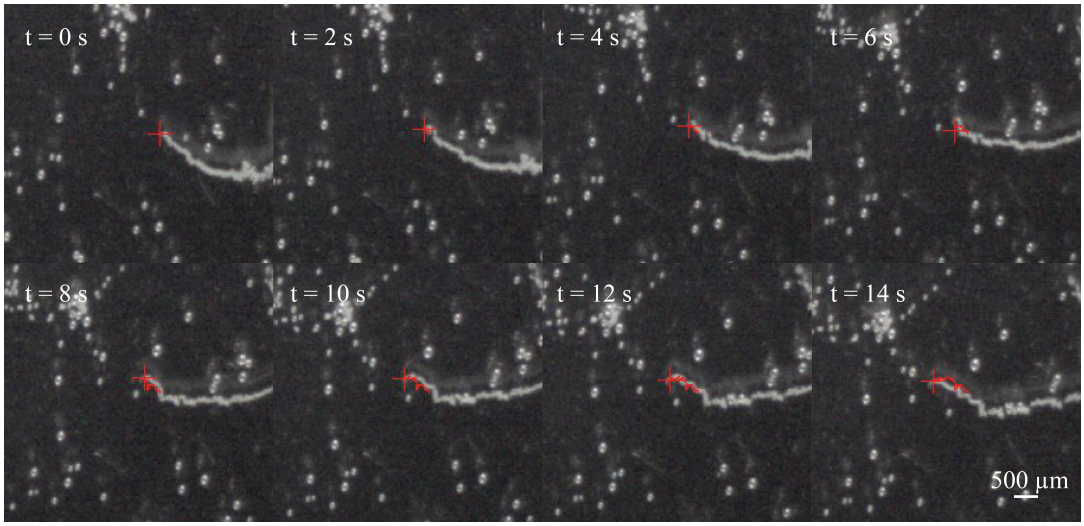

Figure 6-3 Example image captures of 30 µm symmetrical PS/PT colloids in 10% Human Serum and 3 % H_2O_2 with 1 % SDS, red lines and crosses indicate particle trajectory (CD Chapter 6 Movie S6.3).

Comparison of the velocity data obtained for these three previously mentioned samples, see Table 6.2, showed that particles placed in the lowest serum concentration of 1% with the addition of 10% H_2O_2 obtained the highest velocity of ~270 µm/s and an average lifetime of 15 minutes. In contrast, micromotors swimming in 10% serum with 3 % H_2O_2 had a reduced velocity of ~76 µm/s, which is a decrease in velocity of around 70% compared to micromotors in 1% serum. In comparison, velocity data for 10% serum with the addition of 1% SDS showed an increase in velocity to ~118 µm/s (~1.5 times the velocity without SDS). The addition of SDS appeared to increase micromotor lifetime beyond the experimental observation time of 2 hours. The large error obtained for micromotors swimming in 10% serum without SDS is most likely due to the short lifetime of 5 minutes, thus the particles start to slow down rapidly.

Table 6.2 Instantaneous velocities and lifetimes of 30 μm symmetrical PS/Pt swimmers in human serum

Human Serum conc. [% w/v]	H_2O_2 conc. [% w/v]	SDS conc. [% w/v]	Instantaneous velocity [μm/s]	Estimated lifetime [min]
10 %	3 %	None	76 ± 11	~ 5
1 %	10 %	None	270 ± 55	~ 15
10 %	3 %	1 %	118 ± 9	> 60

It is important to note that before addition of SDS to 10% human serum, the sample appeared opaque but after the addition it became clear. This change could indicate that SDS was having an effect on the proteins contained in serum.

Experiments revealed that it is not possible to have micromotors swimming in sheep's blood as the addition of any small amount of H_2O_2 results in vast amounts of bubbling until all H_2O_2 is used up (see Figure 6-4). It also changes the colour of the blood from red to yellow as can be seen in Figure 6-4.

The reason for this is most likely because blood contains the enzyme catalase, but there might also be other components reacting with the hydrogen peroxide. Due to the colour change from red to yellow the iron contained in red blood cells might also be reacting with H_2O_2. This is another indicator why the use of platinum for generating enhanced motion via the decomposition of hydrogen peroxide is not of practical use for swimmers in some biological systems.

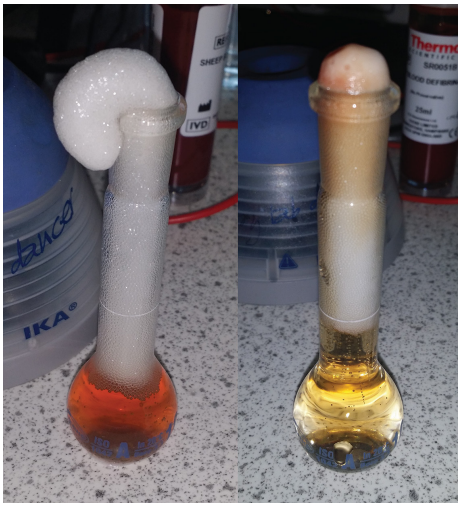

Figure 6-4 Photos showing the effect of adding a few drops of H_2O_2 to 10 % w/v sheep's blood. (left) right after the addition of H_2O_2, (right) when the reaction calmed down after ~ 1 minute.

6.3.3. Surface tension measurements

Based on previous justifications for the requirement for surfactants to promote motion in biofluids, which proposed that the additives role was to reduce surface tension, it is instructive to actually measure the surface tension for the relevant solutions. As shown in Figure 6-5 and Figure 6-6 both human serum and blood in fact showed considerably lower surface tension values than pure water itself. The addition of 1% SDS to these solutions did bring the surface tension down even further in both cases (serum and blood), but these results clearly show that tube-like swimmers might be able to swim in high serum concentrations if low surface tension is the only requirement for them to swim in these solutions. Furthermore, as the spherical swimmers under investigation were able to swim in the higher surface tension aqueous media, it seems unlikely that for swimming to occur in biofluids SDS would need to be added in order to lower surface tension of these fluids (even further). The time dependant nature of the incompatibility within 1%-10% serum, in the absence of surfactant, also strongly argues against surface tension being a limiting factor.

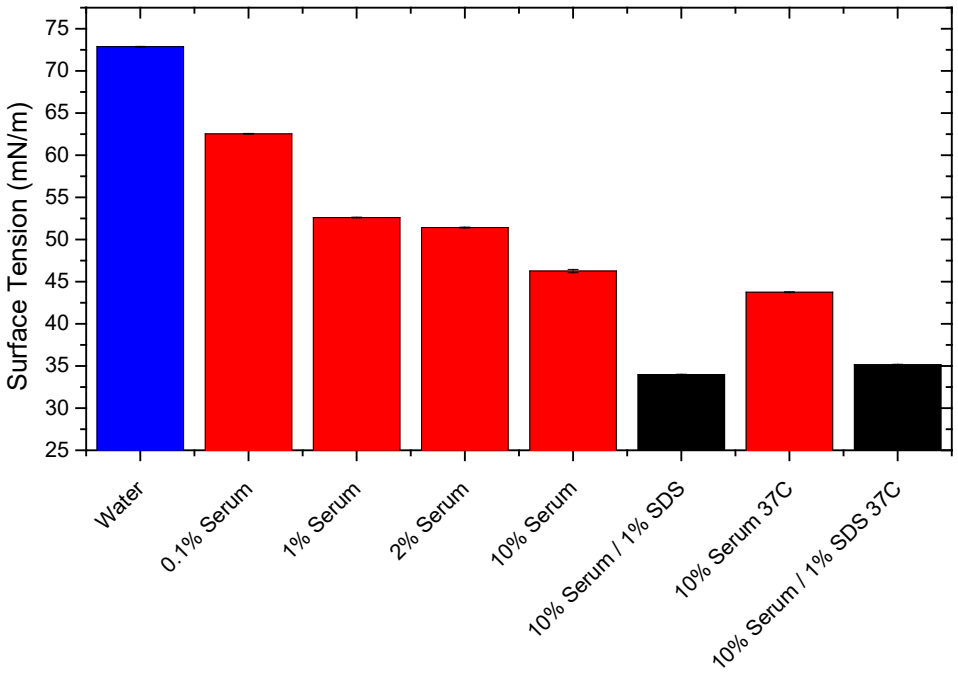

Figure 6-5 Surface tension of water (blue), different serum concentrations) with (black) and without (red) SDS and at physiological temperature (37 °C).

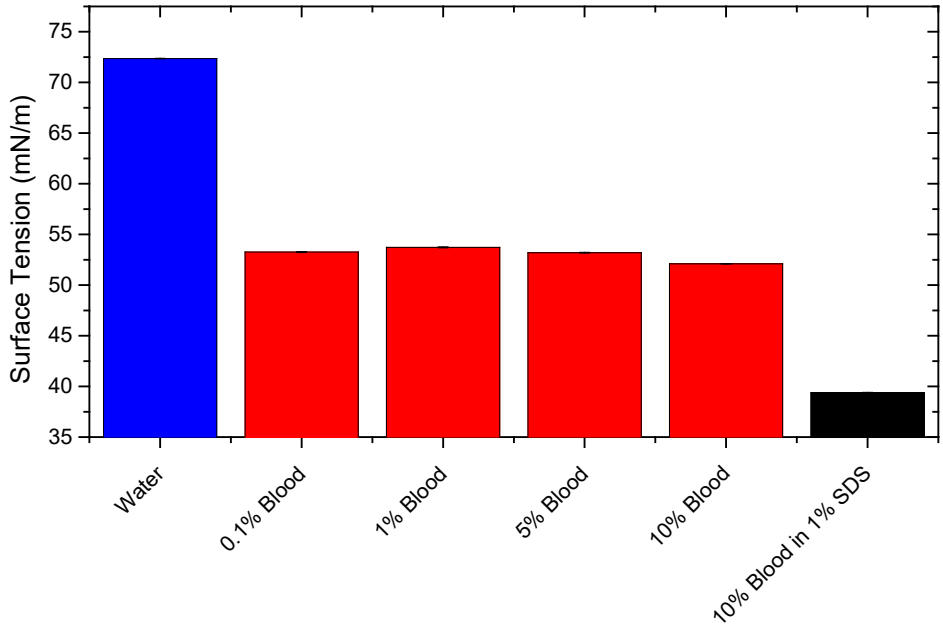

Figure 6-6 Surface tension of water (blue), different dilutions of blood with (black) and without SDS (red).

6.3.4. Effects of Serum on H_2O_2 reaction rate

In the light of the inability to assign the lack of persistent motion within serum to surface tension effects, it was necessary to consider other factors that could impede motion. One obvious factor would be a reduction in reaction rate of the catalyst within the biofluid.

Reaction rate experiments on glass slides coated with platinum revealed that the decomposition of H_2O_2 in 10% fuel containing 10% serum solution was $1/12^{th}$ (0.05 mMol/min/cm^2) of that measured in pure H_2O_2 fuel solution (0.59 mMol/min/cm^2) (see Table 6.3).

One possible explanation for this reaction rate reduction is that the proteins in the serum solution adhere to and mask the catalytic platinum layer and thus halt the decomposition of H_2O_2. Supporting this idea, if the glass slides were washed and placed in pure H_2O_2 fuel solution the reaction rates returned back to standard.

Reaction rate measurements also showed that if 1 % w/v of SDS was added to the serum sample, the reaction rate increased to ~ 7 times (0.34 mMol/min/cm^2) the reaction rate in serum. This indicates that the addition of SDS to serum can recover the reaction rate to a great extent and stop the inhibition of the sample. This may be due to surfactant mediated unfolding of the proteins in the sample [170] and is supported by the previous observation that the solution turns from opaque to clear (after the addition of SDS).

Table 6.3 Influence of Serum and SDS on reaction rate

Sample solution	Reaction Rate [mMol/min/cm^2]	Reaction Rate [$s^{-1}\mu m^{-2}$]
10% H_2O_2	**0.59 ± 0.057**	**6.24 x 10^{10}**
10% H_2O_2 / 10% Serum	**0.05**	**4.82 x 10^{9}**
10% H_2O_2 / 10% Serum / 1% SDS	**0.34**	**3.38 x 10^{10}**

6.3.5. Masking of platinum surface with PEG_{3000}

Having identified a probable issue of protein absorption masking the platinum catalyst, a brief set of experiments were done using Thiol PEG_{3000} in order to attach this to the platinum surface and generate a monolayer, as an attempt to build a barrier layer which would inhibit proteins in the sample solution from masking the surface of the active platinum layer. This experiment however, for reasons unknown, did not work and colloids still lost their activity in human serum containing no surfactant. The reasons for this could be that the PEG_{3000} used was not long enough or possibly the monolayer was not properly formed on the surface of the colloids.

6.4. Conclusions

The above results showed that surface tension is not the only factor that can cause problems for self-motile particle systems in particular based on a catalyst such as platinum. In fact it was observed that for self-motile particles based on platinum catalyst to swim in serum solution it was essential to add a surfactant, such as SDS, in order to inhibit biofouling of platinum surfaces. Unlike micro-rockets which have previously been used in biological fluids [67, 68] and have all needed the addition of a surfactant in order to decrease the surface tension and allow for fuel solution to ingress into the tube-like structures, the spherical swimmers used here did not need surfactants in order to achieve motion. Because there is a need for surfactants by most, currently published, bubble-propelled swimmers in water, it appears that how these swimmers might perform without the addition of surfactant in biofluids has not been tested, because they were believed not to swim. The results here however showed that the surface tensions of solutions such as human serum, are actually a lot lower than that of water. The addition of 1% SDS for

example does lower the surface tension further but the largest contribution in surface tension decrease (compared to water) is due to the sample itself; human serum. Increasing the sample temperature to a physiological temperate of 37 °C was also seen to slightly lower the surface tension; in addition to reductions due to SDS and serum. The need to add high concentrations of SDS to the human serum samples however means that the proteins and enzymes in the sample to be tested, will ultimately be denatured (unfold) [170]. This would defeat the object of being able to use these particles in biological samples for analytical applications.

Spherical 30 μm bubble-propelled micromotors were shown to be tolerant to KNO_3. Experiments revealed that 30 μm micromotors were able to swim in human serum for short periods of time without the addition of SDS, however after a few minutes the catalyst surface area was masked and bubble production halted. Addition of SDS stopped the biofouling process and micromotors continued to bubble although motion was affected by the large decrease in surface tension and micromotors would swim more towards the bottom surface of the sample than in the bulk solution or surface due to sedimentation of the particles. It appeared that SDS affected the bubble release and therefore bubbles detached earlier from the micromotors.

An attempt to mask the platinum surface with a monolayer of PEG_{3000} did not succeed in inhibiting the biofouling process and keep the reaction (decomposition of H_2O_2) going. As this experiment was not rigorously done due to time constraints, there are various aspects of the experiment that may have failed and could be investigated for future possibilities. The most obvious one being that a full monolayer of PEG_{3000} was not properly built up on the platinum surface and therefore the biofouling was not inhibited efficiently.

Finally experiments revealed that hydrogen peroxide as a fuel for self-motile particles will not easily allow for swimming in blood samples.

6.5. Future Work

It may be of interest to attempt another way of attaching PEG to the platinum surface to act as an anti-biofouling barrier but without inhibiting the actual hydrogen peroxide degradation. For this it might be advisable to try out more chain lengths and different concentrations to achieve successful monolayers. In addition to this it might be useful to use other techniques such as Ellipsometry to determine the surface attachment of the Thiol-PEGs used. Finally, it is likely that a system that uses a different catalyst such as an enzyme (e.g. catalase) would be far more useful in biofluids.

Other masking methods might be utilised to cover the platinum surface, e.g. with porous SiO_2, where pores are small enough to stop proteins reaching the platinum surface.

In my final experimental chapter I have attempted to address and build on these findings by using the enzyme catalase as a power source for the micromotors. The enzyme is embedded in a silk scaffold to increase the biocompatibility and active life time of the micromotors in biofluids. Also, moving towards enzyme propulsion provides a route to avoid the requirement for peroxide fuel, which this chapter has shown to be incompatible with blood.

7. Inkjet printing of enzyme powered micromotors

7.1. Introduction

As discussed in detail in Chapter 6 and the introduction Section 1.2.2, the vast majority of autonomous bubble-propelled micromotors to date need to have surfactants added to the working medium in order to achieve any appreciable propulsion [52, 67, 70, 77]. However as explained in Chapter 6, surfactants, e.g. SDS, also cause unwanted side effects, such as enzyme denaturation, which will render the systems useless for many applications [170]. Chapter 5 showed that simple spherical bubble propulsive spherical devices can produce motion without surfactants in water, however Chapter 6 showed that within biological fluids motion does require surfactant. The role of surfactant in this case was found to be to reduce biofouling of the platinum catalyst and restore surface reactivity, rather than to reduce surface tension as had been previously suggested. Fouling of catalytic platinum in human serum illustrates the problem that this expensive catalyst is very far from optimal for most biological applications and therefore there is a clear impetus to move to more biologically based devices that use enzymes as chemically active species rather than metals such as platinum. A variety of devices have been reported that use enzymes as motors to power the catalytic reactions and cause motion of particles. As the catalase enzyme complex decomposes hydrogen peroxide [80] this facilitates comparison with the previous sections of the thesis. However, it is clear that for future applications alternative enzymes could also be used to drive these micromotors instead, removing the reliance on a reactive fuel, which has been shown in Chapter 6 to be incompatible with blood.

All the previously reported enzyme-based systems (Section 1.2.3) have predominantly relied on complex chemical processes to immobilize the enzyme

onto surfaces such as gold. This means that the process is costly, complicated and very inefficient. In addition, the surfaces needed for the immobilization are not always considered to be highly biocompatible and must also be particularly clean upon initial chemical activation. It is therefore desirable to immobilise enzymes in a simple, cheap and yet biocompatible way, along with beneficial enzyme stabilisation. One such material which shows great potential for this sort of application is silk [171-173]. Therefore, silk from the silkworm (Bombyx mori) has been tested as the base for generating particles via silk scaffolds. It has already been shown by Zhang Y.Q. [174] that natural silk fibroin can be used as a support for enzyme immobilization and increased stability [175-177], and there have been various studies into using silk for drug delivery challenges [178-183].

There have been some recent examples of utilising printing methods in order to generate swimming devices as shown in Section 1.3. At present features smaller than 10 μm in size have been produced via inkjet printing [184], which gives the chance of high structural definition on the micron scale. One recently published paper has demonstrated some of the benefits of printing silk scaffolds doped with enzymes onto its surfaces to generate e.g. silk biosensors which can show contamination levels on surfaces via e.g. colour change reactions [185]. In Chapter 5, particular emphasis was given to how the size of the exposed catalytically active area on a masked spherical particle can affect the trajectories of bubble-propelled particles. This is a general feature for many swimming devices, that controlling the location of the catalyst determines performance, and so a key advantage for a print based manufacturing method is the potential ease with which catalyst location can be defined and modified.

As biocompatibility is of essential importance for many prospective applications of self-motile micromotors (Chapter 6), the use of silk together with an enzyme as a propulsion motor is likely to be of great benefit and enzymes are by nature biocompatible. In addition to this silk is already an FDA approved biomaterial and has been used for many biomedical applications [171]. It is a versatile material due to its strong mechanical properties [186], excellent biocompatibility [187], adaptable biodegradability [188], and easy processing [189].

Silk Fibroin (SF) has three different conformations, or polymorphs. Silk I is water soluble (random coil), Silk II is the state which consists of β-sheet secondary structure (spun silk state), and Silk III is an air/water assembled interfacial silk consisting of a helical structure.[171, 190, 191] Secreted silk (Silk II) is commonly processed into water soluble regenerated silk fibroin (RSF) (Silk I) to allow printing.

Therefore a further conversion stage is required to convert the printed material back into the water insoluble rigid scaffold that is required to manufacture solid 3D structures such as the micro-rockets described in this chapter. Exposing Silk I to chemicals such as methanol or potassium chloride, heat, or shear stress converts it to a β-sheet secondary structure (Silk II) and this phenomenon has been widely used to make silk scaffolds for different biomedical applications [171].

Here, reactive inkjet printing (RIJ) was employed for the first time, which included chemical treatment with methanol, in order to ensure a rigid detachable silk scaffold was formed. RIJ is a method of allowing two different ink solutions to react together to generate a new compound, or alternatively as in the deployment here, to produce a change in the silk polymorphic form [192]. RIJ also shares the advantages of conventional ink-jet printing to allow the straightforward

manufacture of 3D objects with well controlled shape and size, for example by utilising a layer-by-layer approach [193-195].

RIJ printing allows the generation of self-motile swimmers with digitally-defined compositions, structures and shapes without the need for multiple step methods to generate complex structures. This allows for rapid development and understanding of how structures will affect the directionality of these particles and will enable the generation of highly efficient structures to be rapidly fabricated. Further to this, in the future additional functionalities can be simply added into silk-ink solutions while generating the silk scaffolds via RIJ [192], so that the other components such as magnetic nanoparticles can be encapsulated / immobilised into the silk scaffold structures.

The following experiments demonstrate how it is possible to use LBL inkjet printing of RSF ink, containing enzyme molecules, to generate different micromotors that undergo different types of motion dependent on their structure, as defined by the printing process.

7.2. Methods

7.2.1. Preparation of silk ink solution

7.2.1.1. Silk Degumming

Silk from bave of *B. mori* was degummed in order to remove sericin by briefly boiling the raw silk in 0.02 M sodium carbonate (Na_2CO_3) (99.5 % Alfa Aesar). After degumming, the resulting silk materials were rinsed with deionized water until the solution was clear and then dried at 30 °C overnight in a drying oven.

7.2.1.2. Dissolution of silk fibroin fibre

For the dissolution of silk fibroin fibre (SF) Ajisawa's reagent was used; the reagent is made up of $CaCl_2$ (93 % Sigma-Aldrich)/ ethanol (99.8 % Sigma) / water in a 1:2:8 molar ratio: as suggested by Ajisawa et al. [196, 197]. 1 g of degummed fibroin was added to 10 g of Ajisawa's reagent. This mixture was then stirred at 75^{o}C for 3 hours and was left to cool down at room temperature before being dialysed in deionized water to remove the salts until the solution recorded a conductivity of less than 1 µS. The dialysed SF solution was then centrifuged at 10,000 rpm for 15 mins.

7.2.1.3. Preparation of Catalase Ink solution

Amorphous bovine liver catalase powder (purity 60 % Sigma-Aldrich) was dissolved in deionised water at a concentration of 20 mg/ml, by inverting the sample several times to ensure no excessive amount of foaming occurred until fully dissolved, and then filtered with a 0.7 µm glass filter. It was ensured that the solution was kept on ice until mixed with the previously made up silk solution. These were carefully mixed and blended (by inverting the vial several times) with PEG_{400} solution giving final concentrations of 4 mg/ml CAT, 10 mg/ml PEG_{400} and 30 mg/ml regenerated silk fibroin (RSF). In the case of silk solution containing no CAT the PEG_{400} concentration was increased to 12 mg/ml.

7.2.2. Inkjet printing process

The basic concept of drop-on-demand inkjet printing using piezoelectric print heads (orifice diameter of 60 µm) is described in the methods chapter Section 2.1.4. Various ink solutions containing RSF as the scaffold material were used to print 3D enzyme-driven self-motile particles. The silk scaffold was turned into a solid

β-sheet structure (Silk II) by printing a drop of methanol via a second print head and switching between these two print heads for every layer.

As the drops of methanol printed on top of the silk drops containing the enzyme were small (droplet diameter ~80 μm resulting in ~3000 pL), the evaporation and beta sheet formation of silk occured before the methanol could denature any significant amount of enzyme. An explanatory schematic of the applied LBL printing is shown in Figure 7-1.

Four print heads were used all with a pore diameter of 60 μm, pure silk solution, silk blended with catalase (4mg/ml) and PEG_{400} and 98.99% pure methanol (Sigma) were used as ink. The addition of brilliant blue FCF ($C_{37}H_{34}N_2Na_2O_9S_3$) into methanol was used to establish the area where methanol (ensuring that alignment was correct) was printed due to the dying of the silk scaffold during this process. In the case of Janus particles a barrier layer of 10 layers of Poly-methyl methacrylate (PMMA) in Dimethylformamide (DMF) was also printed in order to decrease the amount of bubbles leaking from the active half to the inactive half.

5 x 10 dot matrices were programmed into JetLab (Version 6.3 (build 4.0.18.3011), MicroFab Technologies) and columns with a total height of 500 layers of silk scaffolds were printed LBL, which equated to a height of 250~300 μm (see Figure 7-1).

The whole process took around 10 hours to complete, and had to be carefully monitored in order to ensure no excess material accumulated on the tip of the print heads during printing. The blended in PEG_{400} helped decrease the overall accumulation of enzyme residue on the print head but did not entirely stop its accumulation and it was necessary to clean the print head every ~50-100 layers. It

was important for the temperature to be below 25 °C and the humidity 55 % or higher as otherwise the printing procedure would not produce suitable 3D scaffold structures.

Two different approaches were used to generate the micro-rockets. The first process is shown in Figure 7-1 where silk solution containing CAT and PEG was printed into columns of 250 layers and then a further 250 layers of silk solution with PEG at a slightly higher concentration were printed on top of the initial columns. This equated to a total of 500 layers (printed onto smooth Si-wafer substrates). It was essential to print 10 layers of PMMA to act as a barrier between the two halves in order to stop bubbles leaking into the inactive side of the micro-rockets. This process generated Janus micro-rockets that were half active and half inactive.

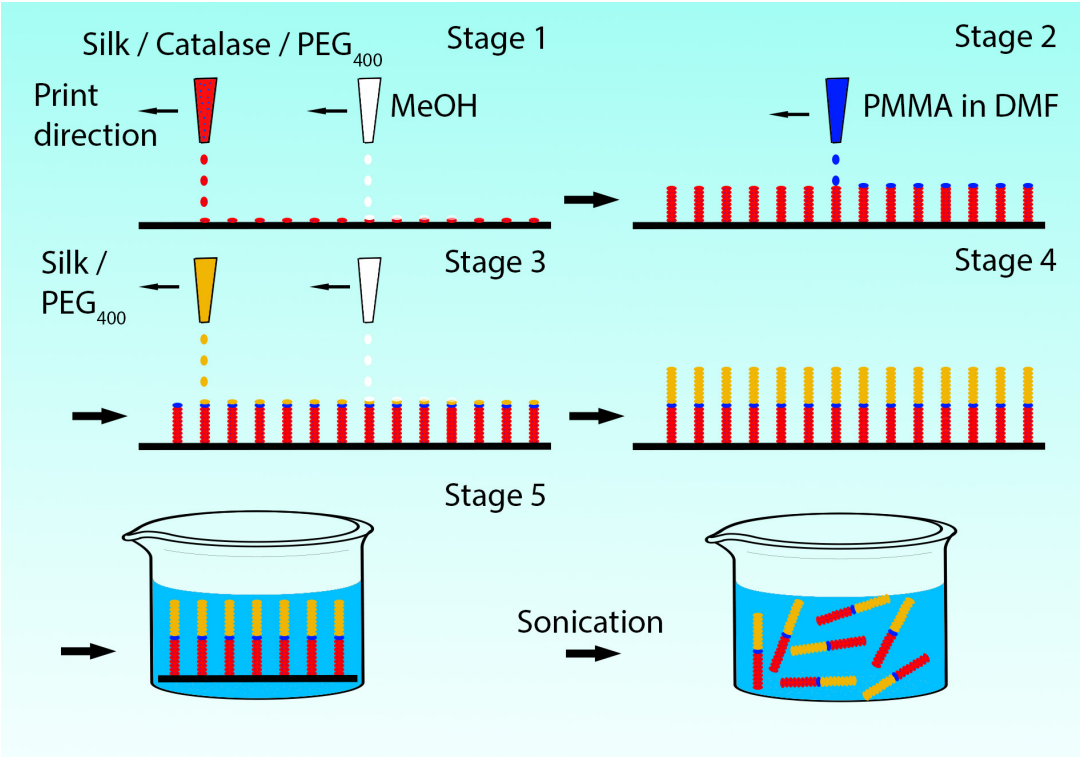

Figure 7-1 Schematic representing the layer-by-layer printing procedure of Silk scaffolds with (red with dots) and without (orange) catalase enzyme molecules, blue represents the PMMA barrier layer: generation of Janus silk micro-rockets.

For comparison, particles of 500 layers of CAT/silk and PEG_{400} of the same concentrations were also printed (fully active micro-rockets), see Figure 7-2.

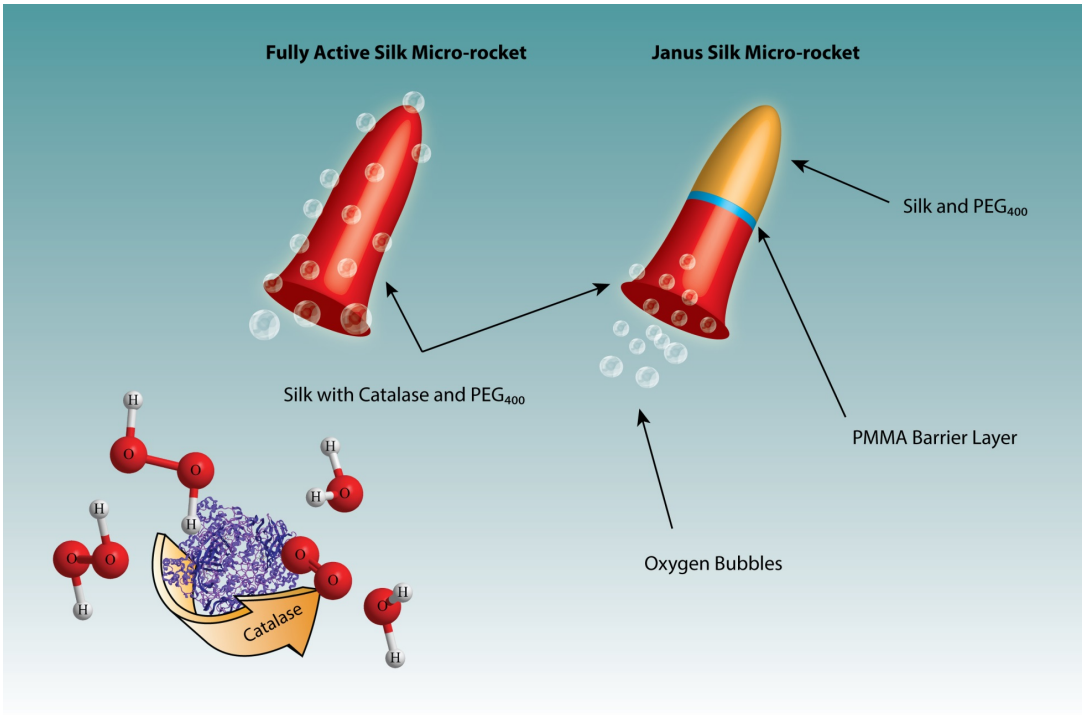

Figure 7-2 Schematic showing the two designed Silk-Microrockets, (left) fully active rockets, (right) Janus rocket.

7.2.3. Particle preparation of silk – based micro-rockets

Silicon wafers were cut up and incubated in filtered (0.2µm glass filter) deionized water, which was then carefully removed via a Pasteur pipette ensuring printed columns were not detached from the surface. Any dust and silk that was not in β-sheet form was removed in this way. This process was repeated 3 to 5 times.

After washing the Si-wafers were placed in a small beaker and the surface was covered with deionized water and held in the centre of a sonicator for < 30 seconds until all or most columns were detached from the wafer. The particles were then transferred into a petri dish (6 cm in diameter) containing 5 % w/v hydrogen peroxide and imaged under a microscope with a connected PixeLink camera, or

under a PixeLink camera with a camera lens attached. Movies were taken at a frame rate of 25 frames per second (fps) for 500 to 1000 frames.

7.2.4. Analysis of movies.

Silk printed particles resembled a cylindrical shape (or rocket-like structure), which is characterized in detail via SEM in Section 7.3.1.1. Particles were therefore manually tracked on both their extreme points (dual point tracking) in ImageJ using a manual tracking plug-in [198].

The dual point tracking allowed determination of the direction of motion and orientational changes of the self-motile particles during their motion. This was calculated for every frame of the movies and is schematically shown in Figure 7-3. A custom built LabVIEW program was used to calculate the angles denoted as θ and ϕ over the whole trajectory. Screen shots of the LabVIEW program are attached in the Appendix (10) Section (10.6). A similar method was used to determine the direction of motion and particle orientation in Ebbens et al. [30] for spherical catalytic swimmers. Figure 7-3 illustrates the calculated angles θ and ϕ, which were used to correlate the change in particle orientation (ϕ) and direction (θ) over time and to compare fully active to Janus particles (half active). Prior to analysis it was important to smooth data track points via a Savitzky-Golay filter using k = 10 side points due to the start-stopping type motion via bubble propulsion.

In the case of samples where a slight drift or wobble was present, tracks were corrected by tracking an inactive particle and subtracting this motion from the particle trajectory allowing for more accurate results. The drift was thought to

emanate from air movement in the lab whereas the wobble that can be seen in some movies probably came from vibrations in the lab and building.

A centre of mass trajectory point was calculated from the dual tracking and fed into a custom made LabVIEW analysis program in order to calculate instantaneous velocity and persistence. These analysis methods are described in Section 2.3 and Gregory, et al. [74].

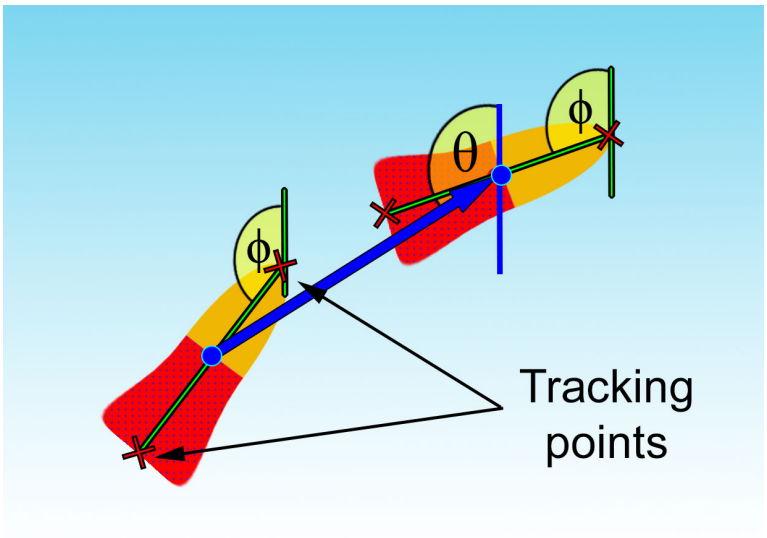

Figure 7-3 Schematic showing the angles to calculate the orientation dependence of the particles (θ (direction) and φ (orientation)).

7.3. Results

7.3.1. Characterization of micromotors

All silk printed particles were checked under an optical microscope, prior to use, to ensure that the structure closely resembled the required one and samples that did not print properly were discarded. The following SEM and Contour GT images were taken from particles prepared in the same way as those used for the swimming experiments (Contour GT is the model name. This is a type of confocal microscope imaging, which allows for 3D roughness measurements of gold coated samples).

7.3.1.1. Final Structures

The SEM images below show the initial arrays of printed columns for both fully active (Figure 7-4 (left)) and Janus (Figure 7-5 (left)) silk particles before particles were detached from the silicon surface. As can be seen the particles all appear very similar in height and diameter. The enlarged views of both the side of the columns (Figure 7-4 (right)) and the top Figure 7-5 (right) show that at this resolution there were no noticeable pores, but rather the surfaces of the particles were smooth and the diameter of the columns near the top measured ~100 μm.

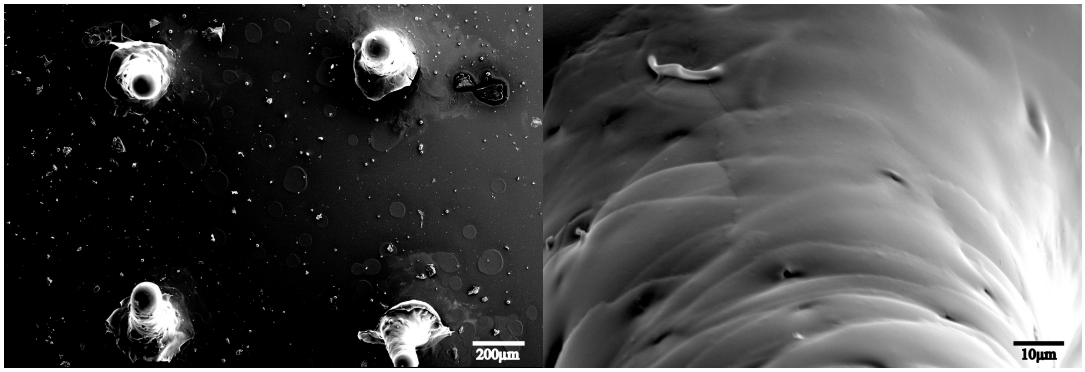

Figure 7-4 Two SEM (secondary electron) images at 15KeV; (left) Array of fully active silk particles made up of 500 layers containing catalase enzyme (4 mg/ml), RSF (30 mg/ml) and PEG_{400}; (right) enlarged view of the side of a column.

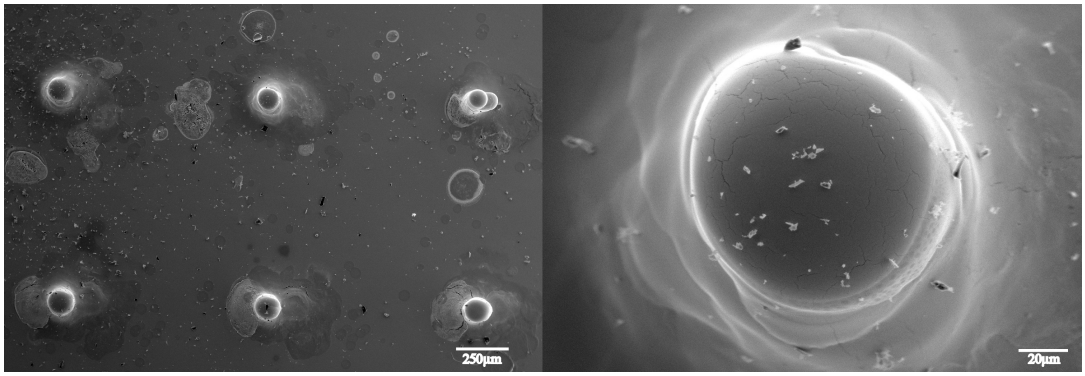

Figure 7-5 Two SEM (secondary electron) images at 10KeV; (left) Array of Janus printed particles viewed from above consisting of 10 layers of PMMA as a barrier layer; (right) close up image of the top surface of a column printed silk swimmer, the diameter of the column is around 100 μm.

Closer comparison of fully active particles and Janus particles showed that despite the difference in the distribution of enzyme, the overall size and shape remained

comparable, as shown representatively by two fully active particles in Figure 7-6 and two Janus particles in Figure 7-7 (which also contain 5 layers of PMMA as a barrier layer between the active and inactive half). The images show that during the printing process a little material sometimes flowed over the sides down the particles. As shown representatively in the initial schematic in Figure 7-1 the lower half of the Janus particle contained silk together with enzyme. During LBL printing of the silk-inks some ink ran along the outer side of the forming rockets. This clarifies why this approach: printing first the half containing the enzyme catalyst resulted in better defined Janus structures than first printing the inactive rocket half, as the enzyme containing silk-ink would have flowed over the inactive side. The localisation of catalase enzyme was verified by printing FITC labelled catalase in fully active and Janus rockets as shown in Figure 7-8, where the fully active rocket clearly contains catalase all over and the Janus rocket only contains catalase on the bottom half of the particle. It can be seen that the columns were slightly wider towards the bottom than the top, giving rise to a rocket-like shape, but measurements suggest that the change was quite minimal with regards to the particle size and to the order of a maximum ~20 μm, but ultimately giving the particles more of a rocket structure than a simple rod-shape.

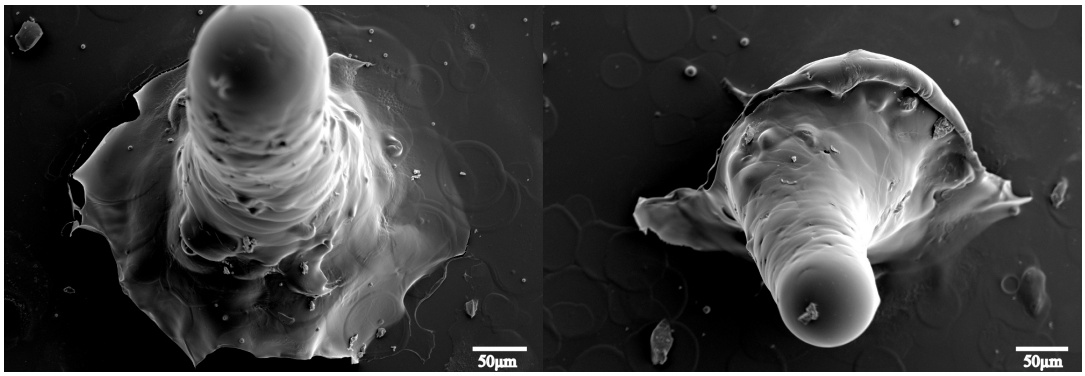

Figure 7-6 Two secondary electron images (at 12 KeV) of fully active silk swimmer particles containing CAT (4 mg/ml), Silk (30 mg/ml) and PEG_{400} (10 mg/ml).

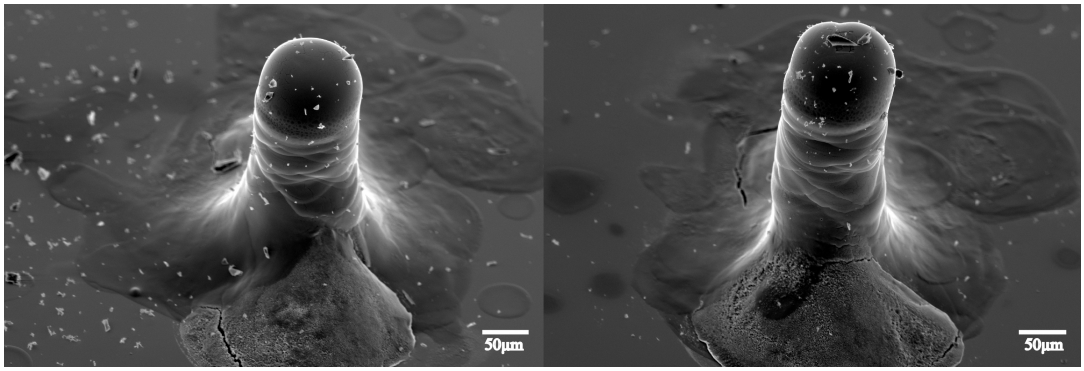

Figure 7-7 Two SEM (secondary electron) images at 14 KeV of representative Janus silk swimmer particles containing CAT (4 mg/ml), Silk (30 mg/ml) and PEG_{400} (10 mg/ml) with 10 layers of PMMA barrier and an inactive part containing silk (30 mg/ml) and PEG_{400} (12 mg/ml).

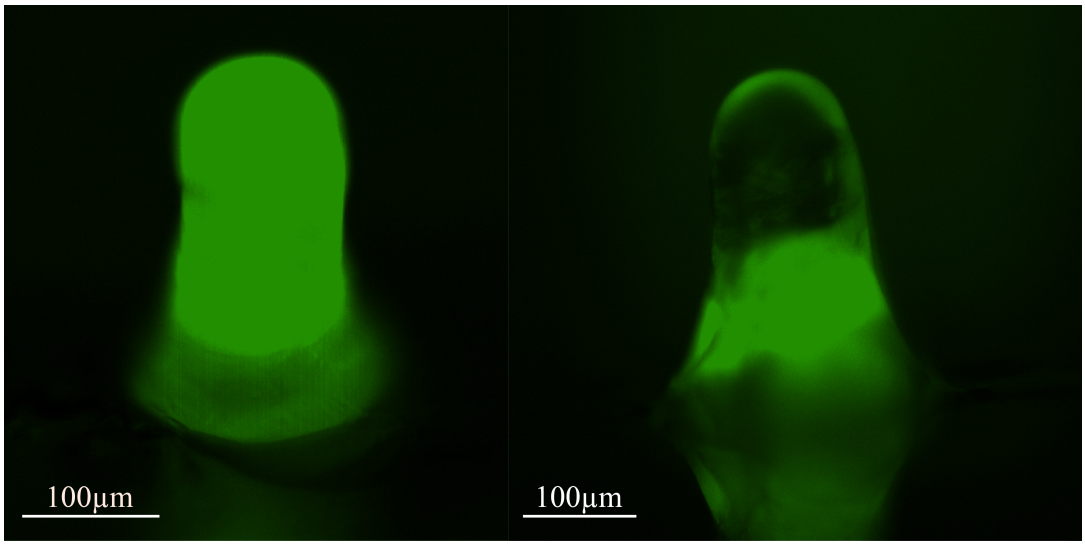

Figure 7-8 Fluorescent microscopy images of FITC labelled catalase in silk rockets, (left) fully active, (right) Janus.

7.3.1.2. Printing Process

In order to compare how mixed-in catalase enzyme affects the printing process, contour GT images were taken of varying layers of silk/PEG with and without catalase. The concentrations used were exactly the same as the concentrations used for the silk swimmer particles. The average height was slightly lower for the layers printed containing catalase enzyme than those without. Example contour GT 3D plots of printed silk scaffolds are shown in Figure 7-9 for silk (30 mg/ml) printed with blended-in PEG_{400} (12 mg/ml) and Figure 7-10 for silk (30 mg/ml) with

catalase (4 mg/ml) and PEG_{400} (10 mg/ml) blended-in. The images also show that in general the printing process containing the enzyme solution generated slightly less defined structures than without the enzyme, seen as a slightly more 'messy' printing result.

The contour GT images showed clearly that for the first few layers printed there was a strong "coffee ring" effect present, where in particular the outer wall seemed to gain height more quickly; but this effect seemed to diminish when more than 20 layers had been printed. However, there was an indication that the inner side of the columns might contain hollow channels, which could allow gas to flow easily though the structure from the active side of the particles to the inactive side, explaining the need for a barrier layer in the case of Janus particles.

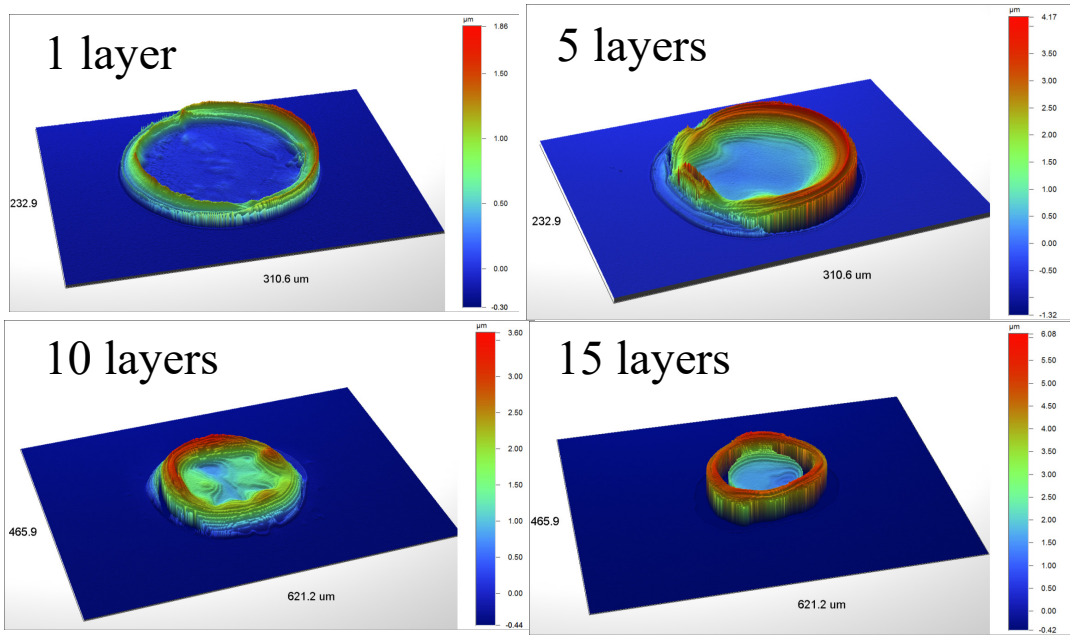

Figure 7-9 Example contour GT images of different amounts of silk (30 mg/ml) containing PEG_{400} (12 mg/ml) printed on Si-wafer substrates showing how the height is affected by the amount of layers printed on top of each other.

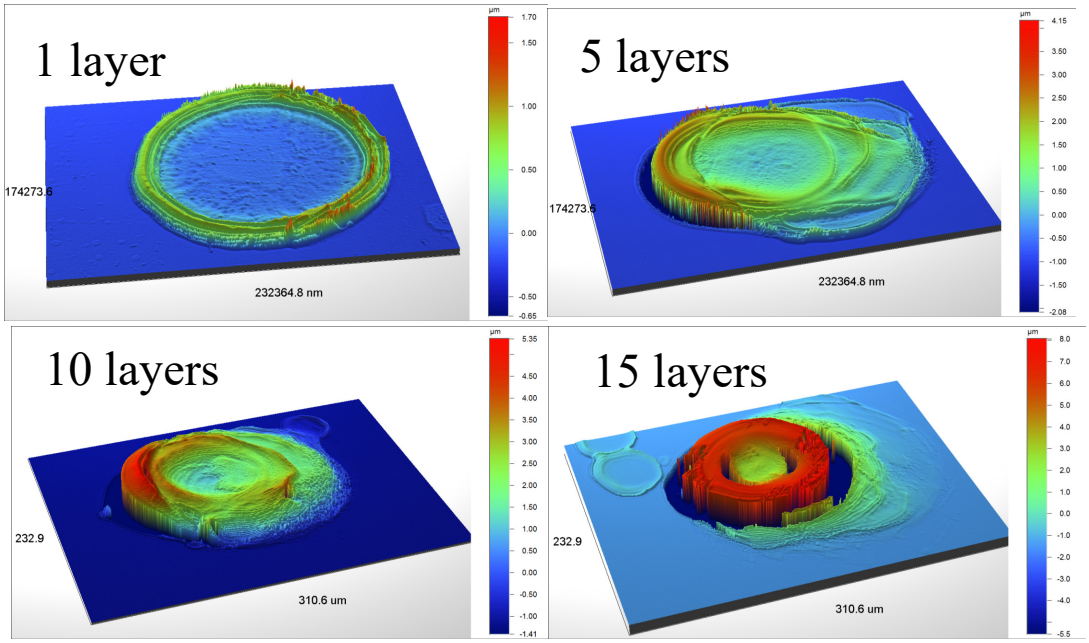

Figure 7-10 Example contour GT images of different amounts of silk (30 mg/ml) containing PEG_{400} (10 mg/ml) and catalase enzyme (4 mg/ml) printed on Si-wafer substrates showing how the height is affected by the amount of layers printed on top of each other.

There was a clear relationship between height and amount of layers printed as shown in Figure 7-11 , which was very similar for both the ink solution containing enzyme and that without, where the ink without enzyme seemed to gain height slightly more rapidly than the one containing enzyme. This would fit in with the observation of the two previous figures, where columns seemed to be formed in a more defined manner for ink without enzymes.

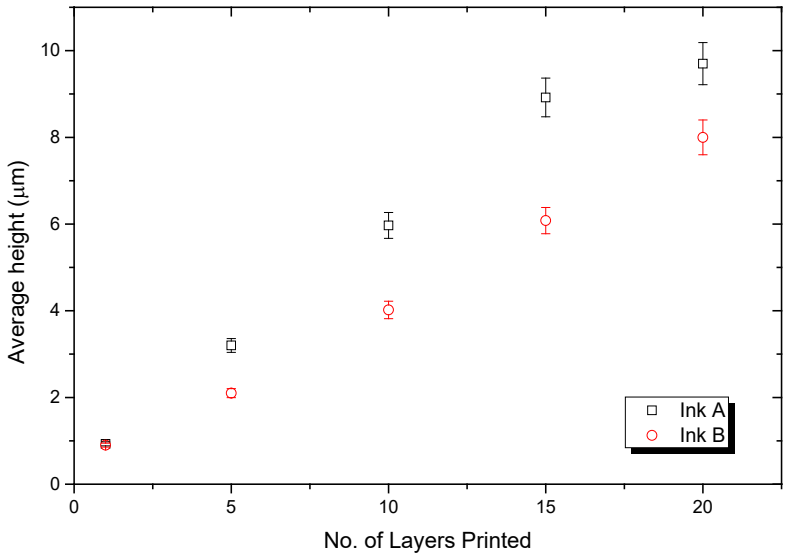

Figure 7-11 Comparison of average height measurements of silk printed columns as used for the Active particles Ink A (30 mg/ml silk, 12 mg/ml PEG_{400}), Ink B (30mg/ml silk, 4 mg/ml catalase, 10 mg/ml PEG_{400}), measurements done kindly by Yu Zhang

7.3.2. Influence of PEG_{400}

During the printing process of the silk solution containing enzyme molecules it became apparent that there was a build-up of materials on the tip of the print head nozzle which meant that the ink jet alignment gradually misaligned, generating less defined structures or even causing the structures to collapse. Frequent cleaning of the print head was therefore required. In order to help minimize this effect PEG_{400} was blended into the silk ink solution. Even though this did not completely remove the problem it did allow for longer printing before too much material accumulated and it was necessary to clean the print head.

In addition to this, initial experimental data showed that when printed silk particles with enzyme but without PEG_{400} were placed into 5% hydrogen peroxide fuel, even though bubbles were readily released from the silk particles in the bulk solution (working medium), there was a high tendency for one or more bubbles to build up at the liquid / air interface sticking to the particles and not bursting. This effect is

shown in Figure 7-12, which depicts a fully active particle with no PEG blended-in before (left) and after 30 seconds (right) in 5% w/v H_2O_2. The bubble can be clearly seen growing over the time period but not detaching. These lingering bubbles would cause the particles to merely swim around the bubble rather than moving freely around. With the addition of PEG_{400} it was then seen that in most cases this type of 'lingering' bubble did not occur and particles moved around freely on the surface interface (Movie S7.1).

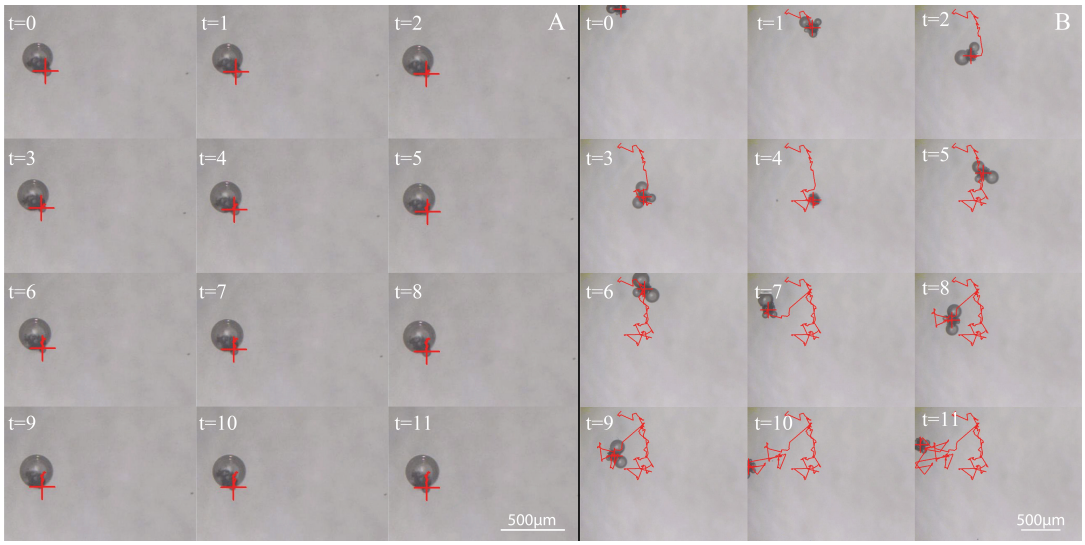

Figure 7-12 Silk swimmer containing catalase enzymes but no blended in PEG_{400} (A) showing the bubble detachment / popping issue - Image is taken from above so looking down onto the particles, (B) Silk swimmer containing PEG_{400}. (CD Chapter 7 Movie S7.1, (S7.2 no PMMA barrier))

In the case of Janus particles it was observed that if the inactive silk side contained no PEG or a lower amount of PEG than the active side there was a high probability of lingering bubbles appearing and inhibiting the free motion of the particles. This was therefore dealt with by having a slightly higher concentration of PEG present on the side containing no enzyme.

In order to be able to understand these results better an attempt was made to look at how the PEG_{400} content affected the hydrophobicity of the silk scaffold by means of contact angle measurement.

5 layers of silk containing different amounts of PEG_{400} were spun cast onto silicon wafer substrates. Between every layer of silk a layer of methanol was spun cast in order to generate the β-sheet silk structure. The samples were then left to dry overnight at room temperature before the contact angle on the dried silk surfaces was measured 5 times per sample with 2 µl water drops. Results indicated that the contact angle decreased with increasing PEG_{400} concentration as shown in Figure 7-13 but errors were high, probably because the process of spin coating multiple layers of silk onto silicon wafers was not very accurate.

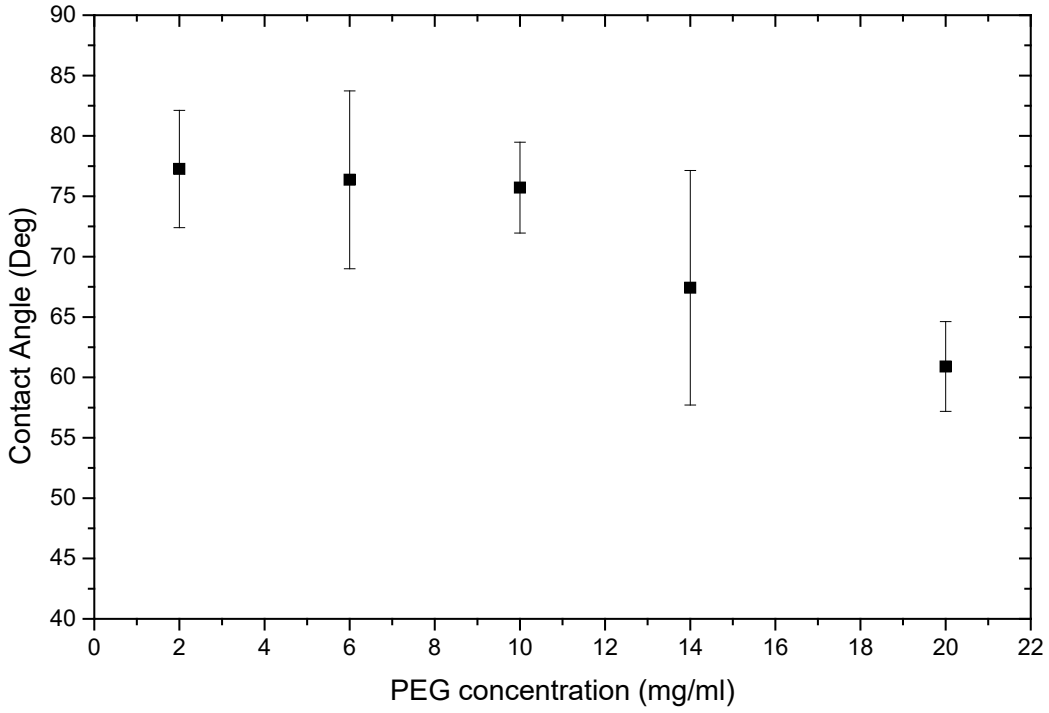

Figure 7-13 Contact angle measurements of 5 layers of spun cast silk (20 mg/ml) with different concentrations of PEG_{400} blended in.

7.3.3. Trajectory Analysis

During imaging it was important to ensure that there was no air movement present in the room and that particles were not too close to the glass walls of the petri dish as otherwise the surface tension effects of water could cause particles to float

towards the edges. For all recorded trajectory data it was therefore ensured these factors were taken into consideration. Representative fully active and Janus Rockets are shown in Figure 7-14 (Movie S7.3) and Figure 7-15 (Movie S7.4) respectively.

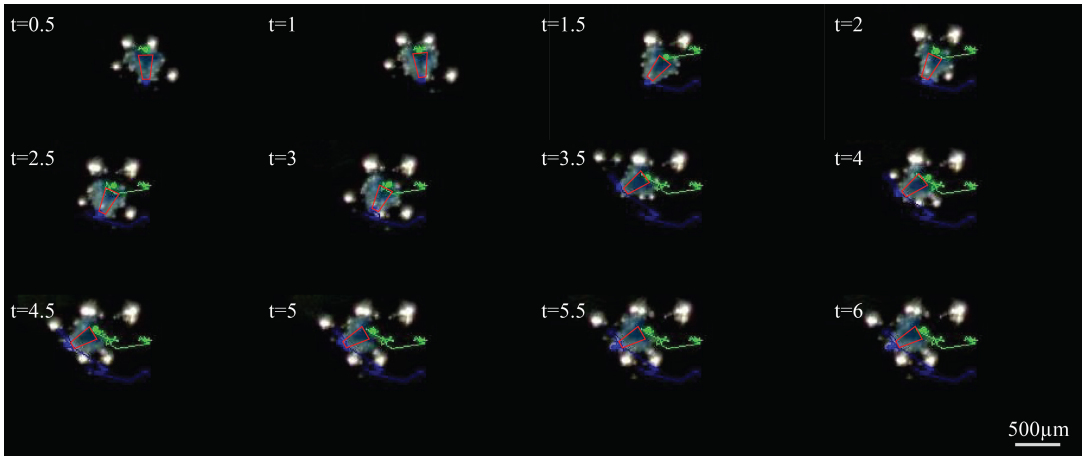

Figure 7-14 Example image captures of a fully active silk rocket swimming in 5% H_2O_2 solution – blue line indicates top and green bottom of the rockets (CD Movie S7.3).

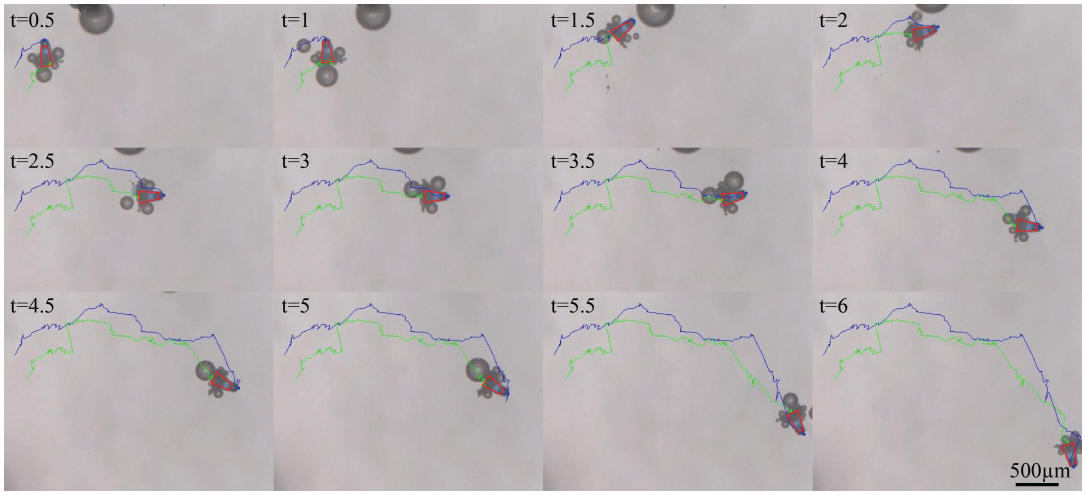

Figure 7-15 Example image captures of a Janus silk rocket swimming in 5% H_2O_2 solution – blue line indicates top and green bottom of the rockets (CD Movie S7.4).

7.3.3.1. Directionality analysis – alignment of particle to its direction of motion

Qualitatively the raw trajectories, plotted in Figure 7-16, of the two different types of micro-rockets showed that the fully active micro-rockets had trajectories that had more turns and twists in them, whereas the Janus micro-rocket trajectories on the

whole were more directional resembling straighter lines. It should be noted that the Janus micro-rockets could not be tracked for the same length of time as the fully active ones as they moved out of the region of interest much more quickly due to their straighter trajectories, hence the overall trajectories were shorter for Janus particles.

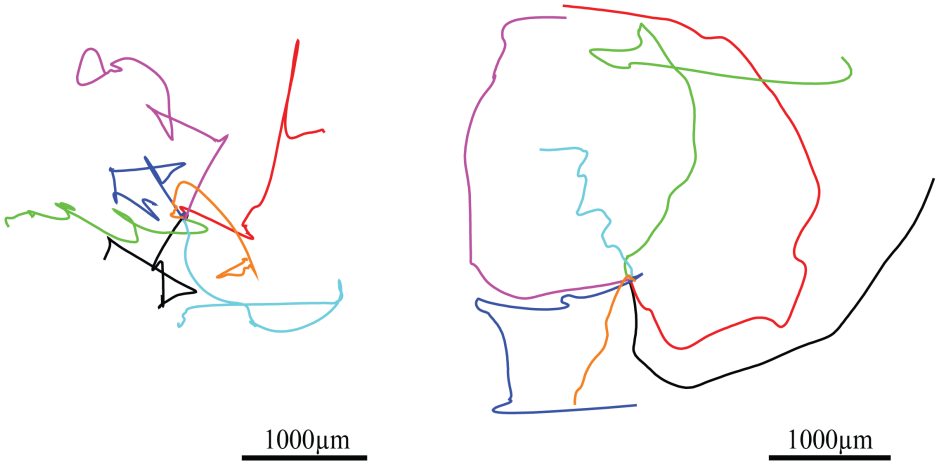

Figure 7-16 Comparison of raw trajectories, (left) fully active particles over a period of ~10 seconds, (right) Janus particles over a period of ~5-10seconds.

Using the directionality analysis previously described in Section 7.2.4 (Figure 7-3) the angles θ (direction) and φ (orientation) were investigated, and showed that fully active and Janus silk swimmers gave strongly different results. As shown in Figure 7-17 there was no noticeable correlation between θ and φ for fully active micro-rockets, where the calculated correlation coefficient over the sample set was $r^2 = 0.003 \pm 0.017$. On the other hand for Janus particles there was a very strong correlation, with the correlation coefficient calculated to be $r^2 = 0.656 \pm 0.023$, as shown with some example correlation data in Figure 7-18. It was also found that sometimes the high correlation of the two angles got interrupted if a bubble grew

larger than the average, as the release of this bubble (popping) would then cause the particle to move a large distance in the opposite direction to the released bubble.

Fully active micro-rockets also showed a slight tendency to move sideways along the longitudinal axis rather than along the transverse axis. This can probably be explained by bubbles being more likely to be released from the wide side of the particle than at the narrow extremities.

It is important to note that the angles for this analysis were calculated using the tangent function and therefore jumps in the data appeared when the angle changed from 0° to 360°.

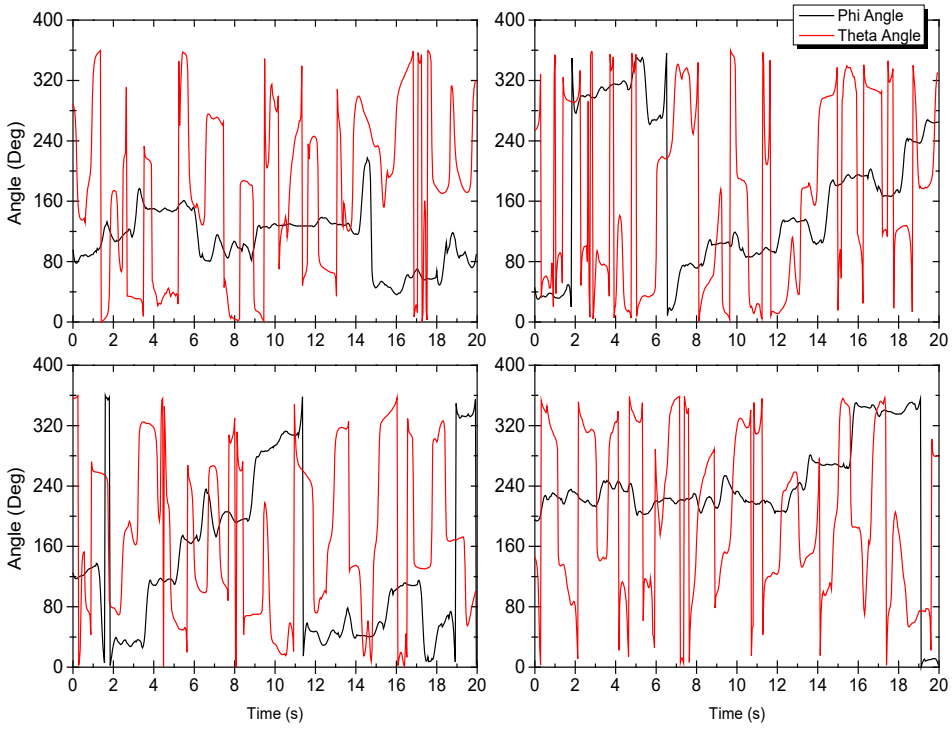

Figure 7-17 Angle Correlation (θ (direction) and φ (orientation)) of fully active silk swimmers overall correlation for all samples was $r = 0.053 \pm 0.130$.

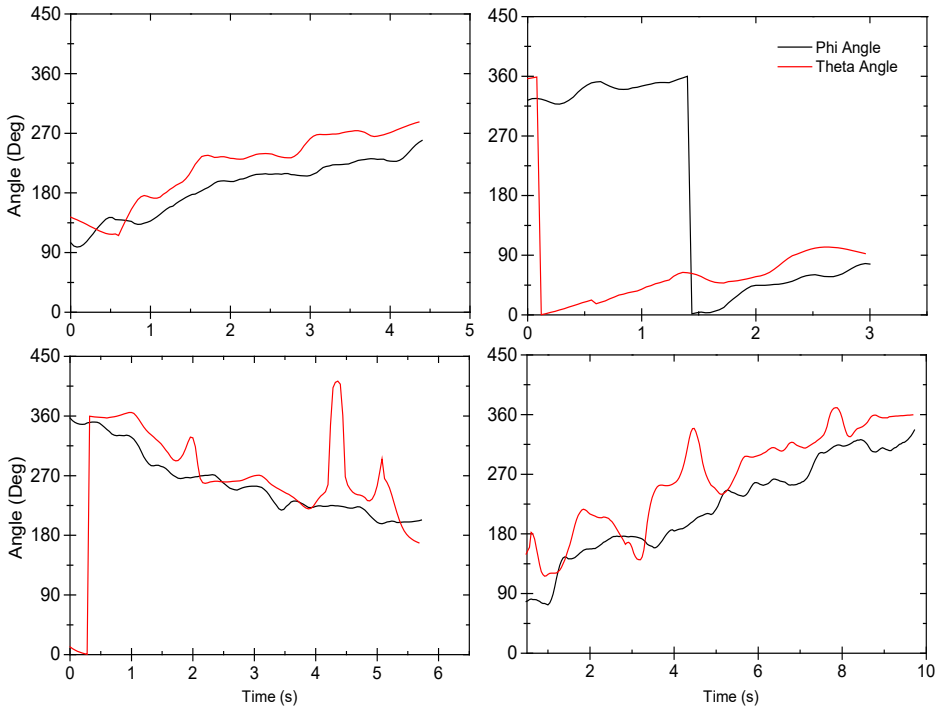

Figure 7-18 Angle correlation (θ (direction) and φ (orientation)) for Janus silk swimming particles overall correlation of $r = 0.806 \pm 0.146$ for all samples.

7.3.3.2. Velocity and Persistence length

Based on the calculated centre of mass trajectory from the dual tracked micro-rockets, trajectories were analysed for their mean instantaneous velocities and their persistence lengths. Instantaneous velocities were calculated for every frame and averaged over the whole trajectory. The results are shown in Table 7.1, and it can be seen that despite the lower amount of catalase present in the Janus micro-rockets, on average these rockets moved ~1.4 times faster than fully active ones. A decrease in velocity of ~1/3rd over the course of 1 hour was observed during the experiment. This velocity decrease was comparable to the decrease in the amount of bubbles observed to be released from the micro-rockets over this time course (comparing the initial and final bubble releases).

Persistence length analysis (shown in Table 7.1), previously described in Chapter 2 Section 2.3.4, of the centre of mass trajectories fitted in with the orientation correlation analysis (Section 7.3.3.1) and confirms that printed Janus silk micro-rockets had on average a ~16 times higher persistence length than fully active ones (persistence length of Janus micro-rockets divided by fully active micro-rockets). Because the trajectories of Janus and fully active particles were of different lengths, the persistence length data was also corrected for the trajectory length (longer length on average for fully active particles) by dividing the persistence length by the total track length. The relative persistence length calculated this way also agreed with the previous results showing a ~13 times higher relative persistence length of the Janus micro-rockets compared to the fully active micro-rockets.

It is interesting to note that MSD data fitting gave very similar velocity results to the instantaneous averaged velocities shown here. Mean squared gyration and fractal dimension analysis techniques were not conclusive, most likely due to trajectories being not long enough for clear results.

Table 7.1 Velocity and persistence length data for Silk swimmers

Type of Micromotor	Average velocity [μm/s]	Persistence length [μm]	L_P/L_C [arb. units]
Fully Active rocket	**370 ± 31**	**26 ± 6**	**0.014 ± 0.002**
Janus rocket	**511 ± 93**	**423 ± 183**	**0.191 ± 0.063**
Fully Active rocket In 2% Serum	**282 ± 13**	**40 ± 4**	**NA**
Janus rocket In 2% Serum	**338 ± 16**	**135 ± 14**	**NA**

7.3.4. Biocompatibility of enzyme-powered micromotors – ability to swim in biological solutions

Silk micromotors were tested in 2 % and 10 % human serum containing 3 % w/v hydrogen peroxide as a fuel source. In both cases particles showed motion but it was hard to pinpoint the exact location of the particles as many bubbles appeared in the solution due to the natural foaming of human serum solution. In the 2 % solution it was much easier to determine the whereabouts of the swimmer, as can be seen from fully active Figure 7-19 (Movie S7.5). In the case of 10 % serum solution bubbles ended up completely covering the surface in the area of the active particles, as shown in Figure 7-20. More directionality could be objectively seen for Janus rockets in 2% human serum as can be seen from Figure 7-21 (Movie S7.6) corresponding to the previously reported increase in persistence length (Table 7.1). In view of the amount of bubbles released by the particles over the course of 30 minutes there was no indication that the reaction rate decreased by any substantial amount in this time. This therefore strongly suggests that the activity barely decreased throughout the experiment, but quantitative measurements were not possible. Visually comparing the same swimmers in pure hydrogen peroxide and human serum containing hydrogen peroxide the amount of bubbling appeared very similar, indicating that unlike for platinum based swimmers as described in Chapter 6 no biofouling, or very little biofouling of the catalyst occurred. Furthermore propulsion was present despite no addition of surfactants to the bulk solution.

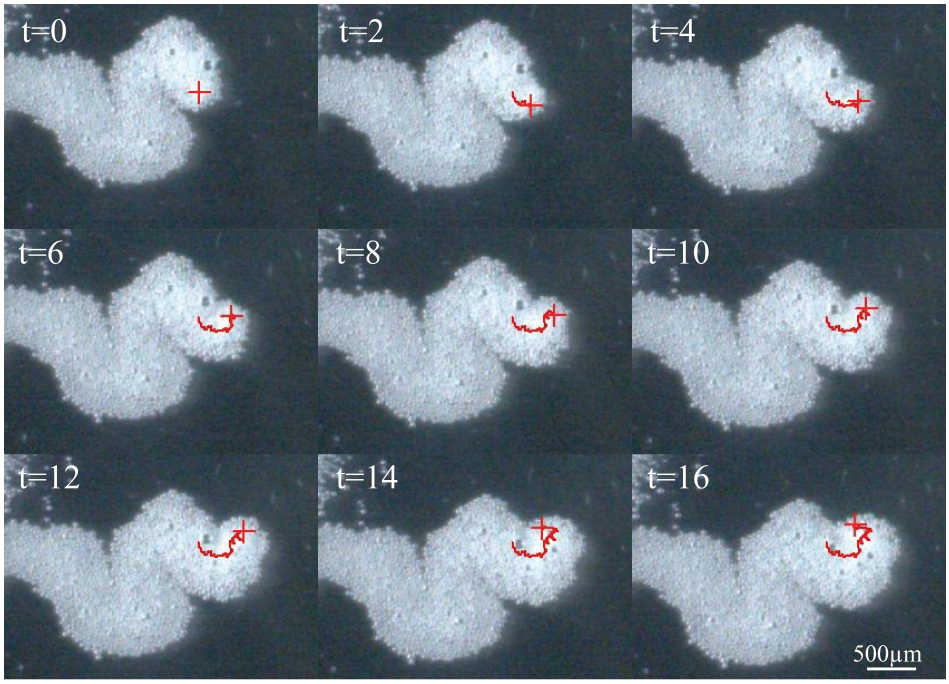

Figure 7-19 example of a fully active silk swimmer swimming in 2% serum containing 3% w/v hydrogen peroxide as a fuel source (CD Movie S7.5).

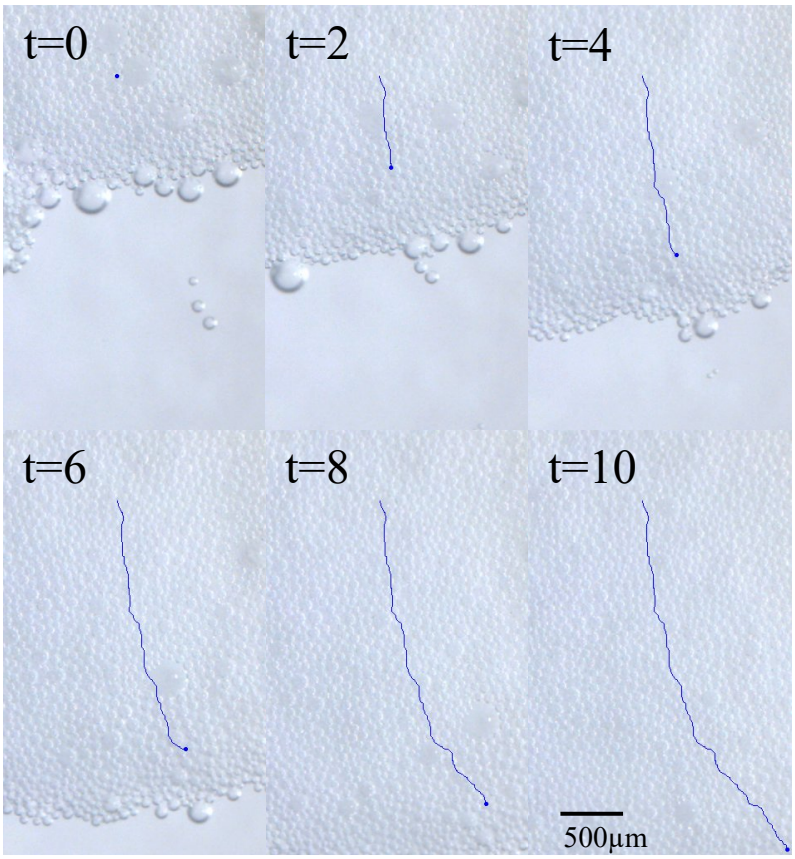

Figure 7-20 example of a fully active silk swimmer in 10% serum solution containing 3% w/v hydrogen peroxide as a fuel source.

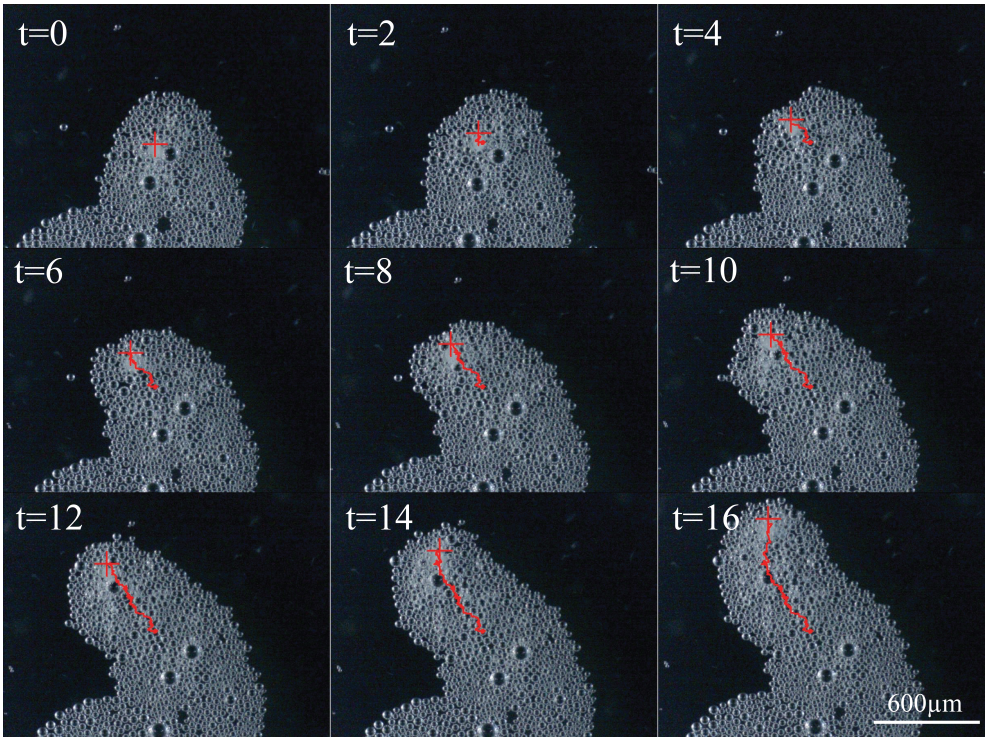

Figure 7-21 Janus silk rocket swimming in 2% Human Serum with 3% H_2O_2 (CD Movie S7.6).

7.3.5. Lifetime of enzyme incorporated in silk structure vs. free enzyme

The pH of 5 % hydrogen peroxide was measured to be ~4.2. This pH is not very suitable for long-term enzyme activity. Activity measurements of free catalase enzyme in 5% H_2O_2 solution showed that within 10 minutes over 90% of enzyme activity was lost. In contrast motion of silk swimmer particles seemed to have dropped by only 1/3rd of the initial speed after at least one hour in 5 % H_2O_2. This was coupled with the observation that the overall bubbling of the particles was slightly lower. It was also quite obvious that bubbling was highest for the first few minutes after incubation.

This could indicate that the initial activity decrease was caused by the outermost layers of enzymes denaturing due to the acid pH, while the enzymes within the silk lattice were still protected from the harsh acidic environment. The results indicate

that the use of silk may allow prolongation of enzyme lifetime and extension of the possible environments in which they can be used.

7.3.6. Optimisation of micro-rockets printing process

The possible denaturing of catalase enzyme via methanol during the printing process was considered, but after testing printed micro-rockets containing catalase printed with methanol, the residual catalase activity was seen to be substantial enough to achieve significant bubble propulsion.

All silk particles containing active catalase enzyme underwent bubble propulsion at the water/air interface throughout the entire experiments. Micro-rockets containing no active enzymes or placed in blank water solutions rapidly dropped to the bottom of the bulk solution and showed no motion at all. In some cases micro-rockets stayed attached to the meniscus.

Initial testing of silk concentrations showed that it was necessary for the ink solution to have at least 20 mg/ml RSF in order to achieve a good and consistent column structure. Micro-rockets that printed successfully at 10 mg/ml RSF appeared as sponge-like structures and did not keep their shape fully, but they did show high retention of enzyme activity for long periods of time: 2 hours or more in harsh pH environments of ~4 (5% w/v H_2O_2 solution).

It is important to note that micro-rockets printed as columns (30 mg/ml RSF), in the manner previously depicted in Figure 7-1, demonstrated specific orientation positions at the air / solution interface; they were either hanging down (Figure 7-22 left) or laying sideways (Figure 7-22 right), as was the intended orientation.

Figure 7-22 Comparison of fully active column printed silk swimmers, oriented downwards (left) and sideways (right).

7.4. Discussion

From the results presented here it has become clear that enzyme immobilization within silk scaffolds in order to generate self-motile particles via RIJ such as the ones made in this experiment, is a convenient manufacturing process without the need for complicated covalent coupling chemistry. It is also possible to generate different trajectory behaviour based on the shape or area where the active species was printed. In the simple experiment reported here, two kinds of particles were made; fully active micro-rockets and Janus micro-rockets. It was shown that the Janus micro-rockets followed much straighter trajectories with a much greater persistence length than micro-rockets that were active on all sides. The latter showed much more undefined trajectories moving equally in all directions as shown by the results in Table 7.1.

The relationship between catalyst distribution and trajectory behaviour found here, can be compared to similar results found for spherical bubble swimmers with different amounts of platinum exposed causing changes in trajectory behaviour [74] (see Chapter 4). Analysis of the particles' orientation angle together with the particles direction agreed with the results obtained from persistence length measurements.

It was shown that despite Janus micro-rockets having half the amount of active enzyme present, the particles showed faster motion due to their directionality, indicating that coordination of the region of bubbling can help to substantially increase swimmer efficiency. The velocities obtained (370-500 μm/s) were comparable to velocities of bubble propelled microjets [71, 73].

This method of immobilizing enzymes via silk is much cheaper, easier and quicker than on metal surfaces because coupling agents use complicated chemistry and often cause high loss of enzyme activity as they, in general, attack several areas of an enzyme which can lead to enzyme denaturation during the immobilization process [82, 199, 200]. In contrast, in the present process enzymes are immobilized via chemisorption and encapsulation into the silk scaffolds during the formation of the β-sheet structure of silk [185] from Silk I to Silk II. It was shown that when printing columns it was of benefit to use a layer of PMMA to help isolate the active printed side from the inactive printed side, as otherwise bubbles would sometimes leak though. Predominantly the bubbles seemed to leak through the centre of the column. It seems possible that there are small hollow channels in the centre of the column structure (caused by the “coffee ring” effect during printing) indicated by the contour GT images which could be implicated in this behaviour. This in itself might be useful for printing other types of self- motile particles for which a hollow channel might be beneficial. It was also shown that immobilising catalase enzyme into the silk scaffold materials resulted in extended enzyme activity even at low pH in comparison to free enzyme molecules, which could be a very useful property when considering possible future uses for silk-based devices.

Results of the height versus number of layers printed showed that there was a slight difference in height when the ink solution contained enzymes. Printing of these

columns was not as well-defined as ones from ink containing no enzymes. This may partly explain why the enzyme containing columns were slightly shorter than those without enzymes incorporated into the columns. The most likely reason for this is that the enzyme containing ink solution accumulated enzyme molecules at the tip of the print head meaning it had to be regularly cleaned during the printing procedure. Thus the alignment of the ink jet would gradually move off centre until the next cleaning step and therefore the ink would not repeatedly print in exactly the same location. Another reason might be that the printed silk ink containing the enzyme did not dry as quickly as silk ink containing only silk.

It was found that blending in PEG_{400} helped minimize the accumulation of enzyme contamination on the tip of the print head, meaning that cleaning of the print head did not need to be done as frequently, but it was still necessary after 50 to 100 layers of printing. Apart from this effect PEG also improved the release of bubbles from the micro-rockets at the air/water interface meaning that there was no need for particles to have any kind of surfactant added to the bulk solution to help with bubble release (as shown in Figure 7-12), unlike the case of most bubble propelled microengines [70, 77].

Further it was shown that silk based micro-rockets powered by catalase do not show signs of biofouling (unlike Pt. surfaces do) [201] in biomaterials such as human serum. They are capable of undergoing motion without any need for surfactants introduced into the sample, as well as being seemingly unaffected by the vast amounts of different salts present in this type of solution. They are able to undergo motion even at very high concentrations of 10% human serum with only 3% w/v hydrogen peroxide fuel added.

7.5. Conclusions

Investigations showed that the immobilization of enzymes in LBL printed silk scaffolds is very easy to achieve without any major loss of enzyme activity. The generated structures are porous enough to allow fuel solutions to seep into the micro-rockets and therefore induce bubble propelled motion of the printed micro-rockets as was demonstrated using catalase as the motor for 5% w/v fuel solutions.

Trajectory analysis using persistence length and comparison of particle orientation and direction showed that trajectories were altered dependent on the printed structure and position of the enzyme molecules. This meant that it was possible to exert some considerable degree of control of the trajectories via the digitally defined printed structure of these micro-rockets. Thus for fully active micro-rockets the trajectories are of random diffusive behaviour, whereas for Janus printed micro-rockets, trajectories mainly follow straight lines, which greatly increases the directionality and overall velocity of the micro-rockets. This indicates a higher efficiency, as the amount of enzyme present in Janus micro-rockets is only half of that in the fully active micro-rockets. Inkjet printing appears to offer a chance to rapidly design, manufacture and test a wide range of swimming devices with different catalyst distributions, shapes and sizes. With the addition of blended-in PEG_{400} it was possible to help the release of bubbles from the silk structures at the air / liquid interface. This also meant that there was no need for the addition of any surfactants into the bulk (sample) solution, thus making these particles highly biocompatible since surfactants added to the test sample can cause adverse effects such as unfolding of enzymes. An additional advantage of this approach is that the entrapped enzyme molecules survive longer in harsh pH environments (e.g. pH ~4), where free enzyme molecules survive only briefly. Thus, silk swimmers could

swim for time periods of over 60 minutes with a loss of only around 1/3rd of their initial velocity whereas in comparison, free catalase could not survive longer than 15 minutes in the same conditions (90% activity loss).

Finally it was shown that silk printed micro-rockets showed excellent biocompatibility: they did not need any addition of surfactant to the bulk solution they swam in, and further showed good swimming capabilities in biological solutions, such as 1-10% human serum.

7.6. Future work

The work presented here shows that there is huge scope for developing more efficient, versatile self-motile particles based on printed silk scaffolds.

As was shown in Figure 7-22 the column printed particles have a slight disadvantage as they can be orientated in two directions. Brief tests carried out on sideways printed particles, as shown in the schematic in Figure 7-23, showed that these particles are always orientated in the sideways direction but printing Janus particles proved to be difficult. Better control of this could generate more efficient particles. In order for this to work properly, particles have to be printed overlapping slightly.

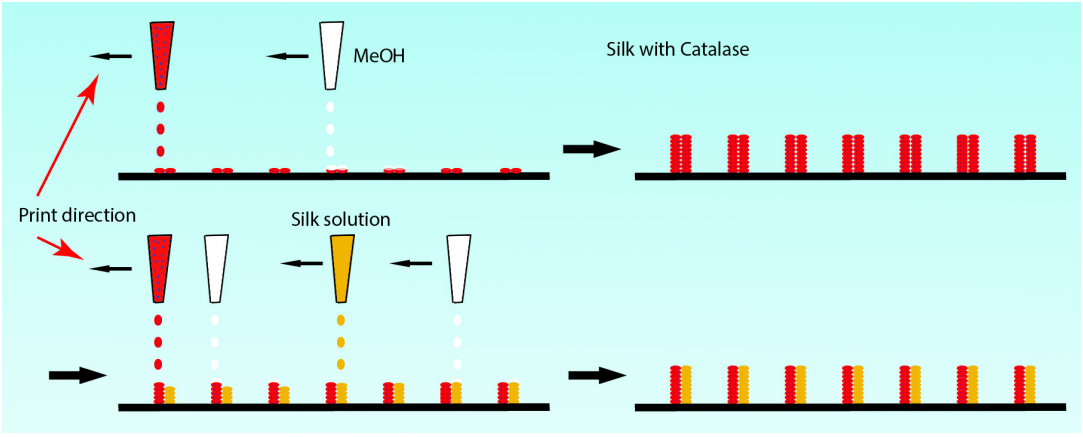

Figure 7-23 Schematic representing the layer by layer printing procedure of Silk scaffolds with (red with dots) and without (orange) catalase enzyme molecules.

There are various possibilities, both using different materials and combining materials, to enable the production of multi-functional particles which can exhibit different functions such as targeted release and delivery of drugs and other substances.

By using print heads with a smaller diameter (e.g. 30 µm) it should be possible to generate even more defined shapes and smaller particles.

Introducing additional external control by incorporating magnetic nanoparticles for example, into silk-based swimmers could give even more control over the particles and also allow for simple recovery of particles from solutions.

Further studies should be made on how the silk concentration and also PEG concentration affects the particles and their motion and bubble behaviour.

Alternative enzyme powered silk micro-rockets powered by a combination of catalase enzyme, together with glucose oxidase enzyme could be a key to being able to generate micro-rockets that do not need the harsh chemical addition of hydrogen peroxide. Instead addition of glucose and good oxygen flow should allow glucose oxidase to produce hydrogen peroxide fuel, which can directly be used by

catalase for generating bubble propelled motion, without the acidic pH values (pH ~4) which accompany the addition of hydrogen peroxide fuel solutions. Further to this development it would be highly interesting to immobilise antibodies or other bio-recognition elements onto the rockets and enable these to get new functions which can help with applications such as targeted cancer cell recognition and transport.

Vepari et al. [202] demonstrate how to use a 3D silk scaffold to immobilise enzymes into a scaffold to generate a gradient of enzyme concentration. This might be interesting in order to generate enzyme gradients for propulsion or pumping applications similar to those I describe in my experimental Chapter 4.

8. Conclusions

This thesis looks at various aspects of self-motile particles that undergo both phoretic phenomena and bubble propulsion. In the first experimental chapter, Chapter 3, I describe my investigations into the effects of reaction rate and salts on the motion of phoretic colloids. These studies have led to a better understanding of self-phoretic propulsion mechanisms, and have resulted in altering the previously accepted model for self-diffusiophoretic propulsive devices which contain a reaction rate gradient on their surface. Here I have found that the reaction rate gradient influences the propulsion mechanism for Janus micromotors in such a way that both self-diffusiophoresis and self-electrophoresis are present, thus making the velocity of these devices sensitive to salt concentrations. The results reported here have been published in *Europhysics Letters* (EPL) [147]. Further to this I investigated the effects of volume fraction on symmetrically active colloids (Chapter 4) and found that at certain volume fractions these induce strong convective flows, whereas at low volume fractions they undergo Brownian motion despite undergoing high reaction rates.

I have looked at the biocompatibility of micromotors, since this could be important for many of their future applications. Having found a low salt tolerance for phoretic micromotors I focused my efforts on bubble-propelled micromotors, because they showed salt tolerance. This is important for biocompatibility, as most systems contain high salt concentrations. Most current bubble-propelled systems have a requirement for surfactants in order to achieve motion, however the spherical platinum based colloids I used did not need the addition of surfactant to swim in pure hydrogen peroxide, therefore it was possible for me to test these particles in human serum without the addition of surfactants (Chapter 6). My experiment

resulted in a better understanding of the effects of surfactants such as SDS on the bubble propulsion of micromotors in biofluids: it was seen that the main effect of surfactants in the fluids studied is to stop the biofouling of the catalytic surface rather than to reduce surface tension, as has been claimed by most of the literature. Having found that platinum-based bubble-propelled micromotors are not compatible with biofluids I ventured to generate micromotors that were based on the enzyme catalase immobilised into biocompatible silk scaffolds (Chapter 7). These showed excellent biocompatibility and swimming motion even at high serum concentrations of 10% and appear to show improved potential for use in biological systems in the future.

The ability to be able to control the resulting trajectories of bubble-propelled micromotors is another highly desirable challenge. As there are multiple examples of trajectory control and analysis of phoretic systems I have looked at bubble-propelled devices and attempted to control their trajectories by altering the area of reactivity, as reported in my experimental Chapter 5. Because to date there are no generally accepted approaches for analysing motion of bubble-propelled devices I successfully investigated various analysis methods (Persistence length, Fractal Dimension and Mean Squared Gyrations) in order to be able to quantitatively compare different devices for the first time. This work resulted in a publication on the effect of catalytic distribution on spherical bubble swimmers in *Journal of Physical Chemistry C* [74]. Following on from this I investigated the feasibility of reactive inkjet printing of catalase powered microrockets (digitally defining catalyst location) using silk as a scaffold material and applied the same analytical methods described above in order to characterise the resulting trajectories (Chapter 7). In this final experimental Chapter I was able, for the first time in the swimmer field, to

digitally define a swimmer structure and to print this via layer-by-layer printing generating versatile microrockets which can incorporate other futuristic components such as magnetic nanoparticles and other enzymes. This work has now been published by *Small [203]* and received the Inner cover page [204] shown in Appendix 10.1.

9. References

[1] A. Einstein, "Zur Theorie der Brownschen Bewegung," *Annalen der Physik,* vol. 324, pp. 371-381, 1906.

[2] E. M. Purcell, "Life At Low Reynolds-Number," *American Journal of Physics,* vol. 45, pp. 3-11, 1977.

[3] M. Leoni, J. Kotar, B. Bassetti, P. Cicuta, and M. C. Lagomarsino, "A basic swimmer at low Reynolds number," *Soft Matter,* vol. 5, pp. 472-476, 2009.

[4] A. Najafi and R. Golestanian, "Propulsion at low Reynolds number," *Journal of Physics-Condensed Matter,* vol. 17, pp. S1203-S1208, Apr 13, 2005.

[5] K. F. Jarrell and M. J. McBride, "The surprisingly diverse ways that prokaryotes move," *Nat Rev Micro,* vol. 6, pp. 466-476, Jul 2008.

[6] E. M. Purcell, "The efficiency of propulsion by a rotating flagellum," *Proceedings of the National Academy of Sciences,* vol. 94, pp. 11307-11311, Oct 14, 1997.

[7] R. Dreyfus, J. Baudry, M. L. Roper, M. Fermigier, H. A. Stone, and J. Bibette, "Microscopic artificial swimmers," *Nature,* vol. 437, pp. 862-865, Oct 6, 2005.

[8] M. Al-Fandi, M. A. K. Jaradat, K. Fandi, J. P. Beech, J. O. Tegenfeldt, and T. C. Yih, "Nano-engineered living bacterial motors for active microfluidic mixing," *Iet Nanobiotechnology,* vol. 4, pp. 61-71, Sep 2010.

[9] S. J. Wang and N. Wu, "Selecting the Swimming Mechanisms of Colloidal Particles: Bubble Propulsion versus Self-Diffusiophoresis," *Langmuir,* vol. 30, pp. 3477-3486, Apr 2014.

[10] J. G. Gibbs and Y. P. Zhao, "Autonomously motile catalytic nanomotors by bubble propulsion," *Applied Physics Letters,* vol. 94, Apr 20, 2009.

[11] R. Kapral, "Perspective: Nanomotors without moving parts that propel themselves in solution," *Journal of Chemical Physics,* vol. 138, Jan 2013.

[12] Z. Ghalanbor, S. A. Marashi, and B. Ranjbar, "Nanotechnology helps medicine: Nanoscale swimmers and their future applications," *Medical Hypotheses,* vol. 65, pp. 198-199, 2005.

[13] A. K. Philip and B. Philip, "Colon targeted drug delivery systems: a review on primary and novel approaches," *Oman medical journal,* vol. 25, pp. 79-87, Apr 2010.

[14] W. Xi, A. A. Solovev, A. N. Ananth, D. H. Gracias, S. Sanchez, and O. G. Schmidt, "Rolled-up magnetic microdrillers: towards remotely controlled minimally invasive surgery," *Nanoscale,* vol. 5, pp. 1294-1297, 2013.

[15] D. Patra, S. Sengupta, W. Duan, H. Zhang, R. Pavlick, and A. Sen, "Intelligent, self-powered, drug delivery systems," *Nanoscale,* vol. 5, pp. 1273-1283, 2013.

[16] A. A. Solovev, S. Sanchez, M. Pumera, Y. F. Mei, and O. G. Schmidt, "Magnetic Control of Tubular Catalytic Microbots for the Transport, Assembly, and Delivery of Micro-objects," *Advanced Functional Materials,* vol. 20, pp. 2430-2435, Aug 9, 2010.

[17] A. A. Solovev, W. Xi, D. H. Gracias, S. M. Harazim, C. Deneke, S. Sanchez*, et al.*, "Self-Propelled Nanotools," *Acs Nano,* vol. 6, pp. 1751-1756, Feb 2012.

[18] L. Baraban, M. Tasinkevych, M. N. Popescu, S. Sanchez, S. Dietrich, and O. G. Schmidt, "Transport of cargo by catalytic Janus micro-motors," *Soft Matter,* vol. 8, pp. 48-52, 2012.

[19] J. Palacci, S. Sacanna, A. Vatchinsky, P. M. Chaikin, and D. J. Pine, "Photoactivated Colloidal Dockers for Cargo Transportation," *Journal of the American Chemical Society,* vol. 135, pp. 15978-15981, Oct 30, 2013.

[20] J. Simmchen, A. Baeza, D. Ruiz, M. Jose Esplandiu, and M. Vallet-Regi, "Asymmetric Hybrid Silica Nanomotors for Capture and Cargo Transport: Towards a Novel Motion-Based DNA Sensor," *Small,* vol. 8, pp. 2053-2059, Jul 9, 2012.

[21] K. E. Peyer, S. Tottori, F. Qiu, L. Zhang, and B. J. Nelson, "Magnetic Helical Micromachines," *Chemistry-a European Journal,* vol. 19, pp. 28-38, Jan 2013.

[22] P. Fischer and A. Ghosh, "Magnetically actuated propulsion at low Reynolds numbers: towards nanoscale control," *Nanoscale,* vol. 3, pp. 557-563, 2011.

[23] L. O. Mair, B. Evans, A. R. Hall, J. Carpenter, A. Shields, K. Ford*, et al.*, "Highly controllable near-surface swimming of magnetic Janus nanorods: application to payload capture and manipulation," *Journal of Physics D-Applied Physics,* vol. 44, Mar 30, 2011.

[24] Y. Wu, Z. Wu, X. Lin, Q. He, and J. Li, "Autonomous Movement of Controllable Assembled Janus Capsule Motors," *Acs Nano,* vol. 6, pp. 10910-10916, Dec 2012.

[25] L. Baraban, D. Makarov, R. Streubel, I. Mönch, D. Grimm, S. Sanchez*, et al.*, "Catalytic Janus Motors on Microfluidic Chip: Deterministic Motion for Targeted Cargo Delivery," *ACS Nano,* vol. 6, pp. 3383-3389, Apr 24, 2012.

[26] L. Soler, C. Martinez-Cisneros, A. Swiersy, S. Sanchez, and O. G. Schmidt, "Thermal activation of catalytic microjets in blood samples using microfluidic chips," *Lab on a Chip,* vol. 13, pp. 4299-4303, 2013.

[27] L. Soler and S. Sanchez, "Catalytic nanomotors for environmental monitoring and water remediation," *Nanoscale,* vol. 6, pp. 7175-7182, 2014.

[28] J. Li, V. V. Singh, S. Sattayasamitsathit, J. Orozco, K. Kaufmann, R. Dong*, et al.*, "Water-Driven Micromotors for Rapid Photocatalytic Degradation of Biological and Chemical Warfare Agents," *ACS Nano,* vol. 8, pp. 11118–11125, 2014.

[29] W. Gao, X. Feng, A. Pei, Y. Gu, J. Li, and J. Wang, "Seawater-driven magnesium based Janus micromotors for environmental remediation," *Nanoscale,* vol. 5, pp. 4696-4700, 2013.

[30] S. J. Ebbens and J. R. Howse, "Direct Observation of the Direction of Motion for Spherical Catalytic Swimmers," *Langmuir,* vol. 27, pp. 12293-12296, Oct 2011.

[31] S. Ebbens, M. H. Tu, J. R. Howse, and R. Golestanian, "Size dependence of the propulsion velocity for catalytic Janus-sphere swimmers," *Physical Review E,* vol. 85, Feb 2012.

[32] J. R. Howse, R. A. L. Jones, A. J. Ryan, T. Gough, R. Vafabakhsh, and R. Golestanian, "Self-motile colloidal particles: From directed propulsion to random walk," *Physical Review Letters,* vol. 99, Jul 27, 2007.

[33] S. J. Ebbens, G. A. Buxton, A. Alexeev, A. Sadeghi, and J. R. Howse, "Synthetic running and tumbling: an autonomous navigation strategy for catalytic nanoswimmers," *Soft Matter,* vol. 8, pp. 3077-3082, 2012.

[34] M. Manjare, B. Yang, and Y. P. Zhao, "Bubble Driven Quasioscillatory Translational Motion of Catalytic Micromotors," *Physical Review Letters,* vol. 109, p. 5, Sep 2012.

[35] N. H. Fletcher, "Size Effect in Heterogeneous Nucleation," *The Journal of Chemical Physics,* vol. 29, pp. 572-576, 1958.

[36] J. Palacci, B. Abecassis, C. Cottin-Bizonne, C. Ybert, and L. Bocquet, "Colloidal Motility and Pattern Formation under Rectified Diffusiophoresis," *Physical Review Letters,* vol. 104, Apr 2, 2010.

[37] J. P. Ebel, J. L. Anderson, and D. C. Prieve, "Diffusiophoresis of Latex-Particles in Electrolyte Gradients," *Langmuir,* vol. 4, pp. 396-406, Apr 1988.

[38] S. Balasubramanian, D. Kagan, K. M. Manesh, P. Calvo-Marzal, G.-U. Flechsig, and J. Wang, "Thermal Modulation of Nanomotor Movement," *Small,* vol. 5, pp. 1569-1574, Jul 3, 2009.

[39] S. Ebbens, R. A. L. Jones, A. J. Ryan, R. Golestanian, and J. R. Howse, "Self-assembled autonomous runners and tumblers," *Physical Review E,* vol. 82, Jul 23, 2010.

[40] U. Choudhury, L. Soler, J. G. Gibbs, S. Sanchez, and P. Fischer, "Surface roughness-induced speed increase for active Janus micromotors," *Chemical Communications,* vol. 51, pp. 8660-8663, 2015.

[41] P. Dhar, T. M. Fischer, Y. Wang, T. E. Mallouk, W. F. Paxton, and A. Sen, "Autonomously moving nanorods at a viscous interface," *Nano Letters,* vol. 6, pp. 66-72, Jan 2006.

[42] J. Kim, S. Garoff, J. L. Anderson, and L. J. M. Schlangen, "Movement of Colloidal Particles in Two-Dimensional Electric Fields," *Langmuir,* vol. 21, pp. 10941-10947, Nov 1, 2005.

[43] Y. Wang, R. M. Hernandez, D. J. Bartlett, Jr., J. M. Bingham, T. R. Kline, A. Sen*, et al.*, "Bipolar electrochemical mechanism for the propulsion of catalytic nanomotors in hydrogen peroxide solutions," *Langmuir,* vol. 22, pp. 10451-10456, Dec 5, 2006.

[44] L. Li, J. Wang, T. Li, W. Song, and G. Zhang, "Hydrodynamics and propulsion mechanism of self-propelled catalytic micromotors: model and experiment," *Soft Matter,* vol. 10, pp. 7511-7518, 2014.

[45] V. Magdanz, G. Stoychev, L. Ionov, S. Sanchez, and O. G. Schmidt, "Stimuli-Responsive Microjets with Reconfigurable Shape," *Angewandte Chemie-International Edition,* vol. 53, pp. 2673-2677, Mar 3, 2014.

[46] N. I. Kovtyukhova, "Toward understanding of the propulsion mechanism of rod-shaped nanoparticles that catalyze gas-generating reactions," *Journal of Physical Chemistry C,* vol. 112, pp. 6049-6056, Apr 17, 2008.

[47] A. A. Solovev, Y. Mei, E. B. Urena, G. Huang, and O. G. Schmidt, "Catalytic Microtubular Jet Engines Self-Propelled by Accumulated Gas Bubbles," *Small,* vol. 5, pp. 1688-1692, Jul 17, 2009.

[48] L. Restrepo-Perez, L. Soler, C. Martinez-Cisneros, S. Sanchez, and O. G. Schmidt, "Biofunctionalized self-propelled micromotors as an alternative on-chip concentrating system," *Lab on a Chip,* vol. 14, pp. 2914-2917, Aug 21, 2014.

[49] V. M. Fomin, M. Hippler, V. Magdanz, L. Soler, S. Sanchez, and O. G. Schmidt, "Propulsion Mechanism of Catalytic Microjet Engines," *Ieee Transactions on Robotics,* vol. 30, pp. 40-48, Feb 2014.

[50] I. S. M. Khalil, V. Magdanz, S. Sanchez, O. G. Schmidt, and S. Misra, "Wireless Magnetic-Based Closed-Loop Control of Self-Propelled Microjets," *Plos One,* vol. 9, Feb 5, 2014.

[51] L. K. E. A. Abdelmohsen, F. Peng, Y. Tu, and D. A. Wilson, "Micro- and nano-motors for biomedical applications," *Journal of Materials Chemistry B,* vol. 2, pp. 2395-2408, 2014.

[52] W. Gao, A. Uygun, and J. Wang, "Hydrogen-Bubble-Propelled Zinc-Based Microrockets in Strongly Acidic Media," *Journal of the American Chemical Society,* vol. 134, pp. 897-900, Jan 2012.

[53] H. Wang, G. Zhao, and M. Pumera, "Crucial Role of Surfactants in Bubble-Propelled Microengines," *Journal of Physical Chemistry C,* vol. 118, pp. 5268-5274, Mar 13, 2014.

[54] W. Gao, M. D'Agostino, V. Garcia-Gradilla, J. Orozco, and J. Wang, "Multi-Fuel Driven Janus Micromotors," *Small,* vol. 9, pp. 467-471, Feb 11, 2013.

[55] W. Gao, A. Pei, and J. Wang, "Water-Driven Micromotors," *Acs Nano,* vol. 6, pp. 8432-8438, Sep 2012.

[56] N. K. Reddy and C. Clasen, "Self-propelling micro-disks," *Korea-Australia Rheology Journal,* vol. 26, pp. 73-79, Feb 2014.

[57] T. Niidome, M. Yamagata, Y. Okamoto, Y. Akiyama, H. Takahashi, T. Kawano*, et al.*, "PEG-modified gold nanorods with a stealth character for in vivo applications," *Journal of Controlled Release,* vol. 114, pp. 343-347, Sep 2006.

[58] K. Knop, R. Hoogenboom, D. Fischer, and U. S. Schubert, "Poly(ethylene glycol) in Drug Delivery: Pros and Cons as Well as Potential Alternatives," *Angewandte Chemie-International Edition,* vol. 49, pp. 6288-6308, 2010.

[59] D. E. Owens and N. A. Peppas, "Opsonization, biodistribution, and pharmacokinetics of polymeric nanoparticles," *International Journal of Pharmaceutics,* vol. 307, pp. 93-102, Jan 2006.

[60] F. Yuan, M. Leunig, S. K. Huang, D. A. Berk, D. Papahadjopoulos, and R. K. Jain, "Microvascular Permeability and Interstitial Penetration of Sterically Stabilized (Stealth) Liposomes in a Human Tumor Xenograft," *Cancer Research,* vol. 54, pp. 3352-3356, Jul 1994.

[61] H. A. Harper, *Review of Physiological Chemistry*, 11th ed. Oxford & Edinburgh: Blackwell Scientific Publications, Lange Medical Publications, 1967.

[62] W. F. Paxton, P. T. Baker, T. R. Kline, Y. Wang, T. E. Mallouk, and A. Sen, "Catalytically induced electrokinetics for motors and micropumps," *Journal of the American Chemical Society,* vol. 128, pp. 14881-14888, Nov 22 2006.

[63] H. Wang, G. J. Zhao, and M. Pumera, "Beyond Platinum: Bubble-Propelled Micromotors Based on Ag and MnO2 Catalysts," *Journal of the American Chemical Society,* vol. 136, pp. 2719-2722, Feb 2014.

[64] J. Orozco, V. Garcia-Gradilla, M. D'Agostino, W. Gao, A. Cortes, and J. Wang, "Artificial Enzyme-Powered Microfish for Water-Quality Testing," *Acs Nano,* vol. 7, pp. 818-824, Jan 2013.

[65] J. Vicario, R. Eelkema, W. R. Browne, A. Meetsma, R. M. La Crois, and B. L. Feringa, "Catalytic molecular motors: fuelling autonomous movement by a surface bound synthetic manganese catalase," *Chemical Communications,* pp. 3936-3938, 2005.

[66] M. Garcia, J. Orozco, M. Guix, W. Gao, S. Sattayasamitsathit, A. Escarpa*, et al.*, "Micromotor-based lab-on-chip immunoassays," *Nanoscale,* vol. 5, pp. 1325-1331, 2013.

[67] F. Kuralay, S. Sattayasamitsathit, W. Gao, A. Uygun, A. Katzenberg, and J. Wang, "Self-Propelled Carbohydrate-Sensitive Microtransporters with Built-In Boronic Acid Recognition for Isolating Sugars and Cells," *Journal of the American Chemical Society,* vol. 134, pp. 15217-15220, Sep 19, 2012.

[68] S. Balasubramanian, D. Kagan, C.-M. J. Hu, S. Campuzano, M. J. Lobo-Castanon, N. Lim*, et al.*, "Micromachine-Enabled Capture and Isolation of Cancer Cells in Complex Media," *Angewandte Chemie-International Edition,* vol. 50, pp. 4161-4164, 2011.

[69] J. Orozco, S. Campuzano, D. Kagan, M. Zhou, W. Gao, and J. Wang, "Dynamic Isolation and Unloading of Target Proteins by Aptamer-Modified Microtransporters," *Analytical Chemistry,* vol. 83, pp. 7962-7969, Oct 15, 2011.

[70] W. Gao, S. Sattayasamitsathit, J. Orozco, and J. Wang, "Highly Efficient Catalytic Microengines: Template Electrosynthesis of Polyaniline/Platinum Microtubes," *Journal of the American Chemical Society,* vol. 133, pp. 11862-11864, Aug 10, 2011.

[71] W. Gao, S. Sattayasamitsathit, J. Orozco, and J. Wang, "Efficient bubble propulsion of polymer-based microengines in real-life environments," *Nanoscale,* vol. 5, pp. 8909-8914, 2013.

[72] S. Sanchez, A. A. Solovev, S. Schulze, and O. G. Schmidt, "Controlled manipulation of multiple cells using catalytic microbots," *Chemical Communications,* vol. 47, pp. 698-700, 2011.

[73] S. Sanchez, A. N. Ananth, V. M. Fomin, M. Viehrig, and O. G. Schmidt, "Superfast Motion of Catalytic Microjet Engines at Physiological Temperature," *Journal of the American Chemical Society,* vol. 133, pp. 14860-14863, Sep 28, 2011.

[74] D. A. Gregory, A. I. Campbell, and S. J. Ebbens, "Effect of Catalyst Distribution on Spherical Bubble Swimmer Trajectories," *The Journal of Physical Chemistry C,* vol. 119, pp. 15339-15348, 06/10/ 2015.

[75] R. Kumar, M. Kiristi, F. Soto, J. Li, V. V. Singh, and J. Wang, "Self-propelled screen-printable catalytic swimmers," *RSC Advances,* vol. 5, pp. 78986-78993, 2015.

[76] W. Zhu, J. Li, Y. J. Leong, I. Rozen, X. Qu, R. Dong*, et al.*, "3D-Printed Artificial Microfish," *Advanced Materials,* vol. 27, pp. 4411-4417, 2015.

[77] X. Wang, B.-T. Lee, and A. Son, "Physical lysis only (PLO) methods suitable as rapid sample pretreatment for qPCR assay," *Applied Microbiology and Biotechnology,* vol. 98, pp. 8719-8728, Oct 2014.

[78] M. J. Rosen and J. T. Kunjappu, "Surfactants and Interfacial Phenomena, 4th Edition," in *Surfactants and Interfacial Phenomena, 4th Edition*, ed, 2012, pp. 1-122.

[79] L. M. Kushner, B. C. Duncan, and J. I. Hoffman, "A viscometric study of the micelles of sodium dodecyl sulfate in dilute solutions," *Journal of Research of the National Bureau of Standards,* vol. 49, pp. 85-90, 1952.

[80] P. Nicholls, "Classical catalase: Ancient and modern," *Archives of Biochemistry and Biophysics,* vol. 525, pp. 95-101, 2012.

[81] M. Alfonso-Prieto, X. Biarnes, P. Vidossich, and C. Rovira, "The Molecular Mechanism of the Catalase Reaction," *Journal of the American Chemical Society,* vol. 131, pp. 11751-11761, Aug 2009.

[82] R. A. Sheldon, "Enzyme immobilization: The quest for optimum performance," *Advanced Synthesis & Catalysis,* vol. 349, pp. 1289-1307, Jun 2007.

[83] S. A. Costa and R. L. Reis, "Immobilisation of catalase on the surface of biodegradable starch-based polymers as a way to change its surface characteristics," *Journal of Materials Science-Materials in Medicine,* vol. 15, pp. 335-342, Apr 2004.

[84] M. Koneracká, P. Kopčansky, M. Antalík, M. Timko, C. N. Ramchand, D. Lobo*, et al.*, "Immobilization of proteins and enzymes to fine magnetic particles," *Journal of Magnetism and Magnetic Materials,* vol. 201, pp. 427-430, 1999.

[85] M. H. Liao and D. H. Chen, "Immobilization of yeast alcohol dehydrogenase on magnetic nanoparticles for improving its stability," *Biotechnology Letters,* vol. 23, pp. 1723-1727, Oct 2001.

[86] A. Prabhune and H. Sivaraman, "Immobilization of Penicillin Acylase in Porous Beads of Polyacrylamide-Gel," *Applied Biochemistry and Biotechnology,* vol. 30, pp. 265-272, Sep 1991.

[87] Y. Ren, J. G. Rivera, L. He, H. Kulkarni, D.-K. Lee, and P. B. Messersmith, "Facile, high efficiency immobilization of lipase enzyme on magnetic iron oxide nanoparticles via a biomimetic coating," *Bmc Biotechnology,* vol. 11, Jun 8, 2011.

[88] Q. A. Feng, X. Xia, A. F. Wei, X. Q. Wang, Q. F. Wei, D. Y. Huo*, et al.*, "Preparation of Cu(II)-Chelated Poly(vinyl alcohol) Nanofibrous Membranes for Catalase Immobilization," *Journal of Applied Polymer Science,* vol. 120, pp. 3291-3296, Jun 2011.

[89] D. Pantarotto, W. R. Browne, and B. L. Feringa, "Autonomous propulsion of carbon nanotubes powered by a multienzyme ensemble," *Chemical Communications,* pp. 1533-1535, 2008.

[90] R. J. Archer, A. I. Campbell, and S. J. Ebbens, "Glancing angle metal evaporation synthesis of catalytic swimming Janus colloids with well defined angular velocity," *Soft Matter,* vol. 11, pp. 6872-6880, 2015.

[91] L. F. Valadares, Y. G. Tao, N. S. Zacharia, V. Kitaev, F. Galembeck, R. Kapral*, et al.*, "Catalytic Nanomotors: Self-Propelled Sphere Dimers," *Small,* vol. 6, pp. 565-572, Feb 2010.

[92] A. I. Campbell and S. J. Ebbens, "Gravitaxis in Spherical Janus Swimming Devices," *Langmuir,* vol. 29, pp. 14066-14073, Nov 19, 2013.

[93] X. Wang, M. In, C. Blanc, M. Nobili, and A. Stocco, "Enhanced active motion of Janus colloids at the water surface," *Soft Matter,* 2015.

[94] S. Das, A. Garg, A. I. Campbell, J. Howse, A. Sen, D. Velegol*, et al.*, "Boundaries can steer active Janus spheres," *Nature Communications,* vol. 6, p. 10, Dec 2015.

[95] G. Dunderdale, S. Ebbens, P. Fairclough, and J. Howse, "Importance of Particle Tracking and Calculating the Mean-Squared Displacement in Distinguishing Nanopropulsion from Other Processes," *Langmuir,* vol. 28, pp. 10997-11006, Jul 2012.

[96] S. J. Ebbens, "Active colloids: Progress and challenges towards realising autonomous applications," *Current Opinion in Colloid & Interface Science,* vol. 21, pp. 14-23, 2015.

[97] P. Fuchs, "Low-pressure plasma cleaning of Au and PtIr noble metal surfaces," *Applied Surface Science,* vol. 256, pp. 1382-1390, Dec 15, 2009.

[98] C. A. Dukes and R. A. Baragiola, "Compact plasma source for removal of hydrocarbons for surface analysis," *Surface and Interface Analysis,* vol. 42, pp. 40-44, Jan 2010.

[99] D. T. W. Toolan, S. Fujii, S. J. Ebbens, Y. Nakamura, and J. R. Howse, "On the mechanisms of colloidal self-assembly during spin-coating," *Soft Matter,* vol. 10, pp. 8804-8812, 2014.

[100] J. R. Groza, "Physical Vapor Deposition," in *Materials Processing Handbook*, ed Boca Raton, FL: CRC Press, 2007, pp. 8-7.

[101] M. Nur-E-Alam, M. Vasiliev, and K. Alameh, "Bi3Fe5O12: Dy2O3 composite thin film materials for magneto-photonics and magneto-plasmonics," *Optical Materials Express,* vol. 4, pp. 1866-1875, Sep 1, 2014.

[102] J. Musil, P. Baroch, J. Vlcek, K. H. Nam, and J. G. Han, "Reactive magnetron sputtering of thin films: present status and trends," *Thin Solid Films,* vol. 475, pp. 208-218, Mar 22, 2005.

[103] M. Nur-E-Alam, M. Vasiliev, and K. Alameh, "Nano-structured magnetic photonic crystals for magneto-optic polarization controllers at the communication-band wavelengths," *Optical and Quantum Electronics,* vol. 41, pp. 661-669, Jul 2009.

[104] P. J. Kelly and R. D. Arnell, "Magnetron sputtering: a review of recent developments and applications," *Vacuum,* vol. 56, pp. 159-172, Mar 2000.

[105] D. Maurya, A. Sardarinejad, and K. Alameh, "Recent Developments in R.F. Magnetron Sputtered Thin Films for pH Sensing Applications—An Overview," *Coatings,* vol. 4, p. 756, 2014.

[106] G. Sauerbrey, "Verwendung von Schwingquarzen zur Wägung dünner Schichten und zur Mikrowägung," *Zeitschrift für Physik,* vol. 155, pp. 206-222, Apr 1, 1959.

[107] B.Mason and L. Berry, *Elements of Mineralogy*: W. H. Freeman & Co. Ltd, 1968.

[108] R. L. Adams and J. Roy, "A One-Dimensional Numerical Model of a Drop-On-Demand Ink Jet," *Journal of Applied Mechanics-Transactions of the Asme,* vol. 53, pp. 193-197, Mar 1986.

[109] J. F. Dijksman, "Hydrodynamics of small tubular pumps," *Journal of Fluid Mechanics,* vol. 139, pp. 173-191, 1984.

[110] D. B. Bogy and F. E. Talke, "Experimental and Theoretical Study of Wave Propagation Phenomena in Drop-on-Demand Ink Jet Devices," *Ibm Journal of Research and Development,* vol. 28, pp. 314-321, 1984.

[111] Y. Noda, H. Minemawari, H. Matsui, T. Yamada, S. Arai, T. Kajiya*, et al.*, "Underlying Mechanism of Inkjet Printing of Uniform Organic Semiconductor Films Through Antisolvent Crystallization," *Advanced Functional Materials,* vol. 25, pp. 4022-4031, Jul 8, 2015.

[112] D. Elkington, M. Wasson, W. Belcher, P. C. Dastoor, and X. Zhou, "Printable organic thin film transistors for glucose detection incorporating inkjet-printing of the enzyme recognition element," *Applied Physics Letters,* vol. 106, Jun 29, 2015.

[113] H.-l. Kao, C.-L. Cho, L.-C. Chang, and Y.-H. Wu, "Inkjet-printed silver film on multilayer liquid crystal polymer for fabricating a miniature stub-loaded bandpass filter," *Thin Solid Films,* vol. 584, pp. 198-203, Jun 1, 2015.

[114] M. Bissannagari and J. Kim, "Inkjet printing of NiZn-ferrite films and their magnetic properties," *Ceramics International,* vol. 41, pp. 8023-8027, Jul 2015.

[115] H. D. Young, R. A. Freedman, and A. L. Ford, "Chapter 36 Diffraction," in *University Physics with Modern Physics*, 13. ed: Addison-Wesley, 2011.

[116] R. N. Wenzel, "Surface Roughness and Contact Angle," *The Journal of Physical and Colloid Chemistry,* vol. 53, pp. 1466-1467, Sep 1, 1949.

[117] Y. Yuan and T. R. Lee, "Contact Angle and Wetting Properties," in *Surface science techniques*, G. Bracco and B. Holst, Eds., ed Berlin; New York: Springer, 2013, pp. 3-34.

[118] T. Young, "An Essay on the Cohesion of Fluids," *Philosophical Transactions of the Royal Society of London,* vol. 95, pp. 65-87, Jan 1, 1805.

[119] P. Samori, "Microcantilever Sensors," in *STM and AFM Studies on (Bio)molecular Systems: Unravelling the Nanoworld*, ed: Springer Berlin Heidelberg, 2009.

[120] H. D. Young, R. A. Freedman, and A. L. Ford, "Chapter 14 Periodic Motion," in *University Physics with Modern Physics*, 13. ed: Addison-Wesley, 2011.

[121] A. Banerjee and K. D. Kihm, "Experimental verification of near-wall hindered diffusion for the Brownian motion of nanoparticles using evanescent wave microscopy," *Physical Review E,* vol. 72, Oct 2005.

[122] A. J. Goldman, R. G. Cox, and H. Brenner, "Slow viscous motion of a sphere parallel to a plane wall—I Motion through a quiescent fluid," *Chemical Engineering Science,* vol. 22, pp. 637-651, 1967.

[123] S. T. Mortimer, M. A. Swan, and D. Mortimer, "Fractal analysis of capacitating human spermatozoa," *Human Reproduction,* vol. 11, pp. 1049-1054, May 1996.

[124] B. B. Mandelbrot and J. A. Wheeler, "The Fractal Geometry of Nature," *American Journal of Physics,* vol. 51, pp. 286-287, 1983.

[125] T. A. Witten and L. M. Sander, "Diffusion-limited aggregation, a kinetic critical phenomenon," *Physical Review Letters,* vol. 47, pp. 1400-1403, 1981.

[126] W. C. K. Poon, A. D. Pirie, and P. N. Pusey, "Gelation in colloid-polymer mixtures," *Faraday Discussions,* vol. 101, pp. 65-76, 1995.

[127] T. Vicsek, M. Cserző, and V. K. Horváth, "Self-affine growth of bacterial colonies," *Physica A: Statistical Mechanics and its Applications,* vol. 167, pp. 315-321, Aug 15, 1990.

[128] A. Takahashi, R. Kita, T. Shinozaki, K. Kubota, and M. Kaibara, "Real space observation of three-dimensional network structure of hydrated fibrin gel," *Colloid and Polymer Science,* vol. 281, pp. 832-838, Sep 2003.

[129] M. J. Katz and E. B. George, "Fractals and the analysis of growth paths," *Bulletin of Mathematical Biology,* vol. 47, pp. 273-286, 1985.

[130] D. Li, S. Banon, and S. L. Biswal, "Bending dynamics of DNA-linked colloidal particle chains," *Soft Matter,* vol. 6, pp. 4197-4204, 2010.

[131] M. G. L. van den Heuvel, S. Bolhuis, and C. Dekker, "Persistence Length Measurements from Stochastic Single-Microtubule Trajectories," *Nano Letters,* vol. 7, pp. 3138-3144, Oct 1, 2007.

[132] R. Golestanian, "Synthetic Mechanochemical Molecular Swimmer," *Physical Review Letters,* vol. 105, Jun 2010.

[133] G. Zhao, S. Sanchez, O. G. Schmidt, and M. Pumera, "Poisoning of bubble propelled catalytic micromotors: the chemical environment matters," *Nanoscale,* vol. 5, pp. 2909-2914, 2013.

[134] D. Kagan, P. Calvo-Marzal, S. Balasubramanian, S. Sattayasamitsathit, K. M. Manesh, G.-U. Flechsig*, et al.*, "Chemical Sensing Based on Catalytic Nanomotors: Motion-Based Detection of Trace Silver," *Journal of the American Chemical Society,* vol. 131, p. 12082, Sep 2, 2009.

[135] R. Golestanian, T. B. Liverpool, and A. Ajdari, "Propulsion of a molecular machine by asymmetric distribution of reaction products," *Physical Review Letters,* vol. 94, Jun 10, 2005.

[136] G. Ruckner and R. Kapral, "Chemically powered nanodimers," *Physical Review Letters,* vol. 98, Apr 13, 2007.

[137] B. Sabass and U. Seifert, "Nonlinear, electrocatalytic swimming in the presence of salt," *Journal of Chemical Physics,* vol. 136, Jun 7, 2012.

[138] M. N. Popescu, M. Tasinkevych, and S. Dietrich, "Pulling and pushing a cargo with a catalytically active carrier," *Epl,* vol. 95, Jul 2011.

[139] J. F. Brady, "Particle motion driven by solute gradients with application to autonomous motion: continuum and colloidal perspectives," *Journal of Fluid Mechanics,* vol. 667, pp. 216-259, Jan 2011.

[140] A. G. Hildebrandt and I. Roots, "Reduced nicotinamide adenine-dinucleotide phosphate (nadph)-dependent formation and breakdown of hydrogen-peroxide during mixed-function oxidation reactions in liver-microsomes," *Archives of Biochemistry and Biophysics,* vol. 171, pp. 385-397, 1975.

[141] V. Guarnieri, L. Biazi, R. Marchiori, and A. Lago, "Platinum metallization for MEMS application: Focus on coating adhesion for biomedical applications," *Biomatter,* vol. 4, p. e28822, Apr 17, 2014.

[142] Z. Y. Li, P. Beck, D. A. A. Ohlberg, D. R. Stewart, and R. S. Williams, "Surface properties of platinum thin films as a function of plasma treatment conditions," *Surface Science,* vol. 529, pp. 410-418, Apr 2003.

[143] M. A. Heath and J. H. Walton, "A Study of the Effect of Salts on the Catalytic Decomposition of Hydrogen Peroxide by Colloidal Platinum," *The Journal of Physical Chemistry,* vol. 37, pp. 977-990, Jan 1, 1932.

[144] A. M. Ferraria, A. P. Carapeto, and A. M. Botelho do Rego, "X-ray photoelectron spectroscopy: Silver salts revisited," *Vacuum,* vol. 86, pp. 1988-1991, Jul 20, 2012.

[145] K. Benaissi, L. Johnson, D. A. Walsh, and W. Thielemans, "Synthesis of platinum nanoparticles using cellulosic reducing agents," *Green Chemistry,* vol. 12, pp. 220-222, 2010.

[146] A. S. Arico, A. K. Shukla, H. Kim, S. Park, M. Min, and V. Antonucci, "An XPS study on oxidation states of Pt and its alloys with Co and Cr and its relevance to

electroreduction of oxygen," *Applied Surface Science,* vol. 172, pp. 33-40, Mar 1, 2001.

[147] S. Ebbens, D. A. Gregory, G. Dunderdale, J. R. Howse, Y. Ibrahim, T. B. Liverpool*, et al.*, "Electrokinetic effects in catalytic platinum-insulator Janus swimmers," *EPL (Europhysics Letters),* vol. 106, p. 58003, 2014.

[148] S. B. Hall, E. A. Khudaish, and A. L. Hart, "Electrochemical oxidation of hydrogen peroxide at platinum electrodes. Part IV: phosphate buffer dependence," *Electrochimica Acta,* vol. 44, pp. 4573-4582, Oct 1999.

[149] T. R. Kline, W. F. Paxton, Y. Wang, D. Velegol, T. E. Mallouk, and A. Sen, "Catalytic micropumps: Microscopic convective fluid flow and pattern formation," *Journal of the American Chemical Society,* vol. 127, pp. 17150-17151, Dec 2005.

[150] S. Sengupta, D. Patra, I. Ortiz-Rivera, A. Agrawal, S. Shklyaev, K. K. Dey*, et al.*, "Self-powered enzyme micropumps," *Nature chemistry,* vol. 6, pp. 415-22, May 2014.

[151] S. Suzuki, T. Onodera, J. Kawaji, T. Mizukami, and K. Yamaga, "Effect of support materials on platinum lattice strain and its oxygen reduction activity," *Applied Catalysis a-General,* vol. 427, pp. 92-97, Jun 2012.

[152] X. Qin, H. Wang, X. Wang, Z. Miao, Y. Fang, Q. Chen*, et al.*, "Synthesis of dendritic silver nanostructures and their application in hydrogen peroxide electroreduction," *Electrochimica Acta,* vol. 56, pp. 3170-3174, Mar 30, 2011.

[153] F. Winkel, S. Messlinger, W. Schopf, I. Rehberg, M. Siebenburger, and M. Ballauff, "Thermal convection in a thermosensitive colloidal suspension," *New Journal of Physics,* vol. 12, p. 18, May 2010.

[154] P. Morier, C. Vollet, P. E. Michel, F. Reymond, and J. S. Rossier, "Gravity-induced convective flow in microfluidic systems: Electrochemical characterization and application to enzyme-linked immunosorbent assay tests," *Electrophoresis,* vol. 25, pp. 3761-3768, 2004.

[155] A. Hamid, J. J. Molina, and R. Yamamoto, "Simulation studies of microstructure of colloids in sedimentation," *Molecular Simulation,* vol. 41, pp. 968-973, Aug 2015.

[156] M. H. G. Duits, S. Ghosh, and F. Mugele, "Measuring Advection and Diffusion of Colloids in Shear Flow," *Langmuir,* vol. 31, pp. 5689-5700, Jun 2, 2015.

[157] A. W. C. Lau and T. C. Lubensky, "Fluctuating hydrodynamics and microrheology of a dilute suspension of swimming bacteria," *Physical Review E,* vol. 80, Jul 2009.

[158] D. T. N. Chen, A. W. C. Lau, L. A. Hough, M. F. Islam, M. Goulian, T. C. Lubensky*, et al.*, "Fluctuations and rheology in active bacterial suspensions," *Physical Review Letters,* vol. 99, Oct 5, 2007.

[159] A. W. C. Lau, B. D. Hoffman, A. Davies, J. C. Crocker, and T. C. Lubensky, "Microrheology, stress fluctuations, and active behavior of living cells," *Physical Review Letters,* vol. 91, Nov 7, 2003.

[160] R. Golestanian, "Anomalous Diffusion of Symmetric and Asymmetric Active Colloids," *Physical Review Letters,* vol. 102, May 2009.

[161] W. C. K. Poon, "Colloidal Suspensions," in *The Oxford Handbook of Soft Condensed Matter*, E. M. Terentjev and D. A. Weitz, Eds., 1st ed: Oxford University Press, 2015.

[162] E. Lattuada, S. Buzzaccaro, and R. Piazza, "Colloidal Swarms Can Settle Faster than Isolated Particles: Enhanced Sedimentation near Phase Separation," *Physical Review Letters,* vol. 116, p. 5, Jan 2016.

[163] S. Ghosh, D. Wijnperle, F. Mugele, and M. H. G. Duits, "Dynamics of colloids confined in microcylinders," *Soft Matter,* vol. 12, pp. 1621-1630, 2016.

[164] R. Golestanian, T. B. Liverpool, and A. Ajdari, "Designing phoretic micro- and nano-swimmers," *New Journal of Physics,* vol. 9, May 15, 2007.

[165] D. A. Wilson, B. de Nijs, A. van Blaaderen, R. J. M. Nolte, and J. C. M. van Hest, "Fuel concentration dependent movement of supramolecular catalytic nanomotors," *Nanoscale,* vol. 5, pp. 1315-1318, 2013.

[166] S. Campuzano, J. Orozco, D. Kagan, M. Guix, W. Gao, S. Sattayasamitsathit*, et al.*, "Bacterial Isolation by Lectin-Modified Microengines," *Nano Letters,* vol. 12, pp. 396-401, Jan 2012.

[167] G. Zhao, H. Wang, B. Khezri, R. D. Webster, and M. Pumera, "Influence of real-world environments on the motion of catalytic bubble-propelled micromotors," *Lab on a Chip,* vol. 13, pp. 2937-2941, 2013.

[168] S. Sanchez, A. A. Solovev, S. M. Harazim, and O. G. Schmidt, "Microbots Swimming in the Flowing Streams of Microfluidic Channels," *Journal of the American Chemical Society,* vol. 133, pp. 701-703, Feb 2, 2011.

[169] A. Agrawal, K. K. Dey, A. Paul, S. Basu, and A. Chattopadhyay, "Chemical locomotives based on polymer supported catalytic nanoparticles," *Journal of Physical Chemistry C,* vol. 112, pp. 2797-2801, Feb 28, 2008.

[170] S. Ghosh, S. Chakrabarty, D. Bhowmik, G. S. Kumar, and N. Chattopadhyay, "Stepwise Unfolding of Bovine and Human Serum Albumin by an Anionic Surfactant: An Investigation Using the Proton Transfer Probe Norharmane," *Journal of Physical Chemistry B,* vol. 119, pp. 2090-2102, Feb 12, 2015.

[171] C. Vepari and D. L. Kaplan, "Silk as a biomaterial," *Progress in Polymer Science,* vol. 32, pp. 991-1007, Sep 2007.

[172] B. Kundu, N. E. Kurland, V. K. Yadavalli, and S. C. Kundu, "Isolation and processing of silk proteins for biomedical applications," *International Journal of Biological Macromolecules,* vol. 70, pp. 70-77, Sep 2014.

[173] L. S. Wray, X. Hu, J. Gallego, I. Georgakoudi, F. G. Omenetto, D. Schmidt*, et al.*, "Effect of processing on silk-based biomaterials: Reproducibility and biocompatibility," *Journal of Biomedical Materials Research Part B-Applied Biomaterials,* vol. 99B, pp. 89-101, Oct 2011.

[174] Y. Q. Zhang, "Natural silk fibroin as a support for enzyme immobilization," *Biotechnology Advances,* vol. 16, pp. 961-971, Nov 1998.

[175] S. Z. Lu, X. Q. Wang, Q. Lu, X. Hu, N. Uppal, F. G. Omenetto*, et al.*, "Stabilization of Enzymes in Silk Films," *Biomacromolecules,* vol. 10, pp. 1032-1042, May 2009.

[176] P. Wang, C. Qi, Y. Yu, J. Yuan, L. Cui, G. Tang*, et al.*, "Covalent Immobilization of Catalase onto Regenerated Silk Fibroins via Tyrosinase-Catalyzed Cross-Linking," *Applied Biochemistry and Biotechnology,* vol. 177, pp. 472-485, Sep 1, 2015.

[177] E. M. Pritchard, P. B. Dennis, F. Omenetto, R. R. Naik, and D. L. Kaplan, "Physical and chemical aspects of stabilization of compounds in silk," *Biopolymers,* vol. 97, pp. 479-498, 2012.

[178] K. Numata and D. L. Kaplan, "Silk-based delivery systems of bioactive molecules," *Advanced Drug Delivery Reviews,* vol. 62, pp. 1497-1508, Dec 30, 2010.

[179] X. Wang, T. Yucel, Q. Lu, X. Hu, and D. L. Kaplan, "Silk nanospheres and microspheres from silk/pva blend films for drug delivery," *Biomaterials,* vol. 31, pp. 1025-1035, Feb 2010.

[180] X. Wang, E. Wenk, A. Matsumoto, L. Meinel, C. Li, and D. L. Kaplan, "Silk microspheres for encapsulation and controlled release," *Journal of Controlled Release,* vol. 117, pp. 360-370, Feb 26, 2007.

[181] E. Wenk, A. J. Wandrey, H. P. Merkle, and L. Meinel, "Silk fibroin spheres as a platform for controlled drug delivery," *Journal of Controlled Release,* vol. 132, pp. 26-34, Nov 24, 2008.

[182] S. Hofmann, C. T. Wong Po Foo, F. Rossetti, M. Textor, G. Vunjak-Novakovic, D. L. Kaplan*, et al.*, "Silk fibroin as an organic polymer for controlled drug delivery," *Journal of Controlled Release,* vol. 111, pp. 219-227, Oct 3, 2006.

[183] E. Wenk, H. P. Merkle, and L. Meinel, "Silk fibroin as a vehicle for drug delivery applications," *Journal of Controlled Release,* vol. 150, pp. 128-141, Mar 10, 2011.

[184] C. E. Hendriks, P. J. Smith, J. Perelaer, A. M. J. Van den Berg, and U. S. Schubert, ""Invisible" silver tracks produced by combining hot-embossing and inkjet printing," *Advanced Functional Materials,* vol. 18, pp. 1031-1038, Apr 11, 2008.

[185] H. Tao, B. Marelli, M. Yang, B. An, M. S. Onses, J. A. Rogers*, et al.*, "Inkjet Printing of Regenerated Silk Fibroin: From Printable Forms to Printable Functions," *Advanced Materials,* vol. 27, pp. 4273-4279, Aug 5, 2015.

[186] B. B. Mandal, A. Grinberg, E. Seok Gil, B. Panilaitis, and D. L. Kaplan, "High-strength silk protein scaffolds for bone repair," *Proceedings of the National Academy of Sciences,* vol. 109, pp. 7699-7704, May 15, 2012.

[187] B. Kundu, R. Rajkhowa, S. C. Kundu, and X. Wang, "Silk fibroin biomaterials for tissue regenerations," *Advanced Drug Delivery Reviews,* vol. 65, pp. 457-470, Apr 2013.

[188] H. J. Jin, J. Park, V. Karageorgiou, U. J. Kim, R. Valluzzi, and D. L. Kaplan, "Water-stable silk films with reduced β-sheet content," *Advanced Functional Materials,* vol. 15, pp. 1241-1247, Aug 2005.

[189] D. N. Rockwood, R. C. Preda, T. Yucel, X. Wang, M. L. Lovett, and D. L. Kaplan, "Materials fabrication from Bombyx mori silk fibroin," *Nature Protocols,* vol. 6, pp. 1612-1631, Oct 2011.

[190] H. J. Jin and D. L. Kaplan, "Mechanism of silk processing in insects and spiders," *Nature,* vol. 424, pp. 1057-1061, Aug 2003.

[191] A. Motta, L. Fambri, and C. Migliaresi, "Regenerated silk fibroin films: Thermal and dynamic mechanical analysis," *Macromolecular Chemistry and Physics,* vol. 203, pp. 1658-1665, Jul 2002.

[192] P. J. Smith and A. Morrin, "Reactive inkjet printing," *Journal of Materials Chemistry,* vol. 22, pp. 10965-10970, 2012.

[193] X. Y. Zhang and Y. D. Zhang, "Tissue Engineering Applications of Three-Dimensional Bioprinting," *Cell Biochemistry and Biophysics,* vol. 72, pp. 777-782, Jul 2015.

[194] A. M. J. van den Berg, P. J. Smith, J. Perelaer, W. Schrof, S. Koltzenburg, and U. S. Schubert, "Inkjet printing of polyurethane colloidal suspensions," *Soft Matter,* vol. 3, pp. 238-243, 2007.

[195] A. M. J. van den Berg, A. W. M. de laat, P. J. Smith, J. Perelaer, and U. S. Schubert, "Geometric control of inkjet printed features using a gelating polymer," *Journal of Materials Chemistry,* vol. 17, pp. 677-683, 2007.

[196] H. Yamada, H. Nakao, Y. Takasu, and K. Tsubouchi, "Preparation of undegraded native molecular fibroin solution from silkworm cocoons," *Materials Science & Engineering C-Biomimetic and Supramolecular Systems,* vol. 14, pp. 41-46, Aug 15, 2001.

[197] A. Ajisawa, "Dissolution of silk fibroin with calciumchloride/ethanol aqueous solution," *The Journal of Sericultural Science of Japan,* vol. 67, pp. 91-94, 1998.

[198] F. Cordelieres. (2005, 01). *Manual Tracking Plugin for ImageJ* [Software]. Available: http://rsb.info.nih.gov/ij/plugins/track/track.html

[199] C. Mateo, J. M. Palomo, G. Fernandez-Lorente, J. M. Guisan, and R. Fernandez-Lafuente, "Improvement of enzyme activity, stability and selectivity via immobilization techniques," *Enzyme and Microbial Technology,* vol. 40, pp. 1451-1463, May 2, 2007.

[200] H. D. Chirra, T. Sexton, D. Biswal, L. B. Hersh, and J. Z. Hilt, "Catalase-coupled gold nanoparticles: Comparison between the carbodiimide and biotin-streptavidin methods," *Acta Biomaterialia,* vol. 7, pp. 2865-2872, Jul 2011.

[201] D. P. Manica, Y. Mitsumori, and A. G. Ewing, "Characterization of Electrode Fouling and Surface Regeneration for a Platinum Electrode on an Electrophoresis Microchip," *Analytical Chemistry,* vol. 75, pp. 4572-4577, Sep 3, 2003.

[202] C. P. Vepari and D. L. Kaplan, "Covalently immobilized enzyme gradients within three-dimensional porous scaffolds," *Biotechnology and Bioengineering,* vol. 93, pp. 1130-1137, 2006.

[203] D. A. Gregory, Y. Zhang, P. J. Smith, S. J. Ebbens, and X. Zhao, "Reactive Inkjet Printing of Biocompatible Enzyme Powered Silk Micro-Rockets," *Small,* vol. 12, pp. 4048-4055, 2016.

[204] D. A. Gregory, Y. Zhang, P. J. Smith, X. Zhao, and S. J. Ebbens, "Reactive Inkjet Printing: Reactive Inkjet Printing of Biocompatible Enzyme Powered Silk Micro-Rockets (Small 30/2016)," *Small,* vol. 12, pp. 4022-4022, 2016.

10. Appendix

10.1. Inner Cover Image in Small Journal

The cover Image as I designed if for the Small publication [203, 204]

The following additional figures show LabVIEW software programmed for this thesis.

10.2. Area Calculation Program

This program was created to calculate the area of the sample that was coated in metal (i.e. Platinum) to allow for accurate reaction rate calculations (Front Panel image shown in Figure 10-1). The program uses State Machine architecture (Figure 10-2) to allow for a more interactive and versatile image processing along with low CPU usage while the user choses what action to do next. The program then generates an automatic excel report with the area calculated for the image accord to the calibration values defined (Figure 10-3).

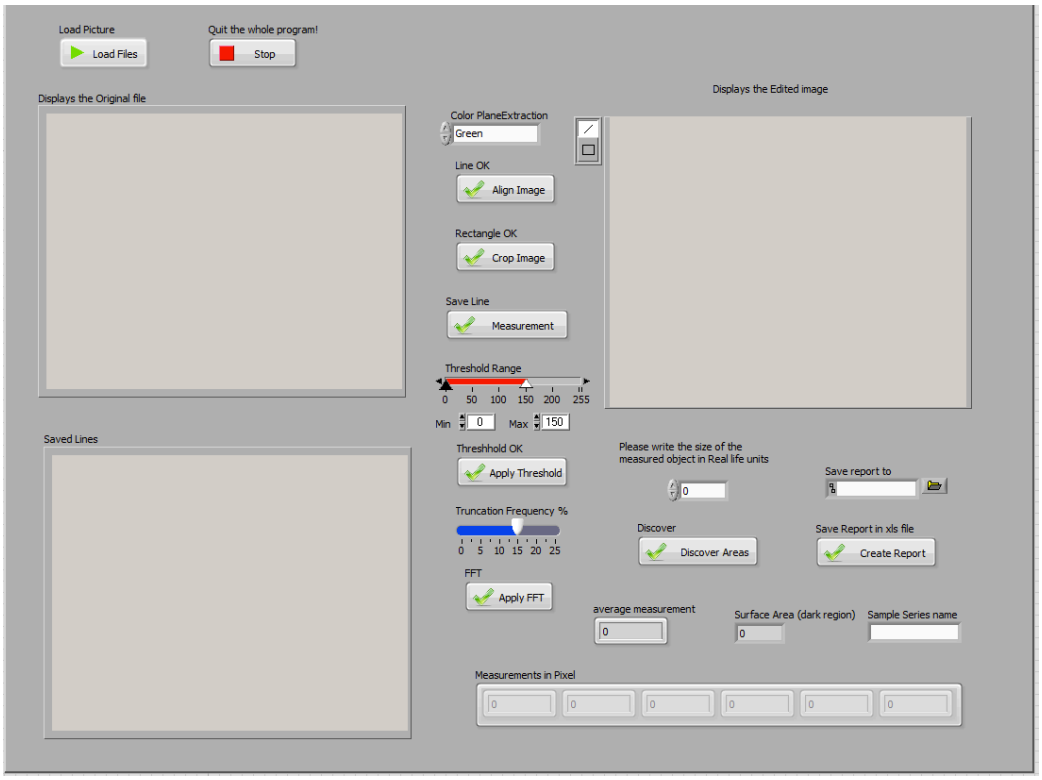

Figure 10-1 Custom made Labview program for image area calculation, Front panel inputs.

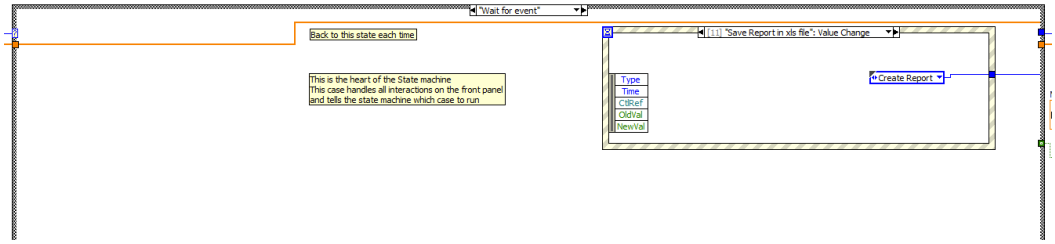

Figure 10-2 Custom Made Labview program for image area calculation, Main loop of the State Machine.

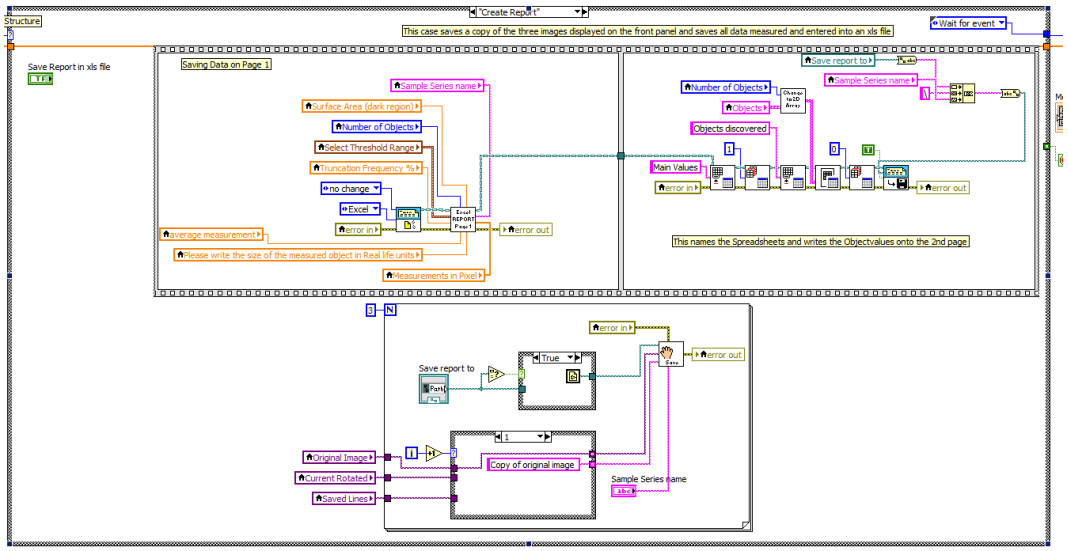

Figure 10-3 Custom made labview program for image area calculation, some of the code for creating the *.xls report document and report images.

10.3. Image Subtraction Program for bubble swimmers

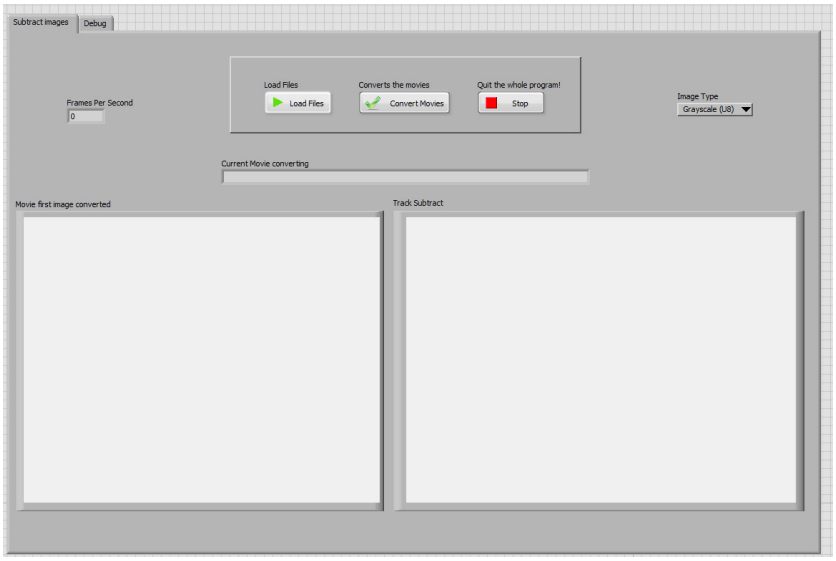

Figure 10-4 From panel of Image subtraction program for bubble swimmers

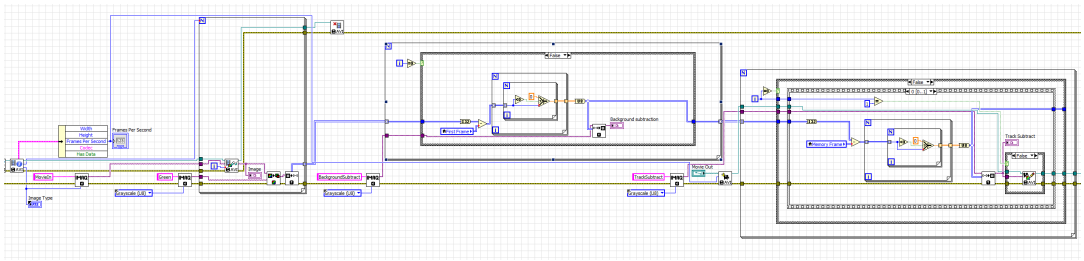

Figure 10-5 Main image subtraction code.

10.4. Trajectory analysis program

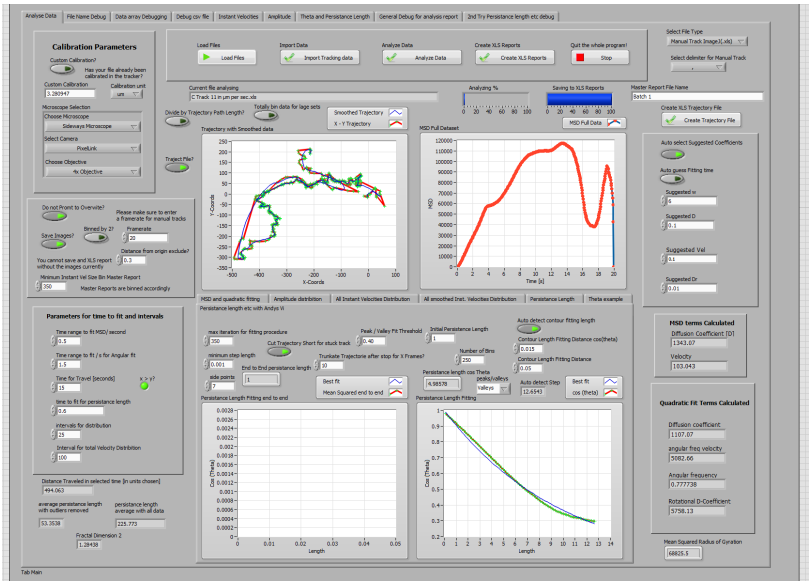

Figure 10-6 Main front panel for multiple data analysis of trajectories.

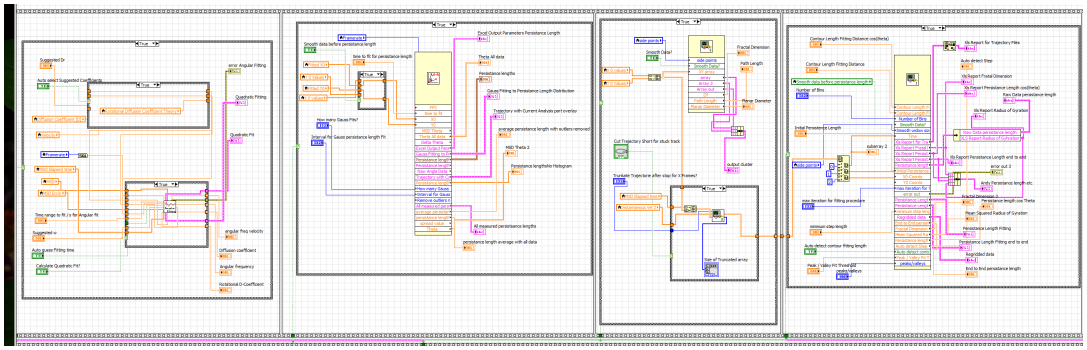

Figure 10-7 Some example program code part 1

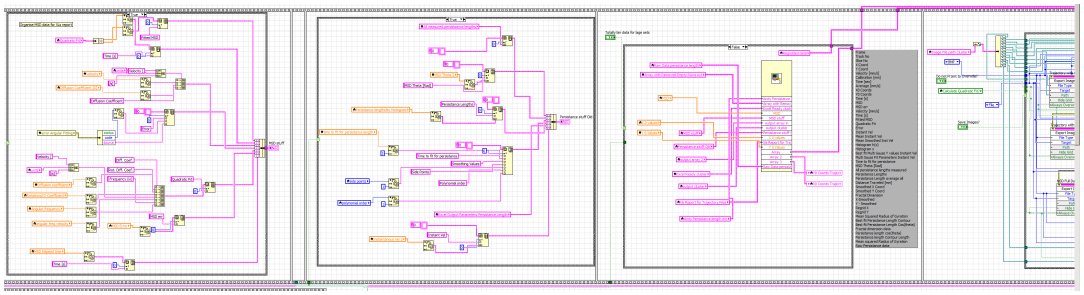

Figure 10-8 Some example program code part 2

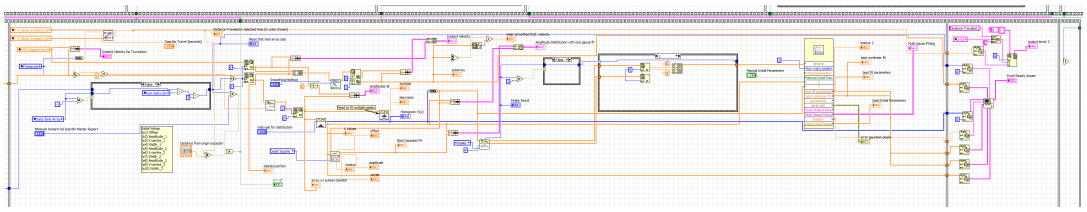

Figure 10-9 Some example program code part 3

10.5. 2D Stochastic Model

This is the LabVIEW program that was developed to simulate bubble propulsion for different catalytically active areas on a colloid (pore size), see Chapter 5.

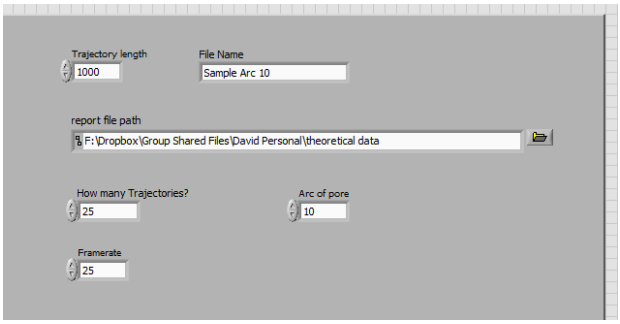

Figure 10-10 The front panel of the program, where multiple trajectory files are generated.

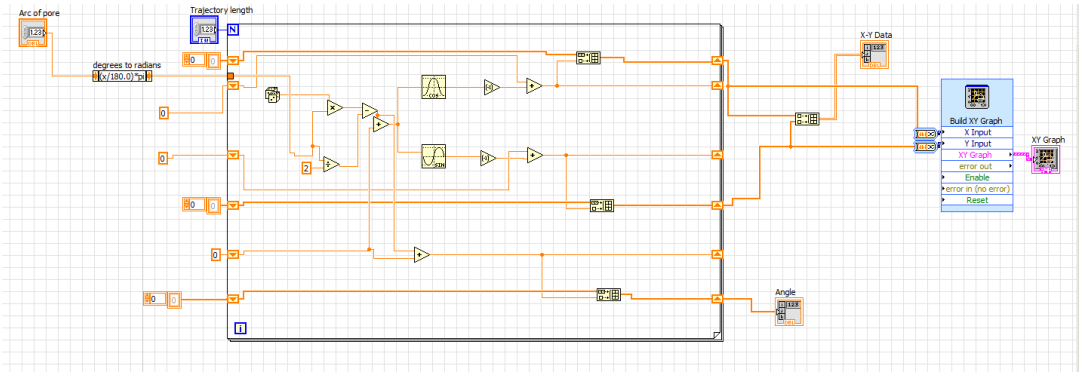

Figure 10-11 The model calculation SubVi for one individual calculation.

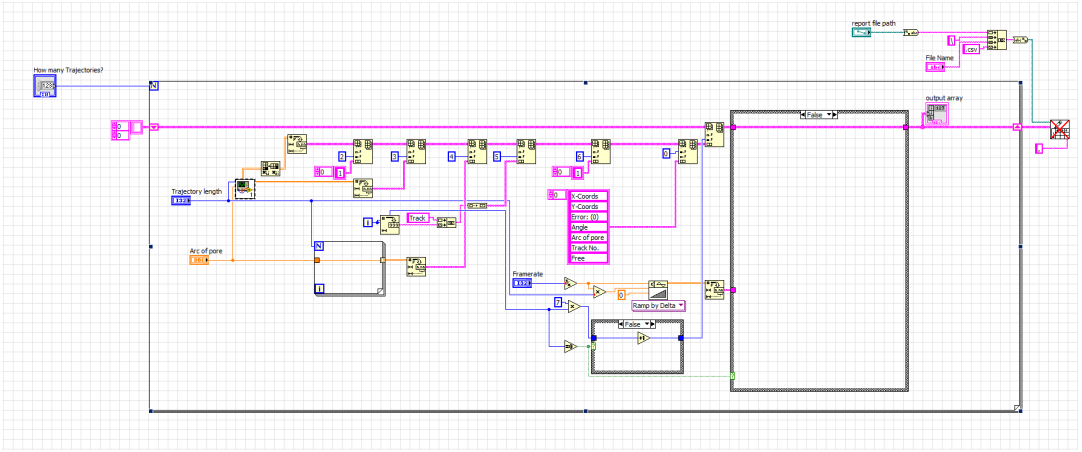

Figure 10-12 The batch processing and trajectory *.csv file output

10.6. Swimmer Particle Orientation Analyser

This program was created to be able to import dual tracks of particles and convert them into the angles theta and phi in order to correlate between the particle orientation and the particle directional angle over time. Figure 10-13 shows part of the code in order to calculate the angles dependant on which points were used.

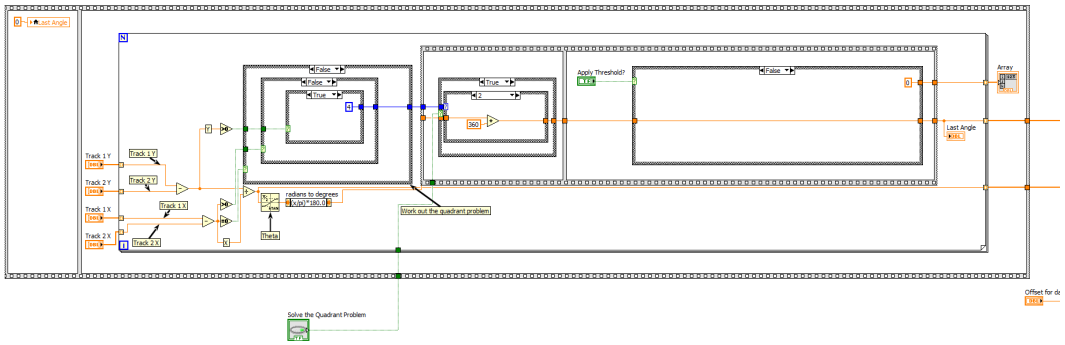

Figure 10-13 Example code of the angle calculation together with solving the quadrant problem for the tangent function

10.7. Particle counting program

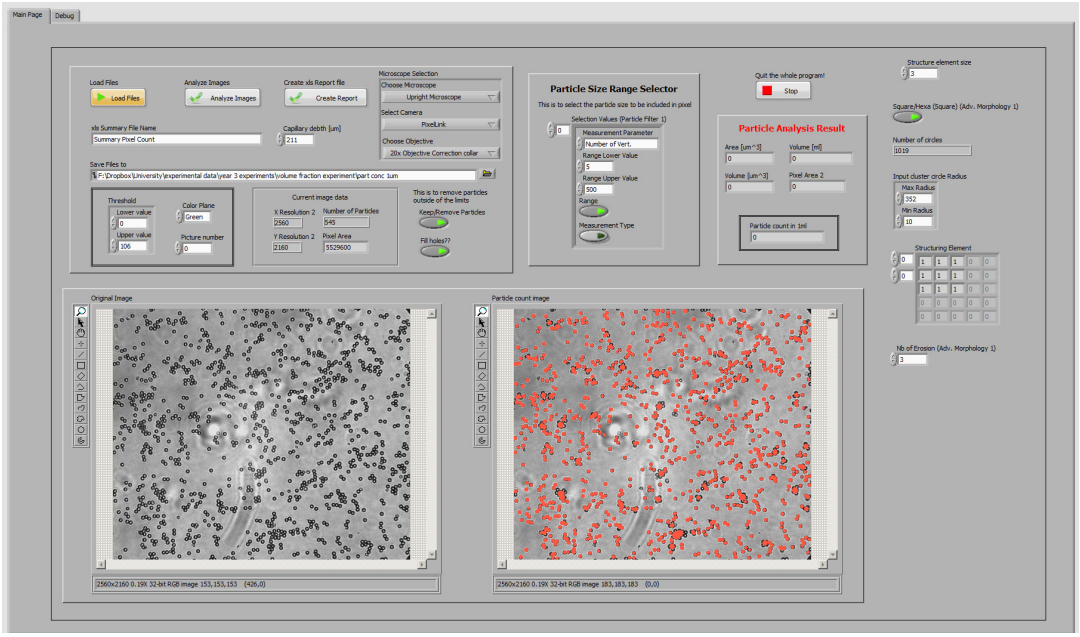

Figure 10-14 Front Panel Particle Counting Program

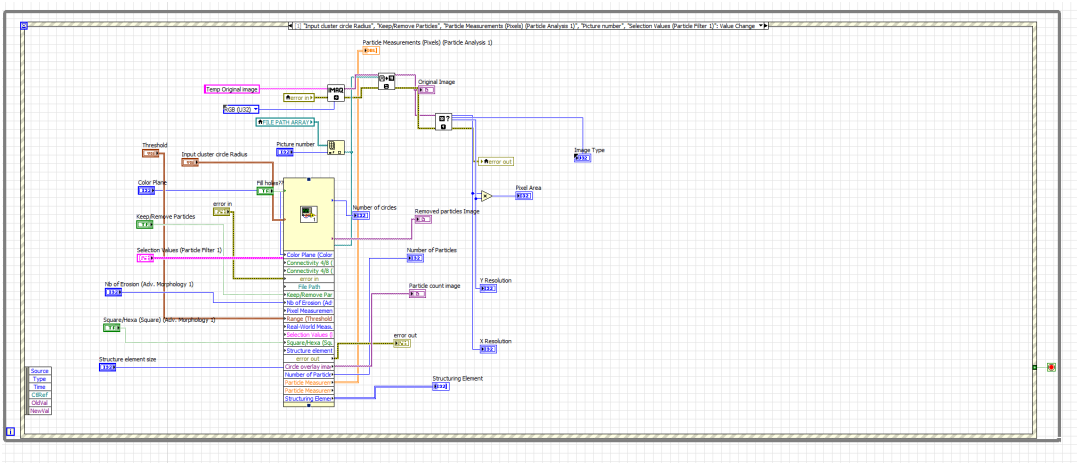

Figure 10-15 Main State Machine code for particle counting program

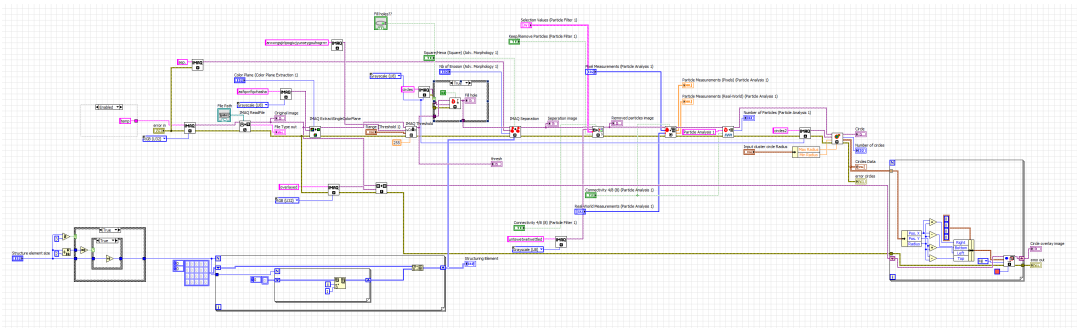

Figure 10-16 The heart of the matter - analysing the particles

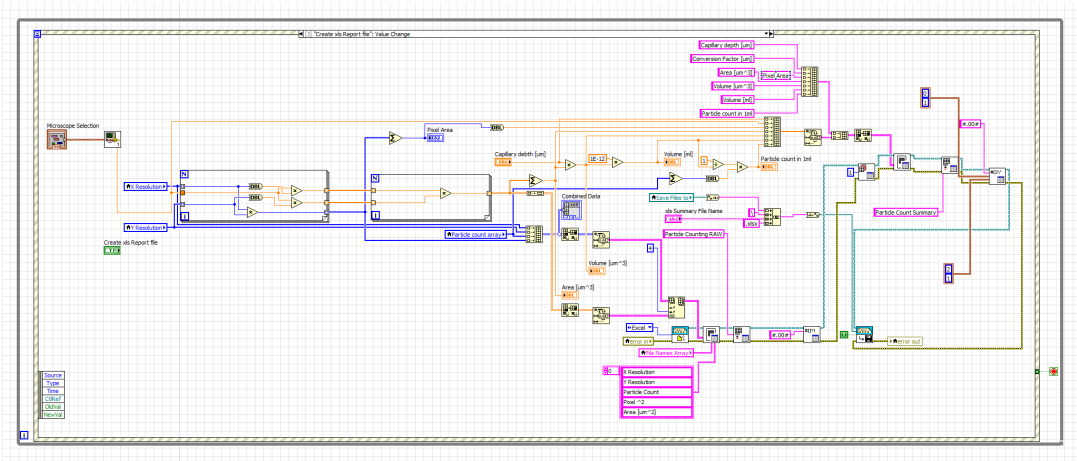

Figure 10-17 Excel Report generation for particle counting program

10.8. Trajectory Overlay program for track representations

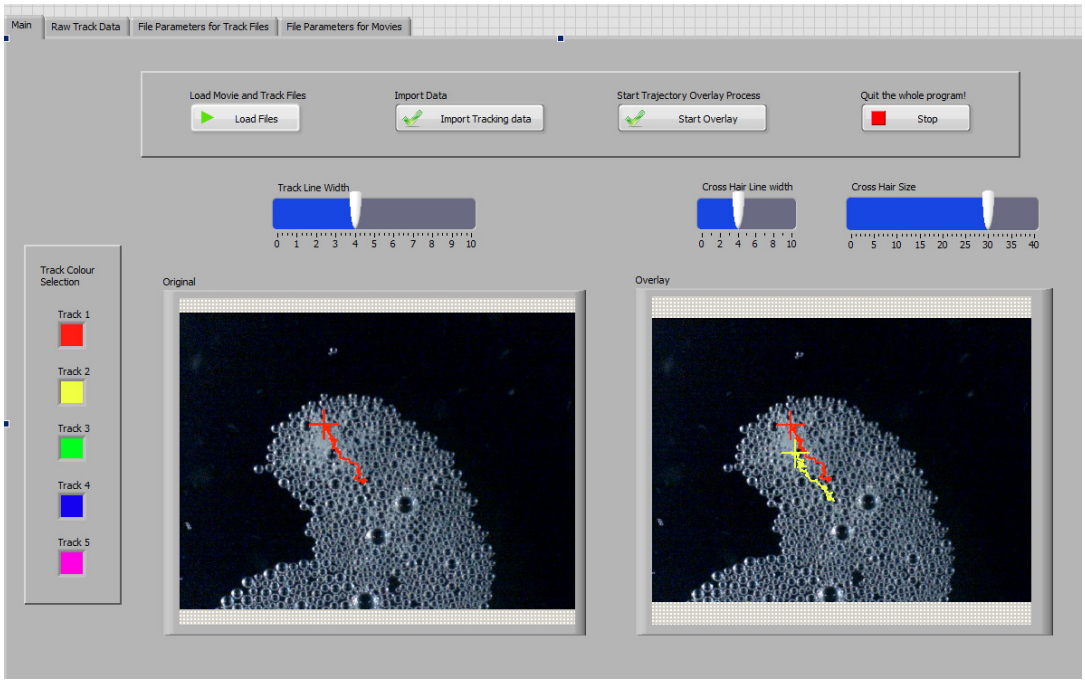

Figure 10-18 Main Panel showing tracks being overlaid onto movies.

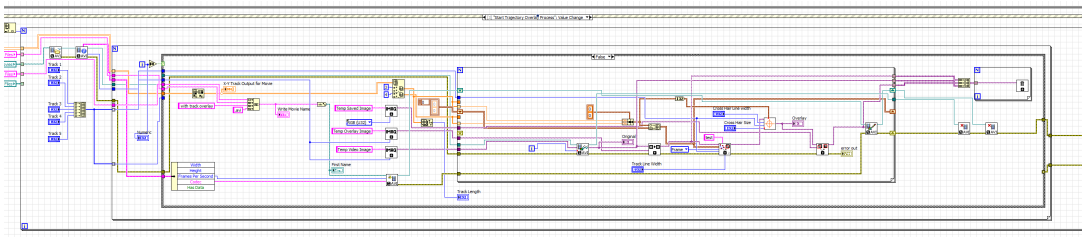

Figure 10-19 Main track overlay code

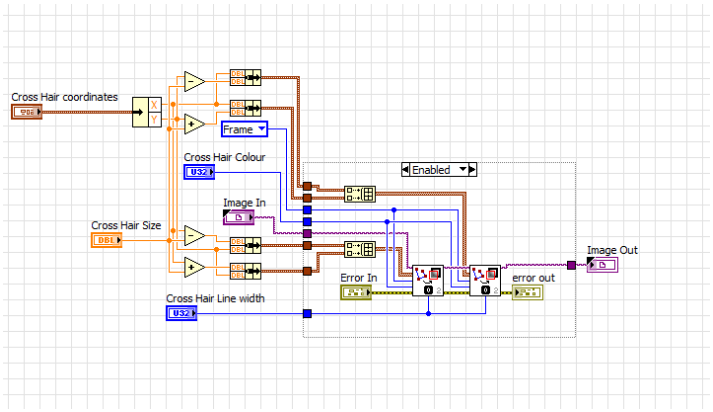

Figure 10-20 Code to generate crosshairs

10.9. On-the-fly MSD and Diffusion coefficients, movie recording and 3D tracking software

An attempt was made to create a program that could calculate the MSD and diffusion coefficient of a tracked colloid on the fly while streaming over a PixeLink camera. In addition to this it was attempted to keep the particle automatically in focus and from this extract the z-values from the focus changes over time to generate 3D tracks of non-fluorescent particles. The program functions properly, however there are still calibrations that need to be done in conjunction with the 3D tracking and possibly a FFT approach might help hold the focus of the selected colloid better.

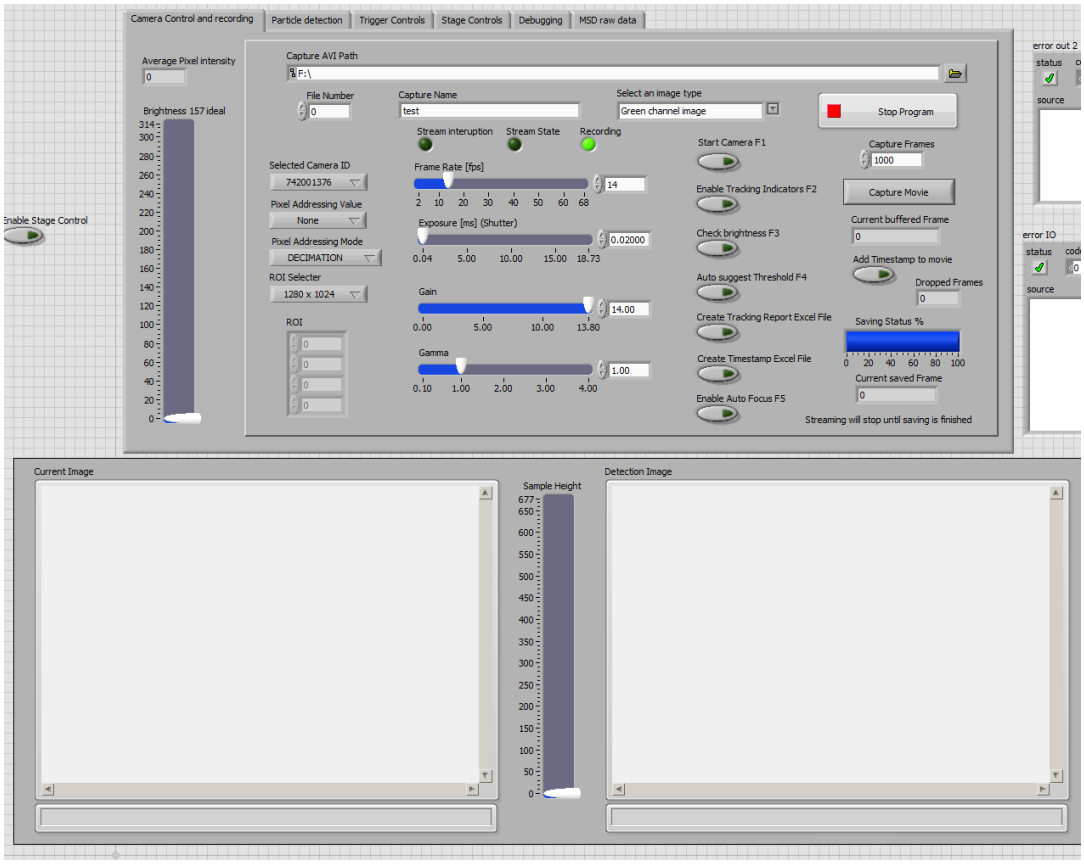

Figure 10-21 Front panel for the on the fly tracking and MSD calculation program.

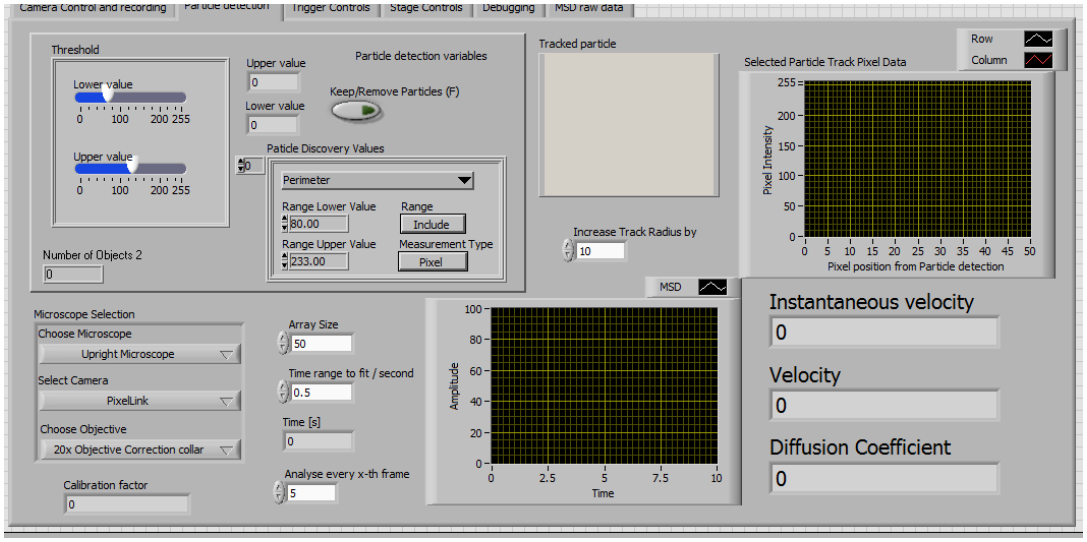

Figure 10-22 Front panel showing the MSD velocity and Diffusion coefficient data calculated on the fly dependant on the selected sample bin (Array size).

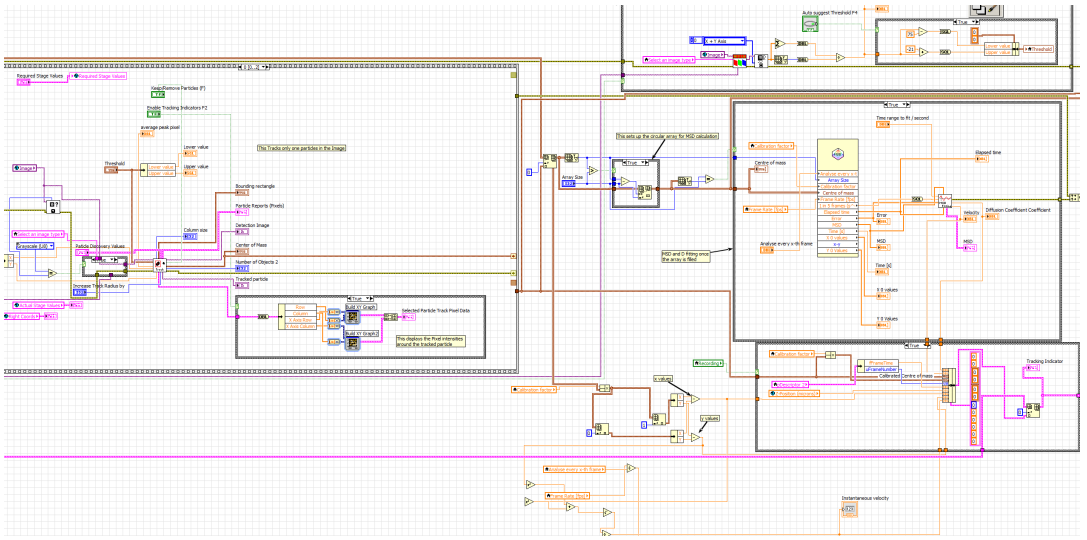

Figure 10-23 Some of the code to calculate the MSD on the fly.